

Toward a First-Principles Evaluation of Transport Mechanisms in Molecular Wires

Dissertation
with the aim of achieving a doctoral degree
at the Faculty of Mathematics, Informatics and Natural Sciences
Department of Chemistry
University of Hamburg

submitted by

Susanne Kröncke

January 2021

The present work was carried out in the period from September 2017 to January 2021 in the Institute of Inorganic and Applied Chemistry at the University of Hamburg in the group of Prof. Dr. Carmen Herrmann.

Examiner: Prof. Dr. Carmen Herrmann

Co-examiner: Prof. Dr. Gabriel Bester

Date of submission: 20.01.2021

Date of oral defense: 12.03.2021

Contents

i	Abstract	iv
ii	Zusammenfassung	vi
iii	Publications	viii
I	INTRODUCTION	1
II	THEORETICAL AND EXPERIMENTAL BACKGROUND	5
1	Charge Transport Phenomena and Concepts	5
1.1	Studying Charge Transport in Molecular Junctions	5
1.2	Length-dependent Transition from Tunneling to Hopping	9
1.3	Intermediate Charge Transport Regimes in DNA	25
2	Charge Localization in Molecular Wires	31
2.1	Charge Transfer in Organic Mixed-valence Systems	31
2.2	Class III–II Transitions in MV Systems – State of the Art	37
2.3	DFT Approaches for Describing Charge Localization	43
III	CHARGE TRANSFER IN MIXED-VALENCE SYSTEMS	55
3	Describing Class III–II Transitions in Mixed-Valence Systems: Validation of DFT Approaches	55
3.1	Introduction	55
3.2	Theoretical Measures for Charge Localization	56
3.3	Describing Class III–II Transitions: DFT Results	60
3.4	Conclusions	69
4	Designing Long-range Charge Delocalization in Molecular Wires	73
4.1	Introduction	73
4.2	Tuning Delocalization in Captodative-substituted DMP_n	74
4.3	Impact of Linkage Topology and Bulky Substituents	77
4.4	Conclusions	83

5	Investigating Electron Transfer in Radical Anions	85
5.1	Introduction	85
5.2	Class III–II Transitions in Radical Anions: DFT Results	85
5.3	Conclusions	100
IV CHARGE TRANSPORT IN MOLECULAR WIRES		103
6	Predicting the Length-dependent Crossover from DFT	103
6.1	Introduction	103
6.2	New Charge Delocalization Measures Tailored for Molecular Wires	104
6.3	Predicting the Length-dependent Crossover: DFT Results	109
6.4	Getting Charge Localization Right – Essential Ingredients	120
6.5	Intermediate Transport Regimes in G-DNA: DFT Results	126
6.6	Conclusions	131
7	Toward More Efficient Approaches to Predicting Charge Transport Mechanisms	137
7.1	Introduction	137
7.2	Semi-empirical Methods for Predicting Charge Transport Mechanisms	140
7.3	Conclusions	145
V CONCLUSIONS AND PERSPECTIVES		147
VI ACKNOWLEDGEMENTS		153
A Appendix		155
A.1	DMP _n – Structural Parameters and Local Properties	155
A.2	(An ₂ N) ₂ T _n and OPV _n – Local Charge Ratios	160
A.3	Bulky Thiophenes and Captodative (An ₂ N) ₂ Ph _n and DMP _n Species	161
A.4	ONI _n and OPE _n Wires – Structural Parameters	167
A.5	Assessing the Degree of Charge Delocalization in Molecular Wires	168
A.6	Potential Energy Surface for Ring Torsion in OPE _n	173
A.7	Isolated OPTI _n Wires: BLYP35, LC-DFT and AM1 Results . .	175
B List of Abbreviations		177
References		179

i. Abstract

The quest for a deep understanding of charge transport through molecular wires is not only driven by its vital importance for biochemical processes, but also by the perspective of establishing novel functionalities beyond conventional silicon-based electronics. A central question in this context is whether the charge transport is governed by a coherent tunneling or by an incoherent hopping mechanism, which are the two main transport regimes observed in molecular conductance experiments. The predominant charge transport mechanism is strongly determined by the molecular length: a transition from the tunneling to the hopping regime is commonly indicated by a change of the length and temperature dependence of the conductance when going from shorter to longer wires around 3 to 4 nm. Since the theoretical descriptions of these two transport regimes are fundamentally different, this work aims at a predictive approach that allows for identifying the crossover length and, thus, the transport mechanism in any kind of molecular wires in an easily applicable and computationally efficient way. The core idea behind the strategy presented in this work relies on the association of the predominating transport mechanism with charge localization properties, where transport by tunneling and hopping would be connected to delocalization and localization of an excess charge, respectively.

Building on this concept, a variety of computational protocols based on Kohn–Sham density functional theory was validated with respect to their performance of describing length-dependent charge localization in organic mixed-valence systems as observed in experiments. These donor–bridge–acceptor complexes function as model systems for molecular junctions in this work due to their close relation to charge transport mechanisms based on equally length-dependent electron-transfer properties, as characterized by their Robin–Day classes.

Here, it is shown that a protocol based on the non-standard BLYP35 hybrid functional combined with a polarizable continuum model, suggested earlier by Renz and Kaupp, performs well in characterizing length-dependent charge localization in mixed-valence compounds in agreement with the experiments, even

when they are located on the borderline between charge delocalization and localization. In contrast, caution needs to be exercised when applying long-range corrected functionals such as ω -B97X-D or ω -PBE with high amounts of exact exchange, as they have a tendency of overlocalization. Moreover, the computational protocol was used to demonstrate how charge delocalization can be tuned toward longer bridge lengths in *para*-phenylene-based wires by exploiting a captodative substitution approach that was proposed earlier in the context of molecular conductance by Stuyver and coworkers.

In the second part of this work, the DFT protocol was combined with a new measure for charge delocalization tailored for molecular wires to predict the charge transport mechanism indicated from experiments on molecular junctions at room temperature. On the example of five different sets of conjugated organic molecular wires, it was demonstrated that the tunneling-to-hopping transition length can be determined with a maximum error of one subunit.

Based on the results obtained with the BLYP35 protocol in this work, it can be anticipated that it performs just as well for estimating the extent of hopping sites that are involved in the charge transport in, for example, biomolecules such as proteins or DNA, where not only the molecular length, but also the chemical structure or base sequence determines the transport mechanism.

Preliminary results were obtained on two variants of guanine-based DNA strands in this work, for which the presence of an intermediate tunneling-hopping regime, as indicated from experiments by Tao and coworkers, was supported by calculations with the BLYP35 protocol. Moreover, promising results obtained for radical anionic mixed-valence systems may pave the way for the extension of the BLYP35 protocol to the prediction of electron rather than hole transport. Altogether, the findings resulting from this work represent a step toward the prediction of length-dependent charge transport mechanisms in molecular wires based on a first-principles protocol that is easily applicable to a variety of species. Moreover, the approach presented here offers the possibility of gaining deeper insights into the extent of hopping sites involved in the transport process. With a view to screening larger data sets of molecules and building on preliminary results from this work, semi-empirical methods may be evaluated in more detail as a less computationally expensive alternative to DFT calculations in the future, thus contributing to an efficient and predictive theoretical framework for molecular electronics.

ii. Zusammenfassung

Das Streben nach einem tiefen Verständnis von Ladungstransport durch Moleküle wird nicht nur durch dessen entscheidende Bedeutung für biochemische Prozesse angetrieben, sondern auch durch die Perspektive, neuartige Funktionalitäten jenseits von konventioneller Silizium-basierter Elektronik zu etablieren. Eine zentrale Frage in diesem Zusammenhang ist, ob der Ladungstransportmechanismus eher durch kohärentes Tunneln oder durch inkohärentes Hopping bestimmt wird; dies sind die beiden vorherrschenden Transportregimes, die in Leitfähigkeitsexperimenten beobachtet werden. Der dominierende Transportmechanismus wird maßgeblich durch die Moleküllänge bestimmt: Ein Wechsel vom Tunnel- zum Hoppingregime zeigt sich üblicherweise beim Übergang von kurzen zu langen Moleküldrähten bei circa 3-4 nm durch eine veränderte Längen- und Temperaturabhängigkeit der Leitfähigkeit. Da sich die theoretische Beschreibung beider Regimes fundamental unterscheidet, zielt diese Arbeit auf einen leicht handhabbaren und effizienten Ansatz für die Vorhersage der Übergangslänge und somit des Transportmechanismus in Moleküldrähten ab. Die hier gezeigte Strategie basiert auf der zentralen Idee, den Transportmechanismus mit der Ladungslokalisierung zu verknüpfen, wobei Transport durch Tunneln und Hopping jeweils mit Delokalisierung oder Lokalisierung der Ladung assoziiert wird. Auf diesem Konzept aufbauend wurden Rechenmethoden basierend auf Kohn-Sham-Dichtefunktionaltheorie validiert in Hinblick auf deren Fähigkeit, die längenabhängige Ladungslokalisierung in organischen gemischtvalenten Verbindungen gemäß dem Experiment zu beschreiben. Diese Donor-Brücke-Akzeptor Verbindungen fungieren hier als Modellsysteme für *molecular junctions*, da deren Elektronentransfer-Eigenschaften ebenfalls längenabhängig sind (charakterisiert durch die Robin-Day-Klasse) und somit eine enge konzeptionelle Verwandtschaft zu Ladungstransportmechanismen besteht. Es konnte gezeigt werden, dass ein Ansatz basierend auf dem BLYP35-Hybridfunktional kombiniert mit einem polarisierbaren Kontinuumsmodell, vorgeschlagen von Renz und Kaupp, die experimentelle längenabhängige Ladungslokalisierung von gemischtvalenten Systemen selbst im Grenzbere-

ich zwischen Delokalisierung und Lokalisierung korrekt beschreibt. Dagegen sind *long-range corrected* Funktionale mit einem hohen Anteil an exaktem Austausch (ω -B97X-D oder ω -PBE) wegen der Tendenz zur Überlokalisierung nicht empfehlenswert. Darüber hinaus konnte anhand des BLYP35-Protokolls gezeigt werden, wie Ladungsdelokalisierung in *para*-phenylene-basierten Drähten auf längere Molekülbrücken erreicht werden kann mithilfe eines *captodative-substitution*-Ansatzes, der vormals von Stuyver *et al.* im Kontext molekularer Leitfähigkeit vorgeschlagen wurde.

Im zweiten Teil dieser Arbeit wurde das BLYP35-Protokoll kombiniert mit einem neuartigen Maß für Ladungsdelokalisierung in molekularen Drähten, um den experimentell beobachteten Transportmechanismus bei Raumtemperatur vorherzusagen. Anhand von fünf Reihen konjugierter organischer Moleküle wurde gezeigt, dass die Moleküllänge, die den Übergang von Tunneln zu Hopping markiert, mit einer maximalen Abweichung von einer Untereinheit bestimmt werden kann. Die Berechnungen mit dem BLYP35-Protokoll legen nahe, dass sich dieser Ansatz gleichermaßen für die Abschätzung der Ausdehnung von *hopping sites* eignet, die in den Ladungstransport involviert sind, z. B. in Biomolekülen wie Proteinen oder DNA, in denen der Transportmechanismus nicht nur durch die Moleküllänge, sondern auch durch die chemische Struktur oder die Basensequenz bestimmt wird. Erste Ergebnisse in dieser Arbeit mit dem BLYP35-Protokoll für zwei Varianten von Guanin-basierter DNA stützen die Annahme eines intermediären Tunnel-Hopping Regimes, wie zuvor von Tao *et al.* postuliert. Aussichtsreiche Ergebnisse für radikal-anionische Systeme ebnen darüber hinaus den Weg für eine erweiterte Anwendung des BLYP35-Protokolls auf die Vorhersage von Elektronentransport neben Lochtransport.

Die Ergebnisse dieser Arbeit stellen einen Schritt zur Vorhersage des längenabhängigen Transportmechanismus in molekularen Drähten dar, basierend auf einem *first-principles*-Protokoll, das leicht anzuwenden ist auf eine Vielzahl an Spezies. Darüber hinaus bietet dieser Ansatz die Möglichkeit für ein tieferes Verständnis der in den Ladungstransportprozess involvierten *hopping sites*. In Hinblick auf die Untersuchung größerer Moleküldatensätze könnte in Zukunft, aufbauend auf ersten Ergebnissen dieser Arbeit, die Evaluation semiempirischer Methoden als weniger rechenintensive Alternative zu DFT-Berechnungen zu einem effizienten und prädiktiven theoretischen Ansatz für molekulare Elektronik beitragen.

iii. Publications

1. Susanne Kröncke and Carmen Herrmann, *Designing Long-Range Charge Delocalization from First-Principles* **2019**, 15, 165-177. (Based on parts of Sec. 3 and of Sec. 4, <https://pubs.acs.org/doi/10.1021/acs.jctc.8b00872>)
2. Susanne Kröncke and Carmen Herrmann, *Toward a First-Principles Evaluation of Transport Mechanisms in Molecular Wires* **2020**, 16, 6267-6279. (Based on parts of Sec. 6, <https://pubs.acs.org/doi/10.1021/acs.jctc.0c00667>)
3. Sebastian Sandl, Thomas M. Maier, Nicolaas P. van Leest, Susanne Kröncke, Uttam Chakraborty, Serhiy Demeshko, Konrad Koszinowski, Bas de Bruin, Franc Meyer, Michael Bodensteiner, Carmen Herrmann, Robert Wolf, and Axel Jacobi von Wangelin, *Cobalt-Catalyzed Hydrogenations via Olefin Cobaltate and Hydride Intermediates* **2019**, 9, 7596-7606. (<https://pubs.acs.org/doi/10.1021/acscatal.9b01584>)

I. INTRODUCTION

The integration of individual molecules in nanoelectronic circuits for the investigation of their electronic transport properties is the core idea behind the constantly growing research field of *molecular electronics* [1–3]. The motivation for exploring charge transport processes through molecular wires mainly stems from two different objectives: First, the application of single molecules as building blocks in nanoelectronic devices allows in principle for their miniaturization compared to conventional silicon-based technologies [1,2]. However, since nowadays the issue of miniaturization can be addressed by lithographic techniques, other challenges are coming to the fore, such as heating and leakage problems [1,4]. Beyond that, unique molecular properties, such as specific intermolecular interactions due to self-assembly or switching and sensing capabilities, can provide new functionalities that are not accessible with established technologies [1,2,5]. For example, molecular wires with greater insulating properties than vacuum may be used as single-molecule insulators [6–8], while diamagnetic helical molecules offer the potential of building more efficient water-splitting or memory devices by exploiting chiral-induced spin selectivity, as found in proteins or DNA [9–16]. At the same time, the practical benefits of using single-molecule devices are limited due to the challenge of forming stable and well-controlled contacts and due to the instability of molecules at high temperatures [1,5]. However, these limitations have been partially overcome, for example by using diazonium-derived molecular layers that are strongly bound covalently to the surface of a flat graphitic carbon substrate to produce more robust junctions [5,17–19].

Second, the investigation of conduction processes on the nanoscale is strongly motivated by the urge of a deeper understanding of fundamental charge transport or transfer mechanisms that are ubiquitous in nature, such as oxidative damage, inducing mutagenesis and carcinogenesis, or signalling pathways in proteins or deoxyribonucleic acid (DNA), and which are therefore of vital importance [20–27].

There are various factors that determine the predominating charge transport mechanism in molecular junctions, *i.e.* a molecule attached to electrodes *via* linking groups on both termini, such as the temperature or the chemical structure of the molecule [1,28–30]. Another key parameter that affects the transport characteristics is the molecular length, which is the focus of this work. Based on molecular conductance experiments, mainly two different transport mechanisms are suggested: coherent tunneling and incoherent hopping, which are strongly dependent on the molecular length [1,31–35]. At short distances, the conductance decreases exponentially as a function of the molecular length as the charge is tunneling from one electrode to the other in a coherent process, which is nearly temperature-independent [1,36]. With increasing distance, the charge transport is dominated by incoherent processes, where the charge “hops” along the molecular backbone on definite subregions, *i.e.* hopping sites. Transport in the so-called hopping regime is indicated by a linear dependence of the conductance on the molecular length and an exponential dependence on the temperature. For most conjugated molecular wires, the crossover length typically ranges between 3 and 4 nm [31–35]. The theoretical first-principles descriptions of the tunneling and the hopping regime are fundamentally different and are usually based on either the Landauer formalism based on scattering theory [37–39] or on the Marcus theory for electron transfer [40–45], respectively. One therefore needs to know at which molecular length the transition between both mechanisms occurs and how large the hopping sites that are involved in the charge transport are.

Indeed, comprehensive multi-scale approaches including *ab initio* molecular dynamics (AIMD) simulations [46,47] were already developed for describing the charge transport in complex biomolecules such as DNA by Elstner and Kleinekathöfer, where no assumptions of the underlying transport mechanism have to be made *a priori* [48,49]. However, these techniques require a high computational cost and a solid technical background on the technical details of the underlying computational framework.

The aim of this work was therefore to establish a predictive tool that allows for deciding whether the transport for a particular molecular wire is dominated rather by tunneling or by hopping from first-principles. To make practical use of first-principles methods for this purpose, a proper validation is a necessary prerequisite, since the underlying approximations are not equally well-

suiting for a variety of molecular systems [50–59]. However, a validation on the basis of molecular junctions is difficult as they are structurally not well-controlled [60]. Therefore, the so-called organic mixed-valence (MV) systems, which can be considered a variant of donor–bridge–acceptor (D–B–A) systems, served as model systems as a basis for the investigations in this work, since they are well-characterized from the experiments and since their three-fold partitioning resembles that of a molecular junction [3, 61–63]. Beyond that, the degree of charge localization in these compounds is also length-dependent and can therefore be associated with the charge transport mechanism in molecular junctions: A transition from charge delocalization to localization occurs with increasing length of the molecular bridge. Building on this idea, the predictive first-principles approach in this work relies on connecting the degree of charge localization in a charged equilibrium state to the underlying mechanism that dominates the charge transport through the molecular wire when it is integrated in a junction.

In the first part of this study, different DFT approaches are validated on the example of various organic mixed-valence systems that are just on the borderline between charge delocalization and localization, regarding their performance in describing the experimentally indicated length-dependent change from a fully delocalized to a localized charge. In addition to other first-principles methods, a DFT protocol based on the non-standard BLYP35 hybrid functional in combination with environmental modeling *via* a polarizable continuum model (PCM) is applied, as it was suggested by Kaupp and coworkers for the correct prediction of charge localization properties in organic mixed-valence systems, both radical cationic and anionic [50–52]. Moreover, it is investigated whether charge delocalization can be extended toward longer molecular lengths in naturally charge-localized molecules by applying a captodative substitution scheme proposed by Stuyver and coworkers, or whether the trend of increasing charge localization can even be reversed to result in anti-Ohmic behavior [64, 65].

In the second part of this work, the successfully validated DFT protocol is applied to organic, conjugated molecular wires, for which a length-dependent transition from tunneling to hopping was previously indicated from the experiments [1, 31–34]. It is evaluated whether the transport mechanism can be predicted based on the degree of charge localization. For this purpose, a quantitative measure is derived that is easily applicable to any type of wire and that

allows for a systematic derivation of the degree of charge localization within a particular series of molecules.

While charge transport is typically described either by tunneling or hopping, an intermediate transport regime was recently proposed by Tao and coworkers for guanine-based DNA strands, where coherent and incoherent processes coexist, depending on the base sequence [66, 67]. In this work, two variants of this highly conductive type of DNA serve as a further test example for predicting transport mechanisms not only as a function of the molecular length, but also of the molecular architecture such as the base sequence.

In the last part of this work, attempts are made to make the predictive DFT calculations even more efficient by using semiempirical techniques as an alternative [68, 69]. Various approaches based on the AM1, PM6 and DFTBA methods are validated to investigate whether they are capable of correctly describing charge localization in molecular wires, in agreement with the transport mechanism suggested from the experiments. Such a predictive approach would be specifically beneficial for the application to larger biomolecules, such as DNA and proteins, as it would allow for the evaluation of transport mechanisms with reduced computational cost in comparison to DFT methods or comprehensive multi-scale frameworks, as suggested by Elstner and Kleinekathöfer [48, 49, 70–72]. Hence, the primary objective of this work was to establish an accurate, yet easily applicable and cost-efficient approach for the prediction of transport mechanisms, based on static first-principles calculations.

II. THEORETICAL AND EXPERIMENTAL BACKGROUND

1 Charge Transport Phenomena and Concepts

In the first part of this section, the most common experimental set-ups for measuring the molecular conductance of molecular wires, including bio-molecules such as DNA, are outlined. In this work, the focus is on the length-dependent crossover from coherent tunneling to incoherent hopping transport, as observed in these experiments. Therefore, characteristic phenomena in the conductance that are indicative of the length-dependence of the underlying transport mechanism are presented on selected examples. The theoretical concepts behind these transport regimes are discussed to allow for a deeper understanding of the processes that give rise to the unique signatures of charge transport mechanisms observed in the experiments. Beyond the coherent tunneling and the incoherent hopping regime, which can be described by the Landauer [37–39] and Marcus [40–45] theory, respectively, evidence of an intermediate regime in between these two extremes is shown on the example of guanine-based DNA, previously studied by Tao and coworkers [66,67].

1.1 Studying Charge Transport in Molecular Junctions

For the integration of molecular wires into nanoelectronic circuits and for a fundamental understanding of relevant factors governing charge transport in biological and chemical processes, the investigation of the relevant transport mechanisms in individual molecules is essential. For single molecules, a well-defined quantity is the conductance G , analogous to the conductivity in bulk materials. The conductance at zero-temperature is defined as the first derivative of the electrical current I with respect to the applied bias voltage V [1,73]

$$G(V) = \frac{dI(V)}{dV}. \quad (1.1)$$

When aiming at determining the conductance of a molecule, the first challenge

is connecting it with two macroscopic electrodes, as the contact needs to be robust and reproducible. Often, a stable contact is realized by attaching the molecule covalently to the metal electrodes *via* suitable anchoring groups, *e.g.* by using thiols that strongly bind to a gold surface [1, 73, 74].

A wide range of experimental techniques is used for performing conductance measurements on molecular junctions, *e.g.* scanning tunneling microscopy (STM) or conductive-probe atomic force microscopy (CP-AFM) and mechanically controlled break junctions (MCBJs) [1, 73]. These experiments can be mainly divided into two categories: measurements on molecular films, such as self-assembled monolayers (SAMs), and on single molecules, as illustrated in Fig. 1.1. When performing conductance experiments on SAMs, generally one can either sandwich them between two electrodes, which involves many molecules, or use nanoelectrodes, *e.g.* a conducting atomic-force microscope tip, to measure the conductance of a relatively small number of molecules [73]. In studies by Frisbie and coworkers, molecular conductance experiments were carried out on molecular junctions based on SAMs of long thiophene-containing π -conjugated oligophenylene-thiophene-imine (OPTI_{*n*})¹ wires with molecular lengths up to 7.4 nm [31]. The chemical structures of the OPTI_{*n*} wires as well as the experimental set-up for the CP-AFM measurements are illustrated in Fig. 1.1 (A). The OPTI_{*n*} wires, capped with a benzaldimine unit, were grown on a gold substrate, and then contacted with a conductive AFM probe as a second electrode. The resistance of the molecular junction, *i.e.* the inverse of the conductance, was then systematically measured as a function of the molecular length for OPTI₁–OPTI₁₂, where a transition from tunneling to hopping transport was observed as described in the following (see Fig. 1.3).

For measurements on single molecules, one needs to make sure that only the conductance of an individual molecule is measured, which needs to be properly attached to the two probing electrodes, and that it is located in a well-defined environment. One way to do so is the use of scanning probe techniques, *i.e.* STM or AFM, depicted in Fig. 1.1 (B). In these experiments, both the mechanical and the electrical properties of molecules can be measured by using a conductive probe. While the molecule–substrate contact is usually well-defined, a more challenging task is to form an equally well-defined contact between the

¹In OPTI_{*n*}, *n* denotes the number of phenylene and thiophene units present in the wire.

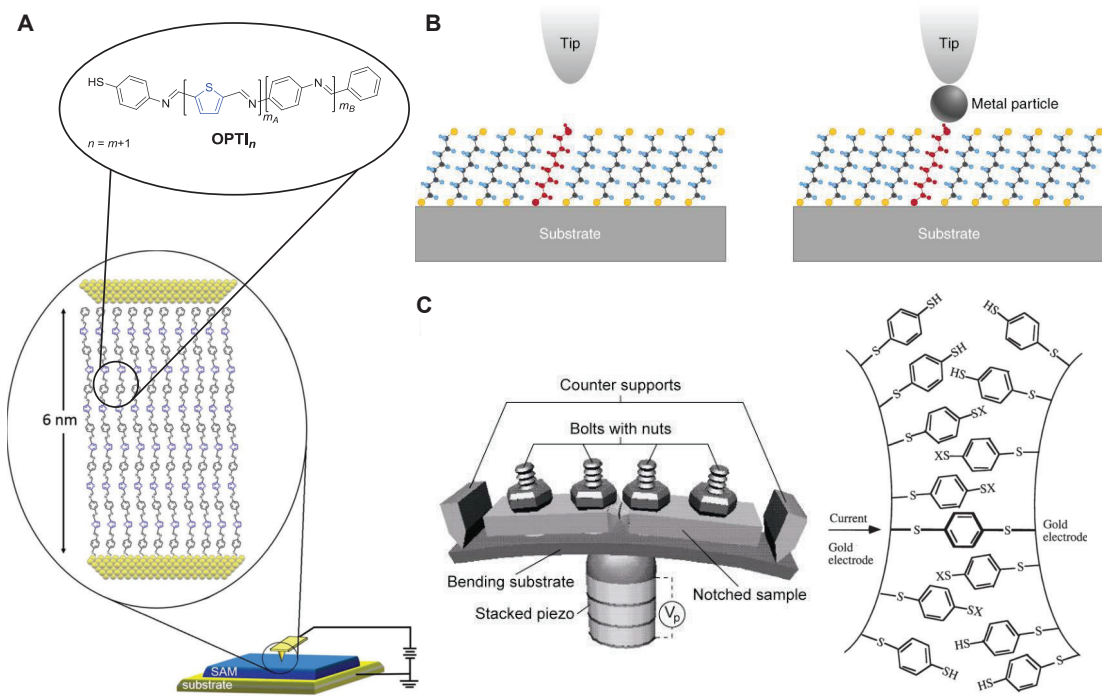


Figure 1.1: Molecular Conductance Experiments (A) CP-AFM experiments on SAMs consisting of OPTI_n molecules, adsorbed on a gold substrate. Adapted from Ref. [31]. (B) Single-molecule STM experiments on a target molecule inserted into an ordered array of reference molecules (left) and STM or AFM measurement of a molecular wire adsorbed on a substrate and bound to a metal nanoparticle (right). Reprinted from Ref. [73]. (C) MCBJ experiment (left), reprinted from Ref. [73], and scheme of a benzene 1,4-dithiolate SAM between proximal gold electrodes formed in a MCBJ (right), where $X = \text{Au}/\text{H}$, depending on whether the second terminus is linked to the gold electrode or not. Reprinted from Ref. [75].

molecule and the tip. As shown in Fig. 1.1 (B), this problem can be addressed by attaching a gold nanoparticle covalently before placing a STM or AFM tip on top of it to form a tunneling junction, where the target molecule is often embedded in a matrix of less-conducting reference molecules, *e.g.* an insulating alkanethiol layer [73].

Another variant of performing conductance measurements on single molecules is realized by forming MCBJs, as illustrated in Fig. 1.1 (C). Here, a metallic wire that is supported on a solid substrate is broken into a pair of facing electrodes by bending the substrate with, for example, a piezoelectric transducer as

a mechanical actuator that pushes the middle part of the substrate vertically. The molecular-scale electrode gap is then exposed to a solution containing the target molecule, *e.g.* benzenedithiol as done in studies by Reed *et al.* [75], which is evaporated after closing the gap by contacting a single molecule between the electrodes. By recording the current as a function of the gap width at a fixed voltage, the formation of a single-molecule contact is then indicated by a stable value of the current that is weakly dependent on the width of the gap [73].

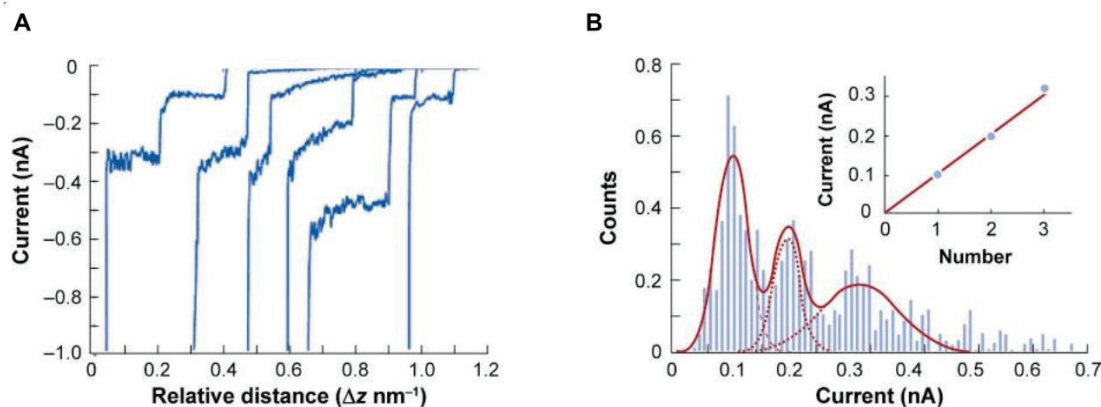


Figure 1.2: Single-molecule Conductance Measurements on STM Break Junctions (A) Plot of the current as a function of the relative distance between the electrodes, recorded during the pulling process for viologen dithiol molecules (bias voltage = -0.1 V). The contact with one of the two electrodes is broken individually by pulling the tip away from the substrate, indicated by a series of stepwise decreases in the current [73,76]. (B) Conductance histogram based on individual measurements of the current as described in Fig. (A), reflecting the statistical distribution of conductance values of molecular junctions with different contact geometries. The peaks (red line) correspond to integer multiples of the single-molecule conductance (~ 1 nS) [73,76]. Figures reprinted from Ref. [73].

Similar measurements can be performed on STM-based break junctions (STM-BJs), where a STM tip is repeatedly moved in and out of contact with target molecules that are bound on a metal substrate until a large number of molecular junctions is created. By pulling away the electrode tip from the substrate, the contact between the molecules and the substrate is broken individually, which is shown by a stepwise decrease of the current (Fig. 1.2, A). The single-molecule conductance is determined from characteristic peaks in the conductance

histograms that represent a statistical distribution of conductance values in an ensemble of molecular junctions with different contact geometries (Fig. 1.2, B). It has to be noted that the experimental techniques for measuring molecular conductance presented here are by no means complete, but rather represent illustrative examples of the most commonly used methods (see Refs. [1,73] for further details on more variants of molecular conductance experiments).

1.2 Length-dependent Transition from Tunneling to Hopping

When studying the charge transport characteristics of molecular wires, the question arises what the dominating transport mechanism is for a particular molecular wire. Mostly, charge transport is described by two fundamentally different transport mechanisms: coherent tunneling and incoherent hopping, showing different signatures in molecular conductance experiments. Beyond the chemical structure of the molecular wire, the charge transport is also dependent on the temperature and especially on the molecular length, which is the focus of this work. From conductance experiments, it was found that in a series of molecular wires with increasing molecular length, the charge transport characteristics change at some point, which was interpreted as a transition from coherent tunneling to incoherent hopping transport. The length-dependent transition between these two transport regimes is nicely illustrated by the example of OPTI_n wires, previously studied by Frisbie and coworkers [31].

Molecular conductance experiments were performed on SAMs that were grown on a gold substrate, as illustrated in Fig. 1.1 (A). In Fig. 1.3, the resistance-versus-length plots from these experiments are shown on a semilog and a linear scale for OPTI_n wires, where $n = 1-12$. There is a clear change in the length-dependence of the resistance around a molecular length of 4 nm, between OPTI₆ and OPTI₇, indicating a transition of the transport mechanism from tunneling to hopping.

The resistance increases exponentially with growing molecular length for shorter wires (OPTI₁–OPTI₆), which is indicative of a tunneling mechanism, while for longer wires the resistance increases linearly when elongating the molecular bridge (OPTI₇–OPTI₁₂), which is characteristic for hopping transport as discussed below. As suggested by the linear fit in the semilog plot in Fig. 1.3 (A), for short wires up to a molecular length of 4 nm, the standard formula of

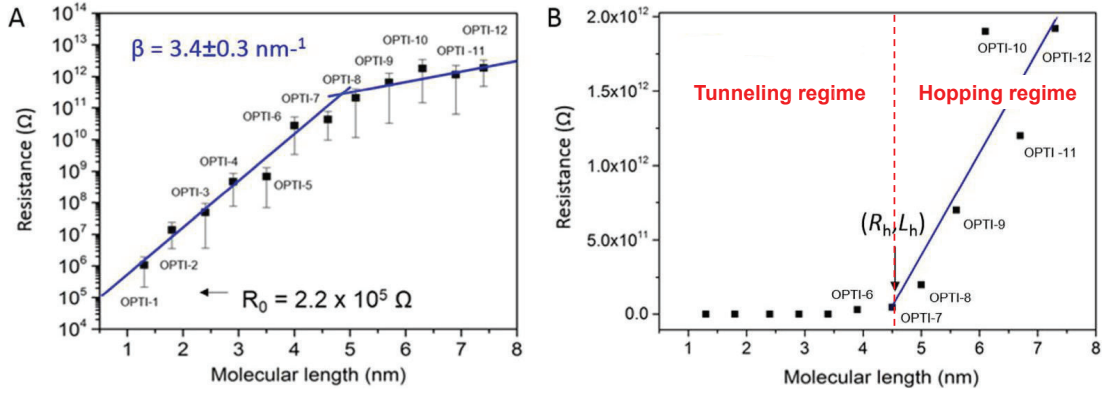


Figure 1.3: Charge Transport Measurements on OPTI_n Wires

(A) Semilog plot of low-bias resistance Ω versus molecular length L of OPTI_n wires ($n = 1\text{--}12$), obtained from CP-AFM measurements by Frisbie *et al.* [31]. Each data point refers to the average resistance obtained from $\sim 100\text{--}200$ $I\text{--}V$ traces in a ± 0.2 V bias range. Error bars are one standard deviation and lines are fits to the data using the least-squares method. The β value was extracted from a linear fit of the data corresponding to OPTI_n wires shorter than 4 nm ($n = 1\text{--}6$) according to Eq. (1.2). (B) Resistance-versus-length plot on a linear scale. R_h and L_h represent the resistance and the molecular length that indicate the beginning of the linear fit in the hopping regime for OPTI_n wires longer than 4 nm ($n = 7\text{--}12$). Figures reprinted and adapted from Ref. [31].

coherent non-resonant tunneling² applies,

$$R = R_0 e^{\beta L}, \quad (1.2)$$

where R is the junction resistance, R_0 is the effective contact resistance, L is the molecular length and β is the tunneling attenuation factor, depending on the nature of the molecular backbone and on the electronic coupling at the metal–molecule interface of the molecular junction [31]. In this regime, it is assumed that phase-coherence is preserved across the junction. Thus, when considering coherent transport, *i.e.* tunneling, it is implied that the information about the phase of the wavefunction of conducting electrons is maintained along the molecule, and that inelastic interactions only take place within the electrodes [1]. From the linear fit of the data, a β value of 3.4 nm^{-1} was obtained, which is close

²For tunneling in an off-resonant situation, neither the HOMO nor the LUMO is within the energy window of the Fermi energy.

to the values typically found in conjugated molecular wires, *e.g.* for oligoarylene-ethynylene wires (OAE, $\beta = 3.3 \text{ nm}^{-1}$) [34] or for oligophenylene-imine wires (OPI, $\beta = 3.0 \text{ nm}^{-1}$) [32,33]. In contrast, for OPTI_{*n*} wires longer than 4 nm, the resistance increases nearly linearly and much less with molecular length, which is in agreement with a hopping transport mechanism (Fig. 1.3, B). Thus, for OPTI₇–OPTI₁₂, the resistance follows the Arrhenius relation,

$$R = R_h + \alpha_\infty(L - L_h)e^{\frac{E_a}{k_B T}}, \quad (1.3)$$

where R_h and L_h denote the resistance and molecular length at which the hopping regime begins³, α_∞ is a molecule-specific parameter with units of resistance per length, also referred to as the hopping attenuation factor, E_a is the hopping activation energy, k_B is the Boltzmann constant and T is the temperature [31]. To provide a more qualitative picture of these two transport regimes on a molecular scale and its association with the degree of charge localization, the transition from coherent tunneling to incoherent hopping upon elongation of the molecular bridge by increasing the number of monomer units is schematically illustrated in Fig. 1.4.

For short molecular wires, transport *via* tunneling predominates, where the charge tunnels through the molecule without intermittently being physically located on the molecular bridge (see Fig. 1.4, left). As it was shown experimentally, charge transport by coherent tunneling may no longer be efficient as the length of the conducting wire in the molecular junction increases [28,31–35]. It rather becomes likely that holes (or electrons) are injected into a filled (or an empty) orbital of the molecule, resulting in the localization of the charge and thus, the formation of a so-called polaron, which is considered a charge associated with a localized structural deformation. The external electric field then acts as the driving force for the polaron to migrate or “hop” across the molecule on hopping sites, where the charge is temporarily located on (see Fig. 1.4, right) [30,31,78,79].

The polaronic nature of the charge carriers in OPTI_{*n*} wires was also investigated in computational studies by Frisbie and coworkers [30,31]. DFT calculations were used to analyze the nature of the charge carriers involved in the trans-

³The change in the transport mechanism is rather indicated by a change in the slope, since the experimental error bars do not allow for a clear distinction between linear and exponential dependence.

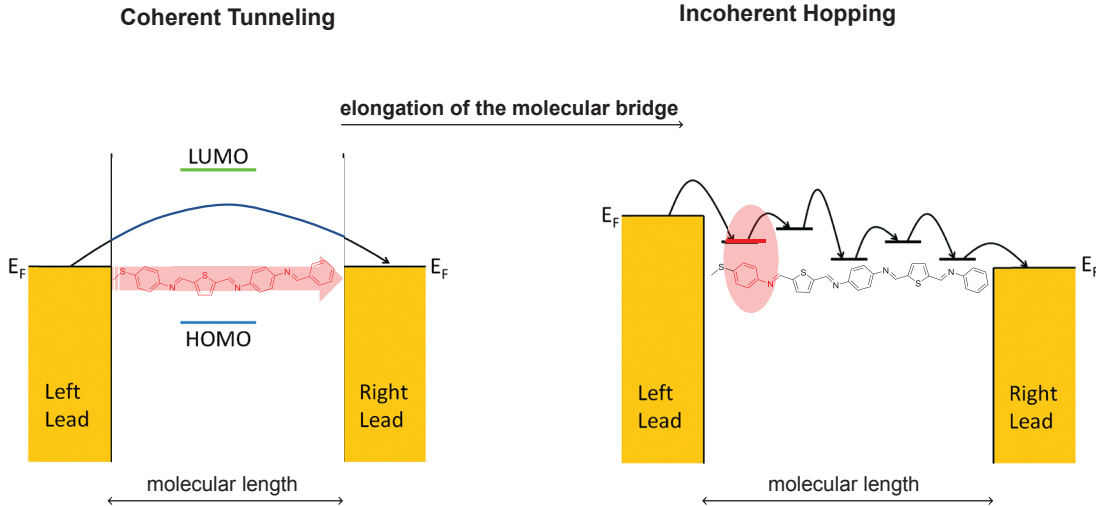


Figure 1.4: Length-dependent Tunneling-to-hopping Transition
 Schematic illustration of the transition from a coherent tunneling mechanism (left) to a multi-step hopping mechanism (right) upon lengthening of the molecular bridges sandwiched between two electrodes. Adapted from Ref. [77].

port regime near a molecular length of 4 nm, where the tunneling-to-hopping crossover was observed [31]. Since the charge localization properties can be associated to the underlying transport mechanism as illustrated by Fig. 1.4, the radical cationic states of the OPTI_n wires were characterized by computing the local spin density at the M06-HF/TZP level of approximation. The starting structures for molecular structure optimizations were obtained from AIMD simulations, where the electrode contact was simulated by a single gold atom and described by a basis set of triple-zeta quality with polarization functions (TZP) during optimizations [31].

It was found that for OPTI₁ through OPTI₄, the spin densities are fully delocalized across the entire wire, suggesting a tunneling transport mechanism for the shorter wires, as found in the experiment [31]. In contrast, for OPTI₅ through OPTI₈, the formation of polarons was indicated by localization of the spin density, consistent with the charge transport occurring predominantly by hopping. For these longer wires, a hopping site comprising roughly three rings was determined, and the calculated activation energies of the polaronic transition states were found to be in agreement with measured values. Thus, it was stated that the experimental and computational results are consistent with a multistep adiabatic hole transport mechanism within longer wires [31]. Based

on this study, the applicability of DFT for the investigation of charge localization in molecular wires and the understanding of the associated transport mechanisms could be demonstrated.

To provide additional validation for the transition from a tunneling to a hopping transport mechanism, resistance measurements of the molecular wires were performed over a large temperature range. It was found that the resistance for the shorter OPTI₄ wire is weakly dependent on the temperature, which is characteristic for the tunneling transport mechanism [31]. In contrast, for the longer OPTI₆ and OPTI₈ wires, thermally activated transport was revealed, indicating a hopping mechanism for wires longer than 4 nm. In this transport regime, the thermal activation energy E_a is required for the injection of the charge from the contacts to the molecules, since discrete molecular radical cation intermediates, *i.e.* polarons, are involved in the net charge transport [31].

The length-dependence of transport mechanisms as illustrated on the example of OPTI_{*n*} wires was equally observed for different molecular wires and experimental set-ups at room temperature: in similar studies, Frisbie and coworkers reported on the transition from tunneling to hopping in long, conjugated oligonaphthalene-fluoroene-imine (ONI) wires with systematically varied lengths up to 10 nm [33]. CP-AFM measurements were carried out on monolayers of the ONI wires, assembled on a gold substrate, from which a crossover was identified at a molecular length of approximately 4 nm, in agreement with previous studies on structurally similar OPI wires [32]. Unlike in the previous study, the charge transport characteristics of oligophenylene-ethynylene (OPE) wires of variable length were investigated by Wang and coworkers on a single-molecule level using the STM-BJ and CP-AFM method, where a transition from tunneling to hopping was found at a molecular length of nearly 3 nm [35]. Tao and coworkers also performed conductance measurements on a single-molecule level by employing the STM-BJ technique in a series of systematically elongated thiophene-terminated oligofluorene wires, where the crossover length ranged roughly between 5 and 7 nm [28]. Using the same experimental technique, Wandlowski and coworkers investigated the charge transport mechanism of OAE wires, where a crossover length of nearly 3 nm was indicated [34].

In all of these examples, the tunneling-to-hopping transition was clearly marked by the change in length-dependence of the resistance. As the dominating mechanism depends on various parameters, such as the molecular length [31, 80], a

thorough understanding of influencing factors on the underlying transport processes is of great importance. It is of particular interest to evaluate, at what molecular length a crossover between these two transport regimes would occur and how the transition can be predicted by computational means. In the following, the relevant theoretical concepts will be outlined in order to provide the foundations for the understanding of charge transport mechanisms.

Coherent Tunneling – The Landauer Formalism

In the coherent tunneling regime, the conductance through nanoscale molecular junctions is routinely described by the Landauer–Imry–Büttiker approach [37–39], which is based on an elastic scattering treatment [80]. In this approach, the transport properties of a conductor are related to the transmission and the reflection probabilities for carriers incident on the sample [1].

The close relation between current and transmission is illustrated by the so-called Landauer formula, which expresses the current as a function of the bias voltage $I(V)$ by the integral over the transmission $T(E)$ as a function of the energy and the difference between the Fermi functions of the left and right electrode $f_{L,R}(E)$

$$I(V) = \frac{2e}{h} \int_{-\infty}^{\infty} dE T(E) [f_L(E) - f_R(E)], \quad (1.4)$$

where e is the elementary charge and h is Planck’s constant. The factor of 2 accounts for the spin degeneracy that usually exists in most of the studied systems [1]. When assuming low voltages, the zero-bias conductance defined in Eq. (1.1) is given by

$$G = \frac{2e^2}{h} T(E_F). \quad (1.5)$$

For evaluating the conductance of a given molecular junction, one therefore has to determine the transmission function at the Fermi energy $T(E_F)$ [1]. A perfect conductor between the electrodes with one open conductance channel ($T(E_F) = 1$) exhibits a finite conductance, which is given by the conductance quantum $\frac{2e^2}{h} \approx (12.9 \text{ k}\Omega)^{-1}$. This characteristic represents a unique difference to macroscopic leads, where zero resistance is expected for the perfectly conducting situation. According to Imry, this behavior is caused by the resistance originating from the interface between the molecule and the electrode [1, 81].

As a standard approach toward first-principles calculations in the coherent electron transport regime, the Landauer–Imry–Büttiker elastic scattering treatment combined with a nonequilibrium Green’s function (NEGF) approach [25, 82–84] and KS–DFT [85, 86] turned out to provide a description close to experiments, at least for describing qualitative behaviour [87].

In addition to the assumption of phase-coherence across the junction, the molecule-electrode coupling is considered sufficiently large to prevent significant accumulation of the charge, and it is assumed that the electrodes are reflectionless. Consequently, there is no backscattering of the charge after having crossed the interface between the electrode and the molecule. A steady-state condition applies to the system, since the number of electrons in the molecular bridge between the electrodes is treated as constant over time [87, 88].

The exponential length-dependence of the conductance is best described by applying a tight-binding bridge model, which is widely used in the context of electron transfer, as schematically illustrated in Fig. 1.5 [1]. In this picture, a molecular bridge formed by a number of N sites, *e.g.* monomer units, with on-site energies ε_i of one orbital per site is coupled to the metallic leads by the hoppings $t_{L,R}$. Within the molecular bridge, only nearest-neighbour hoppings $t_{i,i+1}$ are considered.

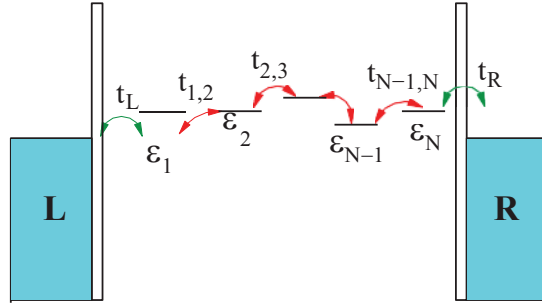


Figure 1.5: Coherent Charge Transport Schematic representation of the bridge model to explain the exponential length dependence of the conductance. A molecular bridge formed by N sites (*e.g.* monomer units) with on-site energies ε_i (considering only one orbital per site) is coupled to two metallic leads *via* the hoppings $t_{L,R}$ (green). In the molecular bridge, only the nearest-neighbour hoppings ($t_{i,i+1}$; red) are considered. Reprinted from Ref. [1].

For calculating the transmission through a molecular bridge, Green’s function techniques can be applied [1, 83, 84], resulting in the following general expression

for the energy- and voltage-dependent total transmission probability $T(E, V)$,

$$T(E, V) \equiv 4\text{Tr}[\mathbf{\Gamma}_L \mathbf{G}_{CC}^r \mathbf{\Gamma}_R \mathbf{G}_{CC}^a], \quad (1.6)$$

where $\mathbf{\Gamma}_{L,R}$ are the scattering rate matrices, determining the strengths of the coupling to the metallic electrodes, which can be obtained from the imaginary parts of the respective self-energies [1]. The Green's function of the central subsystem is denoted with $\mathbf{G}_{CC}^{r,a}$, where the central subsystem can be either defined as the molecule between the electrodes only or as the molecule plus several atoms from the left and right electrode [87].⁴ In the regime of coherent transport, the conductance can therefore be expressed in terms of the transmission function. In the following, the characteristic length-dependence of the conductance in the tunneling regime as observed from the experiments is explained in terms of the transmission function by means of the bridge model. While the charge transport in this regime is typically temperature-independent [1,80], the most characteristic signature of coherent transport *via* tunneling is the exponential decay of the conductance with increasing length L of the molecule, as analogously described by Eq. (1.2), where the so-called attenuation factor β depends on the specific molecular structure, the side groups, the bias voltage and, to a lesser extent, on the bridging unit connecting the molecule to the electrode [1].

Based on Eq. (1.6), the zero-bias transmission coefficient in the tight-binding model described above can be expressed as

$$T(E) = 4\Gamma_L(E)\Gamma_R(E)|G_{1N}^a(E)|^2, \quad (1.7)$$

where the scattering rates are given by $\Gamma_{L,R} = t_{L,R}^2 \text{Im}\{g_{L,R}^a\}$, with $g_{L,R}^a$ being the lead Green's functions [1]. The (advanced) Green's function G_{1N}^a connects the first and the last site in the molecular bridge and $|G_{1N}^a(E)|^2$ reflects the probability of an electron to propagate along the molecular wire [1]. The lowest-order contribution to G_{1N}^a corresponds to the sequential tunneling along

⁴The superscript denotes the retarded and advanced Green's functions of the central subsystem. Further algorithmic details for the application of the combined approach based on the Landauer–Imry and the NEGF formalism can be found for example in Ref. [87]. In this work, the focus is rather on illustrating a qualitative picture of charge transport, providing an understanding for the origin of the main features in molecular conductance experiments.

the bridge without any reflection, which is a good approximation to the exact expression in the weak coupling regime, and can be expressed as

$$G_{1N}^a(E) \approx \frac{1}{E^a - \epsilon_N} \prod_{i=1}^{N-1} \frac{t_{i,i+1}}{E^a - \epsilon_i}. \quad (1.8)$$

Assuming that all bridge elements are identical, that is $t_{i,i+1} = t$ and $\epsilon_i = \epsilon$ (see Fig. 1.5), and substituting the previous result from Eq. (1.8) into the expression of the transmission in Eq. (1.7), the result for the homogeneous bridge reads [1]

$$T(E) \approx \frac{4\Gamma_L\Gamma_R}{|t|^2} \left| \frac{t}{E - \epsilon} \right|^{2N}. \quad (1.9)$$

From the latter expression for the transmission, a simplified form of the attenuation parameter in Eq. (1.2) can be derived, reading

$$\beta(E) = \frac{2}{a} \ln \left| \frac{E - \epsilon}{t} \right|. \quad (1.10)$$

In Eq. (1.10), the bridge length equals Na , since the size of the sites forming the molecular bridge is described by a . In this model, the attenuation factor $\beta(E)$ is independent of the coupling to the leads and is determined only by intrinsic properties of the molecular bridge [1].

The exponential dependence of the conductance on the molecular length is therefore a manifestation of transport by coherent tunneling in an off-resonant situation. However, as pointed out earlier, this theoretical framework is only valid for relatively short molecular lengths. As the molecular bridge gets longer, the transport mechanism is no longer coherent but changes at some point to semi-classical incoherent transport that is based on a fundamentally different theoretical basis [1, 44, 80, 89], which will be described in the following.

Incoherent Hopping – Marcus Theory

Whereas in the coherent tunneling regime, the phase of the wave function associated with a particle moving along the molecular junction is preserved, now the focus is turned on charge transport processes where this coherence is completely lost. The transition from the coherent to the incoherent regime occurs when the time-scale on which the tunneling process takes place is significantly larger than the time that is related to inelastic scattering processes [1, 90]. However, an inelastic component in the tunneling current can be observed even when the dominant transport mechanism is still coherent [44].

In this context, the contact time of the electron with the molecular bridge is decisive for the predominating transfer mechanism: when the electron spends a sufficiently large time on the bridge, it can enter into the time-period of molecular vibrations or motions, which becomes increasingly probable as the length of the molecular bridge in the junction increases [1,36]. As a result of this situation, phase-breaking occurs and the current is mediated by the migration of electrons along the molecular junction *via* a series of sequential hopping steps from one fragment to another, rather than by tunneling from one electrode to the other [1,36,44,91].

The charge transport in the incoherent hopping regime is typically described by the standard theory of electron transfer, known as Marcus theory [41]. As the hopping transport can be considered dominated by Marcus electron transfer kinetics, the model for describing incoherent transport processes in a molecular junction is derived from the field of electron transfer [44,80], which is depicted in Fig. 1.6.

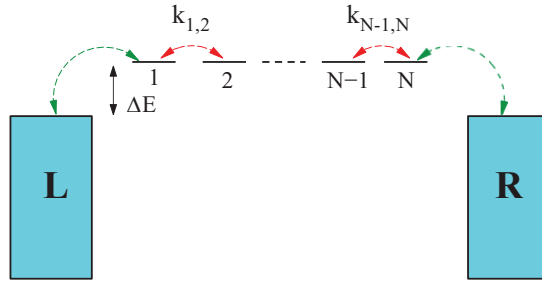


Figure 1.6: Incoherent Charge Transport Schematic representation of the hopping model for a molecular junction, based on the theory of electron transfer [43,92]. A molecular bridge formed by N sites (*e.g.* monomer units), having the same energy and being connected *via* nearest-neighbor transfer rates $k_{j,j\pm 1}$, is coupled to two metallic leads. The continua on the the left and right side correspond to the metallic states in the electrodes, where ΔE is the activation energy. Adapted from Ref. [1].

In the hopping model, the bridge between the electrodes is described by having N adjacent sites j , on which the charge can perform a series of consecutive hopping steps in contrast to coherent transport, where the charge tunnels through the molecule. Each hopping step can be expressed by the nearest-neighbor transfer rate $k_{j,j+1}$ between adjacent sites, and the transfer rates from the first and the last hopping site to the left and right electrode, $k_L = k_{0,1}$ and $k_R = k_{N+1,N}$,

respectively. For the sake of simplicity, it is assumed that all sites within the molecule have the same energy, and all internal transfer rates between them are equal, such that $k_{j,j+1} = k$. Since the energy difference ΔE between each site and the equilibrium Fermi energy of the electrodes is the energy attributed with the injection of a charge onto the bridge, it can be regarded as the activation energy for the transfer process [1]. In contrast to coherent charge transport, charge transport by hopping is therefore a thermally activated process.

According to the Marcus electron transfer kinetics, the electric current in the molecular junction between sites j and $j + 1$ is described as a function of their occupations P_j and P_{j+1} , leading to the expression

$$I_j = e(k_{j+1,j}P_j - k_{j,j+1}P_{j+1}), \quad (1.11)$$

where the current is conserved, therefore making it irrelevant at which site it is determined [1]. When assuming incoherent transport, the occupations P_j fulfill the classical kinetic equations⁵, where P_0 and P_{N+1} correspond to the Fermi functions describing the electron occupations on the left and right electrode, respectively.

Moreover, a stationary situation is considered, where dP_j/dt is zero, and the internal rates within the bridge are assumed to be equal ($k_{j,j\pm 1} = k$). By taking into account that the current must vanish in equilibrium (detailed balance condition) [1], the expressions for the transfer rates involving the left and right electrode are given by

$$k_{1,0} = k_L e^{-(\Delta E - eV)/k_B T}; \quad k_{0,1} = k_L \quad (1.12)$$

$$k_{N,N+1} = k_R e^{-\Delta E/k_B T}; \quad k_{N+1,N} = k_R. \quad (1.13)$$

Note that the influence of the voltage V on the activation energy ΔE (assumed to be applied on the left electrode) is taken into account in Eq. (1.12). By solving the corresponding classical kinetic equations describing the occupations of the sites (see Refs. [1,43] for algebraic details), the charge current is expressed by

$$I = e \frac{e^{-\Delta E/k_B T}}{[1/k_L + 1/k_R + (N-1)/k]} [e^{eV/k_B T} (f_L - f_R)], \quad (1.14)$$

⁵See Ref. [1] for detailed expressions of the corresponding kinetic equations.

where k_B is the Boltzmann constant and T is the temperature [1]. The corresponding conductance G can then be obtained as

$$G = \frac{e^2}{k_B T} \frac{e^{-\Delta E/k_B T}}{[1/k_L + 1/k_R + (N-1)/k]}, \quad (1.15)$$

where the temperature dependence of the Fermi functions of the electrodes is neglected for the sake of simplicity [1]. From the latter expression, two main characteristics of the incoherent hopping regime are indicated, from which it can be identified in molecular conductance experiments: one unique feature is the linear decay of the conductance as a function of molecular length or the number of hopping sites N within the molecule. Basically, the conductance through the molecular junction can be described by Ohm's law, as it can be expressed as the conductance of a combination of resistors in series, which are represented by the two metal-molecule interfaces and the $N-1$ bridge contacts between the hopping sites [1].

Moreover, the conductance depends exponentially on the temperature, which is a common feature in thermally activated processes. In this model, the activation process is assumed to take place at the molecule-electrode interface, but in principle it can take place at any position along the junction [1].

By this model, no quantitative description of the system under study is provided, but it rather gives a qualitative explanation for the main characteristics that can be observed in conductance measurements. Beyond that, this model is not capable of describing the transition from tunneling to hopping as a function of the temperature and the molecular length, as observed from molecular conductance experiments presented earlier. In this context, the most challenging aspect is to evaluate the factors leading to the loss of phase coherence, for example interactions between the migrating charges and the phonons within the molecule [1,30,31]. This process is particularly favored in situations where the adjacent hopping sites are weakly coupled, and the localization of the charge on subregions of the molecule is facilitated. As a consequence of the charging event, a change of the molecular conformation likely occurs in favor of a structure being lower in energy, *i.e.* polaron formation occurs.

As mentioned earlier, the electrical conductance in the incoherent hopping regime is closely related to the well-studied electron transfer based on the Marcus theory, and can therefore profit a lot from this much more elaborated field [1,42,43,92]. In the following paragraph, the basics of electron transfer theory with its im-

plications for the description of incoherent transport processes in molecular junctions will be outlined in more detail. To allow for a direct comparison of charge transport in the coherent and in the incoherent regime, the essential Marcus parameters for describing charge transfer processes are derived on similar grounds as the transmission function $T(E)$, since this is the central quantity in the Landauer theory for coherent transport, aiming at a connection between the theoretical descriptions for both transport regimes.

Charge Hopping and Comparisons to Coherent Tunneling As mentioned, the theoretical description of charge hopping is based on the Marcus theory of electron transfer, while coherent transport processes are adequately described by the Landauer formalism [1,80]. For a direct comparison of both transport mechanisms, the relevant quantities need to be derived from similar grounds, as it was pointed out by Nitzan [43,44]. Thus, analogously to the calculation of the conductance for coherent transport within the single-particle framework of DFT [85,86] in combination with a NEGF approach [83,84], it is advisable to calculate the essential Marcus parameters from first principles as well to make sure that they are obtained on the same single-particle level [44,80]. A DFT-based comparison between coherent tunneling and charge hopping was made by Kastlunger and Stadler on the example of redox-active single-molecule junctions, where the Marcus parameters and the transmission function were both derived within a single-particle framework to evaluate the critical length of the tunneling-hopping transition [80].

Charge hopping is often described by tight-binding models as described earlier in this section, where essential parameters such as the on-site energies are not derived from *ab initio* or other electronic structure calculations and therefore do not reflect their dependence on the molecular structure under study [80]. This treatment results in considering only N -step hopping, where the charge migrates along the molecular chain on a sequence of sites (*e.g.* monomers, base pairs) until the final N th site is reached, which is considered reasonable in simulations on, for example, DNA wires [80]. However, for highly conjugated molecular wires that are widely used in molecular conductance experiments and also investigated in this work (OPV, OPI, OPE and OAE wires [28,32–34]), the charge is assumed to be transferred by the so-called two-step hopping mechanism [44,80].

In this model, the transport mechanism is basically split into two sequential processes, where the charge hops from the donor, *i.e.* the left electrode, onto the molecular bridge in the first step, and subsequently passes over to the acceptor, *i.e.* the right electrode, in the second step. Consequently, when considering hole transfer in a single-molecule junction, the overall conduction process can be described as a chemical reaction by the transfer rates for two separate reactions⁶, where the direction of the charge flow is assumed to be from the left to the right electrode: the oxidation of the molecular bridge in the first step, corresponding to the removal of an electron from the highest occupied molecular orbital (HOMO) in a quantum-chemical picture, and its reduction in the second step, as expressed by Eqs. (1.16) and (1.17) for k_{ox} and k_{red} , respectively [80]. The charge transfer process is then described by the two transfer rates

$$k_{\text{ox}} = \frac{2\pi}{\hbar} V^2 \frac{1}{\sqrt{4\pi\lambda k_{\text{B}}T}} \int e^{-\frac{(\lambda + \Delta G^0 + \epsilon)^2}{4\lambda k_{\text{B}}T}} [1 - f(\epsilon)] d\epsilon, \quad (1.16)$$

and

$$k_{\text{red}} = \frac{2\pi}{\hbar} V^2 \frac{1}{\sqrt{4\pi\lambda k_{\text{B}}T}} \int e^{-\frac{(\lambda - \Delta G^0 + \epsilon)^2}{4\lambda k_{\text{B}}T}} f(\epsilon) d\epsilon, \quad (1.17)$$

where the fundamental quantities are the reorganization energy λ , the transfer integral V , and the driving force ΔG^0 , which will be described below.

To describe hopping transport in molecular junctions, the so-called Marcus–Hush formula [41,93] for the intra- or intermolecular electron transfer rates has to be modified in such a way that all occupied and unoccupied surface states in the electrode are taken into account by integrating over all metal states [80,94]. Here, $f(\epsilon) = \frac{1}{e^{\epsilon/(k_{\text{B}}T)} + 1}$ denotes the Fermi function, which represents the capability of the electrodes of either contributing a positive charge *via* the unoccupied states to the molecular bridge upon its oxidation (left electrode), or receiving it *via* the occupied states upon its reduction (right electrode). The overall conductance in the molecular junction is then obtained by an expression where both transfer rates, k_{ox} and k_{red} , are included, and the electrode–molecule interfaces on both sides are assumed being identical, *i.e.* the electrodes consist of the same material and the molecule is attached in the same surface orientation with the same linker [80],

⁶Depending on various parameters such as the molecular length, several hopping steps may occur within the molecular bridge, which is not accounted for by this model.

$$G_{\text{hop}} = \frac{e^2}{2k_{\text{B}}T} \frac{k_{\text{ox}}k_{\text{red}}}{k_{\text{ox}} + k_{\text{red}}}. \quad (1.18)$$

The expression for G_{hop} in Eq. (1.18) is valid only in the zero-bias regime, where the potential difference between the electrodes is sufficiently small. When dealing with finite electrochemical gate voltages, the respective potential simply has to be added to the value of ΔG^0 . The driving force ΔG^0 is derived from the relative position of the HOMO of the molecule to the Fermi level of the electrode (see Fig. 1.6), taking into account the effect of the adsorption of the molecule on the metal, *i.e.* Fermi-level alignment and charge equilibration [80]. In Eqs. (1.16) and (1.17), the transfer integral V describes the electronic coupling between the molecule and the electrode $V_{\text{Au-Mol}}$ for the two consecutive reactions of oxidation and reduction. In contrast, the conductance in the coherent tunneling regime can be derived from the transfer integral $V_{\text{Au-Au}}$ between the metal electrodes, which is calculated at the Fermi energy [80].

The reorganization energy λ is defined as the change in the free energy associated with the distortion of the reactant state to the equilibrium configuration of the product state without transfer of the charge [80,91], as

$$\lambda_{\text{tot}} = \lambda_{\text{in}} + \lambda_{\text{out}} = \lambda_{\text{in}} + \lambda_{\text{Born}} + \lambda_{\text{image}}. \quad (1.19)$$

The total reorganization energy λ_{tot} considered in Eqs. (1.16) and (1.17) can be split into the sum of inner and outer contributions (λ_{in} , λ_{out}), corresponding to relatively fast changes in the molecular geometry and slower variations in the solvent polarization of the surrounding medium, respectively [91]. The expression for λ_{out} can be divided into a Born term (λ_{Born}), which results from the interactions between the charged molecule and the solvent, and an image term (λ_{image}), which accounts for the screening of the charge by the electrodes. The contribution of λ_{image} to the reorganization energy is expressed by an infinite sum of Coulomb interactions between the charges on the molecule and the infinite number of corresponding image charges in the electrodes, which are induced by the charges on the molecule *via* long-range polarization effects [80,95–98].

The inner reorganization energy λ_{in} refers to the energy gain resulting from the relaxation of the molecular structure upon a charging event [80]. As described earlier, the elementary hopping step in molecular wires comprises two consecutive processes, which are characterized by the reorganization energies λ_1 and λ_2 , as illustrated in Fig. 1.7 [91].

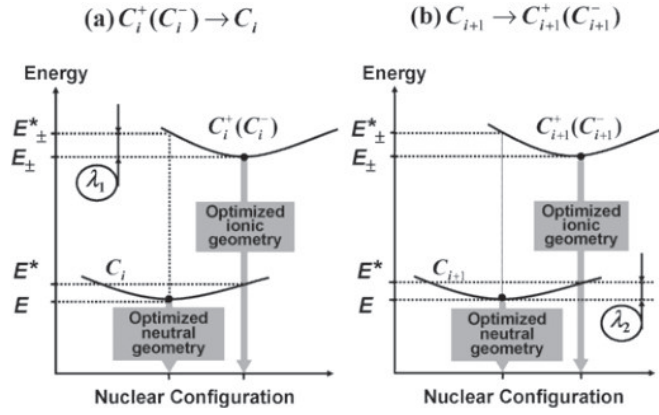


Figure 1.7: Reorganization Energy Scheme of the energetic and geometrical changes related to the elementary step of charge hopping in π -conjugated wires. (a) Removal of a charge from the π -conjugated unit C_i and (b) addition of the charge to the neighbouring unit C_{i+1} correspond to reorganization energies λ_1 and λ_2 , respectively. Reprinted from Ref. [91].

In the first step, the charge (hole or electron) is removed from the C_i site of the molecular wire, which is defined by the difference $E_{\pm}^* - E_{\pm}$ between the energies corresponding to the neutral and ionic geometries of the oxidized (or reduced) unit, denoted by λ_1 (see Fig. 1.7, a). Similarly, the charge transfer to the neighboring site C_{i+1} is defined by the difference $E^* - E$ between the energies referring to the ionic and neutral geometries of the neutral unit, termed as λ_2 (see Fig. 1.7, b) [91]. The overall λ_{in} value is consequently expressed by the sum of λ_1 and λ_2 as follows

$$\lambda_{in} = \lambda_1 + \lambda_2 = (E_{\pm}^* - E_{\pm}) + (E^* - E). \quad (1.20)$$

The conductances G_{hop} and G_{coh} for charge hopping and coherent tunneling, calculated as described based on Eq. (1.18) and from the transmission function by the NEGF-DFT approach based on Eq. (1.5), respectively, can be directly compared within the same single-particle framework to study the crossover point between the two transport regimes, as done by Kastlunger and Stadler [80].

However, rather than determining all essential quantities individually for describing the dominating transport mechanism in a particular molecular wire, the aim of this work is to derive an easily applicable measure for the prediction of transport mechanisms based on charge localization, where no assumptions of the transport mechanism are necessary *a priori*.

1.3 Intermediate Charge Transport Regimes in DNA

The integration of DNA-derivatives as conducting wires in molecular junctions has received interest not only due to their potential as being promising candidates for building blocks in DNA-based molecular electronic circuits [1,99], but also for the thorough understanding of relevant charge transport processes in nature, such as oxidative damage, which is of great biological relevance [20,23,100]. Inspired by these perspectives, several studies have focused on the investigation of charge transport mechanisms in DNA [66,67,99–102].

In studies of Tao and coworkers on guanine-based⁷ DNA derivatives, the influence of the base sequence on the dominating hole transport mechanism was clearly indicated [66,67]. The authors designed two different sets of self-complementary double-stranded (ds)-DNA: one with stacked G–C base pairs and another one with alternating G–C base pairs with the G bases separated from each other by a single C base, as illustrated in Fig. 1.8 (C). This experiment was based on previous studies, where it was found that G doublets and triplets feature lower ionization potentials than a single G base, indicating strong coupling between the π -orbitals of adjacent G bases and thus delocalization of the charge across the G domain [66,67,103]. Charge transport measurements were performed by using the STM-BJ technique (see Fig. 1.8 (A) for the experimental set-up), and the resistance of each DNA derivative was plotted as a function of the number of base pairs, *i.e.* molecular length. The results of the conductance measurements for each DNA sequence are depicted in Fig. 1.8 (B).

As becomes apparent from the resistance-versus-length plot, the charge transport characteristics vary significantly for the two different DNA sequences. Although both have the same molecular length, the alternating G-DNA sequences turned out to be more resistive than the stacked G-DNA sequences with a stronger dependence of the resistance on molecular length, as indicated by a greater slope [66,67]. However, one would assume that the charge transport occurs *via* a hopping mechanism in both DNA sequences, since the overall resistance increases linearly with molecular length in either case.

For the stacked G-DNA sequence a noticeable oscillation of resistance is super-

⁷In the following, the nucleobases adenine, thymine, guanine and cytosine are denoted by A, T, G and C, respectively. In the experiments, G-based DNA was chosen due to the lowest ionization potential of G compared to the other four bases, resulting in HOMO levels close to electrode Fermi level [66,67].

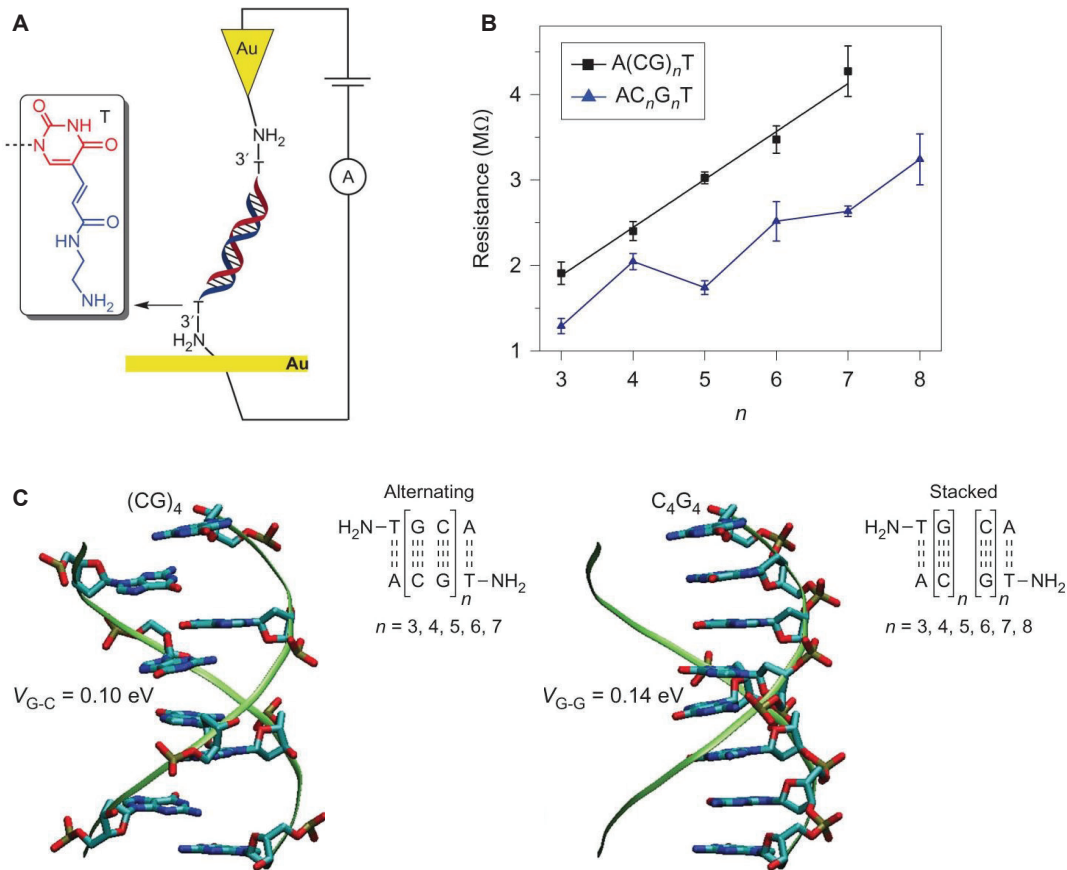


Figure 1.8: STM-BJ Experiments on G-DNA (A) Schematic representation of the molecular junction in STM-BJ experiments for charge transport measurements in ds-DNA by Tao and coworkers [66, 67]. (B) Resistance of alternating (black squares, $A(\text{CG})_n\text{T}$) and stacked (blue triangles, $\text{AC}_n\text{G}_n\text{T}$) G-DNA sequences vs. the number of CG bases. The resistance is smaller for the stacked than for the alternating sequences, and an oscillation is superimposed on the linear trend. Error bars are standard deviations calculated from three to four sets of experiments for each individual sequence, see Ref. [66]. (C) Chemical structures of alternating (left) and stacked (right) G-DNA, showing a better overlap between adjacent G bases for the stacked than for the alternating sequences, which is supported by the corresponding electronic couplings (V_{G-G} and V_{G-C}) between adjacent base pairs, calculated at the INDO/S level. Reprinted from Ref. [66].

imposed on the linearly increasing curve, which could not be described within the hopping transport model, therefore indicating a different charge transport mechanism. In other studies, periodic oscillations in the resistance-versus-length

plot had been observed in one-dimensional atomic wires that are characterized by coherent transport [104], and were also predicted for conjugated molecular systems featuring a strong overlap of π -electrons [105] and for DNA [106]. It was therefore assumed that they can be ascribed to partially coherent charge transport, indicating the presence of an intermediate regime, where coherent and incoherent processes coexist.

The experimental findings were confirmed theoretically by fitting the resistance-versus-length plot for the stacked G-DNA sequences according to the so-called Büttiker approach [107], where partially coherent charge transport is included in the incoherent hopping model, and which was previously applied to semiconductor devices [66,67].

From the model, a coherence length of roughly two to three base pairs was suggested, which was found to be in agreement with former experimental studies by Giese and coworkers on DNA sequences [100] and with theoretical predictions by Renaud and coworkers for poly(A)–poly(T) DNA hairpins [66,67,103]. It was suggested that in alternating G-DNA sequences, each G base acts as a hopping site, while in stacked G-DNA sequences, each hopping site consists of several base pairs. The existence of an intermediate transport mechanism in stacked G-DNA sequences could therefore be validated [66,67].

The proposed nature of the hopping sites was computationally supported by INDO/S calculations of the electronic couplings between neighboring G bases and the localization of the HOMOs in the two different G-DNA sequences [66,67]. It was found that the stacking of the G bases results in stronger electronic coupling between neighboring bases than in alternating G-DNA sequences, as expressed by coupling coefficients of 0.14 eV and 0.10 eV, respectively [66,67]. As indicated by the greater electronic coupling coefficients in stacked G-DNA sequences compared to the alternating ones, the resistance oscillations observed in the experiments were ascribed to partial delocalization of the charge. Hence, from DFT calculations, it was confirmed that the HOMOs of the G bases are delocalized over two to three base pairs, with their energy levels being close to the Fermi energy of the leads (which denotes the chemical potential of the electrons in the electrode) [66,67,103]. In contrast to the alternating G-DNA sequences, where each G base can be considered a hopping site, in the stacked G-DNA sequences a larger domain comprising several base pairs is considered a hopping site.

A wide variety of studies was performed on charge transport in DNA derivatives, all of them showing a strong dependence of the dominating transport mechanism on the base sequence and on the molecular length [66,67,103,108]. In similar STM-BJ experiments by Tao and coworkers on single DNA molecules in aqueous solution, a varying number of A–T base pairs was intercalated in short DNA sequences comprising eight G–C base pairs [101]. It was found that the transport characteristics qualitatively change upon insertion of A–T base pairs into G–C domains, indicating different conduction mechanisms for varying sequences. It was suggested that coherent transport predominates in DNA sequences with eight G–C base pairs only, whereas the A–T base pairs are representing a tunnel barrier, inducing incoherent transport between the G–C domains [1,101].

Related studies have been performed by Giese and coworkers, where the charge transfer rate between two G–C domains was measured as a function of their separation by A–T base pairs [100]. It was shown that the transfer rate between the G–C domains decreases clearly with growing number of A–T base pairs between them when they are separated by no more than three of them. Only weak distance dependence of the charge transfer rates was observed in the case of greater separation, suggesting a shift from coherent tunneling at short distances to thermally induced hopping between A–T domains at long distances. Thus, in the tunneling regime, the bridging A bases act as a mediator of the electronic coupling between the G bases, whereas in the hopping regime, the A bases are oxidized by the G bases and are directly involved in the charge transport process [1,100].

Based on these studies it was indicated that the charge transport in DNA is governed not only by one single mechanism, but is sensitive to the sequence and number of the base pairs, which plays a decisive role for the dominating transport mechanism. This finding can be attributed to the differences between the π -systems of the individual bases, which determines the overlap between the π -orbitals of adjacent base pairs that mediates the charge transport mechanism in DNA derivatives [1,100,101].

For studying charge transfer mechanisms in DNA, the advantage of G as nucleobase over others is its low ionization potential [66,67,102]. Thus, in comparison to other nucleobases, the HOMO of the G base is closest to the Fermi level of the gold electrode linked to the molecule [66,67,103]. For example, Porath

and coworkers performed AFM experiments on G-quadruplex DNA (G4-DNA), consisting of four strands of G nucleotides running parallel to each other and thus forming a braided structure with a G-tetrad as a recurring unit [102]. This G4-DNA enables efficient charge transport within the molecule due to its G-rich content and is more rigid compared to native ds-DNA. It was demonstrated that G4-DNA is capable of transporting current over relatively long distances in a reproducible manner, suggesting that the charge transport occurs *via* thermally activated long-range hopping between multi-tetrad segments of the DNA, which was confirmed by fitting the experimental data to the incoherent hopping model [102].

Based on these investigations, the DNA base sequence as well as the molecular length were identified as key parameters that highly affect the conduction properties of the corresponding wires and determine the transport mechanism in molecular junctions. An additional important aspect is the environment [1]: since the most conductive form of the DNA, *i.e.* the B-conformation, is only available in solution, the presence of a solvent is crucial when performing conductance measurements. Moreover, environmental modeling may be an important factor to be considered in the context of theoretical simulations, as it likely enhances the stabilization of the charge and therefore may have an effect on its degree of localization [1, 53].

2 Charge Localization in Molecular Wires

Motivated by the observation of the length-dependent tunneling-to-hopping transition in molecular conductance experiments, the main goal of this work was to establish an easily applicable and efficient way of predicting the predominating transport mechanism. As the field of molecular electronics is relatively new and molecular junctions are often not structurally well-controlled, a properly characterized model system is a necessary prerequisite for validating computational methods before applying them to molecules in a junction.

In this section, the concept of charge localization is introduced on the example of organic mixed-valence systems as a promising tool to predict transport mechanisms observed in molecular conductance experiments. This variant of donor-bridge-acceptor (D-B-A) systems is particularly interesting, as it can be assumed that their length-dependent charge localization properties can be associated with the dominating charge transport mechanism in a molecular junction based on the same bridge.

The classification of mixed-valence systems based on charge localization properties according to the well-known Robin-Day scheme is introduced and experimental examples of transitions from delocalization to localization with increasing bridge length are presented, which can be linked to the tunneling-hopping crossover in molecular wires. On the example of mixed-valence systems, the influence of the bridge length and the energy gap between the D-B-A levels on charge transfer is discussed in further detail.

Experimental evidence on such transitions is provided for three different organic mixed-valence species along with findings from earlier theoretical investigations, thus providing a state-of-the-art overview and setting the stage for the DFT results on these systems obtained in this work.

2.1 Charge Transfer in Organic Mixed-valence Systems

In this work, the similarities between charge transfer in D-B-A systems and charge transport through a molecular junction were exploited: In both types of experiments, the mechanism governing the migration of the charge along the molecular bridge or wire is related, even though the driving forces are different [1], be it either the free energy difference between initial and final states or the bias voltage, respectively.

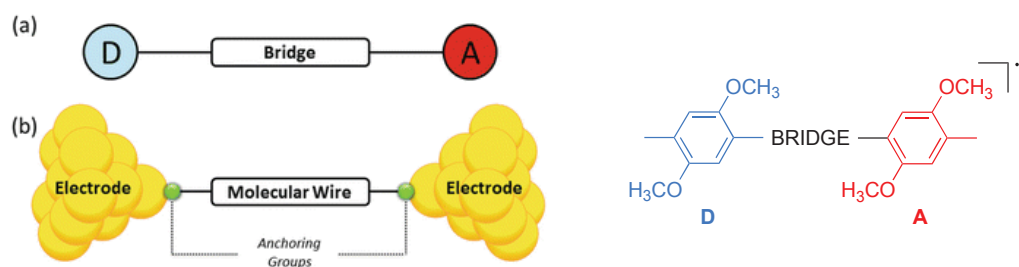


Figure 2.9: Analogy between MV Systems and Molecular Junctions

Left: (a) Scheme of D–B–A complexes and (b) molecular junctions. Figure reprinted from Ref. [3]. *Right:* Scheme of an organic MV radical cationic system as a variant of a D–B–A system, comprising two 2,5-dimethoxy-4-methylphenyl (DMP) redox centers, separated by a conjugated bridge. The donor (blue) and acceptor (red) are represented by identical redox centers.

As depicted in Fig. 2.9, both systems can be subdivided into three subregions, where the donor- and acceptor moieties resemble the electrodes in a molecular junction and the bridge between them is replaced by a molecular wire. Here, the so-called mixed-valence systems are used as model systems, which can be regarded as a variant of D–B–A compounds with two (or more) redox centers, where the first one acts as the electron donor and the other as the electron acceptor [61–63].

Whereas D–B–A compounds typically are closed-shell compounds in the ground state, organic mixed-valence are always open-shell systems. The main characteristic of these systems is the presence of an element in more than one oxidation state, which is usually but not necessarily represented by metal atoms as redox centers [62, 63]. In organic mixed-valence systems, which are studied in this work, the redox centers are substituted by purely organic, non-metallic redox centers, such as in the radical cationic dimethoxy-*p*-phenylene-based species depicted in Fig. 2.9 (right).

Mixed-valence systems are especially interesting in the context of determining the crossover length of transport mechanisms, as the charge transfer in these compounds is equally length-dependent and the degree of charge localization changes with increasing distance between the redox centers, as discussed in the following in the context of semi-classical electron transfer theory [62]. Beyond that, they are well-characterized from experiments, providing a solid foundation for the validation of DFT methods in terms of describing length-dependent charge localization properties [62, 63].

Charge Transfer – The Role of the Molecular Bridge

When describing charge transfer processes in D–B–A systems, there are several crucial factors determining the charge transfer rates. One of them is the chemical structure of the bridge, as for example much higher electron transfer rates from a porphyrin donor to a quinone acceptor are obtained if the molecular bridge consists of unsaturated hydrocarbons compared to saturated ones, although other parameters such as the distance between the donor and acceptor are unchanged [109]. In fact, the electron transfer rate is strongly determined by the D–A distance R_{DA} , but shows different characteristics depending on the dominating transfer mechanism. There are two main pathways for charge transfer: the coherent superexchange mechanism and the incoherent hopping mechanism [63, 92]. The former one shows, similar to the conductance, an exponential dependence of the transfer rate k_{ET} on R_{DA} , of the form

$$k_{ET} = A(T)e^{-\beta R_{DA}}, \quad (2.21)$$

where $A(T)$ is a temperature-dependent prefactor and, again, β is a constant, which reflects and is particularly sensitive to the chemical structure of the bridge (and the donor and acceptor moieties), as in the case of molecular conductance, see Eq. (1.2) [92].⁸ This relation is valid only if the reorganization energy λ is relatively small, as it also depends on the distance between the donor and acceptor, as explained in the following [63, 92]. With increasing distance of the bridge between the donor and acceptor centers, the charge transfer mechanism changes to incoherent hopping, which is indicated by the distance dependence of the electron transfer rate following Ohm's law like

$$k_{ET} \propto \frac{1}{N}, \quad (2.22)$$

where the number of bridge sites between the donor and acceptor, *e.g.* the monomer units on which the charge is transferred stepwise, is denoted by N . In this regime, the electron transfer rate depends linearly on the distance between the donor and acceptor redox centers, resembling the characteristics of the molecular conductance in the hopping regime, see Eq. (1.3).⁸

⁸Note, that the exponential and linear dependence of the transfer rate k_{ET} on the D–A distance R_{DA} is similar to the length-dependence of conductance (or rather resistance) that characterizes charge transport in the coherent tunneling and incoherent hopping regime, respectively, as described in Sec. 1.1 by Eqs. (1.2) and (1.3).

Similarly, in contrast to the superexchange regime, the charge transfer processes in the hopping regime are thermally activated, as the dynamics described by Eq. (2.22) correspond to the charge physically residing on the molecular bridge [92]. The electron transfer rate consequently also depends on the energy gap between the donor and the bridge energy levels. In case the donor level is higher in energy than the lowest bridge level, population of the bridge is also possible without thermal activation [92].

The main difference between charge transfer *via* superexchange and charge hopping is the participation of the bridge states in the transfer process, which is virtual or real, respectively [63]. The transfer mechanism is determined by the energy gap between the levels of the donor and the bridge states: bridge states lying high in energy will result in charge transfer dominated by superexchange, while bridge states lower in energy or even resonant with the donor energy levels are likely leading to charge hopping, where each hopping step may be described by a superexchange process [63]. Consequently, the main charge transfer mechanism is determined by the relative energy of the frontier orbitals of the bridge, as depicted schematically in Fig. 2.10 for radical anionic and cationic mixed-valence compounds, where the donor and acceptor moieties are represented by identical redox centers.

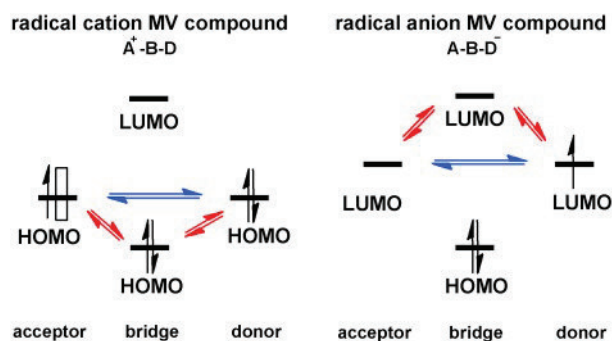


Figure 2.10: Dependence of Charge Transfer on Frontier Orbitals Frontier orbitals of cationic (left) and anionic (right) mixed-valence compounds and the two pathways of charge transfer: superexchange mechanism (blue) and hopping mechanism (red). For the cationic system, a hole rather than an electron is transferred from the acceptor to the donor (illustrated by the white box). For mixed-valence systems, the donor and acceptor are represented by identical redox centers. Figure reprinted from Ref. [63].

In cationic mixed-valence systems, hopping transfer of holes is promoted by the bridge HOMO being relatively high in energy and therefore lying close to the donor HOMO. Likewise, in anionic mixed-valence systems, electron hopping is promoted by the bridge lowest unoccupied molecular orbitals (LUMOs) being relatively low in energy and therefore lying close to the donor LUMO. Both mechanisms, superexchange and charge hopping, contribute concomitantly to the charge transfer, but exhibit different dependencies on the distance, similar to charge transport studied in molecular conductance experiments [63]. However, in either case, the electronic coupling between the two redox centers decreases with increasing distance between them, as will be shown in the following [62,63].

Distance Dependence of Charge Transfer - Experimental Evidence In an experimental study of Kochi and coworkers, the distance dependence of the intramolecular electron transfer was investigated in organic mixed-valence systems, where two redox active DMP units are linked either directly or by oligo-*p*-phenylene bridges variable in length (see Fig. 2.9, right) [110–112].

It was found that the plot of $\log(H_{AB})$ as a function of the distance between the redox centers decreases linearly, in agreement with superexchange theory, whereat H_{AB} was determined from near-infrared (NIR) absorption bands (Fig. 2.11). For organic-mixed valence systems, the electronic coupling matrix element can be evaluated from the analysis of the intervalence charge-transfer (IV-CT) absorption bands within the framework of the Marcus–Hush theory [113–116] (see Sec. 2.2).

Beyond that, the electron transfer rate constants k_{ET} were determined from temperature-dependent electron paramagnetic resonance (EPR) line broadening experiments. Based on the plot of $\log(k_{ET})$ versus the distance between the redox centers, it was indicated that the decrease of the curve is less clearly linear and the exponential distance dependence is less pronounced when compared to the electronic coupling matrix element. However, the slopes for H_{AB} and k_{ET} as obtained from a linear regression fit were found to vary by a factor of two for each data set ($\beta = -0.18\text{\AA}$ versus $\beta = -0.44\text{\AA}$, respectively), which is consistent with electron transfer theory according to the relation $k_{ET} \propto H_{AB}^2$, which is valid in case of weak coupling between the donor and acceptor moieties [62,117]. Thus, k_{ET} is predicted to be proportional to the square of the electronic coupling matrix element H_{AB} , which in turn falls off exponentially with distance as a

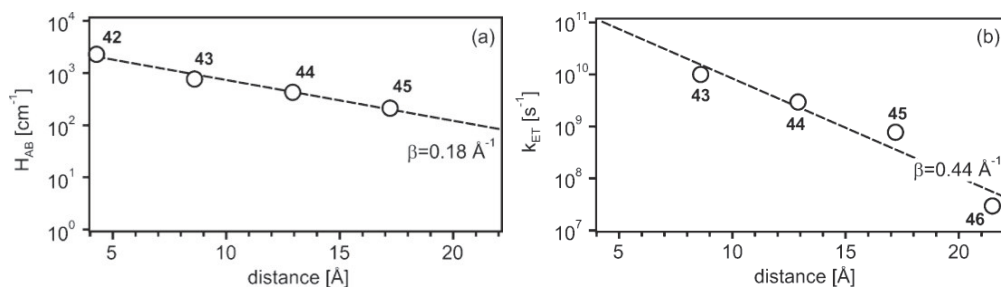


Figure 2.11: Distance-dependent Charge Transfer Plot of the electronic coupling matrix element H_{AB} (a) and the intramolecular electron transfer rate k_{ET} (b) as a function of the distance between the redox centers in organic mixed-valence radical cationic DMP species, obtained from studies by Kochi and coworkers [110–112]. The number of phenylene units between the redox centers ranges between zero (**42**) and four (**46**). The distance decay constants β are obtained from linear regression fits in either case. Reprinted from Ref. [62].

result of the exponential radial character of the electronic wave functions of the donor and acceptor,

$$H_{AB} = V_0 e^{-\beta \frac{(R-R_0)}{2}}. \quad (2.23)$$

In Eq. (2.23), V_0 denotes the donor–acceptor electronic coupling element at the van-der-Waals separation R_0 , and β is a constant that determines the decay rate of H_{AB} with increasing distance R [117]. Since the electron transfer rate is dependent on the electronic coupling matrix element, it is predicted to reflect the exponential decay of H_{AB} with increasing distance as shown earlier in Eq. (2.21), in agreement with a charge tunneling process, as predicted from semi-classical electron transfer theory [63,117].

2.2 Class III–II Transitions in MV Systems – State of the Art

In the past, the distance dependence of the charge transfer in organic mixed-valence systems has been the object of several studies [62, 110–112, 118–122]. Since a transition from a fully delocalized to a charge-localized system occurs with increasing bridge length between the redox centers, the most challenging aspect in this field of research is the characterization of compounds on the borderline between these two cases [62]. Robin and Day derived a useful classification scheme for these different forms of charge localization from full delocalization (class III) to charge localization (class II), as well as for intermediate systems which cannot be clearly assigned to one of these situations but rather feature partial charge localization in between [62].

Several studies have focused on the characterization of class III/II borderline species, using both experimental and computational techniques, and aiming at evaluating the distance between the redox centers where a crossover from class III to class II would occur [110, 111, 118–123]. In order to present an overview over the state of knowledge and to provide a basis for the validation of computational approaches with respect to the prediction of class III–II transitions, the main findings from these studies are presented in this section for organic mixed-valence systems close to the class III/II borderline.

Robin–Day Classification of Mixed-Valence Systems

A paramount question in the context of mixed-valence chemistry is whether the extra charge is localized or delocalized across the system [62]. As the degree of charge localization in mixed-valence system changes with increasing distance between the redox centers, the evaluation of the degree of charge localization is not straightforward in many cases. For radical cationic mixed-valence systems composed of two redox centers ($R_{A,B}$) that are connected by a bridging unit (B), two extreme situations may occur: In the first case, the excess charge is fully localized on one redox center ($R_A^{+1}-B-R_B^0$), whereas in the second case the charge is delocalized across the entire system, resulting in the oxidation numbers of the redox centers being equal ($R_A^{+0.5}-B-R_B^{+0.5}$).

Completely localized systems are assigned to class I, systems with fully delocalized charge belong to class III, and systems with the charge mainly localized on one redox center belong to class II. It has to be noted that the assignment of a particular system is often not clear-cut as the transition from one class to

another is rather gradual. Consequently, there may be situations where a system cannot be unambiguously assigned to one definite class, but is rather considered a borderline compound between two classes, *e.g.* class III and class II, being nearly but not fully delocalized. An additional class III/II regime was therefore introduced to reflect this ambivalent character [62].

For the assignment of organic-mixed valence systems to one of these classes, two key components have to be considered, the electronic coupling H_{AB} , which is a measure of the electronic communication between the two redox sites (R_A and R_B), and the reorganization energy λ , which denotes the energy needed for the optically induced charge transfer between them (see Sec. 1.2) [62]. Based on the Marcus theory for intramolecular charge transfer processes [40, 41, 124, 125], the reactant and product states⁹ can be described by two diabatic (non-interacting) one-dimensional harmonic profiles along the dimensionless reaction coordinate X [63]. In Fig. 2.12, the potential energy surfaces (PES) for the respective Robin–Day classes are shown.

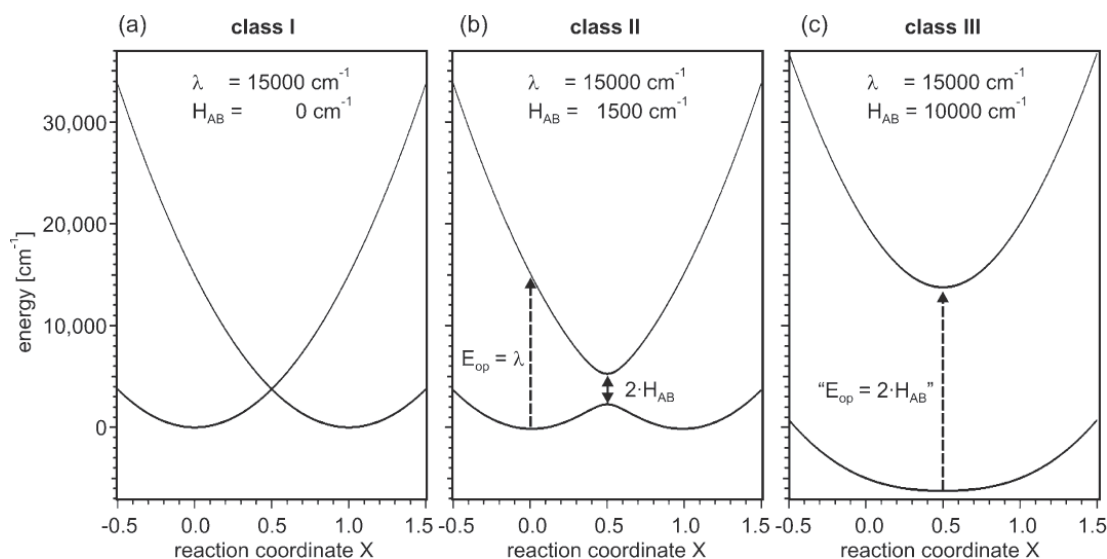


Figure 2.12: Robin–Day Classification of MV Systems Potential energy surfaces for charge transfer in mixed-valence systems with negligible (a), weak (b), and strong (c) electronic coupling H_{AB} between the redox centers A and B. The total reorganization energy, associated with the charge transfer between the redox centers, is denoted by λ . Reprinted from Ref. [62].

⁹The reactant and product states correspond to the charge being located on the first or the second redox center after the transfer has taken place.

In the first case, when there is no electronic coupling between the donor and acceptor moiety ($H_{AB} = 0$), the two redox centers can be considered completely isolated and thus the system belongs to class I [62,63]. As becomes apparent from the corresponding PES (a), the two harmonic potential energy wells, representing the reactant and product states, are diabatic due to the lack of electronic coupling, and the molecule with the electron being localized on one of the redox centers is located in either of them. On the dimensionless reaction coordinate, referring to the interpolation between the molecular structures with the charge being located on the first and the second redox center, the equilibrium positions of the molecule are located at $X = 0$ and $X = 1$. Since it is not possible to induce intramolecular charge transfer between the redox centers in these compounds, neither optically nor thermally, it is questionable whether these species can be regarded mixed-valence systems at all [62,63].

For class II systems (Fig. 2.12, b), the electronic coupling is smaller than half the reorganization energy ($H_{AB} \leq \lambda/2$). In this case, the wave functions defining the two potential wells are mixed, and the diabatic PES are split into two adiabatic PES, where the energy difference at $X = 0.5$ between them corresponds to $2H_{AB}$ according to Marcus–Hush theory [113–116]. This theory represents the adiabatic extension of the classical Marcus theory, where the electronic communication between the donor and acceptor moieties is considered [63]. In this regime of weak electronic coupling between the redox centers, the adiabatic ground state consists of a double minimum at $X = 0$ and $X = 1$. The charge is mainly localized on one redox center and, in contrast to the situation in class I systems, charge transfer to the other redox center can be optically or thermally induced by direct excitation into an IV-CT band, which can be observed as an optical absorption band in NIR spectroscopy experiments. As the probabilities of transitions at $X = 0$ are reflected by a Gaussian distribution and these so-called Franck–Condon transitions occur to a sharply sloping area of the upper potential well, the resulting IV-CT bands are broad and feature a Gaussian shape, and the energetic position of the IV-CT absorption band maximum E_{op} corresponds to the reorganization energy ($E_{op} = \lambda$) [62,63].

When the electronic coupling between the redox centers is greater than half the reorganization energy ($H_{AB} \geq \lambda/2$), the charge is fully delocalized across the molecule and the system is assigned to class III (Fig. 2.12, c). In this case, a single minimum is located at $X = 0.5$ in the lower potential well. Absorption

bands are relatively narrow, since the transitions occur to a moderately sloping region of the upper potential well. Strictly speaking, these absorption bands cannot be considered IV-CT bands, since there is no net charge transfer involved in the transition. In the so-called two-state model [126], where two adiabatic two-dimensional PES are considered, E_{op} directly correlates with the magnitude of the electronic coupling ($E_{op} = 2H_{AB}$) [62].

Setting the Stage – Experimental Evidence for Class III–II Transitions

In this work, various computational approaches for describing the length-dependence of charge localization were validated on the example of three different sets of organic mixed-valence system (see Fig. 2.13), where a transition from class III to class II was observed from the experiments at a certain molecular length. The Robin–Day classification is mostly derived from a combined approach based on NIR and EPR spectroscopy experiments and often complemented by X-Ray crystallographic studies [110, 111, 118, 119, 123]. Since the availability of solid experimental data is a necessary prerequisite for a proper validation of computational methods, the results from a variety of experiments on mixed-valence systems, covering the whole range from charge delocalization (class III) to charge localization (class II), are summarized below.

With the perspective of using the experimentally derived classification as foundation for the validation of DFT methods it has to be noted that the experimental classification is often evaluated from a variety of data that suggests a certain degree of charge localization in relation to another compound. Thus, the experiments rather provide a tendency for the classification of a particular system, which makes the comparison with theory not straightforward in many situations. In addition, the quantities serving as indicator for charge localization in the experiments, for example the shape and solvatochromism of NIR absorption bands, might not be easily computationally accessible. Consequently, when comparing the classification from experiments with theory it is advisable to not consider a particular species in isolation but rather in relation to similar species of different length, especially in case of III/II borderline compounds.

DMP_n In experimental studies of Kochi and coworkers, the distance dependence of intramolecular charge transfer in organic mixed-valence systems was investigated on the example of bridged aromatic radical cations comprising two

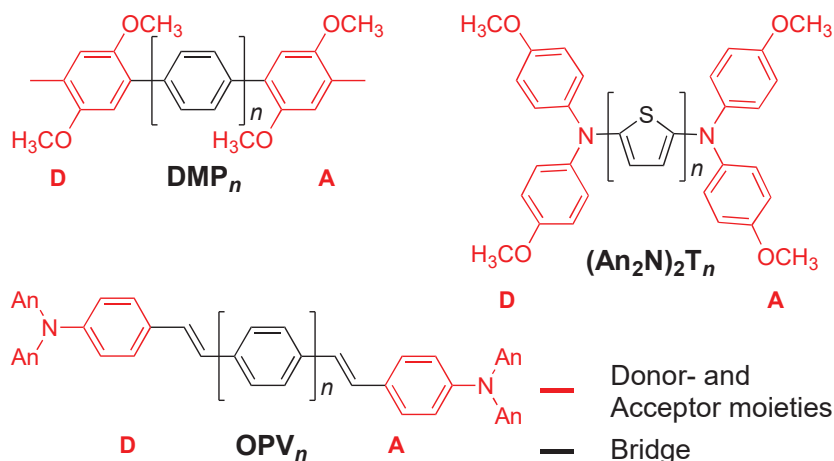


Figure 2.13: Organic Mixed-Valence Systems Chemical structures of radical cationic organic mixed-valence systems under study for the validation of computational protocols for describing charge localization. Donor- and acceptor moieties are marked in red.

DMP units linked by oligo-*p*-phenylene bridges of variable length (DMP_{*n*})¹⁰, which are depicted in Fig. 2.13 [110]. DMP_{*n*} molecules with the number of *p*-phenylene units between the redox centers ranging between zero and four (DMP₀–DMP₄) were classified by means of complementary temperature-dependent EPR and X-ray crystallographic experiments.

Based on the experimental data it was found that DMP₀ can be considered a class III system, whereas DMP₂–DMP₄ belong to class II, with DMP₄ already being on the class II/I borderline. As the temperature-dependent behavior in the EPR experiments of DMP₁ turned out to be intermediate between DMP₀ and DMP₂, it was considered a class III/II borderline compound (see Tab. 2.1 for experimental classification) [110,111].

The rather ambivalent character of DMP₁ regarding charge localization becomes even more clear from the X-ray crystallographic data. Upon oxidation, the DMP_{*n*} unit undergoes a quinoidal deformation (see Fig. 3.1 in Sec. 3.1), resulting in a growing difference between the C–O bond lengths on each redox center with increasing degree of charge localization. This characteristic structural change was exploited to determine the static charge distributions from X-ray crystallographic experiments [110,111].

¹⁰In DMP_{*n*}, *n* denotes the number of *p*-phenylene units in the bridge between the redox centers.

It was found that in the shortest radical cation DMP_0 , the charge is equally distributed across the molecule, with each redox center having a charge of +0.50, pointing to a completely charge-delocalized class III system. For the phenylene-bridged radical cation DMP_1 , an asymmetric charge distribution was observed, where +0.80 charge resides on the first redox center and only a charge of +0.20 on the second redox center. As a rather asymmetric charge distribution was found for DMP_1 , which is polarized between the two redox centers, this system could not be clearly assigned to either class III or class II [110,111]. Given that the temperature-dependent behavior in the EPR experiments of DMP_1 was intermediate between DMP_0 and DMP_2 , it was considered a class III/II borderline compound [110,111]. For the longer DMP_2 radical cation the charge was found being fully located on one redox center, suggesting the categorization as a fully charge-localized class II system.

OPV_n In studies of Barlow and coworkers, the intervalence transitions in organic mixed-valence bis(dianisylamine) radical cations with oligo-*p*-phenylene-vinylene bridges (OPV_n ¹¹) of variable length (OPV_0 – OPV_3) were investigated by means of NIR spectroscopy and complemented by X-ray crystallographic experiments, as was done in the studies on DMP_n by Kochi and coworkers (see Fig. 2.13). [118] The solvatochromism and shape of the NIR absorption bands served as an indicator for the classification, and it was concluded that OPV_0 is a class III system, whereas for the longer species OPV_1 , class II character was suggested, therefore indicating the class III–II transition (see Tab. 2.1).

Oligothiophenes In an experimental study by Wenger and coworkers, the degree of charge localization was investigated in organic mixed-valence bis(diarylamine) radical cations with an oligothiophene bridge of variable length ($(\text{Ar}_2\text{N})_2\text{T}_n$ ¹²) [123], depicted in Fig. 2.13. These systems are particularly interesting for the purpose of this work since they bear structural resemblance to the thiophene-based molecular wires studied in molecular conductance experiments by Frisbie and coworkers [31], as described in Sec. 1.2.

¹¹In OPV_n , n denotes the number of *p*-phenylene units in the bridge between the redox centers.

¹²In $(\text{Ar}_2\text{N})_2\text{T}_n$, n denotes the number of thiophene units in the bridge between the redox centers.

Based on cyclic voltammetry and complementary NIR and EPR spectroscopy experiments, the species with thiophene units ranging from one ($(\text{An}_2\text{N})_2\text{T}_1$) to three ($(\text{An}_2\text{N})_2\text{T}_3$) were considered either delocalized class III or class III/II borderline systems [123]. Hence, a transition to class II was predicted only for oligothiophene molecules with more than three thiophene units (see Tab. 2.1) [123].

2.3 DFT Approaches for Describing Charge Localization

In this section, the theoretical foundations for the description of charge localization based on electronic structure calculations are provided. Here, Kohn–Sham density functional theory (KS–DFT) was used for the optimization of molecular structures and the calculation of charge localization properties. In the past years, several DFT protocols have been applied to organic mixed-valence systems, especially to complexes in the borderline regime, with the aim of classifying them within the Robin–Day scheme [50, 51, 110, 111, 118–123]. These approaches will be outlined and discussed in the context of their performance in describing the degree of charge localization, along with their shortcomings in the underlying formalism and practical considerations on the choice of appropriate exchange–correlation functionals.

Density Functional Theory: Basics

The electronic energy of a system consisting of M nuclei and N electrons, can be obtained by solving the time-independent non-relativistic Schrödinger equation,

$$\hat{H}\Psi_i(\vec{x}_1, \dots, \vec{x}_N, \vec{R}_1, \dots, \vec{R}_M) = E_i\Psi_i(\vec{x}_1, \dots, \vec{x}_N, \vec{R}_1, \dots, \vec{R}_M), \quad (2.24)$$

where \hat{H} denotes the Hamiltonian, E_i the electronic energy, and Ψ_i the electronic wave function of a state i . The electron variable \vec{x} comprises the spatial vector \vec{r} and the spin coordinate s , and thus is expressed as $\vec{x} \equiv (s, \vec{r})$. The spatial vectors of the electrons \vec{r} and nuclei \vec{R} are given in terms of the three spatial coordinates (x, y, z) .

A simplified version of the Schrödinger equation can be derived by introducing the Born–Oppenheimer approximation, where the motions of the electrons and the nuclei are separated as it can be considered that the heavier nuclei move much more slowly than the electrons, which consequently react nearly instantaneously to variations of the nuclear coordinates [127, 128]. Thus, the nuclear kinetic energy becomes zero and the potential energy \hat{V}_{NN} is a constant term, which

has to be added later to the total energy. The resulting expression for the electronic Hamiltonian in atomic units reads,

$$\hat{H}_{el} = -\frac{1}{2} \sum_{i=1}^N \nabla_i^2 - \sum_{i=1}^N \sum_{A=1}^N \frac{Z_A}{r_{iA}} + \sum_{i=1}^N \sum_{j \geq i}^N \frac{1}{r_{ij}} = \hat{T}_e + \hat{V}_{Ne} + \hat{V}_{ee}, \quad (2.25)$$

where $\nabla_i = (\frac{\partial}{\partial x_i}, \frac{\partial}{\partial y_i}, \frac{\partial}{\partial z_i})$ denotes the nabla operator for the electronic coordinates, Z_A is the nuclear charge number, $r_{iA} = |r_i - R_A|$ is the distance between electron i and nucleus A and $r_{ij} = |r_i - r_j|$ is the distance between the electrons i and j . The first term represents the kinetic energy of the electrons \hat{T}_e , and the other two terms, \hat{V}_{Ne} and \hat{V}_{ee} , account for the attractive and repulsive potential energies arising from the nucleus–electron and electron–electron interactions, respectively. The energy can be calculated from the N -electron wave function, depending on $4N$ variables, three spatial variables and one spin variable [129].

The basic idea of DFT is to calculate the energy as a functional of the ground state electron density $\rho(\vec{r})$ instead, which is defined as the integral over all electrons and over all but one of the spatial variables,

$$\rho(\vec{r}_1) = N \int \dots \int |\Psi(\vec{x}_1, \vec{x}_2, \dots, \vec{x}_N)|^2 ds_1 d\vec{x}_2 \dots \vec{x}_N, \quad (2.26)$$

where the index denoting the number of the electron is skipped in the following. As the electron density only depends on the three spatial variables, the $4N$ -dimensional problem of the wave function is reduced to a 3-dimensional problem [129].

The concept of DFT is based on the so-called Hohenberg–Kohn theorems [85,86]. The first of them states that the external potential, generated by the nuclei, is determined by the many-particle ground-state electron density except for an additive constant. As the number N of the electrons can be calculated by integrating over $\rho(\vec{r})$, the properties of a molecule, particularly the ground state energy, determined by the wave function, can be derived from the ground-state electron density. The electronic energy $E[\rho(\vec{r})]$ can be written as a functional of the electron density as

$$\begin{aligned} E[\rho(\vec{r})] &= E_{Ne}[\rho(\vec{r})] + T[\rho(\vec{r})] + E_{ee}[\rho(\vec{r})] \\ &= \int \rho(\vec{r}) V_{Ne}(\vec{r}) d\vec{r} + F_{HK}[\rho(\vec{r})], \end{aligned} \quad (2.27)$$

where the potential energy arising from the nucleus–nucleus interaction \hat{V}_{NN}

needs to be added later in order to obtain the total energy. $E_{\text{Ne}}[\rho(\vec{r})]$ is the potential energy corresponding to the electron–nuclei attraction, and $F_{\text{HK}}[\rho(\vec{r})]$ is the Hohenberg–Kohn functional,

$$F_{\text{HK}}[\rho(\vec{r})] = T[\rho(\vec{r})] + E_{\text{ee}}[\rho(\vec{r})], \quad (2.28)$$

which consists of the functional for the kinetic energy $T[\rho(\vec{r})]$ and the functional for the electron–electron interaction $E_{\text{ee}}[\rho(\vec{r})]$, whose explicit forms are unknown. The second Hohenberg–Kohn theorem states that for any guess for the electron density $\rho(\vec{r})$, the functional $E[\rho(\vec{r})]$ is greater than or equal to the ground state energy E_0 and thus adheres to the variational principle,

$$E[\rho(\vec{r})] \geq E_0. \quad (2.29)$$

Hence, any ground-state energy $E[\rho(\vec{r})]$ calculated from Eq. (2.27) describes an upper bound to the true ground state energy E_0 .

Since the exact form of the $F_{\text{HK}}[\rho(\vec{r})]$ functional is not known and, in particular, since there are no good approximations available for the functional for the kinetic energy $T[\rho(\vec{r})]$ in molecules, Kohn and Sham proposed to express the ground-state electron density $\rho(\vec{r})$ of the real, interacting system as the electron density of a reference system of non-interacting fermions with the same ground-state density as the interacting system [85]. The kinetic energy $T_{\text{S}}[\rho(\vec{r})]$ of the reference system can then simply be calculated by the expectation value of a single Slater determinant, and the expression for the Hohenberg–Kohn functional reads,

$$F_{\text{HK}}[\rho(\vec{r})] = T_{\text{S}}[\rho(\vec{r})] + J[\rho(\vec{r})] + E_{\text{XC}}[\rho(\vec{r})], \quad (2.30)$$

with the electronic energy $E[\rho(\vec{r})]$ of the interacting system in Eq. (2.27) rewritten as,

$$E[\rho(\vec{r})] = T_{\text{S}}[\rho(\vec{r})] + J[\rho(\vec{r})] + E_{\text{XC}} + E_{\text{Ne}}[\rho(\vec{r})]. \quad (2.31)$$

Here, $J[\rho(\vec{r})]$ denotes the term for the classical electron–electron Coulomb interactions, which is also calculated on the basis of the reference system. $E_{\text{XC}}[\rho(\vec{r})]$ is the so-called exchange–correlation functional,

$$E_{\text{XC}}[\rho(\vec{r})] \equiv (T[\rho(\vec{r})] - T_{\text{S}}[\rho(\vec{r})]) + (E_{\text{ee}}[\rho(\vec{r})] - J[\rho(\vec{r})]), \quad (2.32)$$

which is not known exactly except for a few simple model systems and contains all non-classical contributions, the exchange and correlation terms. The first term denotes the difference between the kinetic energy of the reference system and the exact kinetic energy, which is considered to be small.

Exchange–Correlation Functionals

The main concern of KS–DFT [85, 86], which was employed for calculations throughout this work, is the approximation of the unknown exchange–correlation functional $E_{\text{XC}}[\rho(\vec{r})]$ in Eq. (2.32). In the past, a number of approximate exchange–correlation functionals has evolved. Some of them, in particular the hybrid functionals and the newer long-range corrected functionals are presented briefly in this section, as they were applied for calculations within this work.

The basis of all approximate exchange–correlation functionals is the *local density approximation* (LDA), which relies on the model of a uniform electron gas and represents the earliest approximation [130]. However, the LDA has a rather low importance for computational applications in chemistry, since the approximation of inhomogeneous electron densities, as present in molecules, by a uniform electron gas is quite rough.

A more sophisticated approach than the LDA is the *generalized gradient approximation* (GGA), where the gradient of the density $\nabla\rho(\vec{r})$ is considered in the functional. The GGA exchange–correlation functional is usually divided into its exchange and correlation parts, which are then approximated separately. Among the most frequently used forms for the gradient-corrected exchange functionals are the Becke 88 functional, developed by Becke and usually termed B88 [131]. Most commonly, these exchange functionals are combined with the Perdew 86 correlation counterpart, usually termed P86 [132], or the newer LYP correlation functional, designed by Lee, Yang and Parr [133], resulting in the popular BP86 and BLYP density functionals, respectively. Beyond that, the PBE exchange–correlation functional, proposed by Perdew, Burke and Ernzerhof, is also frequently used [134].

In this work, the BP86 density functional was only used for pre-optimizations of molecular structures with the TURBOMOLE program package using the resolution-of-identity (RI) approach, whereas subsequent optimizations were performed mainly by using so-called hybrid functionals. In this category of approximating functionals, the DFT exchange energy is mixed with a portion of exact ex-

change energy, which is obtained from the Hartree–Fock (HF) approximation. In the widely used three-parameter B3LYP [135] functional, the B88 exchange functional is augmented by a part of 20% exact exchange and combined with the LYP correlation functional, resulting in the expression

$$E_{\text{XC}}^{\text{B3LYP}} = a_{x0}E_{\text{X}}^{\text{LDA}} + (1 - a_{x0})E_{\text{X}}^{\text{HF}} + a_{x1}\Delta E_{\text{X}}^{\text{B}} + (1 - a_c)E_{\text{C}}^{\text{LDA}} + a_cE_{\text{C}}^{\text{LYP}}, \quad (2.33)$$

where the three parameters for B3LYP are derived from fitting them to a set of thermodynamical data, resulting in $a_{x0} = 0.80$, $a_{x1} = 0.72$ and $a_c = 0.81$, corresponding to 20% HF–exchange E_{X}^{HF} , 72% Becke gradient correction to exchange $\Delta E_{\text{X}}^{\text{B}}$ and 81% LYP correlation energy $E_{\text{C}}^{\text{LYP}}$. A hybrid functional that is constructed similarly to B3LYP is the B1LYP exchange–correlation functional [136], where a single parameter a_0 is used to admix exact exchange,

$$E_{\text{XC}}^{\text{B1LYP}} = a_0E_{\text{X}}^{\text{HF}} + (1 - a_0)(E_{\text{X}}^{\text{LDA}} + \Delta E_{\text{X}}^{\text{B}}) + E_{\text{C}}^{\text{LYP}}. \quad (2.34)$$

Other single-parameter functionals with customized portions of exact exchange can be obtained according to this expression by adjusting the parameter a_0 . For example, it was proposed by Kaupp and coworkers that the BLYP35 hybrid functional, where 35% exact exchange are included with $a_0 = 0.35$ [51], provides a good description of organic mixed-valence systems when combined with solvent modeling *via* a PCM [50,51,53]. This method was therefore exploited for molecular structure optimization in this work.

A newer class of density functionals is represented by the range-separated functionals, which were designed to overcome the limitations of standard DFT methods [137]. One of the main deficiencies of approximate exchange–correlation functionals is the presence of the self-interaction error (SIE), which is attributed to the fact that there is a spurious interaction of an electron with itself, which is not cancelled in contrast to HF theory [52]. As a consequence of the SIE, another issue emerging within the DFT framework is that the exchange–correlation potential, which models the interaction of one particle with all others, does not show the correct $-1/r$ asymptotic behavior at long-range. Thus, for the exact functional, which contains all electronic interactions beyond the classical electrostatic Hartree contribution $J[\rho(\vec{r})]$, the relation $E_{\text{XC}}[\rho(\vec{r})] + J[\rho(\vec{r})] = 0$ would be fulfilled for any one-electron ground state, since one electron does not interact with itself, but for DFT functionals, a finite value is obtained [138].

As a remedy to this issue, an amount of (HF) exact exchange is introduced to cancel the SIE. For example, in the range-separated functionals, different portions of exact exchange are adopted at short- and long-range, respectively. These functionals are also termed long-range corrected (LC) DFT functionals, referring to the correction of the long-range asymptotic behavior. One of the most commonly used LC-DFT functionals is the CAM-B3LYP functional [139], where 19% HF-exchange is included at short-range and 65% exact exchange at long-range. More recently, LC-DFT functionals were proposed, where 100% HF exchange is adopted at long-range, whereas the conventional DFT functional is employed at short-range. A parameter ω is then introduced to define the length scale over which the long-range correction is switched on [137,140], where a parameter ω equaling zero corresponds to the conventional DFT functional without correction at long-range. In this work, two different LC-DFT functionals were used for molecular structure optimizations, the ω -PBE functional [140] and the ω -B97X-D functional [137]. In the ω -PBE GGA exchange-correlation functional, no exact exchange is employed at short-range, and a long-range correction is introduced beyond a length-scale of $\omega = 0.4a_0^{-1}$. In the ω -B97X-D hybrid exchange-correlation functional, a portion of 22.2% exact exchange is included at short-range, whereas the long-range correction is adopted beyond a length-scale of $\omega = 0.2a_0^{-1}$.

Belonging to the category of the so-called Minnesota DFT functionals, the M06-HF global hybrid meta-GGA functional [141], developed by Truhlar and coworkers, comprises full exact exchange, *i.e.* 100% HF-exchange, and is therefore expected to minimize errors due to self-interaction [31,120,141]. In the meta-GGA functionals, also the second derivative with respect to the spatial coordinates is considered in the exchange-correlation potential as a development building on the GGA functionals, where only the first derivative is included. Moreover, the kinetic energy density $\tau(\vec{r})$ is typically used instead of $\rho(\vec{r})$ [141]. Caution needs to be exercised when applying functionals with a high amount of exact exchange on organic mixed-valence systems, as these methods often tend to result in an overlocalized description [50]. This issue can be attributed to the fact that 100% exact exchange removes all of the semi-local exchange which before mimicked a part of the static correlation, thus leading to an overlocalized description [52]. A balance between reduction of the SIE and partial conservation of static correlation has therefore to be found by varying the amount

of exact exchange. Recently, the so-called Lh-SVWN local hybrid functional was shown to perform well in describing the charge localization properties of mixed-valence oxo-complexes in gas-phase, where a position-dependent admixture of exact exchange is included that is governed by a so-called local mixing function (LMF) [59,142]. However, so far it is much less often used than global or range-separated hybrid functionals, as the efficient implementation of local hybrids into computational software is still challenging [59,142].

Toward Theoretical Descriptions of Class III–II Transitions

To describe charge delocalization in mixed-valence systems by KS-DFT, the molecular structure is optimized, usually starting from guesses for both the molecular and electronic structure, which are symmetric. In class III systems, these structures will remain symmetric during optimizations, and in class II systems, small deviations from symmetry in the initial structure (present by chance or sometimes on purpose) and/or numerical fluctuations will lead to localization of charge on one of the redox centers, accompanied by asymmetric structural rearrangements.

In doing so, one has to take two main aspects into account. First, the choice of the exchange–correlation functional and especially the amount of exact exchange admixture is a decisive factor, as was shown in studies by Zhao and Mangaud on electron transfer in DMP_n radical cations, who mainly used LC-DFT, where different portions of exact exchange are adopted at short and long range [120,121]. It was demonstrated that functionals with high amounts of exact exchange (LC- ω -PBE and M06-HF) are suitable for systems with partly and fully localized charges, whereas those with lower amounts of exact exchange (CAM-B3LYP and ω -B97X-D) give reasonable results for systems with delocalized charge [120]. The finding that a suitable amount of exact exchange is essential for correctly describing charge localization was also emphasized by Kaupp and coworkers on the example of hybrid functionals [50,51,53]. Second, the inclusion of charge-stabilizing effects from the environment is crucial for the application of quantum chemical protocols on organic mixed-valence systems, since experimental data in gas-phase is hardly available [53].

When calculating charge localization properties of organic mixed-valence systems, one has to be aware of these two aspects and their mutual compensation. As it was pointed out by Kaupp and coworkers, the application of

exchange–correlation functionals with high amounts of exact exchange on isolated molecules may lead to the correct degree of charge localization for the wrong reason [50,51]. On the other hand, these functionals bear the risk of over-localization when combined with solvent modeling, which was already shown on the example of range-separated hybrid functionals applied to diquinone radical anions [50]. Taking into account these findings, a DFT protocol based on a hybrid functional, constructed analogously to the B1LYP exchange–correlation functional [136], with 35-42% exact-exchange admixture and combined with a continuum solvent model was proposed by Kaupp and coworkers for the reasonable description of charge localization properties of mixed-valence systems close to the class III/II borderline [50, 51, 53].

To provide an overview over the state of the art on describing charge localization in mixed-valence systems, previous theoretical studies on mixed-valence systems are outlined in the following for three different radical cationic species (introduced in Sec. 2.2, see Fig. 2.13), which form the basis for the validation of DFT methods in this work.

DMP_n In a computational study of Zhao and coworkers, a variety of DFT and HF methods was validated regarding their performance in reproducing the charge localization properties of DMP_n molecules obtained from X-ray crystallographic experiments [120]. Molecular structure optimizations of the DMP₀–DMP₂ species were performed and the calculated structural parameters, *i.e.* bond lengths, as well as partial charges, obtained from natural population analyses (NPA) for the two different redox centers, were compared to the experimental data [110, 111].

For DMP₀, the delocalized character as indicated from experiments was found to be well-described by using the standard hybrid functionals B3LYP and DFT/50-50, as well as the HF method. However, it was found that the experimental data is more accurately reproduced by using the B3LYP functional, whereas shorter bond lengths are predicted with the HF and DFT/50-50 method, indicating that a large part of exact exchange causes considerable deviations in the molecular structure.

In the category of LC-DFT functionals, correct charge distributions were obtained with the CAM-B3LYP and the ω -B97X-D functional [120]. Almost localized class II/III character was predicted by the ω -B97X-D functional with-

out damped dispersion correction and the ω -PBE functional, as the predicted bond lengths showed large deviations from the experimental results. This was also the case for the global hybrid meta-GGA functional M06-HF, providing an overlocalized description. As it was found that the B3LYP functional predicts too large twisting angles compared to the experiment, the application of LC-DFT functionals, CAM-B3LYP and ω -B97X-D, was proposed for molecular structure optimizations for charge delocalized systems, since the results came closest to the experimental data [120].

For the longer species DMP₁, it was found that neither the B3LYP nor the ω -B97X-D functional predict reasonable charge populations compared to the experiment. However, by using the HF method, M06-HF and the long-range corrected ω -PBE functional, the resulting charge localization was found being in good agreement with the experiment. The latter two functionals were considered the best choice for molecular structure optimizations of partly localized class III/II systems, since the HF method was found to predict shorter C–O bond lengths in comparison. These methods performed also well on fully localized class II systems, as the predicted charge distributions and geometries were consistent with the experimental results [120]. However, no method consistently predicted the correct charge distribution and molecular structure when compared to the experiment, across the entire range of molecules.

The same series of DMP_{*n*} molecules was computationally investigated by Mangaud and coworkers. In analogy to the experimental studies of Kochi and coworkers, the relative shortening of the C–O bond length in one redox center with respect to the other redox center, caused by the benzoidal-quinoidal deformation upon oxidation, was exploited as a structural parameter for the localization of the charge (Fig. 3.1 in Sec. 3.1) [121].

It was found that with the pure GGA OPBE functional and the hybrid B3LYP functional, the charge is predicted to be delocalized in either case and, thus, they fail to reproduce the partial and full localization of the charge in DMP₁ and DMP₂. On the contrary, the charge was predicted to be fully localized for all molecules when employing the M06-HF functional in molecular structure optimizations. The relative shortening of the C–O bond length on one redox center was found to be qualitatively well-described when using the ω -B97X-D functional. However, comparisons to the experiment were not based on partial charges in the latter study, in contrast to the study of Zhao and coworkers [120].

Table 2.1: Classification of MV Systems – State of the Art Robin–Day classification of mixed-valence systems based on computational and experimental (EPR, X-ray and NIR) data from the literature for DMP_n [110, 111, 120, 121], OPV_n [118] and $(\text{Ar}_2\text{N})_2\text{T}_n$ [119, 122, 123]. Molecular structure optimizations were performed on isolated molecules without including solvent effects (except for $(\text{Ar}_2\text{N})_2\text{T}_n$, where aqueous solvation was simulated with the SM5C model).

theory	cDFT ω -PBE	OPBE	B3LYP	M06-HF
DMP_0	$\text{II}^{(a)}$ [121]	$\text{III}^{(a)}$ [121]	$\text{III}^{(a,b)}$ [120, 121]	$\text{II}^{(a,b)}$ [120, 121]
DMP_1	$\text{II}^{(a)}$ [121]	$\text{III}^{(a)}$ [121]	$\text{III}^{(a,b)}$ [120, 121]	$\text{II}^{(a,b)}$ [120, 121]
DMP_2	$\text{II}^{(a)}$ [121]	$\text{III}^{(a)}$ [121]	$\text{III}^{(a)}$ [121]	$\text{II}^{(a,b)}$ [120, 121]
	LC ω -PBE	ω -B97X	ω -B97X-D	HF
DMP_0	$\text{II}^{(a,b)}$ [120]	$\text{III}/\text{II}^{(a,b)}$ [120]	$\text{III}^{(a,b)}$ [120, 121]	$\text{III}^{(a,b)}$ [120]
DMP_1	$\text{II}^{(a,b)}$ [120]	$\text{III}/\text{II}^{(a,b)}$ [120]	$\text{III}/\text{II}^{(a,b)}$ [120, 121]	$\text{II}^{(a,b)}$ [120]
DMP_2	$\text{II}^{(a,b)}$ [120]	-	$\text{II}^{(a)}$ [121]	-
	AM1-CI		AM1-UHF	UAM1/SM5C
OPV_0	$\text{III}^{(a)}$ [118]	$(\text{Ar}_2\text{N})_2\text{T}_1$	$\text{III}^{(a)}$ [122]	$\text{III}^{(a)}$ [122]
OPV_1	$\text{II}^{(a)}$ [118]	$(\text{Ar}_2\text{N})_2\text{T}_2$	$\text{III}^{(a)}$ [122]	$\text{II}^{(a)}$ [122]
OPV_2	$\text{II}^{(a)}$ [118]	$(\text{Ar}_2\text{N})_2\text{T}_3$	$\text{II}^{(a)}$ [122]	$\text{II}^{(a)}$ [122]
OPV_3	$\text{II}^{(a)}$ [118]	$(\text{Ar}_2\text{N})_2\text{T}_n, n \geq 4$	$\text{II}^{(a)}$ [122]	$\text{II}^{(a)}$ [122]
exp.	EPR/X-ray		X-ray/NIR	EPR/NIR
DMP_0	III [110, 111]	OPV_0	III [118]	$(\text{Ar}_2\text{N})_2\text{T}_1$ III/II [123]
DMP_1	III/II [110, 111]	OPV_1	II [118]	$(\text{Ar}_2\text{N})_2\text{T}_2$ III/II [119, 123]
DMP_2	II [110, 111]	OPV_2	*	$(\text{Ar}_2\text{N})_2\text{T}_3$ III/II [123]
-	-	OPV_3	*	-

Classification derived from ^(a)structural analysis or from ^(b)charge distribution from NPA.

*No classification possible due to masked NIR absorption bands [118].

OPV_n Experimental studies conducted by Barlow and coworkers on OPV_n-bridged tertiary amines were complemented by computational methods, as only the OPV₀ and OPV₁ species could be classified from the NIR experiments [118]. Molecular structure optimizations of the radical cations were performed using the configuration interaction method with Austin Model 1 (AM1/CI). For OPV₀, a symmetric structure was indicated, with the charge equally distributed across the entire system, suggesting its class III assignment in agreement with the experiments. In contrast, asymmetric molecular structures were obtained for the longer species OPV₁–OPV₃, with the charge being localized on one single redox center, as indicated by the planarization of the nitrogen atom and an adjacent stilbene unit. The increasing degree of charge localization for the OPV₁ species, as indicated from the computational results, agreed with the NIR experiments [62,118].

Oligothiophenes A computational study on the (Ar₂N)₂T_n radical cations, previously experimentally investigated by the groups of Odom and Wenger [119, 123], was performed by Lacroix and coworkers, where molecular structure optimizations were performed using the AM1-UHF method on isolated molecules [122]. Additionally, molecular structure optimizations were carried out employing an approach based on UAM1/SM5C, where aqueous environment was simulated by the SM5C model [122]. From optimized structures of isolated molecules, it was suggested that short (Ar₂N)₂T_n molecules with bridges comprising one or two thiophene units have symmetrical structures and thus, can be considered rather delocalized class III systems, being in agreement with the experimental data [119,123]. For the longer (Ar₂N)₂T_n systems with bridges comprising three or more thiophene units, the formation of a localized charge defect was observed, structurally manifested by a semiquinoidal distortion and the one-sided shortening of the N–C_α bond. However, it was noted that the charge is not fully localized on one redox center, but is rather partially extended onto the bridge. For (Ar₂N)₂T_n molecules with bridges comprising more than four thiophene units, the same localized charge defect was observed, indicating the class II nature of these systems [122]. Upon simulation of aqueous solvation in the molecular structure optimizations, the molecular structure of the bis(diarylamine) radical cation with only one thiophene unit as a bridge remained symmetrical, similar to the isolated species. However, for longer (Ar₂N)₂T_n species with bridges com-

prising two or more thiophene units, an asymmetrical structure was obtained, with the charge being localized on one side of the molecule. A transition from a delocalized class III structure to a localized class II structure was therefore observed upon switching from isolated molecules to a more polarized environment in solution [122]. Apart from these theoretical investigations by Lacroix and coworkers, none of these computational studies were combined with a solvent model. Hence, in this work, in addition to other approaches the potential of the DFT protocol based on the BLYP35 hybrid functional combined with a PCM proposed by Kaupp and coworkers was explored for describing the Robin–Day class of the organic mixed-valence systems under study [50, 51, 53].

III. CHARGE TRANSFER IN MIXED-VALENCE SYSTEMS

3 Describing Class III–II Transitions in Mixed-Valence Systems: Validation of DFT Approaches

3.1 Introduction

In the last section, a variety of experimental and theoretical studies on the length dependence of charge transfer in organic mixed-valence systems was presented [62, 110–112, 118–122], providing the basis for the validation of DFT approaches in describing length-dependent charge localization. As a transition from a fully delocalized class III to a charge-localized class II system occurs with increasing length of the bridge between the redox centers, the characterization of compounds right on the borderline between these two regimes and the evaluation of the class III–II crossover according to the Robin–Day scheme can often be challenging [62].

In this section, theoretical measures for assessing the degree of charge localization in mixed-valence systems are derived: On the one hand, structural measures may be used as an indicator for increased charge localization in some cases, since the formation of charge-localized defects is often manifested in characteristic structural changes in the affected area. On the example of X-Ray crystallographic data on DMP_n radical cations, it is shown that the quinoidal deformation upon charge localization may serve as a measure for charge localization, also in theoretical investigations. On the other hand, one can evaluate the degree of localization based on local properties such as local spins and local charges. For radical cationic systems, the terms of charge and spin localization may be used interchangeably, as the excess positive charge and the free electron are expected to be located on the same site. In the following, both techniques in assessing the degree of charge localization are presented and are then applied to the validation of DFT approaches for describing class III–II transitions. The results of this validation were partly published in Ref. [54].

3.2 Theoretical Measures for Charge Localization

A variety of parameters can be used as a measure for the degree of charge localization, which can be based on local properties (local spins [143–145] and partial charges [146,147]) or on characteristic structural changes. When studying mixed-valence systems, the degree of charge localization is often determined by relating a specific quantity (either structural properties such as bond lengths or local properties such as local spins) on one redox center to the corresponding quantity on the neighbouring redox center, *i.e.* the donor and acceptor moieties. Since one can expect a certain quantity to be equal on both sides in case of charge delocalization, differences regarding this quantity would indicate increasing charge localization. This simple scheme may be easily applicable to mixed-valence systems due to their symmetric architecture; however, as will be shown in Sec. 6.2, more sophisticated measures need to be defined when more asymmetric structures are involved like common molecular wires, which usually exhibit charge localization in a less well-defined manner. Still, for mixed-valence systems simpler methods of assessing the degree of charge localization work sufficiently well, and in this work, the validation of DFT approaches is mainly grounded on the ratio between partial charges on the donor and acceptor moieties. The evaluation of charge localization based on the analysis of local properties such as local charges and spins offers the great advantage of being universally applicable in contrast to analyses based on structural measures, where characteristic changes in the molecular structure are dependent on the system of interest and are manifested in various ways. Nonetheless, the latter may be valuable as a supporting tool in examining borderline compounds with ambiguous charge localization properties, which will be successfully demonstrated on the example of DMP_n radical cations in the following.

Assessment of Charge Localization from Structural Changes

As proposed by Zhao and Mangaud [120,121], the shortening of the C–O bond length $d(d')$ in one redox center relative to the other, emerging from its benzoidal-quinoidal deformation upon oxidation (see Fig. 3.1), can be exploited as a characteristic structural parameter for the degree of charge localization. In case of mixed-valence systems, the notations for the two redox centers (D and A) may be used interchangeably, since the redox centers are identical and can both function either as donor or acceptor moiety.

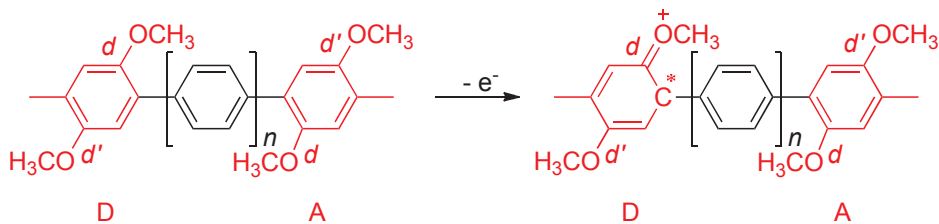


Figure 3.1: Quinoidal Deformation of DMP_n Schematic representation of the relative C–O bond length shortening upon oxidation in DMP_n (assuming a purely class II behavior). Donor- and acceptor moieties are marked in red.

In this work, the benzoidal-quinoidal deformation in one redox center with respect to the other upon oxidation was exploited to derive a measure x that accounts for the relative shortening of the C–O bond length and thus, implicitly allows for the evaluation of the degree of charge localization.

$$x = \frac{d'(D) - d(D)}{d'(A) - \bar{d}} \quad (3.1)$$

In Eq. (3.1), x is expressed by the ratio of the difference between the C–O bond lengths $d(D)$ and $d'(D)$ on opposite sides of the first redox center and the difference between the length of the C–O bond $d'(A)$ on the second redox center and the mean value of d , where the C–O bond lengths $d(D)$ and $d(A)$ on each redox center of the singly positively charged molecule are averaged. A completely charge-delocalized system is indicated by a value of $x = 1$, since each of the C–O bond lengths d (or d') is the same for each redox center and therefore, the mean value of d is equal to $d(D)$, resulting in the numerator and denominator being identical. In contrast, for a fully charge-localized system the C–O bond lengths d and d' are the same on the first redox center where the charge is located, resulting in x being zero. Since the derived quantity is considered as a measure for the agreement with a fully charge-delocalized description (expressed by $x = 1$), the resulting value of x is normalized to 1.

Ratios of Local Charges and Spins as Indicator for Charge Localization

Measures based on local properties and attributed with the two redox centers can be derived similarly to structural parameters. Here, the ratios between local charges q_D/q_A and spins s_D/s_A of the donor and acceptor moieties, serve as a measure for the degree of charge localization, where the index denotes

the first and second redox center. For example, complete delocalization of the charge would be expressed by a ratio of 1, whereas a ratio of zero indicates a fully localized charge on one redox center. In this work, the charges $q_{A,D}$ and spins $s_{A,D}$ were obtained from natural population analyses (NPA) [148] and summed over all atoms belonging to the respective donor or acceptor fragment (defined in Fig. 2.13). The degree of charge localization was evaluated from molecular structure optimizations in the charged state, which is always cationic for the molecules studied in this section. It has to be noted that the Robin–Day classification is mostly derived from experimental reference data that is based on multiple complementary techniques, *e.g.* EPR and NIR spectroscopy and X-ray crystallography [110,111,118,119,123], which is not directly comparable to local properties calculated in this study. Therefore, the comparison between the experimentally derived classification and the assignment based on calculations may be regarded more as a guideline than a clear-cut categorization.

In this study, molecules were considered as class III systems in case of equally distributed charges/spins with q_D/q_A or s_D/s_A equaling nearly one, and as class II systems in case of either the partial charges or spins on one redox center being less than one percent of the total sum. Any situation between these two extreme cases was considered being within the class III/II borderline regime.

Application of Measures for Charge Localization - DMP_n Case Study

As outlined in Sec. 2.2, in experimental studies by Kochi and coworkers it was found that in DMP_n molecules with *p*-phenylene bridges of variable length a transition from class III to class II occurs between DMP₀ and DMP₂, with DMP₁ representing a class III/II borderline system [110–112].

The C–O bond lengths d and partial charges q obtained from X-ray crystallography experiments by Kochi and coworkers are listed in Tab. 3.1 for DMP₀ to DMP₂, as well as the corresponding ratios between the partial charges on the donor and acceptor moiety q_D/q_A , which reflect the relative charge population states. The partial charges were evaluated at each redox center by the investigators, where a linear regression was used that sufficiently accounts for the geometric changes in the redox center upon oxidation, *i.e.* the benzoidal–quinoidal deformation, based on the comparison of a particular bond length to the corresponding bond lengths in the neutral and oxidized state of the redox

Table 3.1: Structural Changes in DMP_n upon Charge Localization

C–O bond lengths d, d' and partial charges q corresponding to the respective redox center D or A, obtained from X-ray crystallography experiments by Kochi and coworkers on *p*-phenylene bridged DMP_n [110]. Structural parameters x were evaluated in this study according to Eq. (3.1) and ratios between partial charges q_D/q_A on the donor and acceptor moieties were derived from X-ray crystallographic data of studies by Kochi and coworkers on DMP_n [110].

		d [Å] [110]	d' [Å] [110]	q [110]	x	q_D/q_A
DMP ₀	D	1.341	1.356	+0.50	0.90	1.00
	A	1.344	1.356	+0.50		
DMP ₁	D	1.331	1.344	+0.80	0.59	0.25
	A	1.363	1.369	+0.20		
DMP ₂	D	1.325	1.324	+1.00	0.03	0.00
	A	1.370	1.385	+0.00		

center [110]. Based on the X-ray crystallographic data originating from these experimental studies, the measures for charge localization, either x or the ratio q_D/q_A , were evaluated in this work.

As can be deduced from the X-ray data, a transition from a delocalized class III system to a fully localized class II system occurs between DMP₀ and DMP₂, which is confirmed by both, the decreasing value of x and ratio of q . The C–O bond lengths of the two redox centers in DMP₀ are nearly identical, and the charge is equally distributed across the molecule, which is expressed by a value of x of 0.90 and a ratio of local charges equaling 1.

In contrast, the redox centers in DMP₂ feature significant differences between their C–O bond lengths, as expressed by a value of x tending toward zero. Here, the charge is fully localized on one redox center, whereas the other redox center exhibits a neutral charge state.

The classification of DMP₁ as a class III/II borderline compound is confirmed by a moderate shortening of the C–O bond length, which is manifested in x equaling 0.59, thus ranging between the ratios for DMP₀ and DMP₂, and by partial but not full localization of the charge on one redox center, indicated by a ratio of 0.25.

It is worth mentioning that the computationally obtained values for C–O bond lengths (Appendix, Tab. A.1) and partial charges by the BLYP35 hybrid functional with PCM [54] in this study deviate from the corresponding values derived from X-ray crystallographic experiments by Kochi and coworkers [110].

However, the data obtained from X-ray crystallographic structures is not directly comparable with data computed from molecules in solution, as the charge may be stabilized to a different extent in a solvent compared to a crystal, where packing or counter ion effects are present [53]. Hence, although no accurate quantitative evaluation of these parameters is obtained in this study by the BLYP35 hybrid functional with PCM, the classification on the basis of the structural x parameter derived from the relative C–O bond shortening and the ratio q_D/q_A is qualitatively in line with the experimental results, since an increasing degree of charge localization with growing bridge length from DMP₀ to DMP₂ is indicated and the borderline character of DMP₁ is well described. More importantly, this comparative study leads to the conclusion that the isolated assessment of single mixed-valence borderline compounds may be error-prone and a proper evaluation of their Robin–Day class should be grounded on a comparative study that encompasses species that reflect the transition from charge delocalization to localization sufficiently well.

3.3 Describing Class III–II Transitions: DFT Results

In this work, various DFT approaches were validated for describing the length-dependent transition from class III to class II with the aim of transferring the successful protocol to the prediction of transport mechanisms in molecular wires. Here, three different sets of organic mixed-valence radical cations were studied: 2,5-dimethoxy-*p*-phenylenes (DMP_{*n*}), oligo-*p*-phenylene-vinylenes (OPV_{*n*}), and oligothiophene-bridged bis(dianisylamines) ((An₂N₂)T_{*n*}), see Fig. 2.13 in Sec. 2.2. In each series, the bridge length increases gradually and a transition from class III to class II is indicated from the experiments. The results from theory are compared to the experiments with the aim of identifying suitable approaches for the reliable description of mixed-valence systems right on the borderline between class III and class II. The major part of the results originating from this investigation were published in Ref. [54], and corresponding data and figures were adapted from this publication.

Computational Methodology

Neutral structures of the organic mixed-valence systems were preoptimized by performing KS-DFT calculations using the resolution-of-identity (RI) approach, implemented in the TURBOMOLE 7.0 package [149]. In the molecular structure optimizations, the BP86 exchange-correlation functional [131, 132], Ahlrich's def2-TZVP basis set [150] of triple-zeta quality with polarization functions on all atoms, and the D3 dispersion correction introduced by Grimme [151] were employed. The convergence criterion in the self-consistent field (SCF) algorithm was set to 10^{-7} hartree for the change of the energy in all calculations and to 10^{-4} a.u. for the gradient in molecular structure optimizations. Subsequent molecular structure optimizations on the neutral preoptimized structures were performed for the organic mixed-valence systems in their radical cationic state by employing the GAUSSIAN 09 program package [152] with Ahlrich's def2-TZVP basis set and the hybrid BLYP35 functional with 35% exact exchange from the Kaupp group, which was constructed analogously to the B1LYP model [136]. Moreover, the long-range corrected ω -PBE [140] and ω -B97X-D [137] functionals were used, since in previous studies it was found that these range-separated functionals provide a reasonable classification for either partly or fully localized class II systems and delocalized class III systems, respectively [120, 121]. Since the classification of these compounds within the Robin-Day scheme is based on complementary EPR, NIR and X-ray experiments and the importance of environmental effects on charge localization properties of organic mixed-valence systems was emphasized by Kaupp and coworkers [53], molecular structure optimizations were performed for both, isolated molecules and molecules in solution. For the inclusion of solvent effects, a polarizable continuum model with the integral equation formalism model (IEFPCM) [153, 154] was employed as implemented in the GAUSSIAN 09 program package by using the SCRF keyword with the available dielectric constants for water ($\epsilon_{\text{H}_2\text{O}}=78.3553$), acetonitrile ($\epsilon_{\text{ACN}}=35.688$), dichloromethane ($\epsilon_{\text{DCM}}=8.93$) and n-hexane ($\epsilon_{\text{HEX}}=1.8819$). Natural population analyses [148] were performed with the GAUSSIAN 09 program package to gain information about the distribution of local spins and charges, which were summed over specific fragments of the molecule. For the local spins, an absolute value of 0.5 refers to one unpaired electron. Molecular structures were visualized with the AVOGADRO editor [155], and spin densities were plotted with MOLDEN [156] applying an isosurface value of 0.001.

Phenylene-bridged 2,5-Dimethoxy-*p*-phenylene

In experimental studies of Kochi and coworkers, the distance dependence of intramolecular charge transfer was investigated on the example of organic mixed-valence DMP_n radical cations (see Fig. 3.2), with the number of *p*-phenylene units ranging between zero and four (DMP_0 – DMP_4). On the basis of complementary temperature-dependent EPR and X-ray crystallographic experiments, it was found that DMP_0 is a class III system, whereas DMP_2 – DMP_4 belong to class II, with DMP_4 already being on the class II/I borderline. As the temperature-dependent behavior in the EPR experiments of DMP_1 was found to be intermediate between DMP_0 and DMP_2 , it was considered a class III/II borderline compound [110,111].

The picture drawn from the experiments is supported by DFT calculations if the appropriate combination of exchange–correlation functional and environment modeling is chosen, as discussed in the following. In Fig. 3.2, the ratios between the partial charges on the donor and acceptor moiety, serving as a measure for charge localization, are shown as a function of the number of bridging units for different functionals.

BLYP35 (+ PCM) As becomes evident from the evenly distributed spin density isosurfaces and charges of the DMP_n molecules in vacuum (ISO), the BLYP35 functional predicts charge-delocalized class III character for any molecule of the series, which is in agreement with the experimental data for DMP_0 , but strongly contradicts the experimentally derived classification of the longer species (Fig. 3.2, top). This observation is not surprising, since it is well-known that localization is highly affected by environmental effects [50,51,53]. Upon inclusion of a PCM modeling dichloromethane (DCM), DMP_0 remains a delocalized class III system, whereas partial localization of the charge on one redox center occurs for DMP_1 , being +0.81 and +0.06 on the other redox center, resulting in a ratio of 0.08 (all charges are given in atomic units). For DMP_2 , a ratio of 0.02 indicates even stronger localization of the charge. The distinct differences regarding the degree of charge localization between DMP_0 and DMP_2 clearly suggest a transition from class III to II. However, whereas in DMP_2 the charge resides nearly completely on one redox center, there is a small amount of it located on the other redox center for the shorter DMP_1 . Since the ratio of the partial charges on the two redox centers ranges between the values

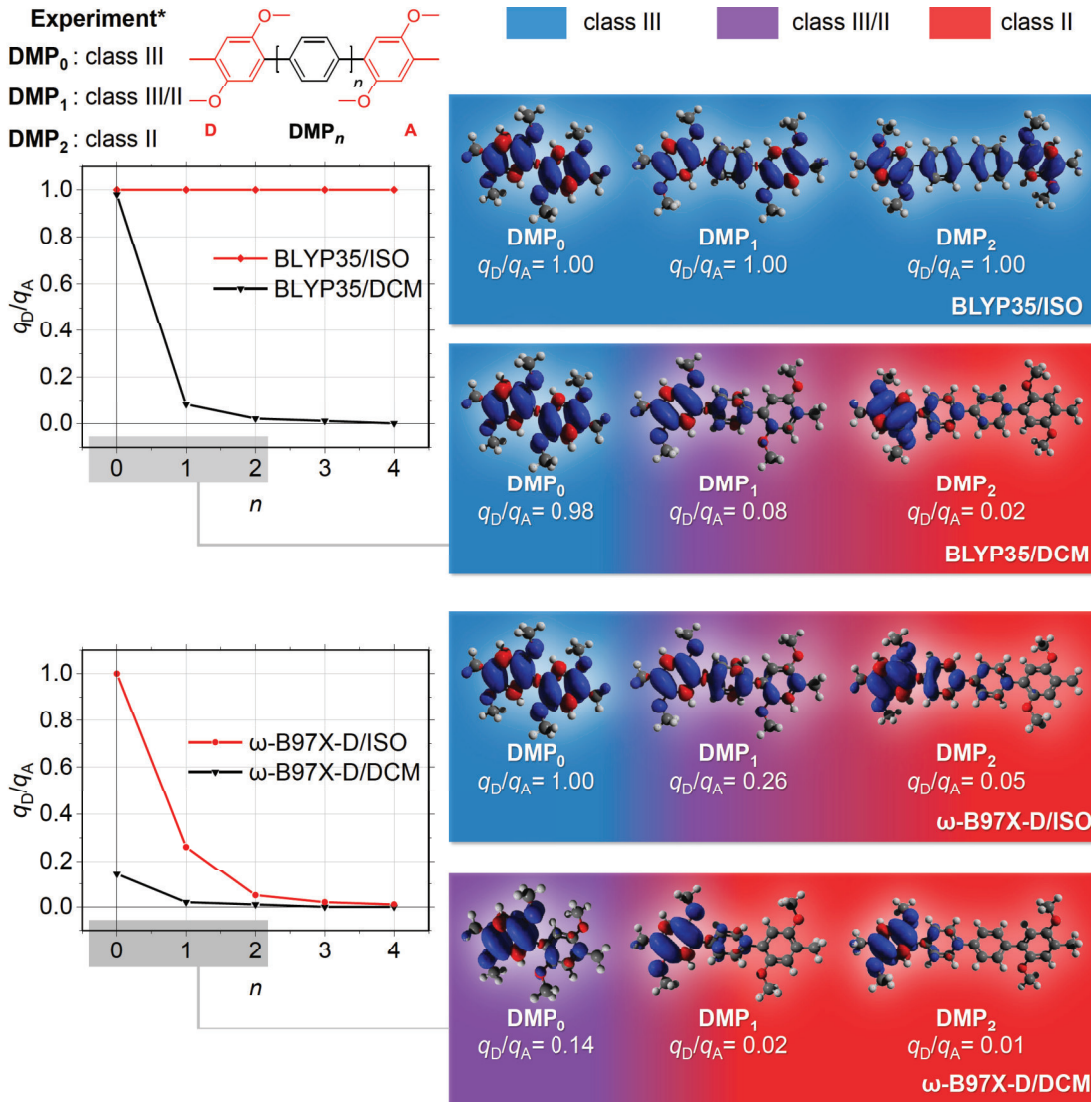


Figure 3.2: Charge Localization in DMP_n – DFT Results *Left:* Ratios q_D/q_A between partial charges on the donor and acceptor moieties of the DMP_n radical cations as a function of the number of bridging units n . Molecular structures are optimized with the BLYP35 hybrid functional (top), the ω -B97X-D functional (bottom) and Ahlrich’s def2-TZVP basis set in their isolated state (ISO) and with PCM for DCM. *Right:* Spin density isosurfaces of the marked compounds with the ratios q_D/q_A as a measure for charge localization and their Robin–Day classification indicated by the background colors (see Sec. 3.1 for the classification criteria). *The experimental classification was derived from EPR [110,111] and X-ray [110] experiments.

for the pure class III system DMP₀ and the class II system DMP₂, DMP₁ can be considered a class III/II borderline compound, tending to a rather localized

description, in agreement with the experimental data. Overall, the inclusion of solvent effects *via* PCM greatly improves the performance of the BLYP35 functional. In addition to local properties, the relative shortening of the C–O bond upon charge localization was analyzed by evaluating the characteristic structural parameter x , as derived in the beginning of Sec. 3.1. The results are qualitatively in line with the classification derived from local properties calculated with the BLYP35 functional with PCM (see Appendix, Tab. A.1).

ω -B97X-D (+ PCM) To evaluate the effect of the approximate exchange–correlation functional on charge localization properties, long-range corrected DFT functionals were explored for their calculation as well (Fig. 3.2, bottom). As can be seen from the equally distributed spin density of the DMP₀ molecule in vacuum optimized with the ω -B97X-D functional, it shows delocalized class III behaviour, whereas partial charge localization occurs for the longer DMP₁, which is illustrated by fractional charges of +0.61 and +0.16 on each redox center. Charge localization is even more present in DMP₂, which features partial charges of +0.73 and +0.04 on the two redox centers and thus can be described as a nearly localized class III/II system. Thus, when employing the ω -B97X-D functional, the transition from charge delocalization to localization from DMP₀ to DMP₂ is quite well described already on isolated molecules. However, the character of the DMP _{n} molecules is clearly biased toward a more delocalized description by this method compared with the more localized nature predicted by the BLYP35 functional with PCM, as illustrated by the ratio of partial charges being 0.26 versus 0.08 for DMP₁, respectively.

When combining the ω -B97X-D functional with a PCM, distinct charge localization is predicted already for the shortest species DMP₀. Since partial charges of +0.87 and +0.13 are associated with the two redox centers, one would consider DMP₀ as a partly localized class III/II system, tending more to the latter, which conflicts with the class III assignment from experiments.

To sum up, the performance of the ω -B97X-D functional in describing the length-dependent class III–II transition in the DMP _{n} series strongly depends on the inclusion of the solvent model. An overall good performance is achieved, presumably through error compensation, when the functional is applied to isolated molecules, whereas a far too localized description is provided when it is combined with a PCM, not only when the assessment is based on local proper-

ties but also when examining structural parameters (see Appendix, Tab. A.2 for structural analysis). Most probably, the fact that the range-separated functional includes full exact exchange at long-range causes overlocalization, as discussed in Sec. 2.3, which is even more pronounced due to the charge-stabilizing effects of the solvent [50, 51, 53].

ω -PBE Being also a member of the long-range corrected category, the ω -PBE functional was used for molecular structure optimizations of the DMP_n series, which gives a too localized description already on isolated molecules (see Appendix, Tab. A.3 for structural analysis as well as Tab. A.4 and Fig. A.1 for analysis of local properties). Presumably, the performance of the ω -PBE functional suffers from introduction of full exact exchange at long-range even more than the ω -B97X-D functional, leading to extensive overlocalization [50]. Further calculations were not pursued as it can be assumed that the inclusion of solvent effects may cause even more pronounced charge localization, thus leading to an erroneous classification.

Two Variants of Bis(dianisylamine) Radical Cations

To validate whether the BLYP35 functional in combination with the PCM maintains its good performance in predicting the Robin–Day classification correctly when extended to other systems, it was used for investigating two other sets of radical cations (OPV_n and $(\text{An}_2\text{N})_2\text{T}_n$), featuring the same two bis(dianisylamine) redox moieties linked by bridges of variable lengths.

Oligo-*p*-phenylene-vinylene-bridged Bis(dianisylamine) In studies of Barlow and coworkers the intervalence transitions in organic mixed-valence bis(dianisylamine) radical cations with oligo-*p*-phenylene-vinylene bridges of variable length (OPV_0 to OPV_3) were investigated by means of NIR spectroscopy, complemented by X-ray crystallographic experiments such as in the DMP_n studies (see Fig. 3.3, top) [118]. Unlike in the latter, here the solvatochromism and shape of the NIR absorption bands served as an indicator for the classification, and it was concluded that OPV_0 is a class III system, whereas for the longer species OPV_1 , class II character was indicated.

When applying the BLYP35 functional to isolated molecules, a completely delocalized class III description is obtained for any of the OPV_n species, as it was

the case for the DMP_n systems, again indicating that the neglect of solvent effects leads to erroneous results for the longer homologues (Fig. 3.3, top).

Upon inclusion of the PCM for dichloromethane, the shortest member of the series, OPV_0 , maintains class III character in agreement with the experiments, whereas increasing localization of the charge occurs for the longer OPV_1 , ex-

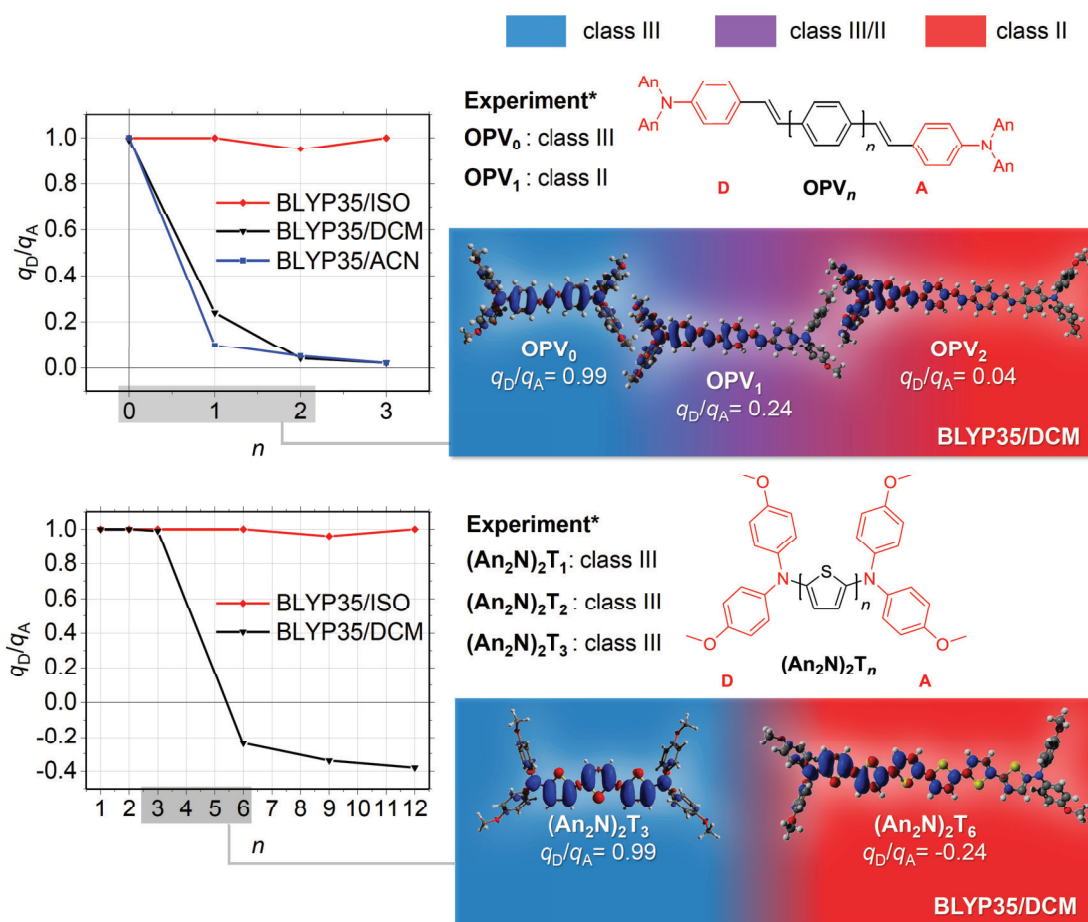


Figure 3.3: Charge Localization in $\text{OPV}_n/(\text{An}_2\text{N})_2\text{T}_n$ – DFT Results

Left: Ratios q_D/q_A between partial charges on the donor and acceptor moieties of OPV_n (top) and $(\text{An}_2\text{N})_2\text{T}_n$ (bottom) radical cations as a function of the number of bridging units n . Molecular structures are optimized with the BLYP35 hybrid functional and Ahlrich's def2-TZVP basis set (isolated and with PCM).

Right: Spin density isosurfaces of the marked compounds with the ratios q_D/q_A as a measure for charge localization and their Robin–Day classification indicated by the background colors (see Sec. 3.1 for the classification criteria); An=Anisyl.

*The experimental classification was derived from X-ray and NIR data [118] for OPV_n and from EPR and NIR data [119,123] for $(\text{An}_2\text{N})_2\text{T}_n$.

pressed by a ratio between the partial charges of 0.24. However, since a rather moderate degree of charge localization is indicated, OPV_1 may be considered a borderline compound between class III and class II, clearly biased toward the latter description. These results do not completely match the experimental data, from which OPV_1 is classified as a clear-cut class II compound. However, since the experimentally derived classification is based on the solvatochromism of NIR absorption bands in dichloromethane and acetonitrile, and in the latter the environment is more polar, charge-stabilizing effects are likely to be stronger than in dichloromethane. Indeed, stronger charge localization occurs for OPV_1 when applying a PCM for acetonitrile, with the ratio between the partial charges being 0.1 compared to 0.24 for dichloromethane, which is chemically reasonable and in closer agreement with the experimental data, see Fig. 3.3.

Although the latter protocol shows a tendency of giving a slightly too delocalized description of the OPV_1 species, it is capable of describing the length-dependent transition from class III to class II fairly well, as increasing charge localization is indicated when going from OPV_0 to OPV_1 . Interestingly, the results obtained with the ω -B97X-D functional in solution come closer to the experimental data than with the BLYP35 functional in the particular case of OPV_1 , as the class II character of this species is more pronounced in the former case (see Appendix, Fig. A.2). The latter may be attributed to the pairing of an intrinsically higher tendency toward localization due to a high amount of exact exchange with pronounced charge-localizing effects arising from the PCM. However, this protocol does not perform consistently well when applied to other systems, as was shown on the example of the DMP_n series. Moreover, it is worth mentioning that a rather similar degree of charge localization is predicted for the OPV_n radical cations in both solvents, DCM and ACN, by the ω -B97X-D functional, contrary to the BLYP35 functional. This finding is rather chemically counterintuitive as one would assume that increased solvent polarity causes a higher degree of charge localization. When applying the ω -B97X-D functional on isolated molecules, the performance is similar to that for the DMP_n molecules. Thus, a more localized description is provided in comparison to the BLYP35 hybrid functional on isolated molecules, but stronger delocalization is predicted compared to the BLYP35 hybrid functional with PCM. This DFT protocol fails in predicting the class II nature of OPV_1 , as complete charge delocalization, and thus class III character is indicated.

Oligothiophene-bridged Bis(dianisylamine)

As a further test example, the DFT protocol based on the BLYP35 functional was applied to organic mixed-valence bis(dianisylamine) radical cations with an oligothiophene bridge $((\text{An}_2\text{N})_2\text{T}_n)$ of variable lengths (see Fig. 3.3, bottom). These systems are particularly interesting for predicting transport mechanisms, as they are structurally similar to thiophene-based molecular wires studied by Frisbie and coworkers [31] and therefore state a good test example. Based on cyclic voltammetry and complementary NIR and EPR spectroscopy experiments by Wenger and coworkers, the species with thiophene units ranging from one to three $((\text{An}_2\text{N})_2\text{T}_1$ to $(\text{An}_2\text{N})_2\text{T}_3)$ were considered either delocalized class III or class III/II borderline systems [123]. Hence, a transition to class II was predicted to occur only for oligothiophene molecules with more than three thiophene units [123]. The class III assignment of the $(\text{An}_2\text{N})_2\text{T}_2$ species was also confirmed by Odom and coworkers on the basis of NIR experiments [119]. With the aim of transferring the DFT protocol to predicting charge transport mechanisms in molecular junctions in mind, molecular structure optimizations of $(\text{An}_2\text{N})_2\text{T}_n$ species comprising increasing numbers of thiophene units ($n = 1-3, 6, 9$) were performed to investigate whether and to what extent a length-dependent increase of charge localization can be observed also for very long wires.

For the first three species, the BLYP35 functional with PCM predicts class III character (Fig. 3.3, bottom), which is in line with the experiments [119,123]. With increasing number of thiophene units, the formation of a charge-localized defect occurs, expressed by a ratio between the partial charges of -0.24 for $(\text{An}_2\text{N})_2\text{T}_6$ and being even more pronounced for the longer homologues $(\text{An}_2\text{N})_2\text{T}_9$ and $(\text{An}_2\text{N})_2\text{T}_{12}$. Since there is no experimental classification for the longer species, their categorization based on calculations in this study is lacking reliable reference data. However, as these systems are structurally similar to the OPV_n radical cations, parallels between these systems can be drawn: since the trend of increasing localization of the charge with growing number of bridging units was experimentally and computationally validated for the OPV_n systems, the results obtained for the $(\text{An}_2\text{N})_2\text{T}_n$ series can be considered reasonable. Moreover, the formation of a charge-localized defect with increasing bridge length is predicted from computational studies by Lacroix and coworkers for these molecules and from experiments for structurally similar oligothiophene chains lacking the dianisylamine redox moiety and modified with alkyl chains [122]. Thus, EPR studies

of Janssen and coworkers suggest that a class III–II transition occurs no later than for oligothiophene chains containing nine bridging units [122,157], whereas calculations of Lacroix and coworkers suggest a transition occurring for species longer than $(\text{An}_2\text{N})_2\text{T}_3$ [122]. Similar to the DMP_n and OPV_n molecules, in all cases of the $(\text{An}_2\text{N})_2\text{T}_n$ species a charge-delocalized class III nature is predicted, when the BLYP35 functional is applied on isolated molecules. This finding is in good agreement with the experimental data for the first three oligothiophene species [119,123], but does not meet the expectations for the longer homologues. The classification given by the ω -B97X-D functional is similar to the one obtained by the BLYP35 functional combined with PCM (see Appendix, Fig. A.3), regardless of whether the molecules are in their isolated state or in solution. Hence, this protocol predicts the transition from class III to class II to occur between $(\text{An}_2\text{N})_2\text{T}_3$ and $(\text{An}_2\text{N})_2\text{T}_6$. Since it is unlikely that the charge is localized to nearly the same degree for isolated molecules as for molecules in solution, the results obtained with the ω -B97X-D functional can be considered unreasonable.

3.4 Conclusions

In this part of the work, different DFT protocols were validated regarding their performance of predicting the experimentally indicated length-dependent transition from full delocalization (class III) to partial localization (class II) of the charge for three families of cationic organic mixed-valence species. This investigation was inspired by the question whether the experimentally observed length-dependent transition from tunneling to hopping transport in molecular junctions can be predicted based on charge localization properties obtained from DFT calculations. The underlying idea is that charge transport by tunneling can be associated with complete charge delocalization, whereas hopping transport is related to increasing charge localization. For the evaluation of DFT protocols in describing length-dependent charge localization, mixed-valence compounds represent well-controlled model systems, since their Robin–Day classification is based on a solid foundation of experimental data as shown in Sec. 2.2.

The classification of the systems studied here is mainly derived based on the ratios of partial charges on the donor and acceptor moieties. From similar analyses based on the ratios of local spins it was found that the same result is obtained compared to local charge analyses, both qualitatively and quan-

titatively (see Ref. [54] for detailed data). In case of DMP_n radical cations, the evaluation of charge localization was successfully complemented by analyses based on characteristic structural parameters.

In Tab. 3.2, the computationally derived Robin–Day classification of the organic mixed-valence systems under study is presented for various DFT protocols tested in the validation. For subsequent investigations, the focus was set on the BLYP35 functional with PCM suggested by Renz and Kaupp, as it turned out to be the protocol providing a description of charge localization closest to the experimental data. In any case, the correct transition from charge delocalization to localization is indicated by using the BLYP35+PCM protocol, in agreement with the experiments. In contrast, complete charge delocalization is predicted for all species in their isolated forms, *i.e.* without PCM, contradicting the experimental findings and leading to the conclusion that environmental effects are essential for the correct description of charge localization.

The long-range corrected ω -B97X-D functional works well in the majority of the cases when applied to isolated molecules but completely fails for OPV_1 , as a too delocalized nature is indicated, whereas in combination with PCM it shows the tendency of overlocalization. Hence, although the ω -B97X-D method works well for OPV_n wires in solution, DMP_n wires are too strongly localized when combined with a solvent model. The ω -PBE functional, belonging to the same family of LC-DFT methods, overlocalizes already without including environmental effects and is therefore not recommended.

These findings can be ascribed to the fact that LC-DFT methods intrinsically favor charge localization due to a high amount of exact exchange, leading to overlocalization in combination with environmental modeling. This conclusion applies to both, the long-range corrected ω -B97X-D and the ω -PBE functional, the latter showing even stronger overlocalization.

It cannot be excluded that the good performance of the BLYP35+PCM protocol relies on error compensation, *e.g.* between the exchange and the correlation parts of the functional, or resulting from the approximate treatment of the solvent *via* a continuum model rather than explicitly considering its atomistic structure and dynamics. This is not unusual as demonstrated, for example, by the success of the harmonic approximation in combination with approximate KS-DFT for vibrational spectroscopy [158], which also relies on the concept of error compensation. While this may be a subject of future studies, the BLYP35+PCM

protocol is well suited for the pragmatic purpose of this work. Altogether, the results obtained in this investigation suggest that structural optimizations of charged molecular wires using the BLYP35+PCM protocol represent a promising method for the prediction of the length-dependent crossover from tunneling to hopping in molecular junctions, as will be demonstrated in Sec. 6.3.

Table 3.2: Validation of DFT Methods – Summary Table Classification of organic mixed-valence systems based on different DFT methods and comparison with the classification derived from experiments. The classification for DMP_n is based on EPR [110,111] and X-ray [110] experiments, for OPV_n on X-ray and NIR experiments [118] and for $(\text{An}_2\text{N})_2\text{T}_n$ on EPR and NIR experiments [119,123]. EPR and NIR experiments were carried out in dichloromethane [110,111,118,119,123] or acetonitrile [118,123].

species	BLYP35	BLYP35	ω -B97X-D	ω -B97X-D	ω -PBE	exp.
	iso	+PCM	iso	+PCM	iso	
DMP_0	III	III	III	III/II	III/II	III [110,111]
DMP_1	III	III/II	III/II	II	III/II	III/II [110,111]
DMP_2	III	II	III/II	II	II	II [110,111]
DMP_3	III	II	II	II	II	II [111]
DMP_4	III	II	II	II	II	II [111]
OPV_0	III	III	III	III	-	III [118]
OPV_1	III	III/II***	III	II	-	II [118]
OPV_2	III	II	III/II	II	-	*
OPV_3	III	II	II	II	-	*
$(\text{An}_2\text{N})_2\text{T}_1$	III	III	III	III	-	III [123]
$(\text{An}_2\text{N})_2\text{T}_2$	III	III	III	III	-	III [119,123]
$(\text{An}_2\text{N})_2\text{T}_3$	III	III	III	III	-	III [123]
$(\text{An}_2\text{N})_2\text{T}_6$	III	II	II	II	-	-
$(\text{An}_2\text{N})_2\text{T}_9$	III	II	II	**	-	-
$(\text{An}_2\text{N})_2\text{T}_{12}$	III	II	**	**	-	-

*No classification possible due to masked NIR absorption bands [118].

**No classification possible due to convergence problems in molecular structure optimizations, but also not necessary here as class III–II transition already observed.

***Experimental classification from solvatochromatism comparing DCM and ACN, theoretical classification based on a PCM modeling DCM. Employing ACN in the calculations leads to stronger localization, tending more towards class II behavior.

4 Designing Long-range Charge Delocalization in Molecular Wires

4.1 Introduction

After validating DFT protocols for describing the length-dependent change of charge localization in organic mixed-valence radical cations, the successful approach was used to investigate the effect of structural changes on the degree of charge localization. Here, based on DFT it was studied how long-range delocalization can be achieved and controlled. The question arose how the trend of increasing charge localization with growing bridge length can be controlled chemically, in particular if and how it could be reversed, which would correspond to anti-Ohmic behavior, and whether the onset of charge localization can be delayed toward longer bridges. It is clear that the chemical nature of the bridge building blocks and the redox centers affects electronic communication and the degree of charge localization [62, 63, 159–161], *e.g.* through varying the relative energies of the redox centers and the bridge [162]. Likewise, the polarizability of the environment plays an important role. The studies on these parameters are shortly outlined in the following while the focus is set on more unconventional mechanisms, which are inspired by the analogy between electron transfer and molecular conductance [45, 163–166]: First, the incorporation of bulky substituents at the redox centers, which could favor anti-Ohmic behavior by reducing electronic coupling for short bridges by tilting induced by steric interactions between the redox centers [62], second, the use of bridge building blocks leading to alternating disjoint and nondisjoint coupling with each added unit, and third, the captodative substitution of bridging units, which has been shown theoretically to increase long-range conductivity in molecular wires [64]. On the example of *p*-phenylene-based wires it is shown that long-range charge delocalization is greatly enhanced by this captodative substitution approach suggested by Stuyver and coworkers and how it can be exploited to tune the charge localization properties. The results are discussed in the light of practical consequences for the design of molecular wires. Since these investigations build on the success of the BLYP35+PCM for describing charge localization in mixed-valence systems, the same computational methodology as in Sec. 3.3 applies to the following results, which were partly published in Ref. [54], from which corresponding data and figures were adapted.

4.2 Tuning Delocalization in Captodative-substituted DMP_n

In computational studies by Stuyver, De Proft and coworkers, it was proposed that the conductivity of *para*-benzene-bridged molecules is enhanced by increasing their diradical character, which therefore represents a promising technique toward chemical control of molecular conductivity [64,65]. The strategy is based on a captodative approach, where two donor- (dative) and acceptor- (capto) pairs are incorporated into the benzene bridging unit to stabilize radical centers on each terminus of the molecule. Here, nitrogen acts as electron donor, whereas boron is the acceptor counterpart [64]. On the basis of transmission calculations, it was deduced that the conductance of the substituted molecules is invariant with increasing length due to the increased diradical character that in turn reduces the tendency of maintaining the naturally most stable sextet form in the parental oligophenylene structure [64]. Here, the captodative substitution pattern was applied to *para*- DMP_n species to evaluate whether charge delocalization can be analogously tuned toward longer bridge lengths, since for this series the class III–II transition has been verified both experimentally and computationally and also a parental *para*-oligophenylene structure is present. When comparing the bare with the substituted *para*- DMP_n in Fig. 4.4, dramatically different charge localization properties show up. While charge localization begins already for DMP_1 with the plain benzene parental structure, charge delocalization can be prolonged up to a number of four benzene rings for the substituted *para*- DMP_n species. Hence, the strategy of substituting the benzene bridge according to the captodative scheme turns out to be a valuable tool for tuning charge delocalization toward longer bridge lengths in DMP_n systems. Beyond that, the same trend can be observed when applying the strategy to the $(\text{An}_2\text{N})_2\text{Ph}_n$ analogues, where the transition from delocalization to localization can be shifted from three to five benzene bridging units (see Tab. 4.3 and Appendix, Fig. A.5).

The extended charge delocalization is also manifested in the corresponding molecular structures. As an increased weight of the diradical resonance structure is equivalent to stronger π -character of the bonds connecting the BN-substituted benzene rings, a higher degree of planarity is anticipated for these structures, leading to more efficient charge delocalization [64]. Indeed, when comparing the inter-ring bonds of the unsubstituted *para*- DMP_3 with the substituted analogue, the former ones have less double-bond character than the latter ones,

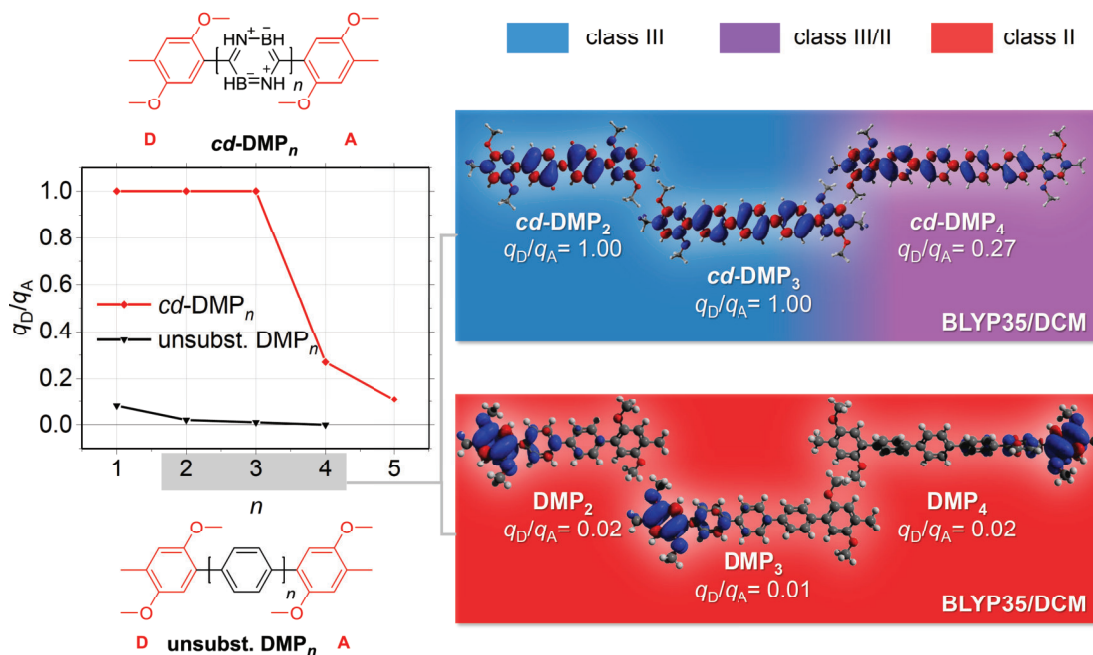


Figure 4.4: Captodative-substituted DMP_n – DFT Results *Left:* Ratios q_D/q_A between partial charges on the donor and acceptor moieties of the DMP_n radical cations with captodative-substituted and unsubstituted benzene-bridge as a function of the number of bridging units n . Molecular structures are optimized with the BLYP35 hybrid functional, Ahlrich’s def2-TZVP basis set and PCM. *Right:* Spin density isosurfaces of the marked compounds with the ratios q_D/q_A as a measure for charge localization and their Robin–Day classification indicated by the background colors (see Sec. 3.1 for the classification criteria.)

being 1.48 Å versus 1.40 Å. As a result, the substituted *para*- DMP_3 structure is completely planarized, whereas in the unsubstituted one the benzene rings are twisted out of the plane, similar to the finding of Stuyver, De Proft and coworkers [64].

The approach adopted here represents an attractive strategy to transform relatively long molecules that are charge-localized into charge-delocalized systems, allowing for chemical control of charge localization. As a further example, employing purely carbon-based diradical-stabilizing bridges also leads to long-range charge delocalization (see Appendix, Fig. A.7), suggesting that the principles underlying the captodative substitution scheme are generally transferable from molecular conductance to mixed-valence systems. The value of such schemes is reinforced by calculations on combining captodative substitution with *meta*-

Table 4.3: Captodative-substitution Scheme – DFT Results Ratios q_D/q_A between partial charges on the donor and acceptor moieties and Robin–Day classification of *para*-benzene-bridged bis(dianisylamine) and 2,5-dimethoxy-*para*-phenylene radical cations with and without captodative substitution pattern on the benzene bridge. Geometries are optimized with the BLYP35 hybrid functional, a PCM modeling dichloromethane and Ahlrich’s def2-TZVP basis set.

D/A=	DMP _n	q_D/q_A	class	D/A=(An ₂ N) ₂ Ph _n	q_D/q_A	class	
DMP ₁	std.	0.08	III/II	(An ₂ N) ₂ Ph ₁	std.	1.00	III
DMP ₁	cd.	1.00	III	(An ₂ N) ₂ Ph ₁	cd.	0.99	III
DMP ₂	std.	0.02	II	(An ₂ N) ₂ Ph ₂	std.	0.99	III
DMP ₂	cd.	1.00	III	(An ₂ N) ₂ Ph ₂	cd.	0.98	III
DMP ₃	std.	0.01	II	(An ₂ N) ₂ Ph ₃	std.	-0.11	II
DMP ₃	cd.	1.00	III	(An ₂ N) ₂ Ph ₃	cd.	0.98	III
DMP ₄	std.	0.00	II	(An ₂ N) ₂ Ph ₄	std.	-0.14	II
DMP ₄	cd.	0.27	III/II	(An ₂ N) ₂ Ph ₄	cd.	0.95	III
DMP ₅	std.	0.00	II	(An ₂ N) ₂ Ph ₅	std.	-	-
DMP ₅	cd.	0.11	III/II	(An ₂ N) ₂ Ph ₅	cd.	0.16	III/II

connected DMP_n compounds, where in some cases even larger delocalization for longer bridges can be found, compared with shorter ones (see Appendix, Fig. A.6). Beyond that, there have been proposed other substitution schemes following the same strategy, which provide even higher stabilization of the diradical resonance forms and thus may pave the way to the design of mixed-valence compounds with unprecedented extended charge delocalization, similar to the theoretically proposed wires with anti-Ohmic behavior [64].

4.3 Impact of Linkage Topology and Bulky Substituents

Changing the Linkage Topology: *Meta*-connected DMP_n

Another approach toward anti-Ohmic behavior is to choose the linkage topology of bridging units to connect *via* two starred or unstarred atoms in an alternant hydrocarbon, for instance *meta*-connected phenylene units, such that going from one to two units leads from connecting *via* two atoms of the same starring type (alike or nondisjoint coupling) to connecting *via* two atoms of different starring types (disjoint coupling; see Fig. 4.5). In molecular conductance, this corresponds to transitioning from an “easy-zero” quantum interference feature to a “hard-zero” one [167–172], and if the donor/acceptor units were replaced by spin centers, from a nondisjoint diradical to a disjoint one [173]. The two types of interference/diradicals lead to quite different physical behavior, *e.g.*, a transmission dip resulting from hard-zero quantum interference is affected by including nearest-neighbor coupling [174], and for a nondisjoint diradical, the ground state is typically clearly a triplet, while for a disjoint one, singlet and triplet tend to be very close in energy [175–177]. One would expect quite pronounced charge localization for DMP_1 molecules linked by one *meta*-phenylene unit, while the change in the type of interference provided by two such units could potentially give rise to a more delocalized charge, resulting in a reverse localization trend.

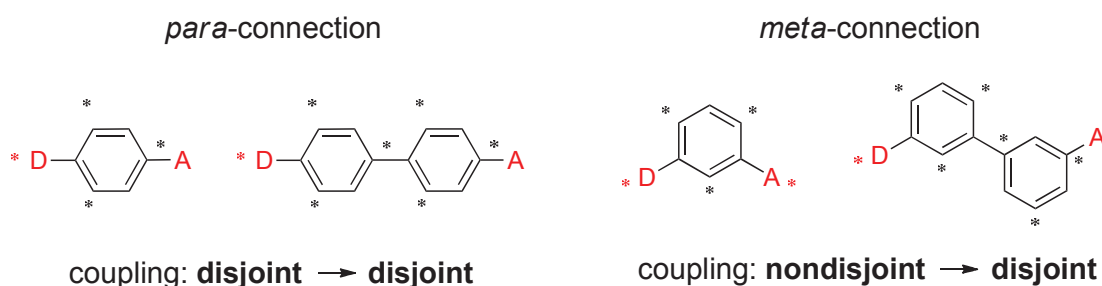


Figure 4.5: Starring Rule for Alternant Hydrocarbons *Left:* When starring every second atom, disjoint coupling is obtained for benzene-bridged molecules connected in *para*-position, as the donor and acceptor moiety are starred and unstarred, respectively. *Right:* When benzene is connected in *meta*-position, disjoint coupling is only obtained for the DMP_2 species, whereas in the DMP_1 species the donor and acceptor moiety are both starred, resulting in nondisjoint coupling.

The first five species of the *para*- and *meta*-series were optimized and their charge localization properties were systematically evaluated in various solvents of increasing polarity (Fig. 4.6). Since environmental effects determine the stabilization of the charge, enhanced charge localization can be expected when switching from relatively nonpolar hexane (HEX) to more polar dichloromethane or even acetonitrile as a solvent [50, 51, 53].

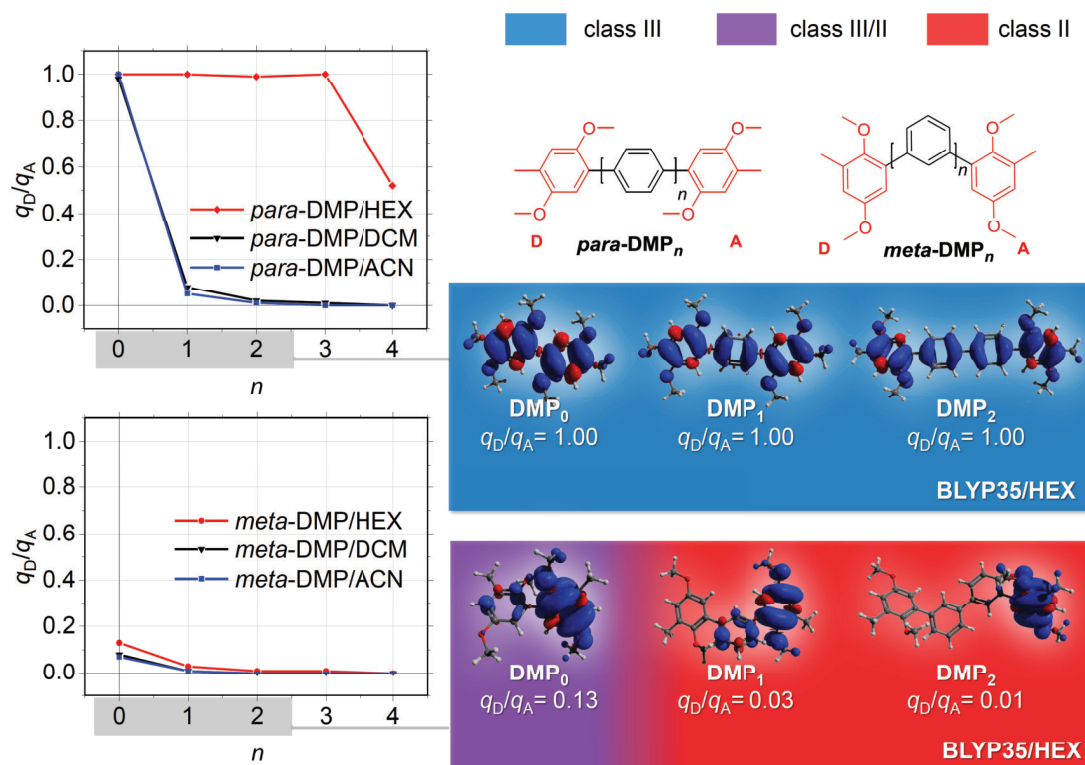


Figure 4.6: Charge Localization in *para*- and *meta*-DMP_n Left: Ratios q_D/q_A between partial charges on the donor and acceptor moieties of the DMP_n radical cations (*meta*-/*para*-connection) as a function of the number of bridging units n . Molecular structures are optimized with the BLYP35 hybrid functional, Ahlrich's def2-TZVP basis set and PCM. Right: Spin density isosurfaces of the marked compounds with the ratios q_D/q_A as a measure for charge localization and their Robin–Day classification indicated by the background colors (see Sec. 3.1 for the classification criteria.)

Upon comparison of the partial charge ratios for the *para*- and *meta*-connected DMP_n species, striking differences appear (Fig. 4.6). Overall, stronger charge localization is obtained for the *meta*-connected species in all solvents, which is in agreement with the assumptions made before. The finding of a higher

degree of charge localization for *meta*-DMP_n species is also consistent with their molecular structures. Whereas the *para*-DMP_n species in hexane are nearly planar, the *meta*-DMP_n species are tilted, resulting in an angled geometry for the longer DMP₂. The higher degree of planarity in *para*- versus *meta*-DMP₀ can be attributed to smaller steric interactions and correlates with the increasing π -character of the inter-ring bonds in the former species, which are 1.45 Å and 1.48 Å, respectively. The coplanar arrangement is facilitated for *para*-DMP₀ with a dihedral angle between the phenyl-rings of 39.3° versus 58.4° for *meta*-DMP₀. The trend of decreasing planarity continues even more for the longer species, where the aromatic stabilization of the benzene rings is likely to diminish the π -character of the inter-ring bonds and thus facilitates non-planar ring arrangements with increasing degrees of freedom. However, no reverse localization trend can be observed for the *meta*-series when going from DMP₁ to DMP₂, as no enhanced degree of charge delocalization can be observed in the latter species, and both remain rather localized structures irrespective of the solvent used. Even when considering the molecules in a quite nonpolar environment such as hexane, no significant delocalization is obtained for *meta*-DMP₂. Still, it is interesting that the *para*-DMP_n species seem to be more sensitive to the polarity of the solvent than the *meta*-analogues. The same is true for replacing the redox centers by An₂N motifs, even though charge delocalization is more pronounced here for the *para*-species compared with the *para*-DMP_n series, see discussion below.

Changing the Redox Center: Phenylene-bis(dianisylamine)

Following the initial idea, it was studied whether the localization trend can be reversed when going from shorter to longer *meta*-(An₂N)₂Ph_n species. When exchanging the DMP_n redox center by (An₂N)₂Ph_n, smaller effective distances between the redox centers might lead to overall stronger charge delocalization [63]. On the other hand, the positive charge is likely more stabilized on the triarylamine unit in (An₂N)₂Ph_n when compared to DMP_n, as the oxidation potential is higher in the latter motif¹, therefore facilitating charge localization, preferably on a triarylamine subunit. While keeping the system size relatively low to promote charge delocalization, the *meta*-topology is expected to result in a rather localized structure for (An₂N)₂Ph₁ in particular, as argued before.

¹E_{1,2}(DMP_n)= 0.99 V [178], E_{1,2}(An₃N_n)= 0.25 V [179]

Moreover, the coplanar arrangement of the terminal anisyl-rings may be impeded in the shorter analogue due to steric constraints in *meta*-connection, which can reduce effective π -delocalization [62]. In contrast, the longer $(\text{An}_2\text{N})_2\text{Ph}_2$ shows disjoint coupling and experiences less steric constraints, which may result in a stronger delocalized structure due to relatively short delocalization pathways. Since it was already observed that the linkage topology affects charge localization in DMP_n , it was investigated whether the overall trend of stronger charge localization in *meta*-connection also applies to the $(\text{An}_2\text{N})_2\text{Ph}_n$ radical cations when compared to *para*-connection. Therefore, also the N,N,N',N'-tetraanisyl-*p*-phenylenediamine (TAPD) radical cations, *i.e.* the *para*- $(\text{An}_2\text{N})_2\text{Ph}_n$ series, were examined, a structure that has been studied widely before [62, 118].

When comparing *meta*- $(\text{An}_2\text{N})_2\text{Ph}_1$ and *meta*- $(\text{An}_2\text{N})_2\text{Ph}_2$ in dichloromethane, no reverse localization trend can be observed (Fig. 4.7). In fact, the charge is even more localized in the latter species, as indicated by a partial charge ratio of -0.13 versus -0.05 for the former species. Although the system is relatively small, it seems that the tilted geometry of *meta*- $(\text{An}_2\text{N})_2\text{Ph}_2$ hinders the planarization of the benzene rings and makes the formation of a charge-localized defect on one single nitrogen center more favorable.²

When changing to *para*-connection, stronger charge delocalization is obtained in comparison to the *meta*- $(\text{An}_2\text{N})_2\text{Ph}_n$ series. Here, the first two members of the series remain class III systems with the rings arranged in a coplanar fashion and thus allowing for effective π -delocalization pathways. This classification is in agreement with the class III assignment from experimental studies of Barlow and coworkers on the *para*- $(\text{An}_2\text{N})_2\text{Ph}_1$ and *para*- $(\text{An}_2\text{N})_2\text{Ph}_2$ species [118].³

²For all *meta*- $(\text{An}_2\text{N})_2\text{Ph}_n$ species, charge localization occurs preferably on triarylamine subunits, which is likely due to the high stability of these radical cations [62].

³For both connection types, the reorganization of the nitrogen center by planarization and thus charge localization on the triarylamine subunit is energetically favored [62]. For the first two *para*- $(\text{An}_2\text{N})_2\text{Ph}_n$ species, the reorganization energy needed for the coplanar arrangement of the two subunits is outweighed by the delocalization energy gained by planarization, whereas sterical constraints in the tilted *meta*-species make the reorganization of only the nitrogen center more favorable than planarization of the whole system [62]. For *para*- $(\text{An}_2\text{N})_2\text{Ph}_n$ species, a quinoidal pattern with increased π -character of the inter-ring bonds is observed: For *para*- $(\text{An}_2\text{N})_2\text{Ph}_1$, identical bond lengths between the *para*-connected carbon atoms and the nitrogen centers are found (1.37 Å), whereas the corresponding C–N bonds lengths in the *meta*- $(\text{An}_2\text{N})_2\text{Ph}_1$ species are different (1.39 Å and 1.42 Å). The same is true for $(\text{An}_2\text{N})_2\text{Ph}_2$, where different degrees of planarization are indicated by dihedral angles between the inner benzene rings of 17.7° versus 37.4° for *para*- and *meta*-connection.

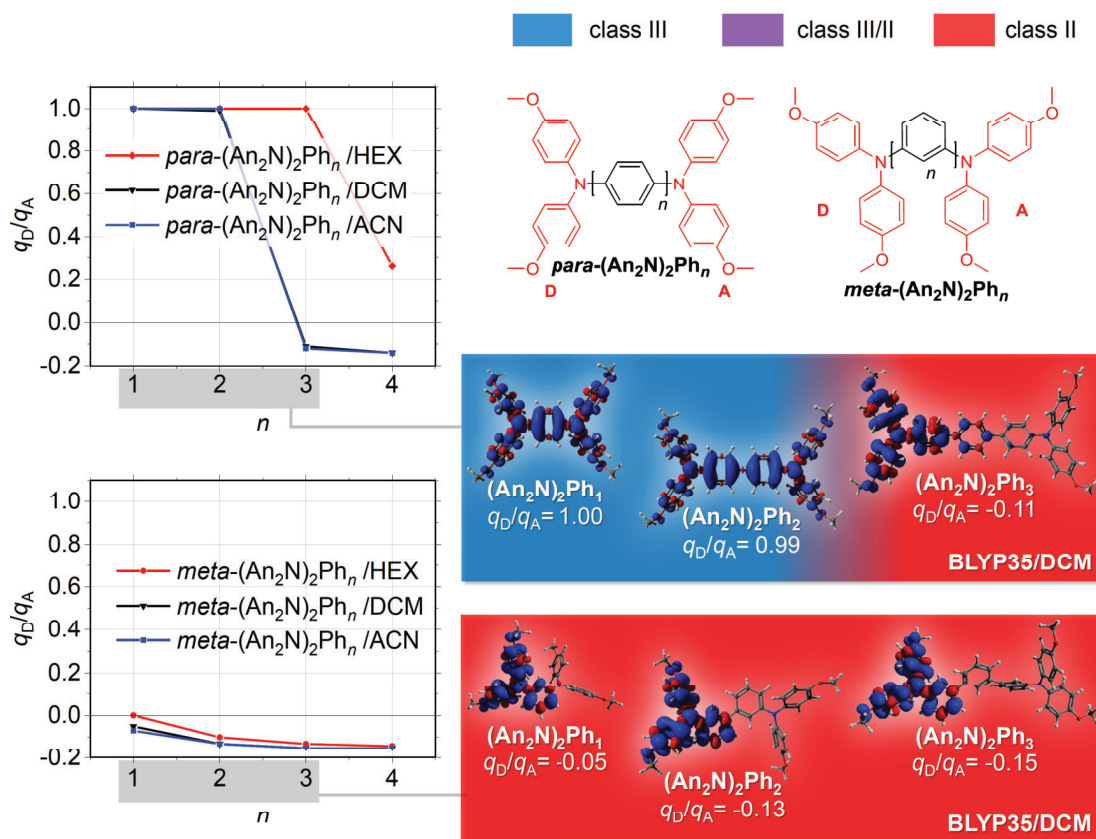


Figure 4.7: Charge Localization in *para*- and *meta*-(An₂N)₂Ph_n
Left: Ratios q_D/q_A between partial charges on the donor and acceptor moieties of the (An₂N)₂Ph_n radical cations (*meta*-/*para*-connection) as a function of the number of bridging units n . Molecular structures are optimized with the BLYP35 hybrid functional, Ahlrich’s def2-TZVP basis set and PCM. *Right:* Spin density isosurfaces of the marked compounds with the ratios q_D/q_A as a measure for charge localization and their Robin–Day classification indicated by the background colors (see Sec. 3.1 for the classification criteria.)

Generally, the overall trend of increasing charge localization when changing from *para*- to *meta*-linkage that has been observed for the DMP_n systems also applies to the (An₂N)₂Ph_n analogues, which is in line with experiments on the influence of the bridge topology in benzene-bridged mixed-valence compounds [62, 180, 181]. Moreover, the *meta*-species seem to be analogously less sensitive to the polarity of the environment.⁴

⁴*Para*-(An₂N)₂Ph_n species remain delocalized at longer lengths than *para*-DMP_n species (*para*-(An₂N)₂Ph₂: class III; DMP₂: class II; DCM), probably due to a greater effective distance between the redox centers in the latter, making charge localization more favorable.

To conclude, it seems that only disjoint coupling is not a sufficient factor for the charge being more delocalized in DMP_2 compared to DMP_1 . The tendency of the *meta*-topology in favoring charge localization can be attributed to the higher degree of twisting in the *meta*- DMP_n species being the predominating factor over electronic effects here, which suggests that for exploiting this design strategy for anti-Ohmic behavior, reducing the importance of steric interactions in nondisjoint bridging units is important.

Introduction of Bulky Substituents: *Tert*-Butyl Bis(dianisylamine)

Given that thiophene-containing conjugated molecules are promising candidates for the use as molecular wires, and since $(\text{An}_2\text{N})_2\text{T}_n$ species with one to three thiophene units are class III systems, it is a challenging task for chemical design to enhance charge localization in these naturally delocalized molecules. Here, bis(dianisylamine) radical cations were modified with sterically demanding *tert*-butyl substituents on the redox centers to promote charge localization by tilting of the geometry. The computational results obtained with the BLYP35+PCM protocol for the first two members of the *tert*-butyl-substituted bis(dianisylamine) series indicate that even in very polar solvents⁵, where charge delocalization is hampered, no stronger charge localization can be observed for the substituted oligothiophenes (see Appendix, Tab. A.5 and Fig. A.4).

Although the ratio of partial charges (0.94) indicates slightly more localized character for the *tert*-butyl-substituted $(\text{An}_2\text{N})_2\text{T}_1$ species compared to the unsubstituted one in all tested solvents, both members remain delocalized class III systems. This finding could be attributed to the dihedral angles changed by the bulky substituents not being the ones that are relevant for charge delocalization pathways. For example, an increase of the dihedral angles around the central C–N bonds up to 22.8° can be observed upon substitution, which is most pronounced for the $(\text{An}_2\text{N})_2\text{T}_1$ species. To employ a steric-hindrance strategy for enforcing anti-Ohmic behavior, it might be promising to study chemical structures with extended charge delocalization in the unsubstituted form for which sterically demanding substituents could have a more direct effect on the relevant dihedral angles, possibly starting from the "captodative" structures discussed in Sec. 4.2.

⁵Here, only results for the PCM modeling DCM are reported as they were qualitatively similar to calculations in H_2O and ACN. Additional data is provided in Ref. [54].

4.4 Conclusions

In this part of the work, the BLYP35+PCM protocol was employed to search for structures with either anti-Ohmic behavior, *i.e.* increasing charge delocalization for increasing wire lengths, or with charge delocalization being pertained at relatively long molecular lengths.

It was anticipated that by changing the linkage topology from *para*- to *meta*-connection in benzene-bridged radical cations, anti-Ohmic behavior might emerge due to a transition from nondisjoint to disjoint coupling when extending the number of bridging units from one to two. Instead, overall stronger charge localization was observed for the longer species, which can presumably be attributed to the larger sterical hindrance in *meta*-connection compared to *para*-connection. This trend was found being true for two different types of redox centers, DMP_n and $(\text{An}_2\text{N})_2\text{Ph}_n$, while the degree of charge delocalization was found being overall greater in the latter motif. Moreover, *para*-species were generally found being more sensitive to the polarity of the solvent.

Similar to the first approach, an attempt to exploit steric hindrance for decreasing electronic coupling at shorter bridge lengths by attaching bulky groups to the redox centers did not lead to the desired drastic increase of charge localization for the shorter bis(dianisylamine) thiophene systems studied here. Nonetheless, the data presented in this section may provide a basis for future studies on similar concepts.

By applying the captodative substitution scheme suggested by Stuyver, De Proft and coworkers for molecular wires it was demonstrated that charge delocalization can be tuned toward longer bridge lengths in *para*-benzene-bridged radical cations [64]. This strategy indeed allows for the transformation of charge-localized into charge-delocalized structures and thus for taking chemical control of charge localization, as charge delocalization was delayed from zero to three and from two to four bridging units for the DMP_n and the $(\text{An}_2\text{N})_2\text{Ph}_n$ series, respectively.

5 Investigating Electron Transfer in Radical Anions

5.1 Introduction

After successfully applying the BLYP35+PCM approach to radical cationic mixed-valence systems for the application to hole transport in molecular wires, here, it was evaluated whether it performs consistently well for anionic mixed-valence systems with the aim of analogously transferring it to electron transport [182–184]. Similarly to studies on radical cationic systems, a variety of experimentally well-characterized radical anionic systems was chosen for revalidating the DFT protocol in this context. In the first part of the validation, the DFT protocol was applied to small dinitroaromatic and diquinone systems, which were previously partly investigated by Kaupp and coworkers [50, 51].

It was found by Kaupp that the BLYP35+PCM approach works very well for reproducing the ground state characteristics of the evaluated mixed-valence anions. However, here, it was studied whether a classification of these compounds in line with the experiments is possible based on the optimized chemical structure and visual analysis of the spin density. In contrast to the previously investigated radical cations, not only the length-dependence of charge localization can be investigated in these radical anions, but also the effect of the linkage position and different substitution patterns of the aromatic system on it.

In the second part of the validation, the DFT protocol was applied to two different types of more wire-like perchlorotriphenylmethyl-terminated radical anionic systems with the focus set on the length-dependence of the transfer mechanism, as in larger molecular wires the formation of localized polaronic states was anticipated [182, 183]. These radical anionic systems are particularly interesting for the purpose of this work, because at a certain molecular length the mechanism of the electron transfer changes from superexchange or a flickering resonance mechanism to incoherent charge hopping [182, 183].

5.2 Class III–II Transitions in Radical Anions: DFT Results

In order to validate the BLYP35+PCM protocol for radical anions near the class III/II frontier, molecular structure optimizations were performed as described before in Sec. 3.3, followed by subsequent visual analysis of the spin density distribution and a comparative evaluation of characteristic bond lengths. As shown in Fig. 5.8, in dinitroaromatic systems, a relative shortening of the

C–N bond occurs on the side of the molecule where the excess negative charge is localized when compared to the opposite side (top). On the other hand, in diquinone systems, a relative lengthening of the two opposite C–O bonds occurs on the quinone redox center where the negative charge is located upon reduction (bottom) in comparison to equivalent C–O bonds on the other (non-reduced) redox center. Here, the relative shortening or lengthening of characteristic bond lengths serves as indicator for an increased degree of charge localization in dinitroaromatic and diquinone radical anions in addition to the visual assessment of the spin density (similarly to the quinoidal deformation in DMP_n radical cations, see Fig. 3.1 in Sec. 3.1). However, in contrast to the structural measure derived for DMP_n radical cations, here, the ratios of relevant bond lengths were compared within a certain molecular family to estimate the degree of charge localization rather than deriving an universally applicable measure. These ratios may therefore rather be regarded as a guideline for assessing charge localization within a series of similar systems, which is not necessarily transferable to a different type of system and should be complemented with other assessments, as done by visual analysis of the spin density distribution.

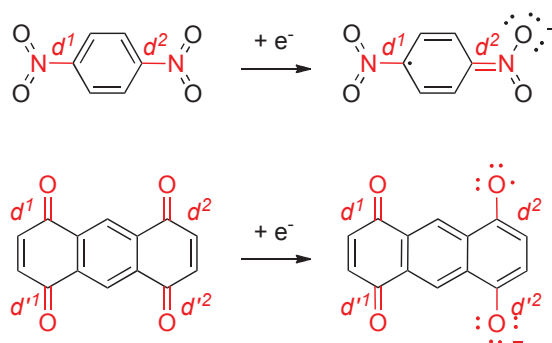


Figure 5.8: Structural Changes in Mixed-Valence Radical Anions

Schematic representation of the relative shortening of the C–N bond and the relative lengthening of the C–O bonds upon reduction in dinitroaromatic (top) and diquinone (bottom) organic mixed-valence species (assuming a purely class II behavior).

Computational Methodology

Neutral structures of the organic mixed-valence systems were preoptimized by performing KS-DFT calculations using the resolution-of-identity (RI) approach, implemented in the TURBOMOLE 7.0 package [149]. In the molecular structure optimizations, the BP86 exchange-correlation functional [131, 132], Ahlrich's def2-TZVP basis set [150] of triple-zeta quality with polarization functions on all atoms, and the D3 dispersion correction introduced by Grimme [151] were employed. The convergence criterion in the self-consistent field (SCF) algorithm was set to 10^{-7} hartree for the change of the energy in all calculations and to 10^{-4} a.u. for the gradient in molecular structure optimizations. Subsequent molecular structure optimizations on the neutral preoptimized structures were performed for the molecular wires in their radical anionic state by employing the GAUSSIAN 09 program package [152] with Ahlrich's def2-TZVP⁶ basis set and the hybrid BLYP35 functional with 35% exact exchange from the Kaupp group, which was constructed analogously to the B1LYP model [136]. Molecular structure optimizations were performed for molecules in solution, since the importance of environmental effects on charge localization properties was pointed out by Kaupp and coworkers and was shown in our previous study on organic mixed-valence systems [53, 54]. For the inclusion of solvent effects, the polarizable continuum model with the integral equation formalism model (IEF-PCM) [153, 154] was employed as implemented in the GAUSSIAN 09 program package by using the SCRF keyword with the available dielectric constants for dichloromethane ($\epsilon_{\text{DCM}}=8.93$), *n,n*-dimethylformamide ($\epsilon_{\text{DMF}}=37.219$) and acetonitrile ($\epsilon_{\text{ACN}}=35.688$), which were used in the corresponding experiments. For the local spin density, an absolute value of 1 refers to one unpaired electron. Molecular structures and spin densities were visualized with the AVOGADRO editor [155], applying an isosurface value of 0.001 for plotting the spin density distributions.

⁶Although it is clear that diffuse basis functions are more important for the description of radical anions than for radical cations, the def2-TZVP was used throughout this study. On the basis of test calculations with a 6-311G++ basis set on the diquinone radical anions presented below, no change in charge localization was observed. The same issue was previously discussed by Kaupp and coworkers on the example of dinitroaromatic radical anionic mixed-valence systems (also investigated in this study), where it was found that changes in the calculated electron-transfer properties from a SVP+(O) basis (diffuse augmentation restricted to oxygen atoms of the nitro groups) to a TZVP basis are minor [51].

Dinitroaromatic Anions

As one of the earliest mixed-valence compounds that have been experimentally classified according to the Robin–Day scheme, the dinitroaromatic radical anions shown in Fig. 5.9 served as a test example for the BLYP35+PCM protocol here and partly in previous studies by Kaupp and coworkers [51]. In these molecules, two nitro redox centers are linked by an aromatic bridge. Based on ESR and NIR spectroscopy experiments, they have been assigned to either class II and class III [185–188], while still being close to the class III/II borderline, which makes their classification from DFT calculations challenging [51,62].

Class III Systems – Species 1-6 From the experiments, species **1-6** are characterized as class III systems in aprotic solvents, like ACN and DMF [51, 62,63,185–188]. This is also in line with strong electronic coupling as suggested for compounds with an odd number of bonds between the nitrogen atoms, representing a so-called a Kekulé substitution pattern [51,62], corresponding to disjoint coupling according to the starring rule for alternant hydrocarbones (Fig. 4.5 in Sec. 4.3). Interestingly, even the two species **5** and **6** were assigned to class III despite their relatively long 9-bond conjugation pathway between the nitrogen atoms [62].

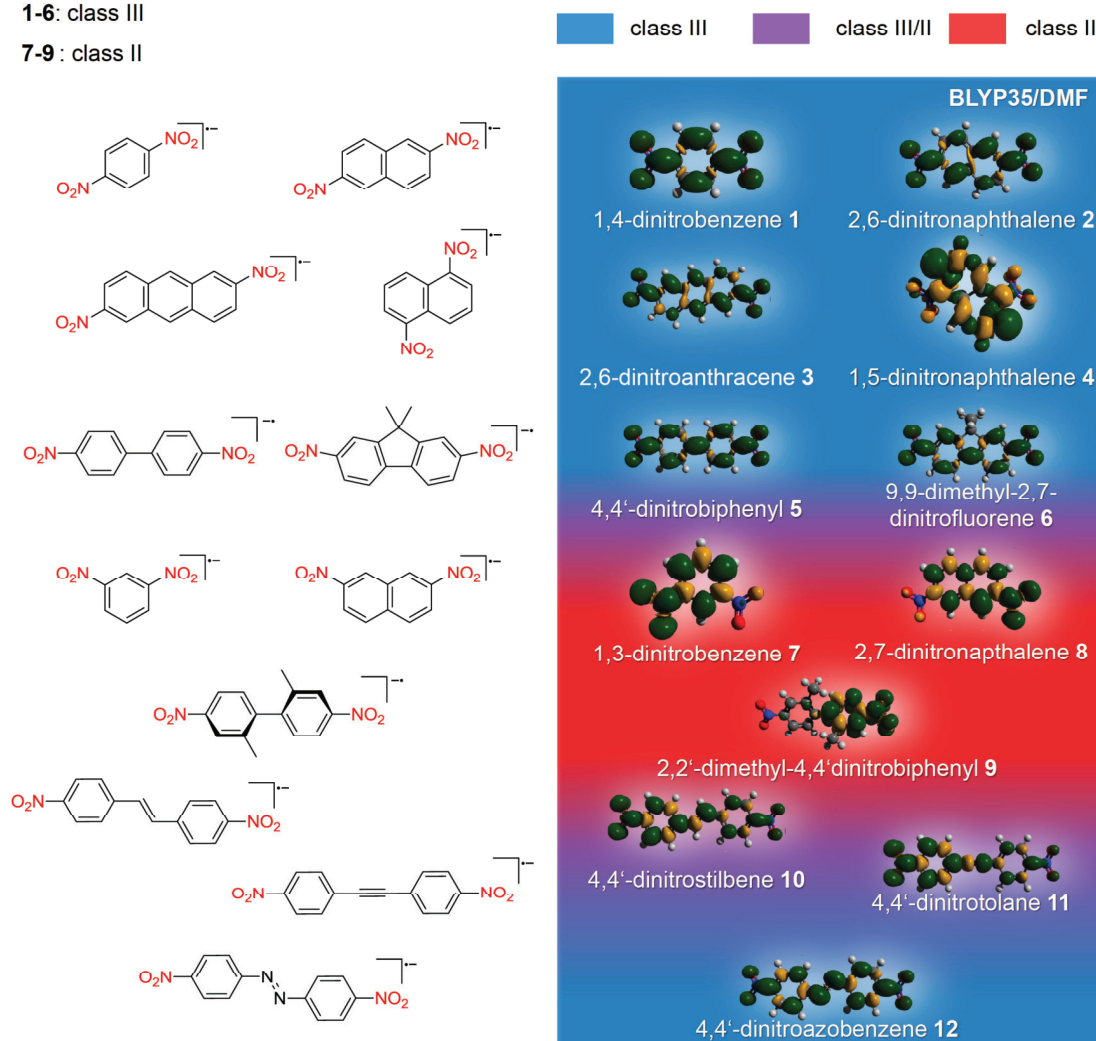
The results from molecular structure optimizations based on the BLYP35+PCM method are in line with the experimental classification of these species, as in both cases a completely delocalized spin density is obtained (see Fig. 5.9). Moreover, charge delocalization is indicated by equal C–N bond lengths on both termini of all molecules, reflected by the ratios of relevant bond lengths equaling 1.00 in any case (see Tab. 5.4). In contrast, a shortening of one bond length relative to the other would be expected upon charge localization.

Class II Systems – Species 7-9 For the species **7-9**, class II character is obtained from the experiments (see Tab. 5.4). This classification can also be derived from DFT calculations based on the BLYP35+PCM approach: Increased charge localization is indicated for all three radical anions, since in any case one redox center bears nearly no spin density (see Fig. 5.9). This is also reflected in a shortening of the C–N bond on the redox center where the charge is localized relative to the opposite redox center, indicated by ratios of relevant bond lengths being 0.95 (see Tab. 5.4).

Experiment*

1-6: class III

7-9: class II

**Figure 5.9: Charge Localization in Dinitroaromatic Systems**

Left: Chemical structures of the dinitroaromatic radical mixed-valence systems under study, where the donor and acceptor nitrogen groups are marked in red. *Right:* Spin density isosurfaces of the corresponding compounds and their Robin–Day classification indicated by the background colors (see Sec. 3.1 for the classification criteria.) *The experimental classification was derived from EPR and NIR spectroscopy in aprotic solvents (DMF/ACN) [185–188].

Class III/II Borderline Systems – Species 10-12 The three dinitroaromatic species 10-12 were investigated by Nelsen and coworkers by NIR spectroscopy experiments [62,188], all of them having a Kekulé substitution pattern with an odd number of bonds between the nitrogen atoms. From the experi-

ments it was suggested that these radical anions are rather localized class III/II compounds except for species **12**, which turns out to be a delocalized class III system in all solvents [62]. Moreover, it was found that the latter species exhibits relatively large electronic coupling between the redox centers, which is even greater than in species **2** despite the longer conjugation pathway *via* a 11-bond connection compared to a 7-bond connection [62]. In fact, the distance between the nitrogen centers is not the only factor influencing their electronic coupling, but also the energy gap between the frontier orbitals of the donor and acceptor states and the bridge state (see Sec. 2.1). If the energy gap is relatively small such as in species **12**, which is due to the low reduction potential of the azo-bridge, the superexchange coupling becomes likewise stronger [62, 63, 188]. The experimental findings are confirmed by DFT calculations, as the charge is completely delocalized in this species and the C–N bond lengths are equal on both termini (see Tab. 5.4).

The results obtained from this study on localization properties of dinitroaromatic species **1,2**, **7-9** and **11** are in line with theoretical studies by Kaupp and coworkers, where it was shown that the DFT protocol works very well in describing the ground state characteristics of these radical anions in aprotic polar solvents [51].

For the two species **10** and **11**, partial charge localization is suggested from theory by an asymmetrically distributed spin density that is mainly located on one side of the molecule, where the C–N bond is also shorter when compared to the opposite one as reflected in ratios of 0.96 (see Tab. 5.4).⁷ Still, the charge is not yet fully localized, since in both cases a small amount of charge is still localized on the opposite redox center. However, as indicated from the experiments, these two species can rather be described as class III/II borderline compounds, which is in line with the slightly localized structures predicted from the DFT calculations. Moreover, the class III/II nature of species **10** and **11** is supported by slightly higher ratios between relevant bond lengths when compared to the class II species described above.

⁷As pointed out earlier in this section, the structural measure based on the ratios of opposite bond lengths derived here is not comparable to the one presented for DMP_n radical cations in Sec. 3.1, which was derived differently and where a value of 0.96 would rather indicate class II behavior. Thus, the ratios of opposite bond lengths evaluated in this section rather serve as a guideline for relative charge localization within a molecular series and must not be compared to other molecular families.

Diquinone Anions

As one of the earliest studies on the length-dependence of charge transfer in organic mixed-valence systems, radical anionic diquinone molecules **1-3** were investigated experimentally based on cyclic voltammetry, NIR, IR and EPR measurements by Miller and coworkers [189,190] and are shown in Fig. 5.10 next to the tetrathiofulvalene radical anion studied by Gautier and coworkers [191]. Moreover, species **1** and **3a,b-4** served as a test example for the BLYP35+PCM protocol earlier in theoretical studies by Kaupp and coworkers [50]. All of them were classified as localized class II systems from the experiments in aprotic polar solvents like DMF or DCM, except for the shortest species **1**, which was found to be a delocalized class III system [189,190].

From DFT calculations with the BLYP35+PCM protocol, the experimental classification is predicted correctly in all cases, as indicated by the spin density distributions shown in Fig. 5.10 and the comparison of C–O bond lengths listed in Tab. 5.4: For the shortest species **1**, the spin density is delocalized across the whole molecule, which is also reflected in identical bond lengths on the two quinone redox centers. Increased localization is indicated for the species **2** with the bridge comprising one additional benzene unit, where the spin density is mainly located on one quinone unit with the corresponding C–O bond lengths being 1.252 Å and 1.219 Å on opposite redox centers. Increased charge localization continues when going to longer bridge lengths such as species **3a** and **3b**: Whether methylated on the redox center or not, the spin density in these pentacene-based radical anions is mainly located on one redox center. The high degree of charge localization is again expressed by the difference in C–O bond lengths, equaling 1.218-1.220 Å and 1.254-1.256 Å on the two opposite redox centers. However, the species **2**, **3a** and **3b** are not fully localized yet, as there is still some spin density visibly located on one side of the molecule with the chosen isosurface value. Although they were characterized as class II systems from the experiments, it was found that in a less polar environment and depending on the concentration of counter-ions⁸, the **3a,b** species may exhibit

⁸In addition to solvent effects, interactions between the charged system and counter-ions need to be considered in principle. However, the HF exchange admixture of 35% may compensate for counter-ion effects (beyond others, such as the electrode contact and intermolecular interactions) that are neglected in the DFT protocol, as pointed out by Kaupp *et al.* [52]. Although being overall non-negligible, the lack of counter-ion modelling does not necessarily invalidate the predictive calculations, as shown by Renz and Kaupp [50].

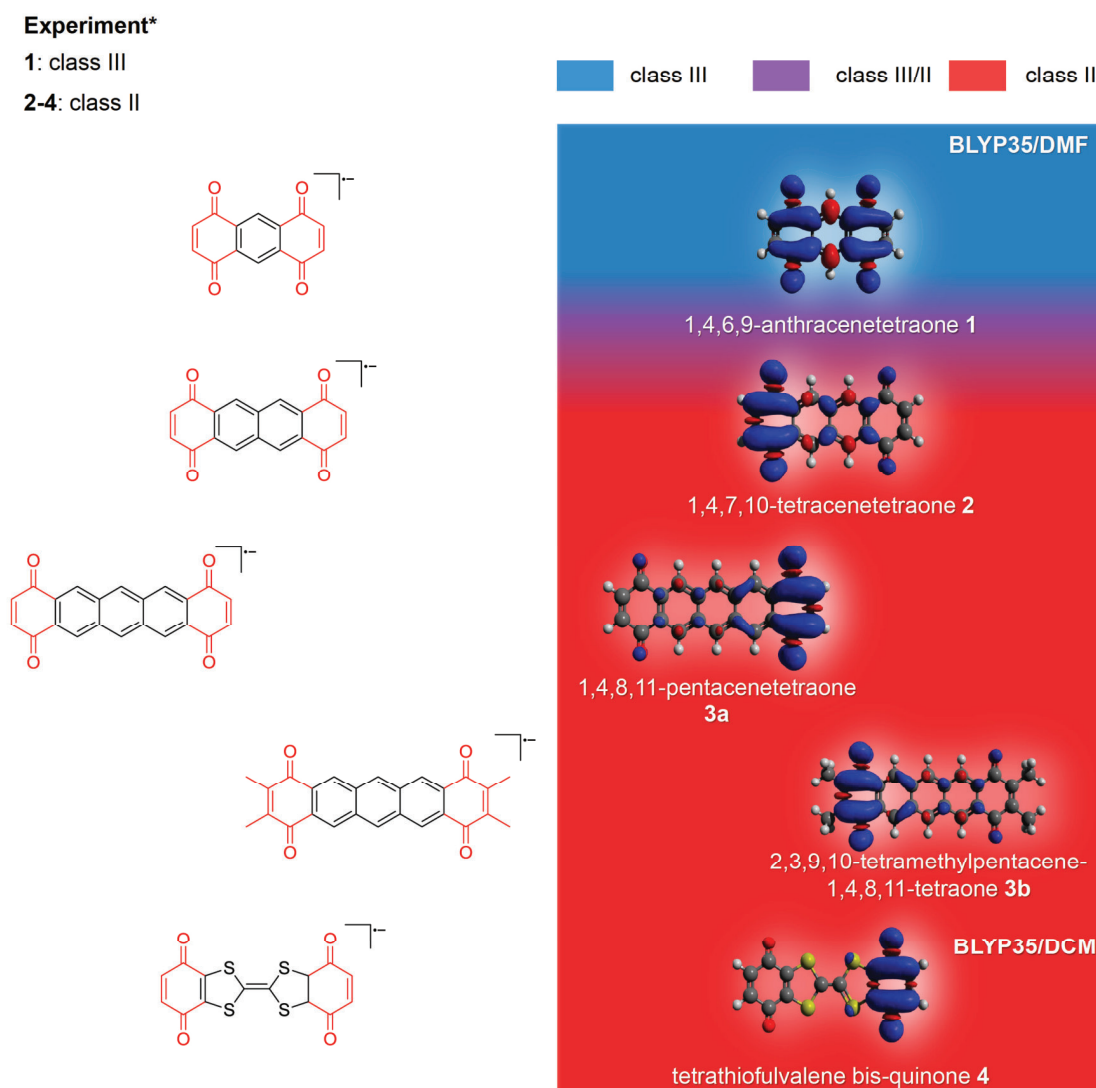


Figure 5.10: Charge Localization in Diquinone Systems *Left:* Chemical structures of the diquinone radical mixed-valence systems under study, where the donor and acceptor diquinone groups are marked in red. *Right:* Spin density isosurfaces of the corresponding compounds and their Robin–Day classification indicated by the background colors (see Sec. 3.1 for the classification criteria.)

*The experimental classification was derived from EPR and NIR spectroscopy in aprotic solvents (DMF/DCM) [189–191].

class III behaviour, suggesting it being close to the class III/II borderline [50]. For the tetrathiofulvalene bis-quinone 4, the highest degree of charge localization is observed, as the spin density is nearly completely localized on one redox center, matching the relatively large differences between the C–O bond lengths,

equaling 1.255 Å and 1.212 Å on the two quinone units, in line with the experimental class II assignment [191] and with theoretical investigations by Kaupp and coworkers [50]. Moreover, the assignment to class III and class II of the diquinone species **1** and **3a,b**, respectively, are in line with theoretical studies by Kaupp and coworkers [50].

The picture above is supported by corresponding ratios between the relevant bond lengths: Only for the shortest species **1** the ratio equals 1.00, whereas ratios of 0.97 for the remaining species indicate a higher degree of charge localization, in line with class II character.

Table 5.4: Charge Localization in Radical Anions – Summary Table

Comparison of the Robin–Day class as determined from DFT calculations with the BLYP35 hybrid functional and Ahlrich’s def2-TZVP basis set with experiments for dinitroaromatic and diquinone radical anions (see Fig. 5.8) [185–190]. The degree of charge localization from DFT calculations was evaluated from visual analysis of the spin density distribution as shown in Figs. 5.9 and 5.10 and from the comparison of characteristic bond lengths, as tabulated below. Molecular structures are optimized with the BLYP35 hybrid functional and Ahlrich’s def2-TZVP basis set, and with a PCM for DMF. The classification is based on NIR and EPR spectroscopy experiments in aprotic polar solvents, either ACN, DCM or DMF.

dinitroaromatic radical anions [185–188]					
no.	$d^1(\text{C–N})$	$d^2(\text{C–N})$	$d^2(\text{C–N})/d^1(\text{C–N})$	theory	exp.
1	1.396	1.396	1.00	III	III
2	1.400	1.400	1.00	III	III
3	1.405	1.405	1.00	III	III
4	1.449	1.449	1.00	III	III
5	1.401	1.401	1.00	III	III
6	1.401	1.401	1.00	III	III
7	1.464	1.384	0.95	II	II
8	1.459	1.383	0.95	II	II
9	1.457	1.386	0.95	II	II
10	1.433	1.382	0.96	III/II	III/II
11	1.446	1.382	0.96	III/II	III/II
12	1.421	1.421	1.00	III	III
diquinone radical anions [189, 190]					
no.	$d, d^1(\text{C–O})$	$d, d^2(\text{C–O})$	$d, d^2(\text{C–O})/d, d^1(\text{C–O})$	theory	exp.
1	1.234	1.234	1.00	III	III
2	1.252	1.219	0.97	II	II
3a	1.254	1.218	0.97	II	II
3b	1.256	1.220	0.97	II	II
4	1.255	1.212	0.97	II	II

PTM-based Anions

As further test examples for the description of charge localization in radical anionic mixed-valence species, the BLYP35+PCM method was applied to two different sets of wire-like perchlorotriphenylmethyl (PTM) radicals, studied by Veciana and coworkers [182, 183]. In both types of wires, the redox centers are represented by PTM units, which are connected *via* a bridge of growing length based on either thiophene-vinylene (n TV) oligomers [183] or *p*-phenylene-vinylene (n PPV) oligomers [182]. Since the length of the linking bridge strongly determines the predominating mechanism of intramolecular electron transfer from one redox center to another, ensembles of species with increasing molecular lengths were investigated in this work. Here, the aim was to predict the experimentally indicated length-dependent crossover of the electron transfer mechanism based on charge localization properties calculated with the BLYP35+PCM protocol. For PTM radical anions, the assessment of charge localization is based on the visual analysis of the spin density, since changes in the chemical structure upon charge localization are less clearly indicated than in the previously discussed examples.

PTM- n PPV-PTM Anions The intramolecular electron transfer phenomena of PTM radical anions with oligomer bridges comprising up to five PPV units were investigated by Veciana and coworkers in their ground state by means of NIR and temperature-dependent EPR spectroscopy experiments in dichloromethane [182] (see Fig. 5.11). It was found that two different charge transfer regimes are present in the [PTM- n PPV-PTM] molecules that compete with each other, resulting in the predominance of one over the other depending on the molecular length: In the shorter wires **1PPV** and **2PPV**, electron tunneling *via* superexchange prevails, while in the longer wires from **3PPV** to **5PPV**, thermally activated hopping becomes predominant. The size of the molecules therefore influences the tunneling efficacy and the activation energy barrier of the hopping process markedly, as the latter decreases with increasing molecular length [182].

From DFT calculations with the BLYP35 functional in DCM, the charge transfer characteristics observed in the experiments are recovered sufficiently well, as shown by the computed spin density distributions in Fig. 5.11 and the comparative Tab. 5.5. While for the shortest species **1PPV** and **2PPV**, the spin

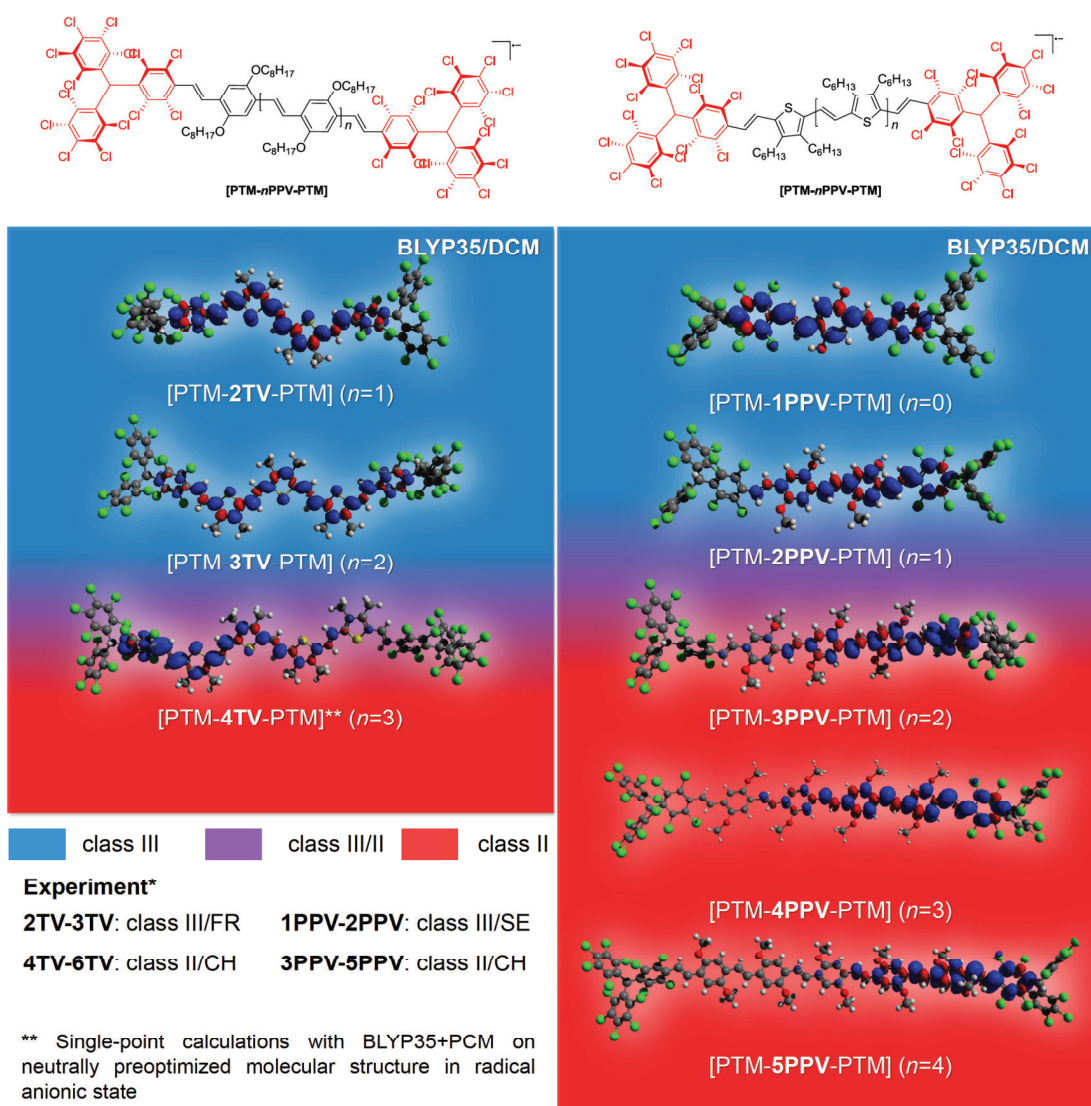


Figure 5.11: Charge Localization in PTM Radical Anions *Top:* Chemical structures of the PTM-terminated radical mixed-valence systems under study, where the donor and acceptor diquinone groups are marked in red. *Bottom:* Spin density isosurfaces of the corresponding compounds and their Robin–Day classification indicated by the background colors (see Sec. 3.1 for the classification criteria.) *The experimental classification was derived from EPR and NIR spectroscopy in DCM [182,183].

density is rather delocalized across the molecule, distinct charge localization is observed for the longer species from **3PPV** to **5PPV**. However, while for the shortest species **1PPV** the spin density is equally distributed across the molecule except the two terminal phenyl rings of the PTM units, localization

slightly sets in for the **2PPV** species, where less spin density is located on one of the inner phenyl rings connected to the bridge. Still, the remainder of the spin density is delocalized across the entire bridge, leading to the conclusion that the degree of charge localization reflects the predominance of the tunneling mechanism sufficiently well. More importantly, rather the difference between subsequent molecular wires may serve as a valuable indicator for the change of charge localization properties as pointed out on the example of radical cationic wires earlier in this work in Sec. 3.1. Here, a notable difference in charge localization between **2PPV** and **3PPV** is observed, as one of the terminal DMP units of the bridge in **3PPV** bears nearly no spin density in contrast to **2PPV**, where the bridge is fully covered by the spin density.

For the longer species **4PPV** and **5PPV**, the increase in charge localization becomes even stronger as the majority of the spin density is located on less than half of the molecule for the longest species. The latter finding perfectly matches the assumption of the electron transfer being dominated by an incoherent hopping mechanism based on the experiments. Still, as indicated by these DFT results and pointed out by the experimenters, both transfer mechanisms operate in parallel but occur and therefore contribute to different extents to the electron transfer rate depending on the molecular length. Consequently, there likely may not be a distinct crossover length but rather a transition regime, gradually leading over from the major presence of one mechanism to another with increasing bridge length. This was already discussed in the context of the Robin–Day classification of organic mixed-valence system, where the transition regime would be analogously represented by the intermediate class III/II species between delocalization and localization.

PTM- n TV-PTM Anions Similar in structure, the electron transfer mechanism of PTM radical anions in their ground state with bridges consisting of n TV oligomers were investigated by Veciana and coworkers [183]. This type of PTM organic mixed-valence anions differs from the previously discussed [PTM- n PPV-PTM] wires only by the connecting bridge, where the phenylene units are replaced by thiophenes (see Fig. 5.11). Due to their electron-rich nature, these π -conjugated wires based on n TV oligomers perform as very efficient hole transmitters, while the use of these wires for charge transfer/transport between two negatively charged redox centers such as in PTM radical anions was not

reported before [182]. Based on NIR and EPR spectroscopy experiments it was suggested that in shorter [PTM- n TV-PTM] species with bridges consisting of up to three thiophene units a flickering resonance (FR) mechanism operates, which is intermediate between superexchange and charge hopping (CH) [192]. Since in this regime the energy levels of the two PTM subunits and those of the bridge subunits come in resonance due to thermal fluctuations but the charge moves through the wire without nuclear relaxations, it is considered a compromise between transport/transfer *via* superexchange and charge hopping. The FR mechanism is assumed to be favored by the more rigid quinoid-like structure of the shorter wires compared to the longer ones [183]. However, in the flickering resonance regime the charge is assumed to be rather delocalized, since it moves with very little or no nuclear relaxation through the energy-aligned sites of the molecular wire until being trapped on the acceptor unit [192].

On the other hand, a biased bidirectional symmetrical charge-hopping mechanism was proposed to dominate in the longer species **4TV-7TV**, which is initiated by the thermally activated intramolecular oxidation of the donor bridge by the acceptor PTM radical unit, formally being in its neutral state. As a consequence, a charge-separated state is formed with a mobile positive polaron on the bridge that is flanked by two PTM anions. The transient positive polaronic species then migrates through the molecule and finally recombines by an electron-hole annihilation on the terminal PTM unit, while restoring the neutrality of the bridge. The negative charge motion is therefore mediated by transient positive charges [183]. To investigate whether the BLYP35+PCM protocol is suitable to predict the length-dependent transition from one transport mechanism to the other in [PTM- n TV-PTM] wires, the spin density distributions from species **2TV** to **4TV** were analyzed (see Fig. 5.11).

As indicated from the calculated spin densities, the charge is fully delocalized for the two shortest species, **2TV** and **3TV** (see also Tab. 5.5). Based on the experimentally indicated charge hopping mechanism, a change to a more localized structure would be expected when going from **3TV** to **4TV**. Since molecular structure optimizations of the longer wires **4TV** to **7TV** were beyond the scope of this work due to their large size and the associated computational effort, single-point energy calculations with the BLYP35+PCM protocol were performed on the neutrally preoptimized molecular structure in its radical anionic state. Interestingly, charge localization is predicted on the symmetrical

Table 5.5: Charge Localization in PTM Anions – Summary Table Comparison of the degree of charge localization from experiments and from DFT calculations with the BLYP35 hybrid functional and Ahlrich’s def2-TZVP basis set for PTM-terminated n TV and n PPV radical anions [182,183]. The degree of charge localization from theory was evaluated from visual analysis of the spin density distribution (Fig. 5.11). Molecular structures are optimized with the BLYP35 functional and Ahlrich’s def2-TZVP basis set, and with a PCM for DCM. The classification is based on NIR and EPR spectroscopy experiments in DCM [182,183].

	exp.	theory
[PTM- n PPV-PTM] [182]	class/ET mechanism	class
1PPV	III/ SE	III
2PPV	III/ SE	III/II
3PPV	II/ CH	II
4PPV	II/ CH	II
5PPV	II/ CH	II
[PTM- n TV-PTM] [183]	class/ET mechanism	class
2TV	III/ FR	III
3TV	III/ FR	III
4TV	II/ CH	II*
5TV	II/ CH	-
6TV	II/ CH	-

*Charge localization evaluated from single-point calculations (BLYP35+PCM) on neutrally preoptimized molecular structure.

neutral geometry for the **4TV** anion by the BLYP35+PCM protocol, as the spin density is localized on roughly one half of the molecule. This finding is in line with the experimentally observed transition to charge hopping for the **4TV** species and it is likely that the increase of charge localization is even stronger for longer wires with even greater distance between the PTM redox centers, as shown for structurally related PTM- n PPV-PTM radical anions.

5.3 Conclusions

In this part of the work it was investigated whether the BLYP35+PCM protocol performs well not only in describing hole transfer but also electron transfer. Similar to the previous validation on the example of radical cationic mixed-valence systems, experimentally well-characterized mixed-valence radical anions were taken as reference systems to provide a solid basis for revalidating the DFT protocol in this context.

This investigation was two-fold: In the first part, the BLYP35+PCM protocol was applied to small dinitroaromatic and diquinone molecules, where not only the length-dependence but rather the influence of the substitution pattern of the aromatic bridge on charge localization was investigated, some of which were investigated before by Kaupp and coworkers [50,51]. In the second part, the protocol was applied to two variants of relatively long wire-like PTM-terminated radical anions with bridges consisting of conjugated oligothiophenes or oligophenylenes comprising up to seven monomer units.

It was found that the DFT protocol performs consistently well in predicting the Robin–Day classification as indicated from the experiments for the dinitroaromatic and diquinone radical anions investigated in this work. For the dinitroaromatic systems, the degree of charge localization suggested by the spin density distributions and characteristic C–N bond lengths is definite in nearly any case and points clearly to either class II or class III as indicated from experiments [185–188]. Here, class III character is unambiguously reflected in equal C–N bond lengths and equally distributed spin densities and the class II nature is universally indicated by localization of the spin density on one side of the molecule and increasing differences in C–N bond lengths. More importantly, the DFT protocol performs well not only in describing either class III or class II character in radical anionic systems, but also reproduces the slightly localized class III/II nature of species **10** and **11** right on the borderline between these two regimes remarkably well and in line with the experiments.

Similar to the dinitroaromatic systems, the theoretical classification of the diquinone systems is clear-cut in any case and agrees well with the experiments: Except for the shortest member, which is completely delocalized and was assigned to class III from the experiments, all species are rather localized structures, which is in line with their assignment to class II from the experiments [189–191].

With the aim of transferring the BLYP35+PCM protocol to predicting length-dependent transport mechanisms in molecular wires, it was employed for investigating electron transfer in PTM-terminated radical anions of different molecular length, bridged by either oligophenylene or oligothiophene linkers. Promising results were obtained from DFT calculations on PTM radical anionic wires: For the phenylene-bridged species, the experimentally indicated change from a superexchange to a charge hopping mechanism is supported from DFT by an increasing degree of charge localization. Although slight charge localization already sets in one species earlier than predicted from the experiments, it still has the majority of the spin density equally distributed on the bridge and, more importantly, the degree of charge localization is distinctly higher in the longer species. As will be discussed in the context of predicting charge transport mechanisms in molecular wires and shown on the example of radical cationic organic mixed-valence systems, the largest relative increase in charge localization is likely most indicative of the transition to charge hopping, which is therefore clearly suggested from DFT in this case.

Similar results were obtained for the thiophene-bridged PTM radical anions: The experimentally suggested crossover to charge hopping at a certain length is indicated by DFT calculations as well, but is based on single-point calculations on the respective neutrally optimized molecular structure only, as a full optimization was beyond the scope of this work. However, good agreement with the experiments is suggested by these preliminary results as the increase in charge localization is relatively strong for this species when compared to shorter members that are fully delocalized.

In future studies, the capability of the BLYP35+PCM approach in describing electron transfer may be confirmed by full molecular structure optimizations of longer thiophene-bridged PTM radical anions based on preliminary results obtained in this work. These studies may pave the way toward predicting electron transport in molecular wires based on charge localization, as was successfully demonstrated in this work for hole transport [193].

IV. CHARGE TRANSPORT IN MOLECULAR WIRES

6 Predicting the Length-dependent Crossover from DFT

6.1 Introduction

After successful validation of the BLYP35+PCM protocol, the aim was to evaluate its capabilities of predicting charge transport mechanisms based on charge localization properties in molecular wires, for which a transition from tunneling to hopping was previously identified from molecular conductance experiments. Since the definition of charge localization in molecular wires is not as clear-cut as in donor-bridge-acceptor molecules such as mixed-valence systems, a quantitative measure for charge delocalization was initially defined and validated on the example of OPTI_n wires. Based on the established charge delocalization measure, the tunneling-to-hopping crossover was systematically evaluated for five different sets of conjugated wires, and the theoretical results were compared to the experiment. Since the results of this investigation were published in Ref. [193], the corresponding data and figures were adapted from this publication. As an alternative approach toward the prediction of transport mechanisms, long-range corrected DFT methods were evaluated on the previously investigated OPTI_n wires. This study was inspired by investigations on organic mixed-valence systems, where the ω -B97X-D functional was found to perform well in describing charge localization in isolated molecules [120, 121], which was also confirmed by calculations in this work (see Sec. 3.3). Moreover, preceding computational studies on OPTI_n by Smith and coworkers suggested the M06-HF functional as promising method for calculating length-dependent charge localization properties [31], while in studies on organic mixed-valence systems it was found to lead to overlocalization [120]. Here, these approaches were revisited in the context of predicting charge transport mechanisms in molecular wires. Additionally, variations of the BLYP35+PCM protocol toward a more realistic description of a molecular junction were evaluated in comparison to the simplified

approach of performing static DFT calculations. While the successful approach turns out to work very well, the excellent performance can be likely attributed to beneficial error compensation. Here, the modelling of the gold electrode contact and its impact on the predictive capabilities of the BLYP35+PCM approach, whether being beneficial or not, was investigated again on the example of OPTI_n wires. Finally, the BLYP35+PCM protocol was used for revealing intermediate transport regimes in guanine-based DNA, which was inspired by studies of Tao and coworkers [66,67], where predominantly incoherent hopping transport was suggested to be accompanied by partial coherent transport. In this study, not only the length-dependence of charge transport mechanisms but also the dependence on the molecular architecture such as the base sequence is illuminated.

6.2 New Charge Delocalization Measures Tailored for Molecular Wires

In the following, the procedure of assessing and quantifying the degree of charge delocalization is described in more detail. For this purpose, first a definition of charge delocalization in the context of molecular wires is provided for the derivation of a quantitative measure. Since there is no universal definition of charge delocalization by its nature, the quantitative measure is then applied to OPTI_n wires to identify essential prerequisites when using it as predictive tool for the derivation of transport mechanisms: As such, different cutoff values for the majority of the spin density are applied and the results are compared with each other in the light of their predictive capabilities.

Definition of Charge Delocalization

To investigate hole transport in the radical cationic molecular wires under study, different approaches of determining the degree of charge delocalization in a well-defined manner were evaluated. As the unpaired electron and the excess positive charge are located on the same position of the radical cationic systems studied here, and free unpaired spins are less basis-set dependent than local charges [144], the assessment of localization is based on the analysis of the local spin density. In previous studies on organic mixed-valence systems, the ratio between the local charges on the donor and acceptor moieties connected by a bridge served as a measure for the degree of charge localization, where complete charge delocalization would be expressed by a ratio of one, whereas a ratio of

zero would indicate a fully localized charge on one redox centre [54]. Since here, the redox centers are replaced by non-redox-active anchoring groups, the degree of charge delocalization r_{deloc} was defined by relating the majority of the spin density to the spatial extent of the smallest possible molecular subregion compared to the full molecular length it is located on, which is expressed by the following ratio

$$r_{\text{deloc}} = \frac{\text{spatial extent of subregion containing majority of spin density [\%]}}{\text{spin density (subregion) [\%]}}, \quad (6.1)$$

where the majority of the spin density represents a predefined percentage of spin density, *e.g.* 70%, but not 100% as this would in practice almost always need the full molecule to be captured.¹ In case of complete delocalization, the spin would be evenly distributed across the entire molecule, while with growing localization, the majority of the spin density would be located on an increasingly smaller fragment of the molecule. Therefore, a molecule would be described as fully delocalized in case of a ratio of one, where for example 70% of the spin density are spread across 70% of the molecule, and so on. In contrast, increasing localization results in a decrease of the ratio due to the subregion hosting the predefined percentage of the spin density becoming smaller. Ideally, a semi-localized molecular wire right on the borderline between localization and delocalization, where 100% of the spin density populates around one half of the molecule, would be characterized by a ratio of 0.5. One could therefore set this value as cut-off value for defining a system as predominantly localized or delocalized, depending on r_{deloc} being lower or greater than 0.5, respectively. Since one can hardly define a clear cut-off value for the prediction of the crossover from delocalization to localization that is consistently valid across a broad range of molecules, as shown in the following, a molecule was rather assigned to either of the regimes based on the similarities of r_{deloc} for consecutive wires. Accordingly, a relatively strong decrease of r_{deloc} from a shorter to a longer wire would indicate distinctly stronger localization in the latter species, particularly if the values for r_{deloc} at smaller and larger molecular lengths than these two wires would be relatively stable. In principle, one could set any value between 50 and 100 percent as the majority of the spin density, provided that it is not

¹The step-by-step procedure of determining the smallest possible subregion containing a predefined amount of spin density is described in detail in the Appendix (Sec. A.5.4).

too close to any boundary of this range. Therefore, several threshold values were tested to evaluate the effect on the calculated delocalization measure, and the predicted crossover lengths from different thresholds were compared with the experiments.

Evaluation of Charge Delocalization on the Example of OPTI_n Wires

In Fig. 6.1, the procedure of assessing the degree of delocalization is illustrated on the example of the shortest member (OPTI_4) of a series of conjugated oligophenylene–thiophene–imine (OPTI_n)² wires, investigated by Frisbie and coworkers [31]. The local spin density as obtained from NPA [148] is plotted per atom along the junction, where the subregions hosting the majority of the spin density are highlighted in different shades of yellow according to the indicated threshold.

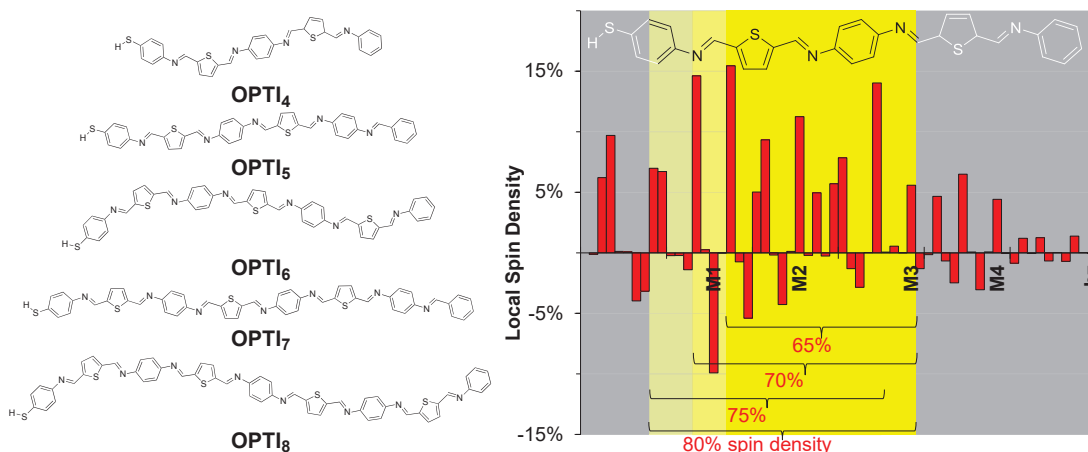


Figure 6.1: Assessment of Charge Localization in OPTI_n wires

Left: Chemical structures of OPTI_n wires, investigated by Frisbie and coworkers [31]. *Right:* Local spin density distribution from NPA per atom along the molecular backbone of OPTI_4 (total amount of local spin density = 1), optimized with the BLYP35 functional and Ahlrich’s def2-TZVP basis set in thiophene (PCM). The smallest possible subregions containing a predefined fraction of the local spin density (65-80%) used for the calculation of the delocalization measure r_{deloc} according to Eq. (6.1) are highlighted in different shades of yellow. Monomer units including the anchoring group according to Fig. 6.3 are indicated by M1-M4 (bz=benzaldimine terminus).

²Here, n denotes the number of monomer units present in the molecular wires according to Fig. 6.3, and Fig. 6.7, including the anchoring group(s).

In Fig. 6.2, the calculated delocalization measure r_{deloc} obtained from Eq. (6.1) for OPTI $_n$ wires is plotted as a function of the number of subunits for different fractions of the spin density, where the experimental crossover between tunneling and hopping from OPTI $_6$ to OPTI $_7$ is indicated by the black dotted line.

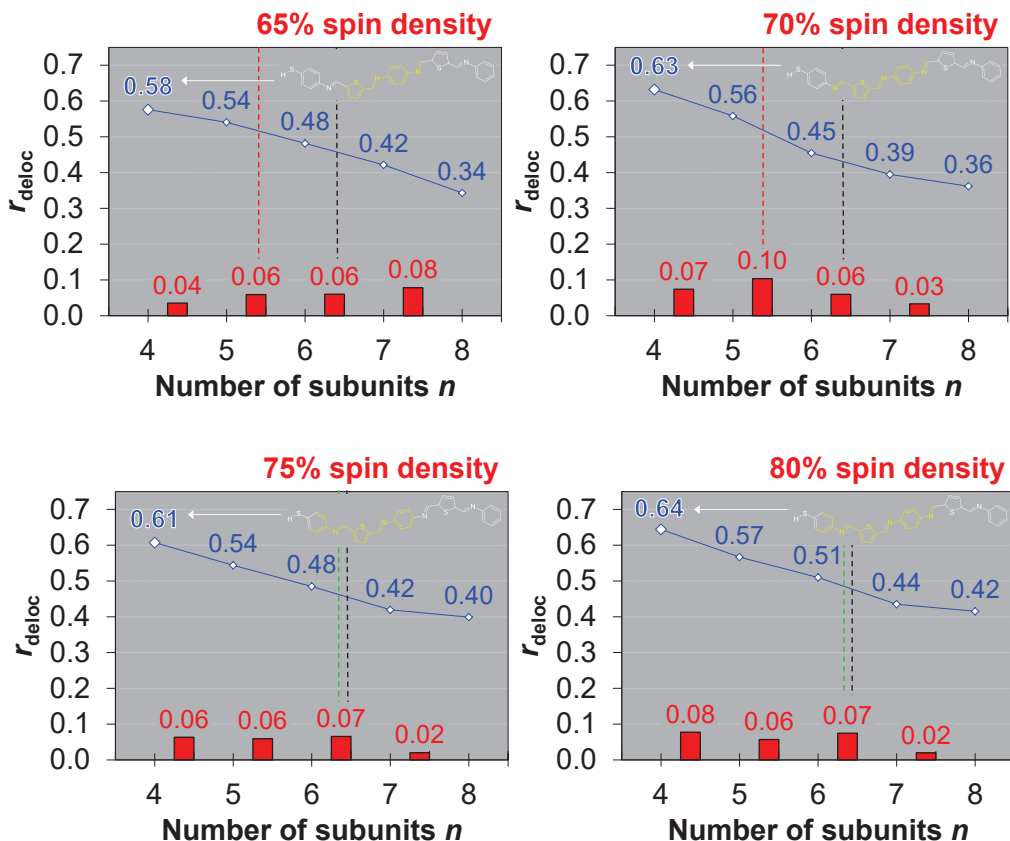


Figure 6.2: Screening of Spin Density Thresholds on OPTI $_n$ Wires Delocalization measure r_{deloc} of OPTI $_n$ wires calculated according to Eq. (6.1) as a function of the number of subunits n , see Fig. 6.3. Molecular structures were optimized with the BLYP35 functional and Ahlrich's def2-TZVP basis set in thiophene (PCM). The selection of each subregion based on different thresholds for the spin density is illustrated by the Lewis structure of OPTI $_4$. The delocalization measure is indicated by the blue line, the corresponding change in r_{deloc} from subunit n to $n+1$ is indicated by red bars. The experimental crossover from tunneling to hopping is marked by the black line. Coloured lines indicate the theoretically predicted crossover and its agreement with experiments (green: good; red: poor)

The crossover was predicted from the change in the delocalization measure r_{deloc} between subsequent wires, marked by red bars in Fig. 6.2. Therefore, molecu-

lar wires were considered in the same transport regime in case r_{deloc} decreased continuously by the same amount or less, while the crossover was determined from the greatest change of r_{deloc} relative to subsequent wires. The crossover predicted from theory is indicated by a second dotted line, coloured according to the agreement with experiments, see Fig. 6.2. As mentioned earlier, the crossover was expected to occur approximately around $r_{\text{deloc}} = 0.5$, which was used as secondary criteria in case the evaluation based on the change of r_{deloc} was not definite.

As can be seen from the plotted delocalization measure based on a threshold of 65% and 70% spin density, the crossover is predicted between OPTI₅ and OPTI₆ in each case and therefore one monomer unit earlier than from experiments. While in the former case, r_{deloc} decreases relatively constantly within a range of 0.04 to 0.08, a more distinct change in r_{deloc} by 0.1 at most is observed in case of a higher threshold of 70%.

In contrast, the crossover predicted from a 75% and 80% threshold for the spin density is in good agreement with experiments and the changes in r_{deloc} are qualitatively similar in both cases. Here, a relatively strong change in r_{deloc} of 0.07 marks the crossover between OPTI₆ and OPTI₇, while r_{deloc} only changes by 0.02 at longer lengths between OPTI₇ and OPTI₈, suggesting them being in the same transport regime.

While for the OPTI_{*n*} wires better agreement with the experiments was obtained in case of higher thresholds for the spin density, no clear trend of this being generally true for any kind of wires could be deduced. In three out of five cases, the same results were obtained for all of the tested thresholds, while differences regarding the predicted crossover were observed only in case of OPTI_{*n*} and OAE_{*n*} wires (see Appendix, Tab. A.8). For example, less agreement with the experiments was obtained for OAE_{*n*} wires when a threshold of 75% spin density was applied. However, best agreement was obtained consistently across all five tested series when a threshold of 80% spin density was applied, which therefore provides the basis for our analysis of the following results.

Beyond this method, a slightly different approach in determining the subregion was tested, where the wires are fragmented into uniformly sized monomer units that are stepwise included into the subregion until a minimum percentage of 65% spin density is reached (see Appendix, Fig. A.9 for results). This approach lead to nearly the same qualitative results as obtained from the analysis based

on a threshold of 80% spin density. However, for OPTI_n wires, the transition from delocalization to localization was indicated less clearly when based on a monomer-wise definition of the subregion. A comparative table of the performance of the different methods in predicting the tunneling–hopping crossover from experiments is provided in the Appendix (Tab. A.8).

In addition to the assessment of charge delocalization based on the calculated delocalization measure, the corresponding spin density distributions of the molecular wires under study were visualized. Ideally, the quantitative measure defined by Eq. (6.1) should reflect the intuitive classification based on a visual assessment of these spin densities, which will be checked in the following.

6.3 Predicting the Length-dependent Crossover: DFT Results

To validate the capability of the BLYP35+PCM protocol in correctly describing charge transport mechanisms, it was applied to the calculation of charge localization properties of conjugated wires that previously had been investigated in molecular conductance experiments by various groups [31–35].

First, the computational approach to predicting the length-dependent crossover from DFT is thoroughly discussed on the example of the thiophene-based OPTI_n wires, investigated by Frisbie and coworkers [31]. In this case, the protocol turns out to work perfectly. The findings are briefly compared to related molecular structures, the OPI_n and OAE_n wires, investigated by Frisbie and by Wandlowski and coworkers, respectively [33,34], for which the protocol also works well. Second, the computational results on molecular wires are presented where the degree of charge delocalization predicted from theory deviates to some extent from the experiments, the ONI_n and OPE_n wires, investigated again by Frisbie and coworkers and by the group of Wang, respectively [32, 35]. Finally, the results obtained from DFT calculations are discussed in the light of capabilities and possible limitations of the presented approach in a conclusive summary.

Computational Methodology

Neutral structures of the molecular wires were preoptimized by performing KS–DFT calculations using the resolution-of-identity (RI) approach, implemented in the TURBOMOLE 7.0 package [149]. In the molecular structure optimizations, the BP86 exchange–correlation functional [131,132], Ahlrich’s def2-TZVP basis set [150] of triple-zeta quality with polarization functions on all atoms,

and the D3 dispersion correction introduced by Grimme [151] were employed. The convergence criterion in the self-consistent field (SCF) algorithm was set to 10^{-7} hartree for the change of the energy in all calculations and to 10^{-4} a.u. for the gradient in molecular structure optimizations. Subsequent molecular structure optimizations on the neutral preoptimized structures were performed for the molecular wires in their radical cationic state by employing the GAUSSIAN 09 program package [152] with Ahlrich's def2-TZVP basis set and the hybrid BLYP35 functional with 35% exact exchange from the Kaupp group, which was constructed analogously to the B1LYP model [136]. Molecular structure optimizations were performed for both the isolated molecules and molecules in solution, since the importance of environmental effects on charge localization properties was pointed out by Kaupp and coworkers and was shown in our previous study on organic mixed-valence systems [53,54]. For the inclusion of solvent effects, the polarizable continuum model with the integral equation formalism model (IEFPCM) [153,154] was employed as implemented in the GAUSSIAN 09 program package by using the SCRF keyword with the available dielectric constants for thiophene ($\epsilon=2.7270$), benzene ($\epsilon=2.2706$) and tetrahydrofuran ($\epsilon_{\text{THF}}=7.4257$). Natural population analyses [148] were performed with the GAUSSIAN 09 program package to gain information about the distribution of local spins and charges, which were summed over specific subregions of the molecule. For the local spin density, an absolute value of 1 refers to one unpaired electron. Molecular structures and spin densities were visualized with the AVOGADRO editor [155], applying an isosurface value of 0.001 for plotting the spin density distributions.

OPTI_n Wires and Other Successful Cases – A Closer Look

OPTI_n Wires In CP-AFM experiments by Frisbie and coworkers at room temperature, a length-dependent transition from tunneling to hopping was observed in junctions based on SAMs of OPTI_n wires up to 6 nm in length (see Fig. 6.3), at a molecular length of approximately 4-5 nm (OPTI₆ to OPTI₇) [31]. The results from DFT calculations are consistent with the experimental crossover length: Distinctly higher localization is observed for the longer wires OPTI₇ and OPTI₈ when compared to the shorter wires. In Fig. 6.3, the local spin density per atom computed with the BLYP35 functional is depicted for each molecular wire next to the corresponding subregions of highest spin density, as defined in

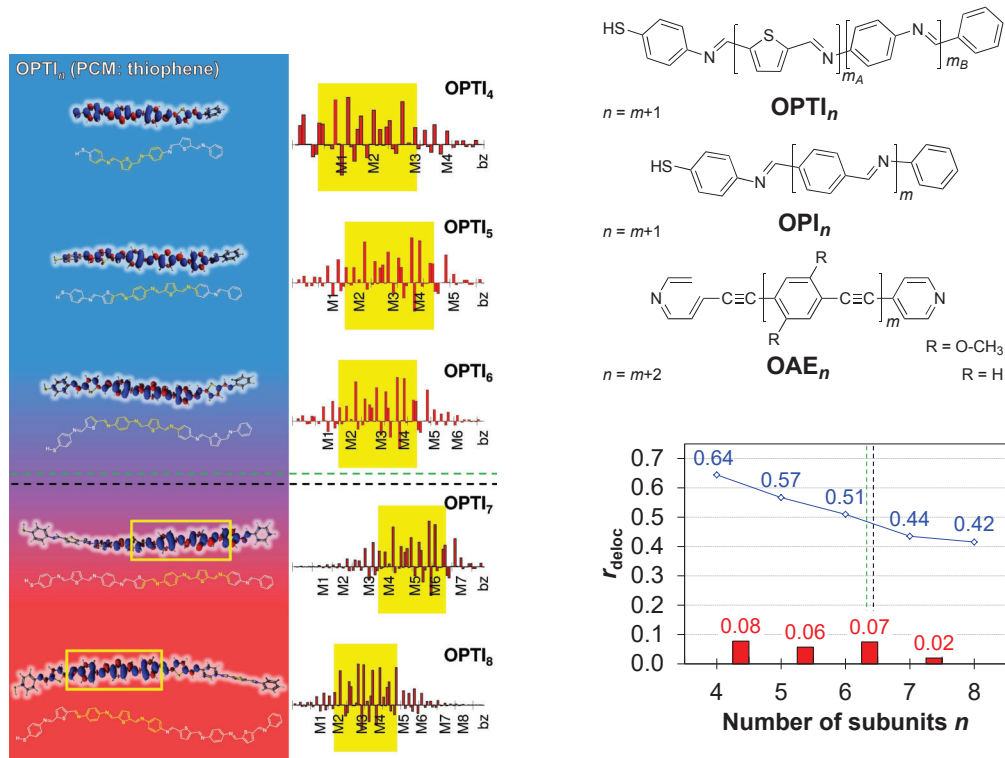


Figure 6.3: OPTI_n Wires – DFT Results *Left:* Radical cationic OPTI_n wires optimized with the BLYP35 functional and Ahlrich’s def2-TZVP basis set in thiophene (PCM). Spin densities and chemical structures of the molecular wires are shown with the local spin density per atom along the molecular backbone (total amount of local spin density = 1). Subregions hosting the majority of the spin density (80-85%) are highlighted in yellow. The degree of charge delocalization is coded by the background colour (charge delocalization: blue; increasing localization: red). *Top right:* Chemical structures of molecular wires, for which the BLYP35+PCM protocol works well. *Bottom right:* Calculated delocalization measure r_{deloc} as defined by Eq. (6.1) for molecular wires as a function of the number of subunits n (blue line) and the corresponding change in r_{deloc} from subunit n to $n+1$ (red bars). Black dotted line: Experimental crossover from tunneling to hopping. Green dotted line: Theoretically predicted crossover based on the calculated delocalization measure (percentage of spin density: 80-85%).

Sec. 6.2, marked in yellow. Since the experiments were carried out on SAMs in vacuum, the PCM for thiophene was employed during optimizations to model environmental effects arising from adjacent wires on charge localization. As can

be seen from Fig. 6.3, the spin density is rather delocalized for the first three members of the series, therefore suggesting OPTI₄ to OPTI₆ belonging to the tunneling regime. This assumption is confirmed by the calculated delocalization measure according to Eq. (6.1) ranging from 0.64 to 0.51 for OPTI₄ to OPTI₆. More importantly, a sudden drop of r_{deloc} down to 0.44 indicates a distinctly increasing degree of charge localization for OPTI₇, where most of the spin density is localized on a subunit comprising roughly three monomer units. The same delocalization length is observed for the longer OPTI₈, characterized by an even lower r_{deloc} of 0.42, although differently located three-ring registers are suggested to be involved in the transport for the two species.

The fact that the length-dependent transition from tunneling to hopping can be predicted based on charge localization properties from static DFT calculations, where environmental effects are entering the model but conformational sampling and dynamics are lacking, is quite remarkable since the number of structures with different spin localization patterns likely rises with growing molecular length due to an increasing number of possible conformations [31, 194, 195]. Hence, although other transport pathways may exist involving not only three- but also one- and two-ring registers, as pointed out by Frisbie *et al.* [31], the static picture considered in this approach is sufficient for reasonably describing the crossover length for these molecular wires and therefore has predictive character.

OPI_n and OAE_n Wires Since the BLYP35+PCM protocol worked well to predict the crossover length in case of the OPTI_n wires, it was applied to structurally related conjugated wires. A length-dependent crossover from tunneling to hopping was equally identified on SAMs of oligophenylene-imine (OPI_n) [33] wires up to 7 nm long at a molecular length of approximately 4 nm (OPI₅ to OPI₆) by the group of Frisbie [33]. Similarly, a crossover to hopping was observed for oligoaryleneethynylene (OAE_n) wires longer than 3 nm (OAE₅ to OAE₆) by Wandlowski and coworkers, where experiments were performed on single molecules in solution up to 6 nm long and functionalized on both termini with pyridyl-groups for the attachment to gold leads [34] (see Fig. 6.3 for chemical structures and Tab. 6.1 for comparisons of crossover lengths).

In Fig. 6.4, the calculated delocalization measure as defined by Eq. (6.1) is plotted for OPI_n and OAE_n wires as a function of molecular length. Since the experiments on OPI_n wires were performed on SAMs in vacuum, the PCM

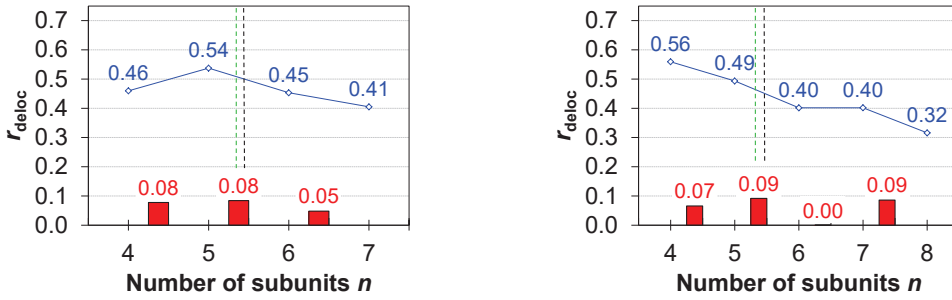


Figure 6.4: Charge Delocalization in OPI_n and OAE_n Wires Calculated delocalization measure r_{deloc} as defined by Eq. (6.1) for OPI_n (left) and OAE_n (right) radical cationic wires (see Fig. 6.3) as a function of the number of subunits n (blue line) and the corresponding change in r_{deloc} from subunit n to $n+1$ (red bars). Black dotted line: Experimental crossover from tunneling to hopping. Green dotted line: Theoretically predicted crossover based on the calculated delocalization measure (percentage of spin density: 80-85%).

for benzene was employed during optimizations to model effects of adjacent wires on charge localization, while the PCM for tetrahydrofuran was employed to model the solvent in case of OAE_n wires. The corresponding spin density distributions of OPI_n and OAE_n wires are shown in Fig. 6.5.

For OPI_n and OAE_n wires, the DFT calculations are in good agreement with the experimental crossover from tunneling to hopping. When comparing OPI_n wires of different lengths, a relatively strong decrease of r_{deloc} between OPI₅ and OPI₆ from 0.54 to 0.45 clearly indicates increasing charge localization. Interestingly, slightly stronger localization is predicted for the shorter OPI₄ when compared to OPI₅. For the longer OPI₇, r_{deloc} decreases much more slightly from 0.45 down to 0.41 when compared to OPI₆, suggesting the latter two species being in the same transport regime. The latter is also reflected in the spin density distributions (Fig. 6.5, left), where stronger charge localization is observed for the two longest species when compared to shorter ones.

For the OAE_n wires, a distinctly higher degree of charge delocalization is observed for the shorter species OAE₄ and OAE₅ when compared to longer ones. Here, increasing charge localization is indicated between OAE₅ and OAE₆ by the highest change in r_{deloc} from 0.49 to 0.40, being the same for the longer OAE₇. Again, the increased degree of charge localization manifests in the spin density distributions (Fig. 6.5, right), where the local spin is predominantly localized on two to three DMP units for the longest three wires.

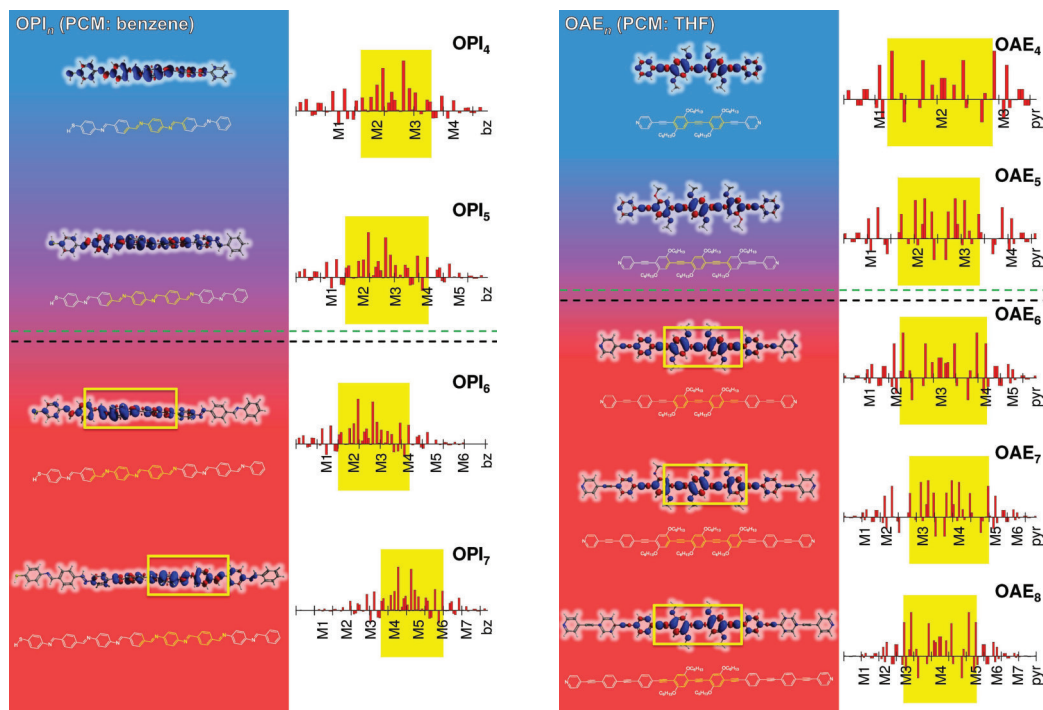


Figure 6.5: OPI_n and OAE_n Wires – DFT Results OPI_n (left) and OAE_n (right) radical cationic wires optimized with the BLYP35 functional and Ahlrich’s def2-TZVP basis set in benzene and THF (PCM). Spin densities and chemical structures of the molecular wires are shown with the local spin density per atom along the molecular backbone (total amount of local spin density = 1). Subregions hosting the majority of the spin density (80-85%) are highlighted in yellow. The degree of charge delocalization is coded by the background colour (charge delocalization: blue; increasing localization: red). Black dotted line: Experimental crossover from tunneling to hopping. Green dotted line: Theoretically predicted crossover based on the calculated delocalization measure (percentage of spin density: 80-85%).

Concluding these results, the BLYP35+PCM protocol is capable of predicting the length-dependent crossover from tunneling to hopping as observed in conductance experiments on the molecules under study. Moreover, in any case of these wires the crossover is predicted to occur around a value of 0.5 for the delocalization measure. Consequently, the degree of charge localization as deduced from the calculated delocalization measure serves as a valuable tool for evaluating the underlying transport mechanisms in these molecular wires.

OPE_n and ONI_n Wires – Borderline Cases

To put the DFT approach on more solid ground, it was applied to molecular wires similar in structure to the former species, the oligonaphthalene-fluorene-imine (ONI_n) and oligoparaphenylene-ethynylene (OPE_n) wires (see Fig. 6.6 and Fig. 6.7), investigated by the groups of Frisbie and Wang [32,33,35].

Interestingly, these molecular wires provide an example of situations where the calculated localization properties point less clearly to the experimental crossover lengths. Our DFT results for these species are therefore discussed in more detail in the light of possible limitations of the BLYP35+PCM protocol, with the aim of identifying situations where caution needs to be exercised in applying it for the prediction of transport regimes.

On SAMs of ONI_n wires up to 10 nm long and consisting of alternating fluorene and naphthalene units (see Fig. 6.6), the tunneling-to-hopping crossover was observed at a molecular length of around 4 nm in the experiments (ONI₃ to ONI₄) [32,33]. Increasing charge localization is indicated between ONI₃ and ONI₄ by a strongly decreasing r_{deloc} from 0.42 to 0.35, matching the experimental crossover (see Fig. 6.7). In contrast, values of r_{deloc} ranging from 0.39 to 0.42 for the first two members of the series indicate charge delocalization to a similar extent and therefore the same transport regime. The majority of the spin density is located on one fluorene subunit in any case for $n \geq 3$, which was also found previously in computational studies by the group of Frisbie [33]. Although the change in r_{deloc} is in line with the experimental crossover, an overall rather localized description of the ONI_n wires is provided by the calculations, as indicated by r_{deloc} never exceeding a value of 0.5 and as also illustrated by the spin densities in Fig. 6.6.

One probable cause for the ONI_n wires showing a rather high degree of charge localization may arise from the isolated-molecule description by the DFT calculations, which cannot capture the spatial confinement resulting from the monolayer present in the experiment. The conformation of the freely moving single wires considered in the calculations might differ from the relevant conformations in the experiment in such a way that the degree of charge localization is affected. For example, the electronic properties of conducting polymers strongly depend on their conformation, since torsion angles between adjacent rings determine the magnitude of the overlap between participating molecular orbitals, as pointed out by André and Brédas [196]. However, unless torsion angles between adja-

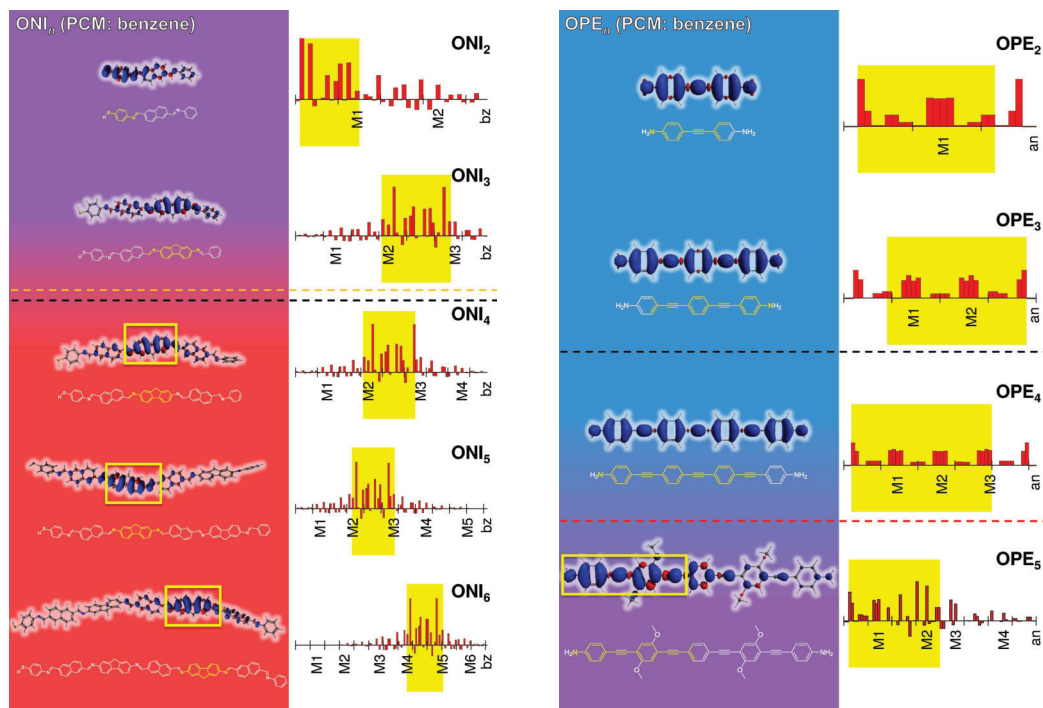


Figure 6.6: ONI_n and OPE_n Wires – DFT Results ONI_n (left) and OPE_n (right) radical cationic wires optimized with the BLYP35 functional and Ahlrich’s def2-TZVP basis set in benzene (PCM). Spin densities and chemical structures of the molecular wires are shown with the local spin density per atom along the molecular backbone (total amount of local spin density = 1). Subregions hosting the majority of the spin density (80-85%) are highlighted in yellow. The degree of charge delocalization is coded by the background colour (charge delocalization: blue; increasing localization: red). Black dotted line: Experimental crossover from tunneling to hopping. Red/ orange dotted line: Theoretically predicted crossover based on the calculated delocalization measure (percentage of spin density: 80-85%).

cent ring units do not exceed a value of 40 degrees, the electronic properties are not expected to be substantially different in comparison to the coplanar situation [196].

As can be seen from Fig. 6.6, the molecular structures of the optimized ONI_n molecules are considerably twisted. Still, torsional angles around the C–N bond between adjacent ring units of more than 40 degrees are exclusively present in the longer wires from ONI_3 to ONI_6 , whereas for the shorter ONI_2 species they do not exceed 35 degrees (see Appendix, Sec. A.4, Tab. A.6).

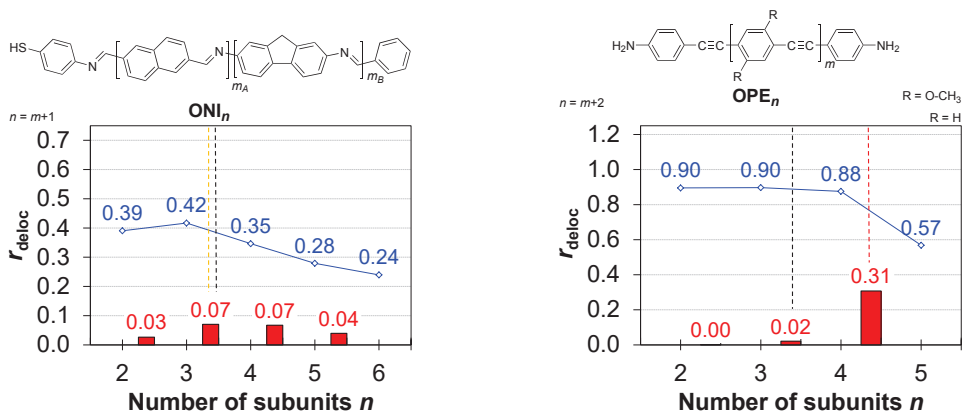


Figure 6.7: Charge Delocalization in ONI_n and OPE_n Wires Chemical structures and calculated delocalization measure r_{deloc} as defined by Eq. (6.1) for ONI_n (left) and OPE_n (right) wires as a function of the number of subunits n (blue line) and the corresponding change in r_{deloc} from subunit n to $n+1$ (red bars). Black dotted line: Experimental crossover from tunneling to hopping. Coloured dotted line: Theoretically predicted crossover based on the calculated delocalization measure (orange: fairly well, red: poor; percentage of spin density: 80-85%).

The twisting of the single-molecule structures in the calculations is likely not occurring to the same degree in the experiments, as their flexibility is limited by the presence of adjacent wires in SAMs, therefore possibly leading to a higher degree of planarization. Moreover, π -interactions between the relatively large fluorene and naphthalene building blocks of adjacent wires may lead to an overall more flattened structure in the latter scenario, resulting in more efficient charge and spin delocalization [196].

In order to reveal steric effects in a densely packed environment on the molecular structures, the structural optimization or MD simulation of dimers or trimers comprising a small number of wires may provide valuable insight into the mutual impact of molecular wires on their structure and therefore their localization properties. Still, despite a rather localized description possibly due to the lack of more detailed environmental modelling, the experimental crossover is correctly described for the ONI_n wires by the present DFT approach.

The charge transport characteristics of amine-terminated OPE_n wires up to 5 nm long were investigated at the single-molecule level using the STM-BJ technique (see Fig. 6.6) [35], where the crossover from tunneling to hopping was observed at a molecular length of around 3 nm (OPE₃ to OPE₄), see Tab. 6.1. For

the longer wires, DMP units were incorporated into the molecular backbone to increase the solubility without affecting the conductance properties.

For the first three species, OPE₂ to OPE₄, a relatively high degree of charge delocalization is indicated on the basis of the calculated r_{deloc} as it ranges from 0.90 to 0.88. A distinct increase of charge localization is observed with growing molecular length when going from OPE₄ to OPE₅, as r_{deloc} decreases from 0.96 to 0.56.

The increase of charge localization setting in for OPE₅ in the calculations is not fully in line with the experiments, where the crossover is observed already one monomer unit earlier for OPE₄. Consequently, a slightly overdelocalized description of the OPE_{*n*} wires is provided by the DFT calculations when compared to the experiment, which is also indicated by r_{deloc} of the longest member OPE₅ not falling below 0.5. For the latter species, the hopping site comprises roughly three ring units, hosting the majority of the spin density.

The rather delocalized description of the OPE_{*n*} wires compared to the experiments might be attributed to discrepancies between the bonding situation of the molecular wire to the electrode surface modeled in the calculations and in the experiments. For the first three members of the series, a shortening of the lengths of the C–N bond, connecting the molecular backbone to the amine linker unit, is observed from 1.37 Å to 1.34–1.35 Å on both termini when compared to the molecular structure optimized in the neutral state (see Tab. A.7 in Appendix).

In contrast, for the longer OPE₅ species, a shortening of the C–N bond length to 1.34 Å is observed only on one side of the molecule where the charge is predominantly localized. The bond length shortening indicated by the calculations might be caused by π -backbonding of the free electron pair of the nitrogen atom to the adjacent carbon atom, leading to stronger planarization and therefore facilitating charge delocalization.

However, a different situation may prevail in the actual experiments [64]: One can assume that the free electron pair is less strongly donated to the molecular backbone than suggested from the calculations, but is rather binding to the gold electrode surface by the formation of a donor-acceptor bond [197]. Still, as pointed out by Venkataraman and coworkers, this bond is weakened due to partial delocalization of the lone pair into the molecular π -system when the amine group is connected to an aromatic system, such as in case of OPE_{*n*} [197].

In the calculations, however, not only partial but full delocalization into the molecule can be assumed due to the lack of the electrode contact. Thus, while strongly twisted conformations are likely not accessible at room temperature for isolated OPE_n wires (see Appendix, discussion and Fig. A.10 in Sec. A.6), in the conductance experiment, torsions leading to charge localization are likely more easily accessible (as found in experimental and computational studies [198,199]) and could lead to stronger charge localization than is indicated from calculations in this work.

In the case of amines, the molecule-electrode bond is relatively weak when compared to previously discussed molecular wires with different anchoring groups, such as thiols and pyridines, therefore leading to weaker coupling to the gold electrode. As pointed out by van der Zant and coworkers [200], the formation of so-called image charges is particularly apparent in these weakly coupled molecules, where charges residing on the molecular backbone are screened by the electrodes, consequently leading to long-range polarization effects (see Sec. 1.2) [95].

Accordingly, in a theoretical study of Thygesen and Mavrikakis it was found that the dipole moment at the interface of junctions with a diamine anchoring group is larger than for a dithiol group [201]. As these interface effects, caused by different anchoring groups in the experiments, are not covered in the calculations, the degree of charge localization present in the experiments might be underestimated in the DFT simulations. Interestingly, as discussed earlier in this section, the DFT results are in good agreement with the experiments in case of the structurally similar OAE_n wires, where the anchoring units are represented by pyridyl linkers instead of amines. In both cases, the crossover is indicated around the same length of 3 nm by the DFT calculations, irrespective of the anchoring unit, suggesting that effects on charge localization resulting from the anchoring groups are neglected in the single-molecule calculations.

6.4 Getting Charge Localization Right – Essential Ingredients

As the BLYP35+PCM protocol proved valuable for predicting transport mechanisms in molecular wires, one may ask the question which parameters are crucial for obtaining results in agreement with the experiment. On the one hand, the amount of exact exchange and the dielectric constant entering *via* the PCM, both promoting charge localization, need to be in appropriate balance as was shown by our studies [54,193] and by Kaupp and coworkers [50–52]. However, one might equally opt for structure optimizations on isolated molecules, thus neglecting environmental effects, and increase the amount of exact exchange at the same time for achieving the same qualitative result. This was shown in studies by Mangaud and coworkers, where the ω -B97X-D functional worked well for predicting the transition from class III to class II on isolated DMP_n molecules (see Tab. 2.1) [121], which was also confirmed by calculations in this work (see Fig. 3.2 in Sec. 3.3). LC-DFT methods were therefore evaluated on the example of OPTI_n wires as an alternative approach toward the description of charge localization in molecular wires. In contrast, a tendency toward overlocalization was indicated by studies on mixed-valence systems using the long-range corrected M06-HF functional, belonging to the Minnesota class functionals [121], see Tab. 2.1. Interestingly, the same method was found to perform well for OPTI_n in a computational study by Frisbie and coworkers [31].

To investigate whether LC-DFT is a valuable alternative to the BLYP35+PCM protocol for predicting transport mechanisms, both methods were used for structure optimizations of isolated OPTI_n molecules. An additional PCM was not applied, as it was found from studies on DMP_n that overlocalization results when a PCM is combined with LC-DFT, which has the tendency of being overlocalizing by nature (see Sec. 3.3). On the other hand, the success of the BLYP35+PCM protocol is likely based on error compensation, where certain corrections to the model need to be included with caution, as pointed out by Elstner and coworkers [48,49]. Hence, modifying various parameters in the description at the same time may either change the predictive capabilities of the approach or leave them unaffected, when the parameters compensate each other. Besides environmental effects, the gold surface may influence the degree of charge localization, *e.g.* by the induction of image charges [95] or the formation of dipole layers in case of SAMs [97,98,202–210]. To investigate whether and how the modelling of the electrode impacts the predictions of charge transport

mechanisms, an approximate description was realized by linking the molecular wires to small gold clusters. However, these investigations are only first steps toward a proper description of the electrode–molecule interface. For example, image charge effects are not captured by standard DFT, but better described by calculations within the *GW* approximation, as shown by Thygesen and coworkers [95,97].

Computational Methodology

Modelling of the Gold Electrode The same computational methodology as described earlier in this section applies to the results presented in the following. For the inclusion of solvent effects, the polarizable continuum model with the integral equation formalism model (IEFPCM) [153,154] was employed as implemented in the GAUSSIAN 09 program package by using the SCRF keyword with the available dielectric constants for thiophene ($\epsilon = 2.7270$). The terminal gold electrode was modelled by either one or three gold atoms, which were kept fixed during molecular structure optimizations. For the local spin density, an absolute value of 1 refers to one unpaired electron. Molecular structures and spin densities were visualized with the AVOGADRO editor [155], applying an isosurface value of 0.001 for plotting the spin density distributions.

LC-DFT Calculations Neutral structures of the molecular wires were preoptimized by performing KS–DFT calculations using the resolution-of-identity (RI) approach, implemented in the TURBOMOLE 7.0 package [149]. In the molecular structure optimizations, the BP86 exchange–correlation functional [131,132], Ahlrich’s def2-TZVP basis set [150] of triple-zeta quality with polarization functions on all atoms, and the D3 dispersion correction introduced by Grimme [151] were employed. The convergence criterion in the self-consistent field (SCF) algorithm was set to 10^{-7} hartree for the change of the energy in all calculations and to 10^{-4} a.u. for the gradient in molecular structure optimizations. Subsequent molecular structure optimizations on the neutral preoptimized structures were performed for the isolated molecular wires in their radical cationic state by employing the GAUSSIAN 09 program package [152] with Ahlrich’s def2-TZVP basis set and the M06-HF global hybrid meta-GGA functional with full exact exchange [141]. Molecular structures and spin densities (isosurface value: 0.001) were visualized with the AVOGADRO editor [155].

OPTI_n Wires – Modeling of the Gold Electrode

In Fig. 6.8, the spin densities of the optimized OPTI_n wires are shown, where one or three gold atoms were attached to the terminal sulfur atom to approximate the gold electrode. DFT results are shown for optimizations of isolated molecular structures and with PCM for thiophene to model intermolecular interactions.

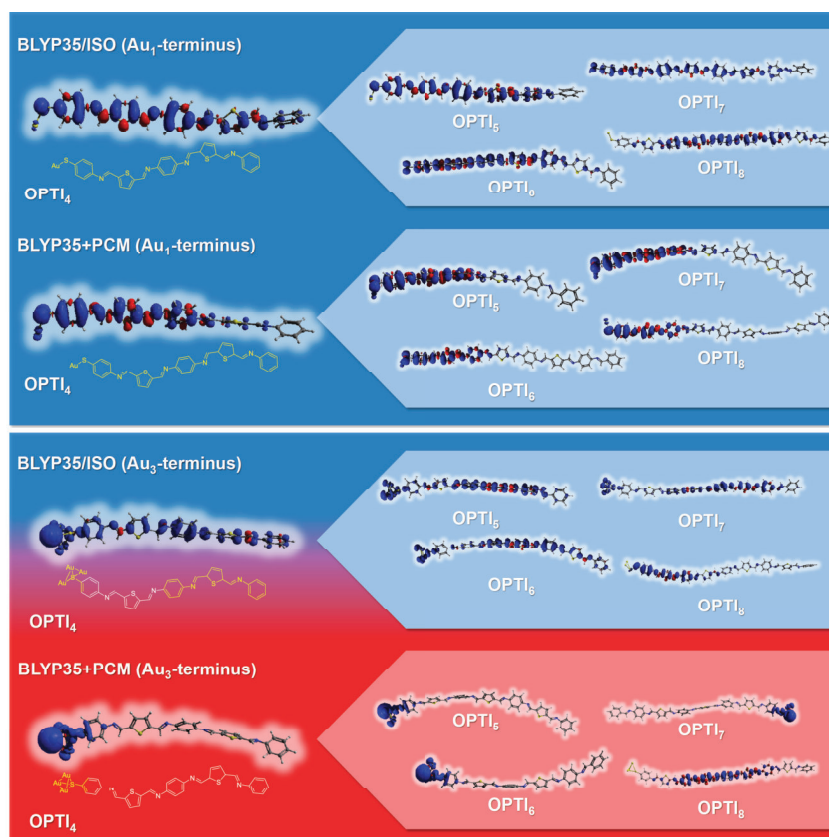


Figure 6.8: Modeling of the Gold Electrode – DFT Results Spin density isosurfaces of gold-terminated OPTI_n radical cations from molecular structure optimizations with the BLYP35 functional and Ahlrich’s def2-TZVP basis set in their isolated state (ISO) and in thiophene (PCM). Molecular structure optimizations were performed with an Au₁- (top) and an Au₃-cluster (bottom). The degree of charge delocalization is coded by the background colour (charge delocalization: blue; increasing localization: red).

The effect of the gold terminus on charge localization depends strongly on the environment considered in the calculation. Whereas on isolated Au₁-terminated wires the shorter members up to OPTI₇ have a rather delocalized charge, for the longer OPTI₈ the charge starts localizing onto a subregion of approximately five rings, which is not quite in agreement with the experiments since

the tunneling–hopping crossover is observed between OPTI_6 and OPTI_7 (see Fig. 6.8, top). However, the charge has an even higher degree of delocalization in OPTI_7 than in OPTI_6 , as it populates a span of seven and five ring units, respectively, which is chemically counterintuitive. For the same wires optimized in the presence of the PCM for thiophene, an extremely overlocalized description is provided, where the charge is localized onto a subregion spanning roughly three ring units irrespective of the molecular length. Therefore, in none of the cases the experimental crossover is predicted correctly as the degree of charge localization is either over- or underestimated. Moreover, the trend of increasing charge localization as a function of molecular length cannot be modeled in any case. Overall it can be stated that one gold atom alone has indeed a localizing effect, as a higher degree of charge localization is obtained for single-contacted wires compared to the same wires without gold linker (see Appendix, Fig. A.12). However, an overlocalized description is obtained when combining the modelling of both the environment and the gold electrode at the same time, as each of these parameters has a rather localizing effect that somehow adds up. The latter approach may therefore not be well-suited for providing a chemically correct picture of localizing effects induced by the metal electrodes attached to the molecular wires.

The same conclusion can be drawn from results where the same range of OPTI_n wires was optimized with an electrode contact consisting of three gold atoms (see Fig. 6.8, bottom). Overall, in any case overlocalization of charge is observed irrespective of whether a PCM is applied or not, although the degree of localization is highest in case of environmental modelling. Hence, from OPTI_4 to OPTI_7 , the spin density is nearly completely confined to the gold cluster, with none of the spin density left on the molecular bridge. Although on the isolated molecules there is some spin density localized on the molecular bridge, a high proportion is also localized on the metal cluster, leading to an overlocalized description. Interestingly, a considerable amount of spin density is always located on the electrode, except for OPTI_8 . Here, the spin is localized on either a middle subregion on the molecular backbone spanning five ring units (Au_3 -terminated with PCM; Au_1 -terminated, isolated) or the first three ring units (Au_1 -terminated with PCM; Au_3 -terminated, isolated), with nearly none of the spin density on the gold cluster. One possible explanation for this finding may be that the localization of the charge or spin and the associated relaxation

of the molecular structure becomes increasingly probable with growing bridge length and outweighs the tendency of having more charge attached to the metal cluster. However, although a reasonable description of charge localization may be provided for the longest member OPTI₈, in none of the cases the degree of charge localization is in line with the transport mechanism suggested from experiments, as mostly an overlocalized description is provided, especially when a solvent model is included. On the other hand, one single gold atom attached on isolated wires is equally not a sufficient description, as it results in overdelocalization for the shorter wires.

Based on these results one may conclude that aiming at a more realistic description of the molecular junction by including two parameters, *i.e.* the environment and the electrode contact at the same time an erroneous description is obtained: While the inclusion of environmental modelling is found to be highly important for the correct description of charge localization properties, the simulation of the electrode by attaching one or three gold atoms to the molecular termini impairs the predictive potential of the method. Simulating the environment and the gold substrate at the same time leads to extensive overlocalization, as shown on the example of OPTI_{*n*} wires. Consequently, a more realistic description closer to the experiment, such as the electrode contact and environment, does not necessarily provide a better prediction of the crossover length, as previously pointed out by the groups of Elstner and Kleinekathöfer [48, 49]. In particular the accurate first-principles description of molecule–metal interfaces in general is not trivial due to the formation of dipole layers in this region, which is particularly important in case of SAMs [97, 98, 202–210].

OPTI_{*n*} Wires – Increasing the Amount of Exact Exchange by LC-DFT

In Fig. 6.9, the spin densities of isolated OPTI_{*n*} wires, optimized with M06-HF are illustrated. The spin densities resulting from similar calculations with the ω -B97X-D functional are shown in the Appendix (Fig. A.13).

Either from molecular structure optimizations with the ω -B97X-D or the M06-HF functional, a stronger degree of charge localization is predicted than what would be expected from the experiments, as only for the shortest species OPTI₄ the charge is delocalized. For species that are assigned to the tunneling regime from the experiments, *i.e.* OPTI₅ and OPTI₆, distinct charge localization on a region of around three monomer units is indicated, which is not in agreement

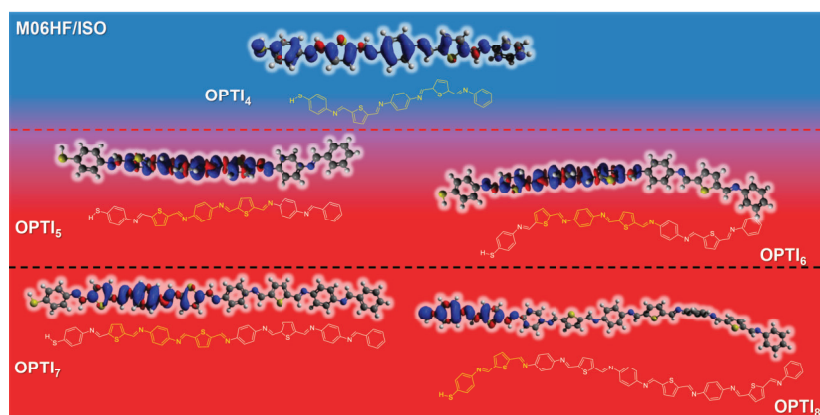


Figure 6.9: Spin density isosurfaces of isolated OPTI_n radical cations from molecular structure optimizations with the M06-HF functional and Ahlrich's def2-TZVP basis set. The degree of charge delocalization is coded by the background colour (charge delocalization: blue; increasing localization: red). Black dotted line: Experimental crossover from tunneling to hopping. Red dotted line: Theoretically predicted crossover based on the visual assessment of charge localization.

with the experiments. The finding of a relatively high degree of charge localization already for the shortest wires is quite remarkable and appears chemically unreasonable considering the fact that calculations were performed on isolated wires. As an even higher degree of charge localization is expected in a more polarized environment, further molecular structure optimizations with additional PCM were not pursued. In fact, as was shown on the example of DMP_n , when adding a PCM in molecular structure optimizations with the ω -B97X-D functional, an overlocalized description is obtained (see Sec. 3.3).

Altogether, as discussed in the context of organic mixed-valence radical cations, it seems that LC-DFT methods may provide the correct answer in some specific cases regarding charge localization properties, such as shown on the example of DMP_n radical cations, but probably for the wrong reasons. Moreover, they work not universally well when applied to molecular wires. The latter finding may be attributed to the tendency of LC-DFT being overlocalizing due to the high amount of exact exchange and leads to the conclusion that it is not suited well for the prediction of transport mechanisms based on charge localization.

6.5 Intermediate Transport Regimes in G-DNA: DFT Results

The understanding of charge transport mechanisms in DNA molecules is interesting not only due to the biological relevance of these systems [20,23,100], but also because they have been investigated as components for molecular electronic circuits [99]. For example, Porath and coworkers reported on reproducible charge transport in G4-DNA molecules, which were investigated in AFM experiments (see Sec. 1.3) [102]. Based on their transport measurements combined with theoretical modeling, it was suggested that charge transfer occurs *via* a thermally activated long-range hopping mechanism. Generally, the charge transport in DNA is mainly characterized by coherent tunneling at short-range, whereas the long-range transport can be described within the incoherent hopping regime, similar to the situation for other molecular wires under study here [31,66,67]. Beyond that, Tao and coworkers showed evidence of an intermediate transport regime, in which coherent and incoherent processes coexist (see Sec. 1.3) [66,67]. In their studies, charge transport measurements using a STM-BJ technique were performed on two different sets of self-complementary ds-DNA, one with stacked G–C base pairs and another one with alternating G–C base pairs (Fig. 1.8). From the experiments, it was found that the resistance increases linearly with length in both cases, indicating a hopping transport mechanism. However, for the stacked G sequences a noticeable oscillation of the resistance was found to be superimposed on the linearly increasing curve, which could not be described within the hopping transport model and rather indicates partially coherent transport [66,67]. Based on the results of semi-empirical calculations, the partial coherence in the stacked G-DNA was attributed to the strong coupling between the π -electrons of neighboring base pairs, causing delocalization of the charge over several base pairs. Thus, in contrast to the alternating G-sequences, where each G base acts as a hopping site, it was found that in stacked G-sequences each hopping site is extended across two to three base pairs, which was illustrated by the delocalization of the corresponding HOMOs [66,67]. This delocalization domain was previously found on similar systems comprising stacked A bases [22] and stacked GAG bases [21,66].

As the BLYP35 functional was successfully applied to the prediction of charge localization properties in organic mixed-valence systems, this method was adopted for describing the degree of charge localization in stacked and alternating G-DNA sequences. It needed to be evaluated whether the given DFT protocol is

capable of reproducing the partial delocalization of the charge in the stacked G-DNA sequences in agreement with the interpretation of the experimental results of Tao and coworkers [66,67]. In contrast, stronger localization of the charge would be expected for the alternating G-DNA sequences according to the experiments. Here, single point energy calculations were performed rather than optimizations of the molecular structures owing to the large size of the system. Since the STM measurements were performed in aqueous ds-DNA solution, calculations with the BLYP35 functional were complemented with a PCM for water.

Computational Methodology

Single point energy calculations were performed on stacked and alternating G-DNA sequences comprising a number of eight base pairs in their radical cationic state. The respective DNA sequences were set at the conformation of canonical B-DNA, where the backbone was removed and only the base pairs were considered. The calculations were performed on DNA sequences in solution by using the PCM for water ($\epsilon = 78.3553$), as well as on isolated DNA molecules. In each case, the GAUSSIAN 09 program package [152] was employed with Ahlrich's def2-SVP basis set [150]. Here, a smaller basis set was used than in previous calculations on molecular wires due to the large size of the G-DNA molecules. Moreover, the hybrid BLYP35 functional with 35% exact exchange was used, which was constructed analogously to the B1LYP model [136]. The spin density isosurfaces of the respective DNA molecules were visualized in order to gain further information about the localization of the spin.

DFT Calculations: G-DNA Sequences

The calculated spin density isosurfaces for alternating and stacked G-DNA sequences in their isolated state and in aqueous environment are shown in Fig. 6.10. As becomes apparent from the distribution of the spin density in isolated alternating G-DNA strands, the charge is localized onto single G bases, whereas no charge is located on the C bases. Since the G base features the lowest ionization potential of the four DNA bases (A, T, G and C), the preferential localization of the charge on the G bases rather than on C bases is reasonable [211]. The situation is similar in the case of the stacked G-DNA sequences, where the charge also exclusively resides on G bases.

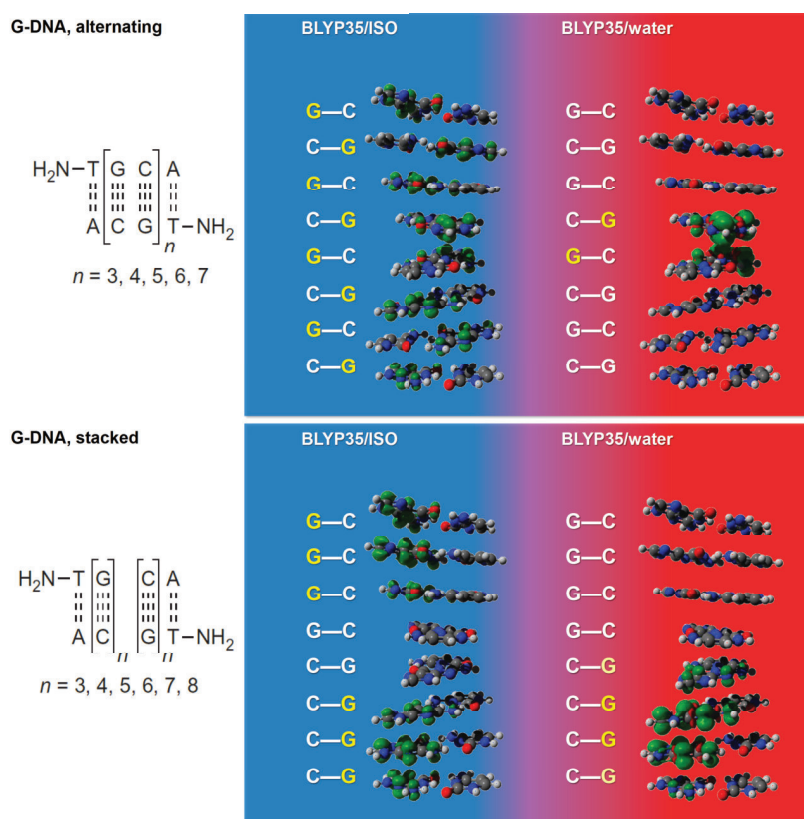


Figure 6.10: Charge Localization in G-DNA – DFT Results Spin density isosurfaces and corresponding chemical structures of G-DNA radical cations with alternating (top) or stacked (bottom) G-base pairs, optimized with the BLYP35 functional and Ahlrich’s def2-TZVP basis set in their isolated state (ISO) and in water (PCM; isosurface value: 0.001).

However, a clearly different distribution of the charge is indicated when compared to the alternating G-DNA, as there is no spin density located on the inner two base pairs but rather on the outer three G bases of the pairs on each side of the DNA molecule. Thus, the charge can be regarded as being localized on subregions comprising three G bases on each terminus of the molecule. However, within these subregions, the charge remains delocalized.

Significant changes can be observed in comparison to the isolated molecules considered combined with a PCM for water: Distinct charge localization occurs for the alternating G-DNA sequence, with the charge being fully concentrated on the inner two G bases, whereas no charge is located on the remaining bases. In the stacked G-DNA sequence, also clear localization of the charge is indicated, but other subregions of the DNA molecule are involved. Thus, similar to the case of the respective isolated G-DNA sequence, the charge is localized

on a subregion comprising roughly two G bases. However, a small amount of the spin density is located on the adjacent G bases on the outer sides of this subregion, but to a much smaller extent than on the inner two base pairs. More importantly, there is no charge attributed to the other terminus of the system, as this was the case for the corresponding isolated G-DNA sequence.

Based on these results, it can be stated that clear localization of the charge occurs upon the inclusion of solvent effects in the calculations. As was shown on isolated molecules, the charge is equally distributed across single G bases in the alternating G-DNA sequence, whereas localization of the charge onto definite subregions comprising several G bases already takes place in the stacked G-DNA sequence. However, these subregions are not preferentially located on a particular side of the DNA molecule but are rather symmetrically separated. It seems that when considering an aqueous environment, the charge is stabilized on a single side.

The delocalization of the charge across a subregion of roughly two G bases in stacked G-DNA is in agreement with the results of Tao and coworkers, as the involvement of partial coherence in the hopping transport mechanism was indicated in the experiments, where a hopping site comprises two to three base pairs [66,67]. In contrast, for the alternating G-DNA sequence the charge is symmetrically located on two adjacent G bases in the middle of the molecule, which conflicts with the observation of Tao and coworkers that a single G base acts as a hopping site [66,67]. However, it can be assumed that the indicated delocalization across two base pairs is rather a result of the chosen method and the initial guess molecular orbitals, since no molecular structure optimizations were performed, but only single point energy calculations on the frozen B-DNA geometry.

Since it was shown on the example of the organic mixed-valence systems, *e.g.* the DMP_n molecules, that the localization of the charge is presumably accompanied by changes within the molecular structure, it may be the case that there is no preferential side for the charge to be localized, as both sides are structurally identical. Hence, it is probable that the charge will be localized on a single G base when the relaxation of the molecular structure is allowed in the calculation. Since no molecular structure optimizations of the G-DNA sequences were performed in this study owing to time constraints, this aspect will be a subject of further studies.

To sum up, promising results are obtained by applying the BLYP35 functional in combination with a PCM to predicting charge transport mechanisms in G-DNA sequences. Distinct charge localization can be observed by incorporating solvent effects in both cases, indicating the formation of particular subregions, *i.e.* hopping sites, on which the charge is delocalized. The differences regarding the extent and location of these subregions between both types of G-DNA are clearly indicated by this method, predicting a hopping site comprising two to three G base pairs in stacked G-DNA, which is in line with the experimental and computational results of Tao and coworkers [66,67].

From the experiments, each guanine base can be considered a hopping site in alternating G-DNA, which is not predicted by the BLYP35+PCM method. As pointed out earlier, this may be attributed to the restricted flexibility of the molecular geometry in our calculations, which does not allow for structural relaxation due to localization of the charge. Moreover, it has to be noted that protic solvents, such as water, may not be appropriately described by continuum solvent models. For example, hydrogen bonding is not taken into account in the PCM, but may affect the stabilization of the charge, as was shown on the example of organic mixed-valence compounds by Renz and coworkers [50,51]. In case of protic solvents, more sophisticated solvent models such as the direct conductor-like screening model for real solvents (D-COSMO-RS) may be a better suited choice [50,51]. However, the fact that the relaxation of the molecular geometry as a consequence of charge localization is not taken into account in the present model is much more likely the decisive factor in correctly describing the charge transport characteristics in these systems. For example, the structural deformation due to charge localization was already shown and exploited as its indicator in the context of organic mixed-valence systems (see Sec. 3.1) and is also known in molecular wires as polaron formation [31].

To overcome these limits and make molecular structure optimizations of such large systems feasible, more efficient computational methods such as semi-empirical techniques may be a potential alternative to the present DFT protocol. Still, it needs to be carefully investigated whether more efficient methods are capable of describing charge localization properties just as well as the BLYP35+PCM. First steps toward the evaluation of semi-empirical methods in predicting charge transport mechanisms in molecular wires are presented in Sec. 7.1.

6.6 Conclusions

In this study, a DFT protocol suggested by Renz and Kaupp and previously validated in this work based on the BLYP35 hybrid functional was used with a continuum solvent model to calculate the charge localization properties of molecular wires. Based on these properties, the aim was to predict the length-dependent crossover from tunneling to hopping obtained from molecular conductance experiments [31–33,35]. In Tab. 6.1, the results of the DFT calculations regarding the crossover from tunneling to hopping are compared to the experiments for five different series of molecular wires investigated in this study. The theoretical crossover was derived from the change in the delocalization measure r_{deloc} of consecutive wires with growing bridge length, which describes the degree of charge delocalization as defined in Sec. 6.2 by Eq. (6.1).

As primary criterion, the largest relative change, *i.e.* a sudden drop in r_{deloc} for consecutive molecular wires was taken as an indicator for increasing charge localization, meaning a crossover from tunneling to hopping. As secondary criterion, a value of $r_{\text{deloc}} = 0.5$ was used as guideline for identifying the crossover length, as the crossover likely occurs in this transition zone from delocalization to localization. Depending on the experimental conditions, the optimization of the molecular structures was performed with linker units either attached to one terminus (SAMs) or to both termini (single-molecule experiments).

The computational results suggest that the BLYP35+PCM protocol works well not only in describing the general trend of increasing charge localization with growing bridge length, but also correctly predicts the crossover length in most cases. For all wires except for OPE_n , good agreement between theory and experiment was found regarding the transition length when the protocol is used for calculations on single molecular wires³.

When applying the DFT protocol with PCM to ONI_n and OPE_n wires, a slightly overlocalized or overdelocalized description is obtained, respectively. Still, for ONI_n , the crossover between tunneling and hopping is predicted correctly based on a sudden drop in the delocalization measure, whereas for OPE_n the crossover is delayed by one monomer unit in the calculations compared to the experiment.

³As was shown in the context of describing charge localization in mixed-valence systems, the inclusion of a PCM is a prerequisite for the good performance of the BLYP35 functional, since calculations on isolated wires without environmental modeling resulted in an overdelocalized description compared to results from calculations with PCM.

Table 6.1: Predicting Transport Mechanisms – Summary Table Comparison of tunneling–hopping crossover from molecular conductance experiments at room temperature and from DFT calculations with the BLYP35 hybrid functional and Ahlrich’s def2-TZVP basis set for various systems. The theoretical crossover is derived from the major change in r_{deloc} , calculated according to Eq. (6.1) (Sec. 6.2) and indicating increasing charge localization (percentage of spin density: 80-85%). Molecular structures are optimized with a PCM as specified.

experiment		theory				
conditions	linker	monomer	crossover	crossover	PCM	
			n	n		
OPTI _n	SAMs, vac.	SH	thio-phe	6 → 7	6 → 7	thiophene
OPI _n	SAMs, vac.	SH	phe	5 → 6	5 → 6	benzene
ONI _n	SAMs, vac.	SH	fluo-naphtha	3 → 4	3 → 4	benzene
OAE _n	single mol., sol.	PYR	phe-DMP	5 → 6	5 → 6	THF
OPE _n	single mol., vac.	NH ₂	phe-DMP	3 → 4	4 → 5	benzene

thio: thiophene; phe: phenylene; fluo: fluorene

The approximate DFT protocol used in this study therefore works well in predicting the experimental crossover in most cases, but must be used carefully where effects arising from the electrode–molecule interface are likely having an influence on charge localization, since some aspects are neglected: First, the calculations lack the description of the gold electrode. In case of amine anchoring groups such as in OPE_n, π -backbonding of the free electron pair from the nitrogen atom to the molecular backbone rather than binding to the electrode may lead to a more planarized molecular structure in the calculations, suggesting stronger charge delocalization compared to the experiments.

Second, amine linkers might induce the formation of larger dipole moments at the molecule–electrode interface when compared to thiols due to weaker coupling to the substrate, as pointed out by Thygesen and Mavrikakis [201]. The formation of image charges might therefore be facilitated, leading to long-range polarization effects that are not covered in the calculations.

The neglect of interface effects possibly results in the underestimation of charge

localization in the calculations compared to the experiments. For example, for both wires, OPE_n and OAE_n , which share a similar molecular backbone but are terminated by different anchoring groups, the DFT protocol predicts the crossover at the same molecular length of around 3 nm in contrast to the different lengths found in the experiment. It therefore can be presumed that the effect of the anchoring group on charge localization in the experiments is not fully covered by the DFT protocol.

As mentioned earlier, in the DFT protocol the concept of error compensation may be exploited, based on the idea that the lack of conformational sampling (*e.g.* by MD simulations), of nonequilibrium effects and of the interface description are likely partially compensated by the approximate DFT protocol. Since the first two factors are dependent on the molecular length and on the experimental setup, *i.e.* experiments on SAMs or single molecules, it can be assumed that the BLYP35+PCM protocol does not perform consistently well across a broad range of molecular wires of different length and under different experimental conditions.

It has to be noted that the incorporation of a particular correction to a model might not necessarily lead to a more reasonable description. On the example of OPTI_n wires terminated by small gold clusters, it was shown that the approximate inclusion of both effects, the gold electrode and the environment *via* PCM, at the same time results in a completely overlocalized description in the calculations and therefore dramatically impairs its performance. Therefore, caution needs to be exercised when choosing the parameters that are entering in the calculations, as also pointed out by Elstner and Kleinekathöfer [48, 49]. To sum up, although the transition length is not predicted perfectly in case of OPE_n , the DFT protocol still describes not only the increasing trend of charge localization as a function of length qualitatively well, but also correctly predicts the crossover from tunneling to hopping with an error of at most one monomer unit, possibly through error compensation.

The approach presented in this study is easily applicable to a variety of conjugated organic molecular wires and has predictive character as it is based on first-principles approaches, at least when applied to molecules studied at room temperature. Since the transport mechanism is not only dependent on the length but also on the temperature [1], the approach may be limited to experiments performed in this temperature range.

The validated protocol may prove useful not only to gain insight into the charge transport characteristics of a particular molecular system to identify the underlying transport mechanism, but also to reveal the nature and extent of the hopping sites that are involved in the charge transport. The latter aspect is of vital importance, especially in the context of charge transport through biomolecules, *e.g.* proteins and DNA, which not only strongly depends on the molecular length but also on the architecture of the molecular backbone and thus on the number and sequence of amino acids and base pairs, respectively [60,100].

As a first step toward this subject, the BLYP35 functional was applied to G-DNA derivatives with the aim of predicting intermediate transport mechanisms identified from molecular conductance measurements [31,66]. Here, promising results were obtained by applying the BLYP35 functional in combination with the PCM for water, as distinct charge localization is indicated by the spin density isosurfaces compared to the situation where isolated molecules are considered. Particularly in the case of the stacked G-DNA sequences, the computational results are in good agreement with the experimentally derived coherence length of approximately two to three base pairs. For alternating G-DNA sequences the experiment indicates that each base pair acts as a hopping site, whereas a larger coherence length of approximately two base pairs is predicted from the calculations [66]. However, since in this work only single point energy calculations were carried out on frozen B-DNA geometries, molecular structure optimizations may be pursued by using more efficient computational methods to investigate the effect of structural changes on the degree of charge localization. Additionally, the inclusion of more advanced solvent models, such as D-COSMO-RS, may provide an even more realistic description of the environment particularly in the case of protic solvents such as water [50,51].

As the established BLYP35+PCM protocol most likely relies on the exploitation of error compensation resulting in predictions close to the experiment, the question arises whether and how the predictions are affected by a more realistic description of the molecular junction. Here, the effect of modelling the electrode contact on the degree of charge localization was studied by attaching small gold clusters to the molecular termini to clarify whether it improves or impairs the predictions. Interestingly, the presence of gold termini leads to an overlocalized description, being more pronounced with growing size of the gold cluster and becoming extensive in case of using a PCM in the calculations.

From these results it can be deduced that there is a sensitive interplay of parameters in the calculations that may have contrary effects in terms of localization, leading to the conclusion that they need to be carefully balanced and validated before applying them to the prediction of transport mechanisms. As such, the amount of exact exchange is a decisive factor in predictive calculations, since charge localization is promoted by an increasing amount of HF exchange. As previously pointed out by Kaupp and coworkers, an amount of 35 to 42 percent exact exchange in the present hybrid DFT approach in combination with an PCM provides reasonable charge localization properties in class III/II mixed-valence borderline compounds [50–52], as was shown earlier in this work (see Sec. 3.1) and also in molecular wires as was shown here and in related studies [54,193]. An alternative approach toward describing the class III/II character is the application of LC-DFT methods, such as ω -B97X-D or M06-HF, including 100 percent exact exchange, while neglecting environmental effects *via* PCM. Although these approaches proved useful for describing charge localization in some class III/II borderline mixed-valence systems [121], they were found to have an overlocalizing tendency in DMP mixed-valence systems and also in OPTI_n wires (see Sec. 3.4 and Sec. 6.4). Beyond the inherent inflexibility regarding environmental modelling by the prerequisite of performing calculations on isolated molecules to avoid overlocalization, LC-DFT methods are not considered an equivalently reasonable alternative to the BLYP35+PCM approach. An interesting objective of following studies is to verify the validity of the present DFT protocol in predicting transport mechanisms not only as a function of molecular length, but also of the molecular structure, *e.g.* the base sequence in DNA [60], as already initiated in this work on the example of G-DNA. Beyond that, it appears worthwhile to evaluate semi-empirical methods as an even more efficient and therefore promising alternative to the present DFT protocol, as they were previously applied to the investigation of charge transfer in organic mixed-valence systems [118,122,212]. Such an approach would represent a more efficient alternative to comprehensive multiscale approaches based on first-principles calculations [48,49] with the advantage of being less expensive and therefore suited for the screening of larger data sets. The results of early investigations on using semi-empirical approaches for the prediction of transport mechanisms are presented in the following Sec. 7.1.

7 Toward More Efficient Approaches to Predicting Charge Transport Mechanisms

7.1 Introduction

After successfully applying the BLYP35+PCM protocol to the prediction of transport mechanisms in molecular wires, efforts were made to increase the efficiency of the predictive calculations. For this purpose, semi-empirical approaches were evaluated as a less computationally expensive alternative to the validated DFT protocol. In the framework of semi-empirical methods, the *Zero Differential Overlap* (ZDO) approximation is central, where only one- and two-center integrals are considered, allowing for the use of Slater-type orbitals [129]. As a compensation to this approximation, the remaining integrals are made into parameters and their values are assigned based on other calculations, *e.g.* by fitting to many, mostly molecular experimental data, or based on a few, mostly atomic experimental data [129].

The great variety of semi-empirical methods available nowadays originates from the different numbers of integrals that are neglected and the way the parameterization is done: For example, in the *Neglect of Diatomic Differential Overlap* (NDDO) approximation, no further approximations than those mentioned above are made for the one- and two-electron parts, while in the *Intermediate Neglect of Differential Overlap* (INDO) approximation, all two-center two-electron integrals that are not of the Coulomb type are additionally neglected. In terms of approximations, the INDO method is intermediate between the NDDO and CNDO methods, the latter denoting the *Complete Neglect of Differential Overlap* approximation. Here, all Coulomb two-electron integrals are neglected, including the one-center integrals, which are then parameterized. The main difference between CNDO, INDO and NDDO is therefore the treatment of the two-electron integrals: While all the one- and two-center integrals are preserved in the NDDO approximation, the latter are reduced to only two parameters in the CNDO and INDO methods [129].

In this work, methods based on the NDDO approximation, such as the Austin Model 1 (AM1) [213] and the Parametric Method 6 (PM6) [214] were investigated, the latter being a further developed variant of the original PM3 model [69]. While both are derived from the same basic NDDO approximations and share the parameterization in terms of atomic variables, *i.e.* referring only to the

nature of a single atom, the only difference between them is the way how core–core repulsion is treated and how the parameters are assigned. Hence, the PM3 method is basically a reparameterized variant of the AM1 model, where the expression for the core–core repulsion is kept, except that only two Gaussian functions are assigned to each atom. The Gaussian parameters are allowed to vary freely and are fully optimized in contrast to the underlying AM1 method [129].

Moreover, tight-binding versions of KS-DFT (DFTB) such as the analytical DFTB approach (DFTBA), were investigated [215]. While the former semi-empirical methods belonging to the NDDO family are regarded as approximations to the Hartree–Fock formalism, the DFTBA methods have been developed as approximation to DFT [129]. Similar to the NDDO approximations, in DFTB methods a minimal basis set and only valence electrons are considered, while three- and four-center integrals are neglected [129]. The core–core repulsion energy is considered as not having any electronic contribution, which is equivalent to the bare nucleus repulsion, and is typically parameterized and fitted to corresponding all-electron DFT results [129]. The DFTBA method used in this work is a variant of the DFTB approach, where analytic expressions are used for the matrix elements rather than tabulated ones [215].

The main advantage of semi-empirical methods based on the NDDO approximation is the drastic reduction of computational cost by making the calculation of electron–electron repulsion integrals much more efficient, thus leading to a significant speed-up [68]. Hence, all NDDO models describe a way to efficiently approximate the Fock matrix, which is computationally quite expensive, since its assembly usually requires the processing of M^4 electron–electron repulsion integrals during the iterative solution of the SCF equations. By applying the NDDO approximation, the number of electron–electron repulsion integrals that needs to be calculated explicitly is drastically reduced down to M^2 [68]. On the downside, these calculations may be associated with quite a high degree of uncertainty for systems that are not well-known and, thus, for which not much experimental information is available. The problem of insufficient experimental data is somehow remedied by DFTB approaches due to the parameterization with respect to all-electron DFT calculations. However, this kind of parameterization inherently introduces the deficiencies of the underlying DFT method, whereby the errors arising from the DFTB approximations themselves are still

likely to be larger in comparison to the parent DFT model [129].

In previous computational studies, semi-empirical approaches have already been successfully applied to $(\text{An}_2\text{N})_2\text{T}_n$ and OPV_n bis(dianisylamine) mixed-valence radical cations, systems that were discussed earlier in Sec. 3.3. For example, the distance dependence of charge delocalization in $(\text{An}_2\text{N})_2\text{T}_n$ radical cations comprising one to 22 thiophene units was studied by Lacroix and coworkers by means of semi-empirical calculations based on the most widely used AM1 and the PM3 techniques [122, 216]. A transition from class III to class II was indicated by the formation of a charge-localized defect for singly oxidized isolated species with more than three thiophene units, while shorter species retained a symmetric structure in agreement with experiments by Odom and Wenger [62, 119, 123].

In similar studies by Barlow and coworkers, the distance dependence of mixed-valence characteristics was investigated on the example of OPV_n radical cations with the number of phenylene units ranging from two to five, where the experimental crossover from class III to class II occurring between the first two species of the series was supported by AM1 calculations [118].

Inspired by these studies, molecular structure optimizations of OPTI_n and OPI_n wires were performed in this work by using the AM1 and PM6 functional as well as the DFTBA method to evaluate their performance in predicting charge transport mechanisms based on localization properties. The results will be discussed in the following and be compared to those obtained from the BLYP35+PCM protocol, which was shown to perform very well for these systems earlier.

Computational Methodology

Molecular structure optimizations were performed on neutrally preoptimized structures for molecular wires in their radical cationic state by employing different semi-empirical approaches, *i.e.* AM1, PM6 and DFTBA, as implemented in the GAUSSIAN 09 program package [152]. In the preceding molecular structure optimizations of molecules in their neutral state, the same methodology as used in subsequent optimizations of the corresponding radical cations was employed. Molecular structure optimizations were performed on both, isolated molecules and molecules in solution, since the importance of environmental effects on charge localization properties was pointed out by Kaupp and coworkers and was also shown in our previous study on organic mixed-valence systems [53, 54]

and molecular wires [54] (see Sec. 3.3 and Sec. 6.3). The convergence criterion in the self-consistent field (SCF) algorithm was set to 10^{-7} hartree for the change of the energy in all calculations and to 10^{-4} a.u. for the gradient in molecular structure optimizations. For the inclusion of solvent effects, the polarizable continuum model with the integral equation formalism model (IEF-PCM) [153, 154] was employed as implemented in the GAUSSIAN 09 program package by using the SCRF keyword with the available dielectric constant for thiophene ($\epsilon = 2.7270$). Molecular structures and spin densities were visualized with the AVOGADRO editor [155], applying an isosurface value of 0.001 for plotting the spin density distributions. The thiol terminus of the OPTI_n wires was replaced by amine groups due to technical reasons, since DFTBA is not parameterized for sulfur, but all pairs of H, C, N, and O [152].

7.2 Semi-empirical Methods for Predicting Charge Transport Mechanisms

OPTI_n Wires – AM1 Results

In Fig. 7.11 (top), the spin density distributions of OPTI₄ to OPTI₈, optimized with the AM1 functional in thiophene (PCM), are illustrated. For all wires, a rather delocalized spin density is obtained, irrespective of the molecular length. Although slightly increasing localization is indicated for OPTI₆ and longer wires, there is no clear-cut transition between a rather localized to a delocalized structure. However, a considerably twisted geometry is observed for OPTI₆ to OPTI₈, where in any case less spin density is hosted on the third monomer unit starting from the terminus. Aside from the fact, that the crossover deduced from the experiments occurs between OPTI₆ and OPTI₇, the spin density remains delocalized across the whole molecule also for the longest wires, despite being interrupted by the less populated third monomer unit. Moreover, no definite hopping site can be determined from these results in contrast to the results obtained from the DFT hybrid approach based on the BLYP35 functional discussed earlier (see Sec. 6.3).

Consequently, the AM1+PCM method is not capable of describing the tunneling-to-hopping crossover from the experiments for these wires. Interestingly, the same results are obtained qualitatively when performing molecular structure optimizations on isolated OPTI_n wires (see Appendix, Fig. A.14). This outcome is fundamentally different from what was observed in the frame of DFT

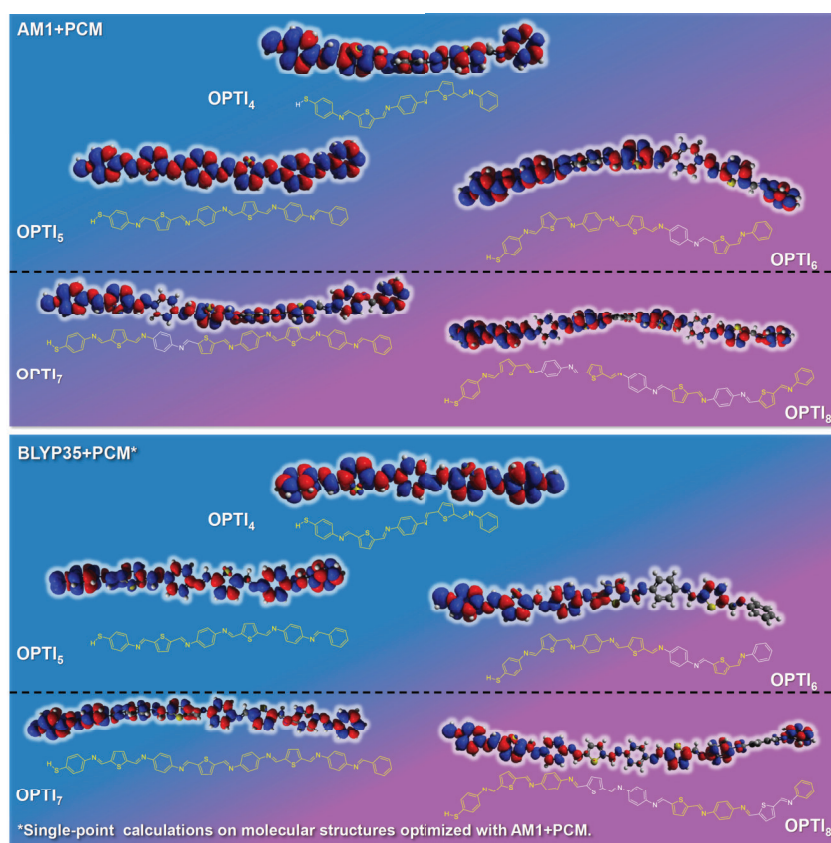


Figure 7.11: Charge Localization in OPTI_n Wires – AM1 Results

Top: Spin density isosurfaces of OPTI_n radical cations from molecular structure optimizations with the AM1 functional in thiophene (PCM). *Bottom:* Spin density isosurfaces of OPTI_n radical cations from single-point calculations with the BLYP35 functional and Ahlrich's def2-TZVP basis set in thiophene (PCM) on molecular structures optimized with the AM1+PCM method. The degree of charge delocalization is coded by the background colour (charge delocalization: blue; increasing localization: red). Black dotted line: Experimental crossover from tunneling to hopping.

molecular structure optimizations with and without PCM, where a change from overdelocalization to a reasonably localized description was indicated, respectively.

As discussed earlier, an increasingly polarized environment as incorporated by a PCM is expected to induce stronger charge localization. The results obtained from AM1 calculations for the OPTI_n wires therefore appear rather unreliable, since it is unlikely and chemically counterintuitive that the degree of charge

localization remains unaffected by such a drastic change of the polarizability of the surrounding. This finding may possibly be attributed to the minimal basis set used in the AM1 approach, thus leading to a less polarizable electronic structure. Altogether, the crossover from tunneling to hopping occurring between OPTI₆ and OPTI₇ cannot be predicted by performing molecular structure optimizations with the AM1 functional, irrespective of whether a PCM is applied or not.

Since clearly overdelocalized molecular structures were obtained from optimizations with the AM1 method even when applying a PCM, single-point calculations with the successfully validated BLYP35+PCM protocol were carried out on the final molecular structures (see Fig. 7.11, bottom). This approach aimed at a more accurate description of charge localization by the BLYP35+PCM protocol, while maintaining the computational cost relatively low by performing molecular structure optimizations with the AM1 method. Ideally, a compromise between accuracy in correctly describing the degree of charge localization and computational efficiency could be found. Interestingly, the degree of charge localization does not change much by this extension when compared to molecular structure optimizations only: While for OPTI₆, charge localization increases slightly, less pronounced charge localization is observed for OPTI₇, which is chemically counterintuitive given the greater molecular length. The localization increases again for OPTI₈, where two adjacent monomer units are nearly free from any spin density. Altogether, performing single-point calculations with the more precise BLYP35+PCM protocol on AM1-preoptimized geometries is not sufficient for predicting transport mechanisms in the radical cationic wires under study, as neither the calculated degree of charge localization is consistently increasing with growing molecular length, nor the tunneling-to-hopping transition from the experiments is indicated at all.

OPTI_n and OPI_n Wires – PM6 and DFTBA Results

Similar to the results obtained from calculations with the AM1 functional, an overdelocalized spin density distribution is obtained for all OPTI_n wires when the PM6 functional is used in molecular structure optimizations of isolated wires (see Fig. 7.12, top). In contrast to calculations with the AM1 functional, the first monomer unit is notably bent for OPTI₅ and OPTI₆, while the remainder of the molecule is arranged in a rather planarized fashion.

When adding a PCM during molecular structure optimizations, completely delocalized structures are obtained in any case, similar to the isolated molecular wires. Interestingly, the resulting molecular structures differ dramatically from the isolated ones: all of them are considerably bent in the middle, while the two halves of the molecule itself are nearly planar. As it appears unlikely that full charge delocalization is maintained to such a great extent despite the broken planarization due to extensive bending in the middle, the results obtained from PM6+PCM can be considered rather unreliable.

Altogether, the experimentally observed tunneling-to-hopping crossover cannot be described based on PM6 calculations, where overall even stronger charge delocalization than from AM1 calculations is predicted. Most likely, the compensation of certain errors made in the description of charge localization, as successfully exploited in earlier optimizations with BLYP35+PCM, operates differently in the framework of the chosen semi-empirical approaches and not in an equally beneficial way.

As a different semi-empirical approach beyond the AM1 and PM6 method, the DFTBA method (parametrized *via* the results of DFT calculations [217]) was evaluated for molecular structure optimizations of isolated OPI_n wires. As can be seen from Fig. 7.12 (bottom), charge localization already sets in for the shortest member OPI_4 and is maintained in longer species.

Interestingly, the localization pattern differs fundamentally from the results obtained with the BLYP35 hybrid DFT approach (see Sec. 6.3): While definite subregions of concentrated spin density, *i.e.* hopping sites, are obtained from DFT, a different localization pattern results from DFTBA calculations, where monomer units are populated by the spin density in an alternating fashion. As the charge is predicted to be localized to a very high extent already for isolated wires, no further optimizations with a PCM were pursued, since an even higher degree of charge localization is expected due to a more strongly polarized environment.

Building on similar studies described earlier in this section, subsequent single-point calculations with the BLYP35+PCM protocol were performed on OPI_n wires obtained from molecular structure optimizations with the DFTBA method to evaluate whether this approach allows for the derivation of charge transport mechanisms. Similar to calculations in the AM1 framework, the aim was to find a compromise between accuracy in describing the degree of charge localization

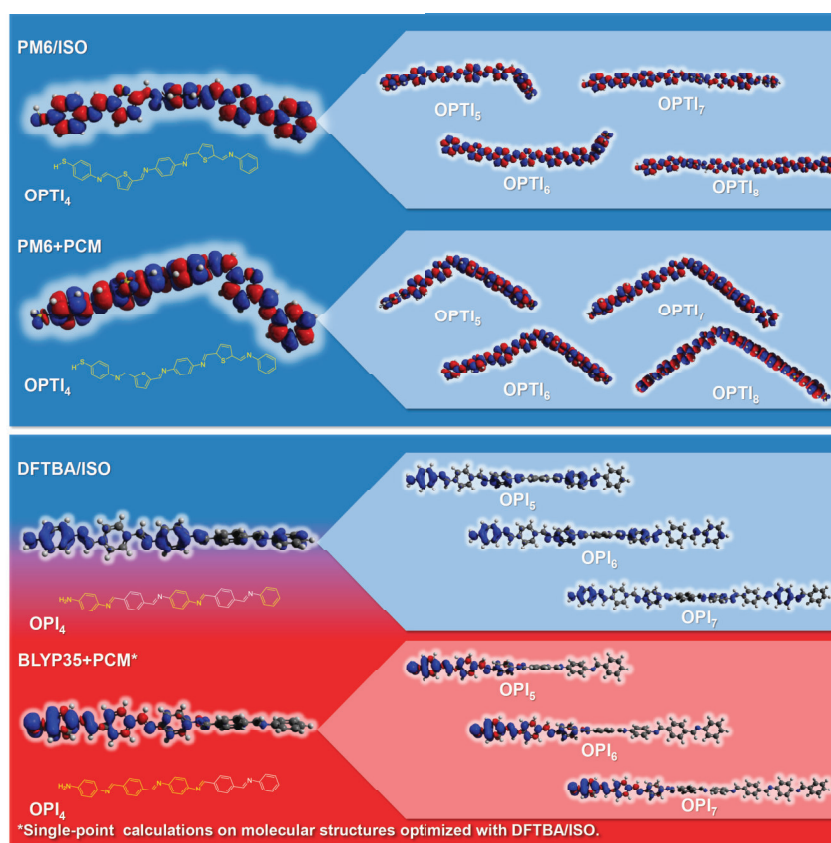


Figure 7.12: OPTI_n and OPI_n Wires – PM6/DFTBA Results *Top:* Spin density isosurfaces of OPTI_n radical cations from molecular structure optimizations with the PM6 functional and Ahlrich’s def2-TZVP basis set in their isolated state (ISO) and in thiophene (PCM). *Bottom:* Spin density isosurfaces of OPI_n radical cations from molecular structure optimizations with the DFTBA method in their isolated state (ISO). Spin density isosurfaces of OPI_n radical cations from single-point calculations with the BLYP35 functional and Ahlrich’s def2-TZVP basis set in benzene (PCM) on molecular structures optimized with the DFTBA method. The degree of charge delocalization is coded by the background colour (charge delocalization: blue; increasing localization: red).

and computational efficiency as the crossover from tunneling to hopping could not be predicted based on molecular structure optimizations with the DFTBA approach only. As can be seen from Fig. 7.12 (bottom), an overlocalized description is obtained already for the shortest member, similarly to the results obtained from DFTBA calculations only. However, distinctly different spin density distributions are obtained when performing additional single-point BLYP35+PCM calculations on optimized molecular structures: In contrast to the alternating

spin density distribution pattern of DFTBA-optimized molecules, localization of the charge on definite and continuous subregions is observed. Nonetheless, as the majority of the spin density is located on a subregion of three monomer units irrespective of the molecular length, these results are considered unreasonable. Therefore, the transition from tunneling to hopping is not predicted correctly either by optimizations with the DFTBA technique only or by subsequent DFT single-point calculations on the resulting molecular structures, since in any case an overlocalized description is drawn.

7.3 Conclusions

Aiming at a more efficient way of calculating charge localization properties, semi-empirical approaches were validated on the example of OPTI_n wires. None of the tested approaches performs well in predicting the transition from tunneling to hopping from the experiments based on the degree of charge localization. Calculations with either the AM1 or the PM6 method result in an overdelocalized description of the charge and unreasonable molecular structures in case of the PM6 method, as they are artificially bent in the middle.

More importantly, nearly identical results are obtained irrespective of whether a PCM is used or not in combination with the AM1 or PM6 method, leading to the suggestion that they result in chemically unreasonable descriptions of charge localization (a stronger degree of charge localization would be expected in a more polar environment compared to calculations on isolated molecules, as was shown on the example of DFT calculations with the BLYP35 functional in Sec. 3.3). Since no distinct differences between results on isolated molecules versus molecules in a polarizable environment are found, they can be considered rather unreliable.

In contrast to the AM1 and PM6 functional, the DFTBA method provides an overlocalized description already for the shortest isolated OPTI_n wires. Here, the charge is localized on single alternating monomer units for all wires. This finding again is unreasonable in a chemical sense, as the degree of charge localization is expected to change with increasing molecular length.

As the prediction of transport mechanisms based on semi-empirical methods did not succeed, subsequent single-point calculations with the successfully validated BLYP35+PCM protocol were performed on molecular structures obtained from optimizations with the AM1 and DFTBA method, which were more reasonable

when compared to PM6 optimizations. The aim was a proper description of charge localization properties using the validated DFT protocol, while keeping molecular structure optimizations efficient using semi-empirical methods.

Altogether, no clear tunneling-to-hopping transition was identified from this combined approach either when performing single-point calculations on molecular structures optimized with the AM1 or the DFTBA method. The results lead to the conclusion that the relaxation of the molecular structure within an appropriate computational scheme such as the validated BLYP35+PCM protocol is essential and it should not be simply replaced by more efficient semi-empirical approaches, even when they are augmented by subsequent DFT single-point calculations of the electronic structure.

For future studies it would be of great interest to investigate the reasons for the semi-empirical approaches failing in predicting the charge localization properties of molecular wires under study in more detail and to revalidate them on mixed-valence systems, as suggested from earlier studies [118,122,216]. Beyond that, valuable insight may be gained by performing energy decomposition analyses in order to identify energy contributions leading to a different description compared to the BLYP35 approach, as suggested by Tonner and coworkers [218].

V. CONCLUSIONS AND PERSPECTIVES

This work aimed at predicting the length-dependent transition from tunneling to hopping transport in molecular junctions, as observed in molecular conductance experiments, on the basis of charge localization properties obtained from first-principles calculations. These studies were inspired by the idea of associating the degree of charge localization to the underlying transport mechanism, thus connecting tunneling and hopping transport to charge delocalization and localization, respectively. Three different series of radical cationic organic mixed-valence systems served as model systems for the validation of various DFT approaches with respect to their performance in describing the length-dependent transition from full delocalization to partial localization of the charge.

The DFT protocol suggested by Renz and Kaupp based on the BLYP35 hybrid functional [50–52] worked consistently well in describing length-dependent charge localization in agreement with the experiments, when combined with a polarizable continuum model. In contrast, caution needs to be exercised when using DFT methods where a high amount of exact exchange is involved, which intrinsically favors charge localization: long-range corrected DFT approaches such as ω -B97X-D or ω -PBE resulted in rather overlocalized descriptions, especially when combined with a PCM, as was shown on the example of DMP_n radical cations. These methods can therefore not be recommended for the calculation of charge localization properties.

The successfully validated BLYP35+PCM protocol was furthermore employed to identify molecular structures that either show anti-Ohmic behavior, *i.e.* where charge delocalization increases, or is pertained when going toward longer bridge lengths. The strategy was based on increasing the degree of charge localization in typically delocalized species at short molecular lengths by exploiting either electronic or steric effects. However, the desired result was not obtained, neither by changing the linkage topology in benzene-bridged radical cations from *para*- to *meta*-connection to invoke destructive quantum interference in the shorter species, nor by incorporating bulky groups to the redox centers to increase the

steric hindrance in shorter bis(dianisylamine) thiophene molecules as opposed to longer ones. Contrary to the assumption, compared to the longer species no stronger charge localization was observed in the shorter species, where destructive quantum interference would be expected based on the starring rules for alternant hydrocarbons in benzene-bridged systems and a more tilted geometry in bulky thiophenes would be assumed.

In contrast, charge delocalization could be extended in *para*-benzene-bridged DMP_n and bis(dianisylamine) radical cations from zero to three and from two to four bridging units by applying a captodative substitution scheme suggested by Stuyver, De Proft and coworkers [64] for high-conductance molecular wires. Based on these results it was demonstrated that charge-localized structures can be transformed into charge-delocalized structures by chemical modifications, representing a promising approach toward designing long-range delocalization. Calculations with the BLYP35+PCM protocol on radical anionic mixed-valence systems showed that the validated DFT method works not only well for describing hole transfer, but also for electron transfer. Thus, as was done for the prediction of hole transport in molecular wires in this work, the DFT protocol may be used equally for predicting the dominating mechanisms for electron transport in future studies.

In the second part of this study, the BLYP35+PCM protocol was applied to predicting the length-dependent crossover from tunneling to hopping observed in molecular conductance experiments in five different series of molecular wires. In this work, a quantitative measure for charge delocalization was developed that allows for the prediction of the theoretical crossover within a particular molecular series based on spin delocalization, which was used as a proxy for charge delocalization. Based on the comparison of local spin distributions between consecutive wires, the crossover length was derived from the largest relative drop of the measure for charge delocalization. The computational results obtained with the BLYP35+PCM protocol are in excellent agreement with the experiments, not only in terms of generally describing the increasing degree of charge localization with growing bridge length, but also in predicting the crossover length for most wires. In four out of five cases the transition length is predicted correctly by the DFT protocol, when used for calculations on single molecular wires. However, for OPE_n wires the crossover predicted from theory is delayed by one monomer unit when compared to the experiments, and is

therefore not in perfect agreement with the experiments. For ONI_n wires, the BLYP35+PCM protocol provides an overall rather too localized description, but still predicts the crossover length correctly in agreement with the experiments. Possibly, the either slightly overdelocalized or overlocalized theoretical descriptions can be attributed to the neglect of interface and environmental effects in the calculations, respectively. Thus, in case of OPE_n wires, the molecular structure obtained from the calculations may be more planarized than in the experiments due to π -backbonding of the free electron pair of the amine anchoring group to the molecular backbone rather than binding to the electrode. Beyond that, the formation of larger dipole moments at the molecule–electrode interface is likely more pronounced in case of amine linkers due to weaker binding to the metal substrate when compared to thiol linkers, thus facilitating the formation of image charges [95,200]. The underestimation of charge localization compared to the experiments is therefore likely a result of lacking interface effects in the DFT framework used in this work.

In contrast, the rather localized description of ONI_n wires may be attributed to the fact that the single-molecule calculations lack environmental effects arising from adjacent molecules in the monolayers, as present in the experiments. Slightly twisted molecular structures are obtained for these wires from the calculations, which likely deviate from the more planarized structures in the experiments due to π -stacking, which facilitates charge delocalization.

It has to be noted that the success of the computational approach used in this work is likely based on the partial compensation of errors in the theoretical description, such as the lack of conformational sampling or the neglect of nonequilibrium and interface effects, which was shown earlier on the example of more extensive multi-scale approaches toward the description of charge transport by Elstner and Kleinekathöfer [48,49].

Interestingly, a particular correction toward a more realistic model does not necessarily result in predictions closer to the experiments, but in fact might even lead to a less reasonable description. For example, the modeling of the electrode contact in the calculations led to an unreasonably high degree of charge localization in OPTI_n wires that was even more pronounced in combination with a PCM. One therefore needs to be careful when incorporating additional components in the theoretical descriptions, as was pointed out by Elstner and Kleinekathöfer [48,49].

As these aspects may have a varying impact depending on the experimental setup and the molecular length, the overall good performance of the BLYP35+PCM protocol may be occasionally hampered when applied to a broad range of molecular wires.

Nonetheless, the overall positive impression of the DFT protocol is not diminished since the predictions were found being in good agreement with the experiments in the majority of the cases and only minor deviations were observed. Thus, the increasing trend of charge localization with growing bridge length is qualitatively well described by the DFT protocol, and the crossover length is correctly predicted with an error of at most one monomer unit. Altogether, the BLYP35+PCM protocol represents an easily applicable first-principles approach for predicting transport mechanisms in a variety of conjugated molecular wires, at least when considering experiments at room temperature.

Beyond that, the use of this DFT approach may not be limited to identifying the predominating transport mechanism, but may be also applied to investigations of the nature and the extent of hopping sites that participate in the charge transport. Promising preliminary results on evaluating the hopping sites involved in the charge transport were obtained in this work by performing single-point energy calculations with the BLYP35+PCM protocol on guanine-based DNA strands. Here, the presence of an intermediate transport regime in DNA strands with stacked guanine bases could be validated by DFT calculations, in agreement with the experiments and calculations by Tao and coworkers [66], from which the coexistence of coherent and incoherent processes was postulated. Consequently, the BLYP35+PCM protocol not only proved useful in predicting charge transport mechanisms in dependence of the molecular length, but also in dependence of the molecular architecture, which is of particular importance in biomolecules such as proteins and DNA with a varying number and sequence of amino acids and base pairs, respectively.

Further investigations focused on the evaluation of semi-empirical methods as a more efficient alternative to the present DFT protocol, which becomes more important when applying this predictive method to larger and more complex systems, such as biomolecules. In comprehensive multi-scale approaches that were previously presented by Elstner and Kleinekathöfer [48, 49] for describing charge transport processes in such systems, no assumptions of the transport mechanism have to be made *a priori*. However, these approaches are computa-

tionally expensive and complex due to the combination of various computational techniques, whereas more cost-efficient techniques would offer the advantage of screening larger data sets.

As semi-empirical methods had been proven useful for predicting charge transfer mechanisms in organic mixed-valence systems in earlier studies [118, 119, 122, 123, 216], they were applied for calculating the charge localization properties of molecular wires, for which the BLYP35+PCM protocol worked well.

However, as indicated from results obtained with the AM1, the PM6 and DFTBA method in this work for OPTI_n and OPI_n wires, either an overdelocalized (AM1, PM6) or an overlocalized (DFTBA) description is obtained. More importantly, the trend of an overall increasing charge localization with increasing molecular length could not be described by any of these methods, and the addition of a PCM did not have a significant effect on the results when compared to isolated molecules, which can be considered chemically unreasonable. Subsequent single-point energy calculations with the BLYP35+PCM protocol on molecular structures optimized with semi-empirical methods did also not lead to reasonable predictions in agreement with the experiments, which suggests that the relaxation of the molecular structure within an appropriate computational framework is of crucial importance for the quality of the predictions.

For future studies, it appears worthwhile to evaluate whether the reasons for the poor performance of semi-empirical approaches in predicting transport mechanisms can be determined in more detail. Further insights may be gained by identifying the energy contributions that are responsible for the erroneous description of charge localization in comparison to the experiments. For this purpose, energy composition analyses, as proposed by Tonner and coworkers [218], could provide a deeper understanding.

Altogether, the results of this work represent a promising step toward the simulation of transport mechanisms in molecular wires based on first-principles calculations of charge localization properties, allowing for the prediction of the length-dependent crossover from coherent tunneling to incoherent hopping.

VI. ACKNOWLEDGEMENTS

First of all, I would like to thank Prof. Dr. Carmen Herrmann for supervising me and for her great support during my stay in her research group. She always provided a cooperative working environment and offered me numerous opportunities to get a deeper scientific understanding, not only by critical discussions but also by encouraging me to present my research at international conferences and to publish it in scientific journals. Beyond that, she greatly assisted me by proof reading reports, manuscripts and this thesis: I gained a lot from her sense of good writing and scientific curiosity.

Furthermore, I thank the members of my PhD committee Prof. Dr. Gabriel Bester, Dr. Tobias Vossmeier and PD Dr. Tobias Kipp for their interest in my work.

From the beginning, the atmosphere in Carmen's group provided by my colleagues was supportive and friendly. I would like to thank the current and former group members, Martin Zöllner, Philipp Bahlke, Michael Deffner, Haitao Zhang and Alexander Voigt, who were always eager to help and gave useful input on my work. In particular, I would like to thank Martin for being such a great supervisor already during my master's studies. He introduced me to the GAUSSIAN and TURBOMOLE program packages and transport calculations with ARTAIOS, reviewed a lot of my work and was always a good company.

Moreover, I would like to thank my collaboration partners Prof. Dr. Jacobi von Wangelin and Sebastian Sandl from the Institute of Inorganic and Applied Chemistry for giving me the opportunity to assist them in the investigation of the electronic structure of cobalt hydrides.

I am also thankful for the constant help provided by the IT Service of the chemistry department, in particular by Christian Schmidt and Sören Ziehe, who were always willing to help solving technical problems or software issues. Additionally, I thank the high-performance computing center (HPC) of the University of Hamburg for computational resources and particularly Dr. Thomas

Orgis and Dr. Hinnerk Stüben for taking care of the high-performance computer cluster and software and for their assistance in technical issues.

Equally important, I would like to acknowledge the support by the University of Hamburg in financial and administrative issues, in particular by Beate Susemihl, Ingke Klemm and Susanne Breidohr. Moreover, I gratefully acknowledge financial support from the German Research Foundation (DFG) and from the Pro Exzellenzia 4.0 initiative at Hamburg, who granted me a doctoral fellowship and offered a lot of interesting workshops on leadership.

Last but not least, I am deeply grateful to my family and friends who supported me in their own way not only during my PhD, and helped me reaching my goals with their constant encouragement.

A. Appendix

A.1 DMP_n – Structural Parameters and Local Properties

A.1.1 Structural Parameters from BLYP35, ω -B97X-D and ω -PBE

In Tab. A.1, A.2 and Tab. A.3, the C–O bond lengths and structural parameters x for the *para*-DMP _{n} radical cations ($n = 0-4$) optimized with the BLYP35 hybrid functional, the ω -B97X-D functional and the ω -PBE functional (isolated and with PCM) are listed, respectively.

Table A.1: C–O bond lengths and structural parameters x for DMP _{n} radical cations optimized with the BLYP35 hybrid functional and Ahlrich’s def2-TZVP basis set (isolated and in DCM). The parameter x is evaluated according to Eq. (3.1).

		BLYP35					
		isolated			DCM		
		d [Å]	d' [Å]	x	d [Å]	d' [Å]	x
DMP ₀	D	1.330	1.336	1.00	1.327	1.339	0.96
	A	1.330	1.336		1.328	1.339	
DMP ₁	D	1.336	1.340	1.00	1.311	1.317	0.24
	A	1.336	1.340		1.357	1.359	
DMP ₂	D	1.340	1.344	1.00	1.309	1.314	0.10
	A	1.340	1.344		1.360	1.362	
DMP ₃	D	1.342	1.346	1.00	1.309	1.314	0.19
	A	1.342	1.346		1.361	1.362	
DMP ₄	D	1.343	1.346	1.00	1.309	1.314	0.18
	A	1.343	1.346		1.361	1.363	

Table A.2: C–O bond lengths and structural parameters x for DMP _{n} radical cations optimized with the ω -B97X-D functional and Ahlrich’s def2-TZVP basis set (isolated and in DCM). The parameter x is evaluated according to Eq. (3.1).

		ω -B97X-D					
		isolated			DCM		
		d [Å]	d' [Å]	x	d [Å]	d' [Å]	x
DMP ₀	D	1.328	1.335	1.00	1.308	1.313	0.19
	A	1.328	1.335		1.350	1.355	
DMP ₁	D	1.320	1.327	0.45	1.306	1.309	0.11
	A	1.349	1.350		1.358	1.359	
DMP ₂	D	1.313	1.320	0.33	1.306	1.309	0.11
	A	1.358	1.357		1.359	1.360	
DMP ₃	D	1.312	1.318	0.26	1.306	1.309	0.12
	A	1.359	1.359		1.360	1.359	
DMP ₄	D	1.311	1.317	0.24	1.306	1.308	0.07
	A	1.359	1.360		1.359	1.360	

Table A.3: C–O bond lengths and structural parameters x for DMP_n radical cations optimized with the ω -PBE functional and Ahlrich’s def2-TZVP basis set (isolated). The parameter x is evaluated according to Eq. (3.1).

ω -PBE (isolated)				
		d [Å]	d' [Å]	x
DMP ₀	D	1.307	1.313	0.29
	A	1.351	1.350	
DMP ₁	D	1.306	1.311	0.15
	A	1.358	1.355	
bridge				
DMP ₂	D	1.305	1.311	0.17
	A	1.359	1.358	
bridge				
DMP ₃	D	1.305	1.310	0.19
	A	1.360	1.359	
bridge				
DMP ₄	D	1.305	1.310	0.18
	A	1.360	1.360	
bridge				

A.1.2 Local Spins and Charges from ω -PBE

In Tab. A.4, the local spins and charges for the *para*-DMP_{*n*} radical cations (*n* = 0-4) optimized with the ω -PBE functional (isolated) are listed, along with the corresponding ratios between the respective local properties on the donor and acceptor moieties. In Fig. A.1, the corresponding spin density isosurfaces are shown.

Table A.4: Local spins and charges obtained from NPA for DMP_{*n*} radical cations optimized with the ω -PBE functional and Ahlrich’s def2-TZVP basis set (isolated), next to the ratios s_D/s_A and q_D/q_A , with the index corresponding to the respective redox center D or A. The percentage of local spins relating to the sum of all local spins is given in parentheses for different fragments of the molecule.

		DMP _{<i>n</i>} (isolated)			
	ω -PBE	local spins	q	s_D/s_A	q_D/q_A
DMP ₀	D	0.45 (90.9)	+0.85	0.10	0.18
	A	0.05 (9.1)	+0.15		
DMP ₁	D	0.46 (91.6)	+0.84	0.01	0.06
	A	0.01 (1.3)	+0.05		
	bridge	0.04 (7.0)			
DMP ₂	D	0.46 (92.0)	+0.85	0.00	0.02
	A	0.00 (0.1)	+0.02		
	bridge	0.03 (7.9)			
DMP ₃	D	0.47 (93.1)	+0.86	0.00	0.01
	A	0.00 (0.0)	+0.01		
	bridge	0.03 (6.8)			
DMP ₄	D	0.47 (93.4)	+0.86	0.00	0.00
	A	0.00 (0.0)	+0.00		
	bridge	0.03 (6.6)			

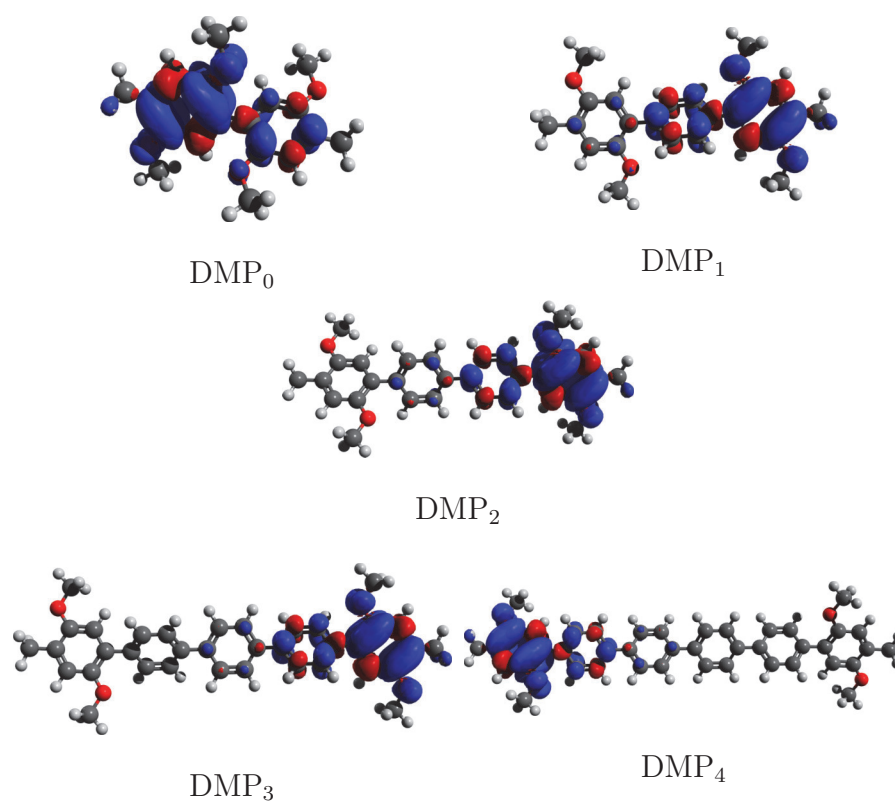


Figure A.1: Spin density isosurfaces of the isolated DMP_n radical cations optimized with the ω -PBE functional and Ahlrich's def2-TZVP basis set (isosurface value: 0.001).

A.2 $(\text{An}_2\text{N})_2\text{T}_n$ and OPV_n – Local Charge Ratios

In Fig. A.2 and Fig. A.3, the ratios between partial charges on the donor and acceptor moieties of the $(\text{An}_2\text{N})_2\text{T}_n$ radical cations ($n = 1-3, 6, 9, 12$) and of the OPV_n radical cations ($n = 0-3$) are plotted as a function of the number of bridging units. The molecular structures were optimized with the BLYP35 hybrid functional and the ω -B97X-D functional (isolated and with PCM).

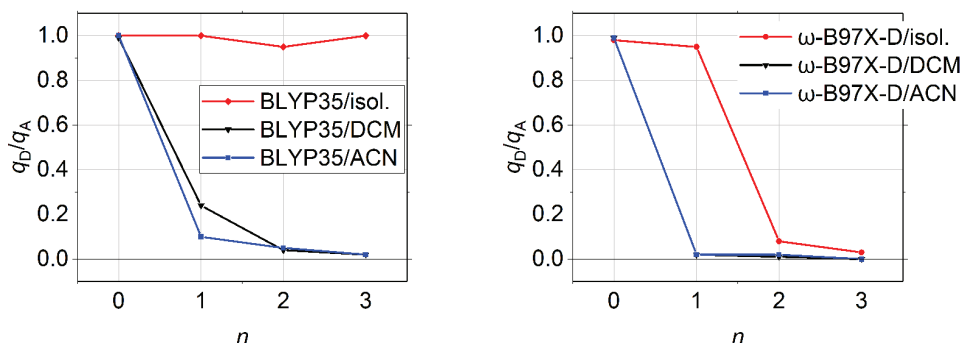


Figure A.2: Ratios q_D/q_A between partial charges on the donor and acceptor moieties of the OPV_n radical cations as a function of the number of bridging units n . Molecular structures are optimized with the BLYP35 hybrid functional (left), the ω -B97X-D functional (right) and Ahlrich's def2-TZVP basis set (isolated and with PCM).

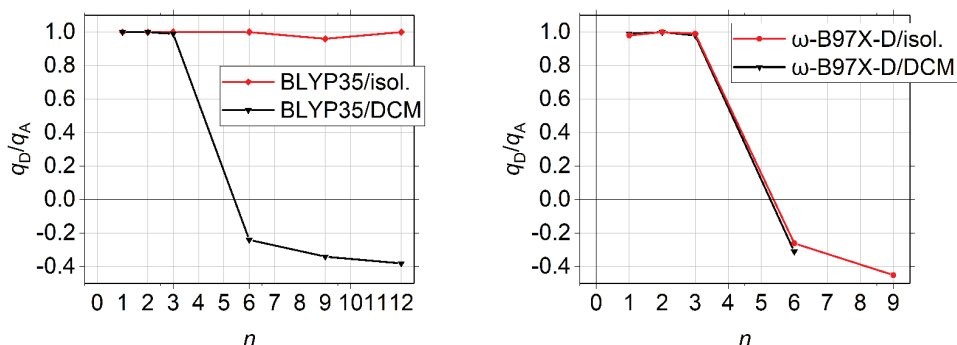


Figure A.3: Ratios q_D/q_A between partial charges on the donor and acceptor moieties of the $(\text{An}_2\text{N})_2\text{T}_n$ radical cations as a function of the number of bridging units n . Molecular structures are optimized with the BLYP35 hybrid functional (left), the ω -B97X-D functional (right) and Ahlrich's def2-TZVP basis set (isolated and with PCM).

A.3 Bulky Thiophenes and Captodative $(\text{An}_2\text{N})_2\text{Ph}_n$ and DMP_n Species

A.3.1 Bulky Thiophenes: Local Spins and Charges

In Tab. A.5, the local spins and charges for the *tert*-butyl-substituted and unsubstituted $(\text{An}_2\text{N})_2\text{T}_n$ radical cations ($n = 1, 2$), optimized with the BLYP35 hybrid functional (PCM), are presented along with the corresponding ratios between the respective local properties on the donor and acceptor moieties. In Fig. A.4, the corresponding spin density isosurfaces are shown for molecules in DCM (nearly identical results were obtained for the same species with the PCM for ACN and water).

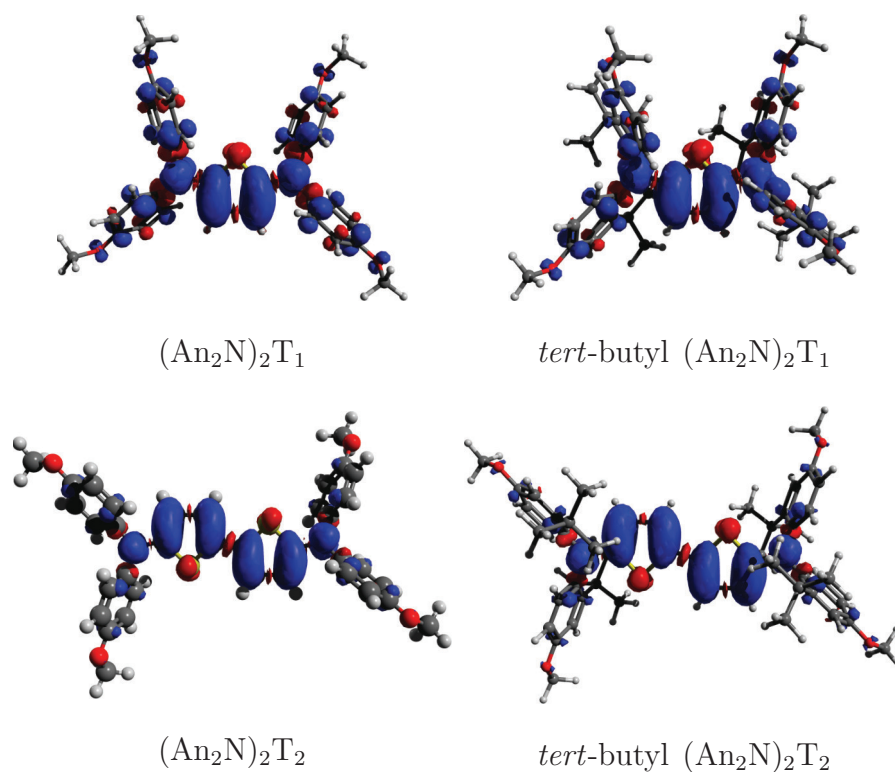
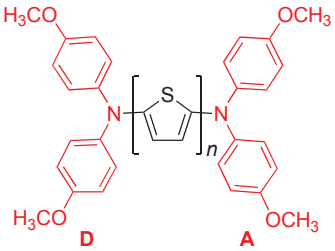
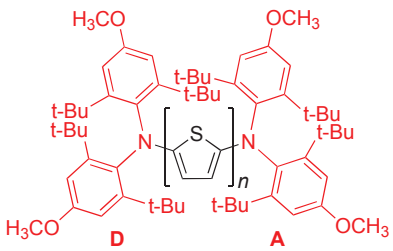


Figure A.4: Spin density isosurfaces of the *tert*-butyl-substituted and unsubstituted $(\text{An}_2\text{N})_2\text{T}_n$ radical cations optimized with the BLYP35 hybrid functional and Ahlrich's def2-TZVP basis set in DCM (isosurface value: 0.001).

Table A.5: Local spins and charges obtained from NPA for *tert*-butyl-substituted and unsubstituted $(\text{An}_2\text{N})_2\text{T}_n$ radical cations optimized with the BLYP35 hybrid functional and Ahlrich’s def2-TZVP basis set (PCM), next to their ratios $s_{\text{D}}/s_{\text{A}}$ and $q_{\text{D}}/q_{\text{A}}$, with the index corresponding to the respective redox center D or A. The percentage of local spins relating to the sum of all local spins is given in parentheses for different fragments of the molecule.

		$(\text{An}_2\text{N})_2\text{T}_n$				<i>tert</i> -butyl $(\text{An}_2\text{N})_2\text{T}_n$			
DCM		local spins	q	$s_{\text{D}}/s_{\text{A}}$	$q_{\text{D}}/q_{\text{A}}$	local spins	q	$s_{\text{D}}/s_{\text{A}}$	$q_{\text{D}}/q_{\text{A}}$
$n=1$	D	0.14 (27.2)	+0.19	1.00	1.00	0.13 (26.3)	+0.18	0.99	0.94
	A	0.14 (27.1)	+0.19			0.13 (26.0)	+0.17		
	B	0.23 (45.7)				0.24 (47.7)			
$n=2$	D	0.09 (17.5)	+0.14	1.00	1.00	0.08 (16.8)	+0.12	1.00	1.00
	A	0.09 (17.5)	+0.14			0.08 (16.8)	+0.12		
	B	0.33 (65.1)				0.33 (66.3)			
ACN									
$n=1$	D	0.13 (26.8)	+0.19	1.00	1.00	0.13 (26.1)	+0.17	0.98	0.94
	A	0.13 (26.7)	+0.19			0.13 (25.7)	+0.16		
	B	0.23 (46.4)				0.24 (48.2)			
$n=2$	D	0.09 (17.0)	+0.13	1.00	1.00	0.08 (16.7)	+0.11	1.00	1.00
	A	0.08 (17.0)	+0.13			0.08 (16.7)	+0.11		
	B	0.33 (66.0)				0.33 (66.7)			
H₂O									
$n=1$	D	0.13 (26.7)	+0.19	1.00	1.00	0.13 (26.1)	+0.17	0.98	0.94
	A	0.13 (26.7)	+0.19			0.13 (25.6)	+0.16		
	B	0.23 (46.5)				0.24 (48.3)			
$n=2$	D	0.08 (16.9)	+0.13	1.00	1.00	0.08 (16.6)	+0.11	1.00	1.00
	A	0.08 (16.9)	+0.13			0.08 (16.6)	+0.11		
	B	0.33 (66.1)				0.33 (66.8)			

A.3.2 Captodative-substituted $(\text{An}_2\text{N})_2\text{Ph}_n$ and *meta*-DMP $_n$: Spin Density Isosurfaces

In Fig. A.5, the spin density isosurfaces for captodative-substituted $(\text{An}_2\text{N})_2\text{Ph}_n$ radical cations ($n = 1-5$) optimized with the BLYP35 hybrid functional (PCM) are shown.

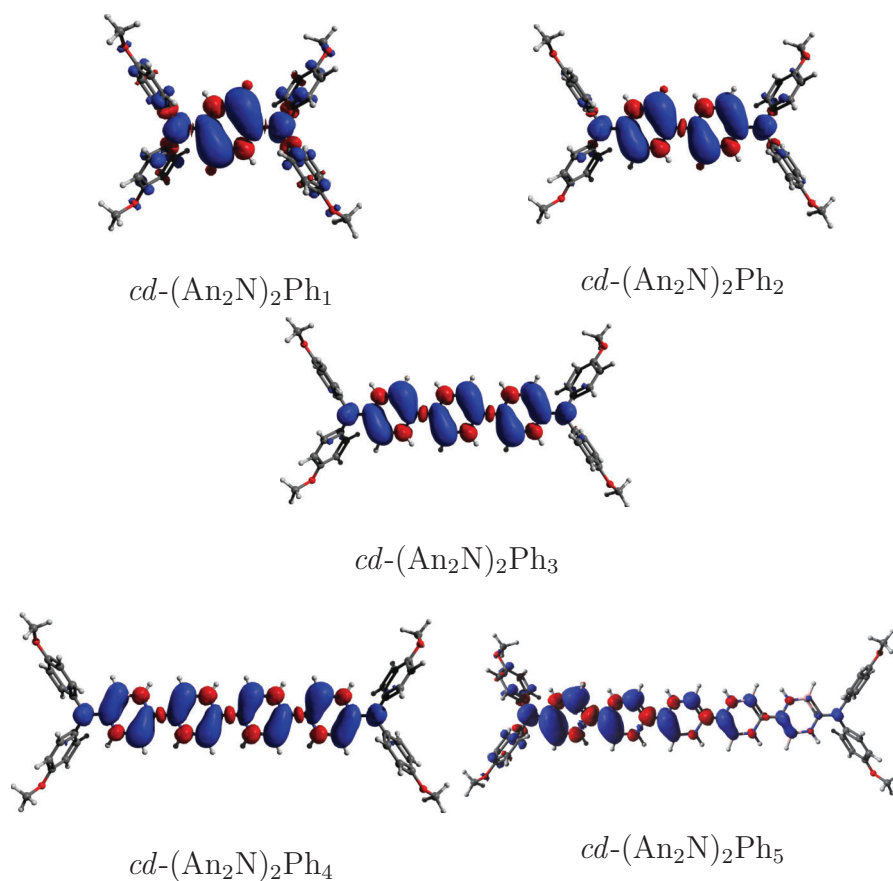


Figure A.5: Spin density isosurfaces of captodative-substituted *para*- $(\text{An}_2\text{N})_2\text{Ph}_n$ radical cations optimized with the BLYP35 hybrid functional and Ahlrich's def2-TZVP basis set in DCM (isosurface value: 0.001).

In Fig. A.6, the spin density isosurfaces for the *meta*-connected DMP_n radical cations ($n = 1-2$), optimized with the BLYP35 hybrid functional (PCM) are shown along with the corresponding chemical structures. The aim was to investigate whether an inverse trend of charge localization can be observed when going from shorter to longer DMP_n molecules in captodative-substituted *meta*- DMP_1 and *meta*- DMP_2 analogues. According to the starring rule of alternant hydrocarbons (see Fig. 4.5), one would expect non-disjoint coupling for the former and disjoint coupling for the latter member, meaning that a higher degree of charge delocalization can be assumed when extending the number of bridging units from one to two. This idea is based on the previous finding of captodative-substituted DMP_n radical cations maintaining charge delocalization over longer bridges compared to the bare DMP_n analogues. While no quantum interference effects could be observed for the bare *meta*- DMP_n members, it was studied whether they show up on naturally rather delocalized species.

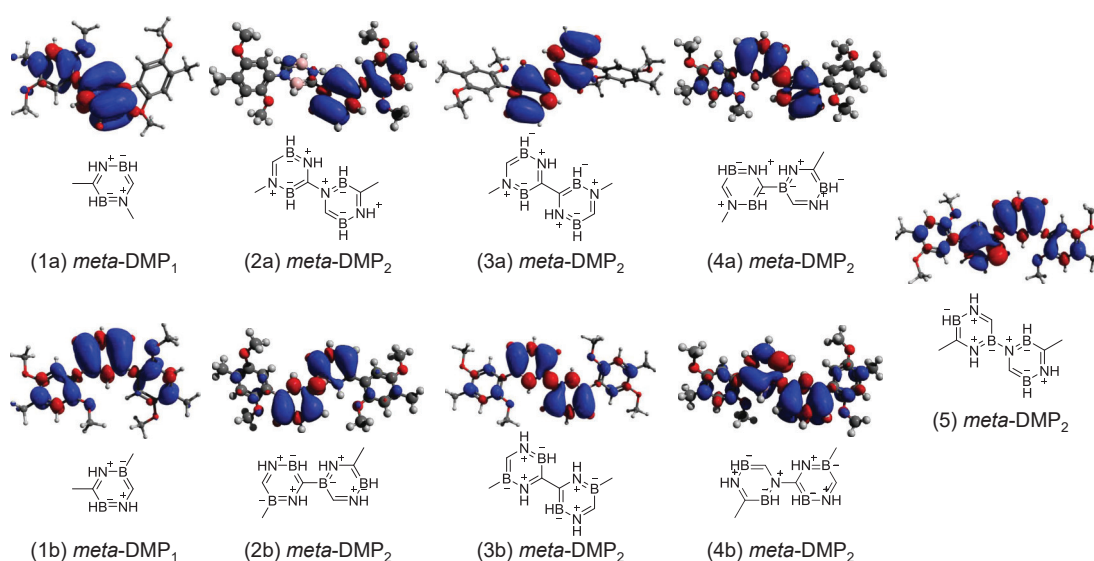


Figure A.6: Spin density isosurfaces of captodative-substituted *meta*- DMP_n radical cations optimized with the BLYP35 hybrid functional and Ahlrich's def2-TZVP basis set in DCM (isosurface value: 0.001).

As can be seen from the spin density isosurfaces shown in Fig. A.6, the charge localization properties of the captodative-substituted *meta*- DMP_n analogues differ dramatically from their *para*-analogues (see Fig. 4.4). As the linkage in *meta*-position can be realized in various ways, it was analyzed how it affects the

degree of charge localization. First, the linkage position of the DMP redox unit on either boron or nitrogen is decisive for the species being delocalized or localized, respectively. Moreover, stronger charge localization in the latter member is accompanied by a larger dihedral angle between the redox unit and the linking (N) atom, being 61.3° versus 2.7° (B). Generally, the localization pattern goes along with geometrical distortions, as can be observed for the *meta*-DMP₂ species. Especially in the cases where nitrogen serves as the linking atom between two ring subunits, relatively large dihedral angles and thus charge localization are present.

For example, the dihedrals comprising a central C–N bond for the molecules (2a)–(4a) range from 45.4° to 66.5° , whereas the dihedrals formed by a central C–B bond for the molecules (2b)–(4b) range from 3.3° to 25.7° , resulting in overall more delocalized spin distributions. Strong delocalization of the charge on the inner two ring units is obtained for the (3a) and (3b) species, which is accompanied by relatively small dihedrals comprising the central C–C bond (6.8° and 1.2°) compared to the outer dihedrals, and indicating the planarization of the bridging unit.

Based on these findings it is likely that sterical effects may play a role for the degree of charge localization in these captodative-substituted DMP_n analogues. Interestingly, full delocalization of the charge is obtained for the longer DMP₂ species with a central B–N bond and with both redox centers connected to the carbon atoms (5) and also the (4b) species, whereas the shorter (1a) molecule is localized. Consequently, these captodative-substituted DMP_n analogues indeed set an example of increasing delocalization with growing bridge length, where the common localization trend indicated in previous studies is found being reversed.

A.3.3 Oligo(pheno)-*p*-quinodimethane DMP_{*n*}

In Fig. A.7, the spin density isosurfaces for oligo(pheno)-*p*-quinodimethane DMP_{*n*} radical cations ($n = 2-3$), optimized with the BLYP35 hybrid functional (PCM) are shown along with the corresponding chemical structures. These species are obtained by adding ethynylene linkers to the *para*-DMP_{*n*} radical cations and were found to exhibit enhanced conductance with increasing bridge lengths in studies by Stuyver and coworkers, resulting in a qualitative behaviour similar to the captodative-substituted analogues but without the need of introducing azaborine chemistry [65].

As can be seen from the spin densities shown for the DMP₂ and DMP₃ species, the crossover between charge delocalization and localization occurs when going from two to three bridging units. Compared to the DMP_{*n*} analogues lacking ethynylene linkers, delocalization can thus be extended from zero to two bridging units. The introduction of linkers in related quinoid chains can therefore be used as a tool to tune delocalization toward longer bridge lengths similar to the captodative substitution scheme, by which delocalization could be maintained up to the DMP₃ species. Interestingly, this case sets the example of a compound which bears a higher degree of delocalization compared to its shorter analogues despite its greater molecular length.

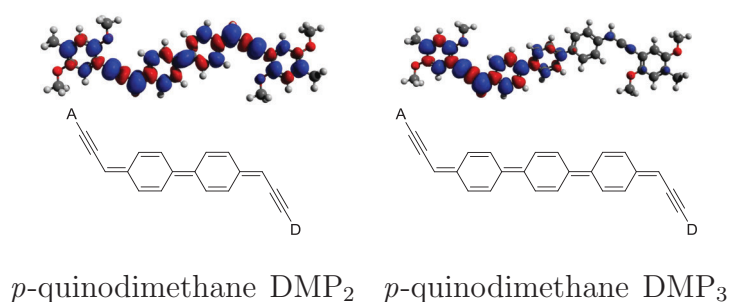


Figure A.7: Spin density isosurfaces of oligo(pheno)-*p*-quinodimethane DMP_{*n*} radical cations with ethynylene linkers optimized with the BLYP35 hybrid functional and Ahlrich's def2-TZVP basis set in dichloromethane (isosurface value: 0.001).

A.4 ONI_n and OPE_n Wires – Structural Parameters

In Tab. A.6 and Tab. A.7, the torsion angles of ONI_n wires ($n = 2-6$) and the bond lengths of the two terminating C–N bonds of OPE_n wires in their neutral and radical cationic state ($n = 2-5$) are listed, respectively.

Table A.6: Torsion angles of ONI_n wires around C–N bonds between adjacent ring units in degrees (starting at the anchoring group). Molecular structures were optimized with the BLYP35 functional and Ahlrich’s def2-TZVP basis set in benzene (PCM).

	ϕ_1	ϕ_2	ϕ_3	ϕ_4	ϕ_5	ϕ_6
ONI ₂	29.8	34.7	-	-	-	-
ONI ₃	34.2	38.2	45.5	-	-	-
ONI ₄	33.5	40.4	41.6	39.1	-	-
ONI ₅	34.2	41.4	39.3	33.3	40.7	-
ONI ₆	38.3	39.9	31.1	38.2	40.4	39.2

Table A.7: Lengths of the two terminating C–N bonds of OPE_n wires in Å. Molecular structures were optimized with the BLYP35 functional and Ahlrich’s def2-TZVP basis set in benzene (PCM) in their neutral and radical cationic state.

species		neut.	cat.
OPE ₂	d_1	1.37	1.34
	d_2	1.37	1.34
OPE ₃	d_1	1.37	1.34
	d_2	1.37	1.34
OPE ₄	d_1	1.37	1.35
	d_2	1.37	1.35
OPE ₅	d_1	1.38	1.34
	d_2	1.38	1.37

A.5 Assessing the Degree of Charge Delocalization in Molecular Wires

A.5.1 Comparison of Methods – Subregion by Monomer and Atom

In Tab. A.8, the theoretical tunneling-to-hopping crossover as derived from the degree of charge delocalization, given by Eq. (6.1), is provided for different thresholds of the spin density for defining the smallest possible subregion of charge localization. The results obtained from two different methods of determining the subregion (by atom or by monomer) are compared to the experimentally indicated crossover.

Table A.8: Comparison of the performance of different methods in predicting the tunneling–hopping crossover from molecular conductance experiments at room temperature. The theoretical crossover is derived from the degree of charge delocalization according to Eq. (6.1). Molecular structures were optimized with the BLYP35 hybrid functional and Ahlrich’s def2-TZVP basis set with a PCM (according to Tab. 6.1). The subregion for the assessment of the degree of localization was chosen either by atoms or by monomer units and according to different percentages of the spin density located on that subregion, ranging from 65 to 85%.

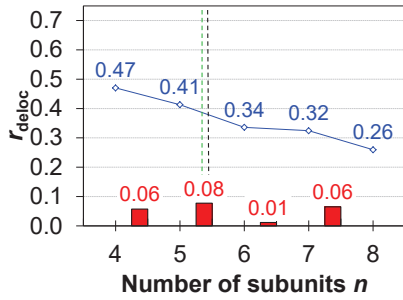
choice of subregion by threshold (spin density)	atom				monomer	exp.
	65-70%	70-75%	75-80%	80-85%	65-85%	
OPTI _n	5 → 6*	5 → 6	6 → 7	6 → 7	6 → 7**	6 → 7
OPI _n	5 → 6	5 → 6	5 → 6	5 → 6	5 → 6	5 → 6
ONI _n	3 → 4*	3 → 4*	3 → 4*	3 → 4*	3 → 4*	3 → 4
OAE _n	5 → 6	5 → 6	4 → 5	5 → 6	5 → 6	5 → 6
OPE _n	4 → 5	4 → 5	4 → 5	4 → 5	4 → 5	3 → 4

*Generally rather overlocalized description as indicated by a delocalization measure below 0.5 across the whole range of molecular lengths.

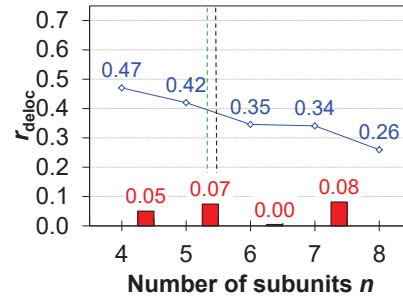
**Theoretical crossover solely based on the cut-off value $r = 0.5$ due to a relatively consistent change in the charge delocalization measure with growing molecular length.

A.5.2 Choice of Subregion by Atoms – OAE_n Wires

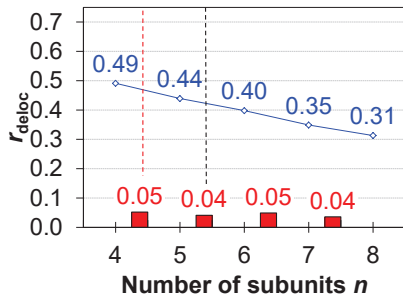
In Fig. A.8, the calculated delocalization measures r_{deloc} as defined by Eq. (6.1) are plotted for OAE_n wires as a function of the number of subunits n (blue line) and the corresponding change in r_{deloc} from subunit n to $n+1$ (red bars). Results are provided for different thresholds of the spin density for defining the smallest possible subregion of charge localization (by atom).



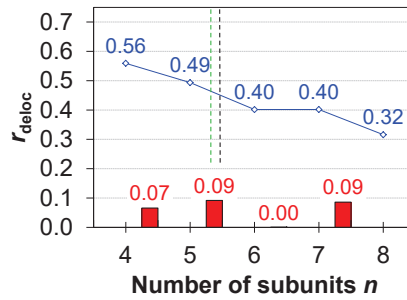
spin density (subregion): 65%



spin density (subregion): 70%



spin density (subregion): 75%



spin density (subregion): 80%

Figure A.8: Calculated delocalization measure r_{deloc} according to different percentages for the spin density as defined by Eq. (6.1) for OAE_n cationic radical wires as a function of the number of subunits n (blue line) and the corresponding changes from subunit n to $n+1$ (red bars). Black dotted line: Experimental crossover from tunneling to hopping. Coloured dotted line: Theoretically predicted crossover and its agreement with experiments (green: good; red: poor).

A.5.3 Choice of Subregion by Monomers – All Wires

In Fig. A.9, the delocalization measures r_{deloc} calculated from Eq. (6.1) are plotted for molecular wires as a function of the number of subunits n (blue line) and the corresponding change in r_{deloc} from subunit n to $n+1$ (red bars). The smallest possible subregion of charge localization was evaluated by step-wise inclusion of monomer units and holds 65-85% of the full spin density.

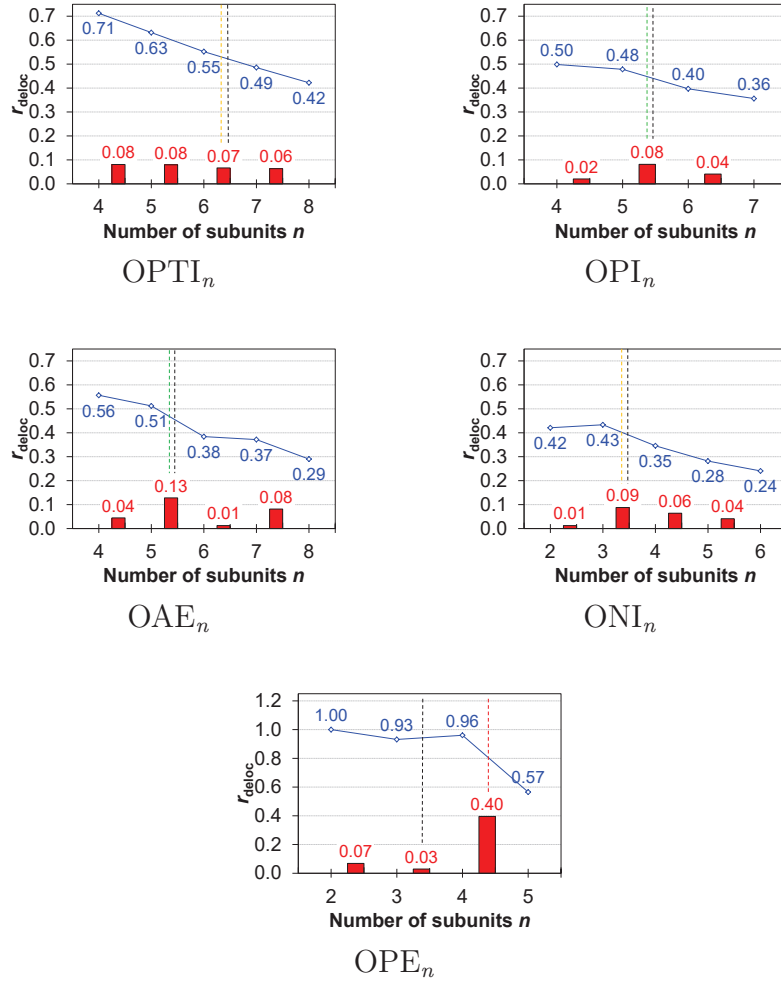


Figure A.9: Calculated delocalization measure r_{deloc} according to Eq. (6.1) for different molecular wires as a function of the number of subunits n (blue line) and the corresponding changes from subunit n to $n+1$ (red bars). Spin density on smallest possible subregion of charge localization: 65-85% (defined by monomer). Black dotted line: Experimental crossover from tunneling to hopping. Coloured dotted line: Theoretically predicted crossover and its agreement with experiments (green: good; orange: fairly well; red: poor).

A.5.4 Details on the Algorithm for Assessing the Degree of Charge Delocalization

In the following, details on the procedure of assessing the degree of charge delocalization according to Eq. (6.1) in Sec. 6.2 are provided: First, a certain threshold defining the majority of spin density needs to be defined, which is 80% in this work, as this range was found to give results in best agreement with the experiments.

Second, the smallest possible subregion hosting this predefined amount of spin density is determined as follows:

- The atoms of the molecule are sorted from most positive to most negative values for the local spin density (assessed by NPA partitioning).
- The largest positive value of local spin density is identified and defined as centre of the smallest possible subregion, where most of the spin density is located.
- Atoms in the vicinity (directly connected by chemical bonds) of this centre of highest local spin density are included stepwise into the region while summing the local spin densities up until the predefined spin density is reached or just exceeded (the exact threshold of, say, 80% can usually not be hit exactly owing to the atom-wise summation of spin densities; in practice, this leads to spin densities between 80% and 85% for the systems under study when a threshold of 80% is set). The subregion encompassing this amount of spin density represents the smallest possible subregion.

It has to be noted that the procedure described here works very well in all systems under study, since the center of highest spin density can always be identified unambiguously as there is only one such center present, and in all cases one continuous fragment bearing the majority of the spin density is found. If there were several regions within the molecule holding a similar high amount of spin density, the identification of the smallest possible subregion with a predefined amount of spin density would be less straightforward. One could then encounter a scenario where several centers of equally high spin density are found. In this case, one would need to repeat the procedure starting from each centre and then pick the smallest continuous unit holding the predefined amount of spin density.

Another aspect that needs to be considered when summing the spin density into the subregion is the treatment of negative contributions, as they can possibly lead to ambiguities in the assignment. For example, an extreme scenario would be the presence of two unpaired spin-up electrons and one unpaired spin-down electron, still resulting in a total spin density of one.

In this work, the negative contributions of the spin density are comparatively low and the greatest negative value obtained for the spin density per atom amounts to -0.1 for OPTI₄. The spin density is therefore used as an approximation to the excess positive charge due to the smaller basis-set dependence of local spins compared to local charges [144]. However, if very large amounts of negative spin density are present in the molecule under study, it may be advisable to rather use local charges instead of local spins for the determination of the degree of charge delocalization. One should then also consider employing partitioning schemes with smaller basis-set dependence, as for example Bader's scheme of Atoms in Molecules (AIM) [146] or Hirshfeld [219] population analysis despite being computationally more demanding.

A.6 Potential Energy Surface for Ring Torsion in OPE_n

As mentioned earlier in this work, charge delocalization is promoted by planarization of adjacent ring units and is likely pertained by torsion angles up to 40 degrees. However, the rotation of the benzene rings exceeding the critical torsion angle and therefore breaking charge delocalization could in principle lead to more localized structures. Therefore, single-point energy calculations were performed on OPE₄ molecules with the first ring unit rotated step-wise up to 90 degrees to evaluate whether these rotations are accessible at room temperature (Fig. A.10).

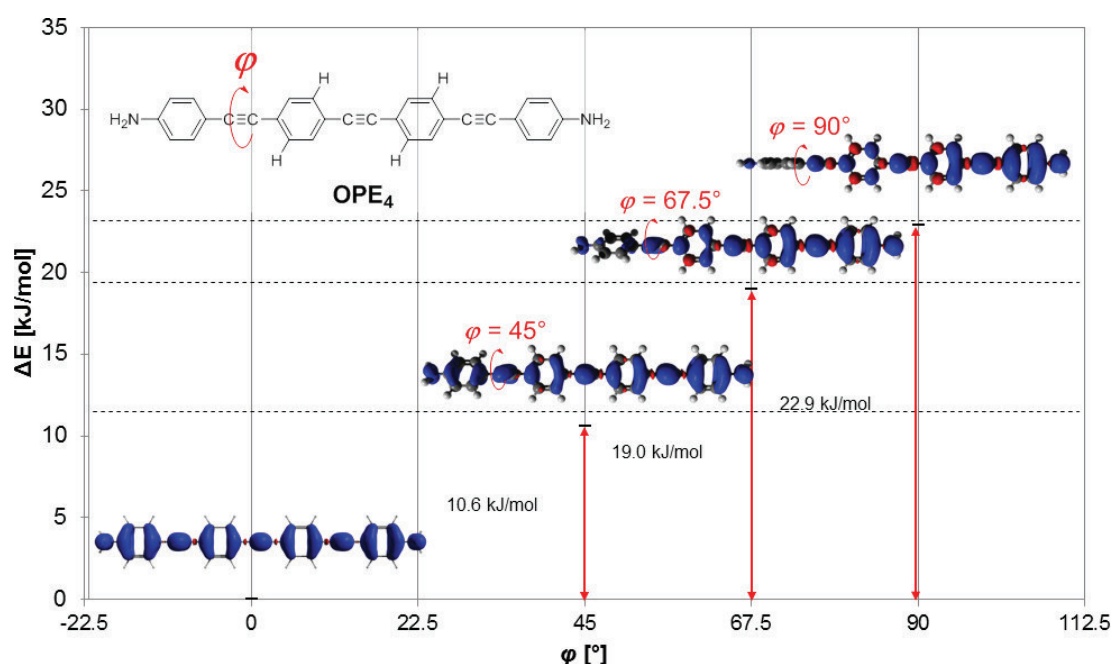


Figure A.10: Relative energies in kJ/mol of OPE₄ radical cationic wires and corresponding spin density surfaces from single-point calculations with the BLYP35 functional and Ahlrich's def2-TZVP basis set in benzene (PCM) as a function of the first inter-ring rotation by an angle ϕ . Relative energies are given for molecular structures, where the first ring unit is rotated around 45, 67.5 and 90 degrees with respect to the untilted molecular structure.

It was found that the barrier for the rotation by around 68 degrees, where charge delocalization is nearly broken, amounts to 19 kJ/mol and rises up to 23 kJ/mol for the rotation by 90 degrees. This would suggest that this rotation, leading to more strongly localized structures, is not likely to be accessible at room temperature.

However, as discussed in this work, it is likely that back donation of the nitrogen's free electron pair affects the electronic structure and thus the torsional profile, and that this back donation would be much less pronounced if the amine groups were bonded to a gold electrode surface (see Fig. A.11).

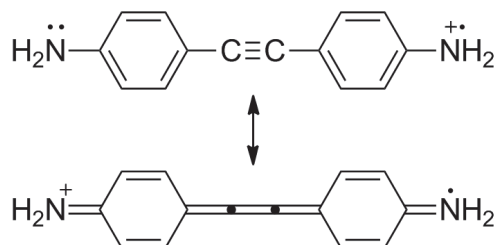


Figure A.11: Illustration how participation of the free electron pair in the π -system of the backbone may contribute to a more cumulene-like structure and thus to an increased barrier for ring torsion, compared with bare OPE_{*n*}.

A.7 Isolated OPTI_n Wires: BLYP35, LC-DFT and AM1 Results

In Fig. A.12, A.13 and Fig. A.14, the spin density isosurfaces of isolated OPTI_n wires, optimized with the BLYP35, the ω -B97X-D and the AM1 method, are shown, respectively.

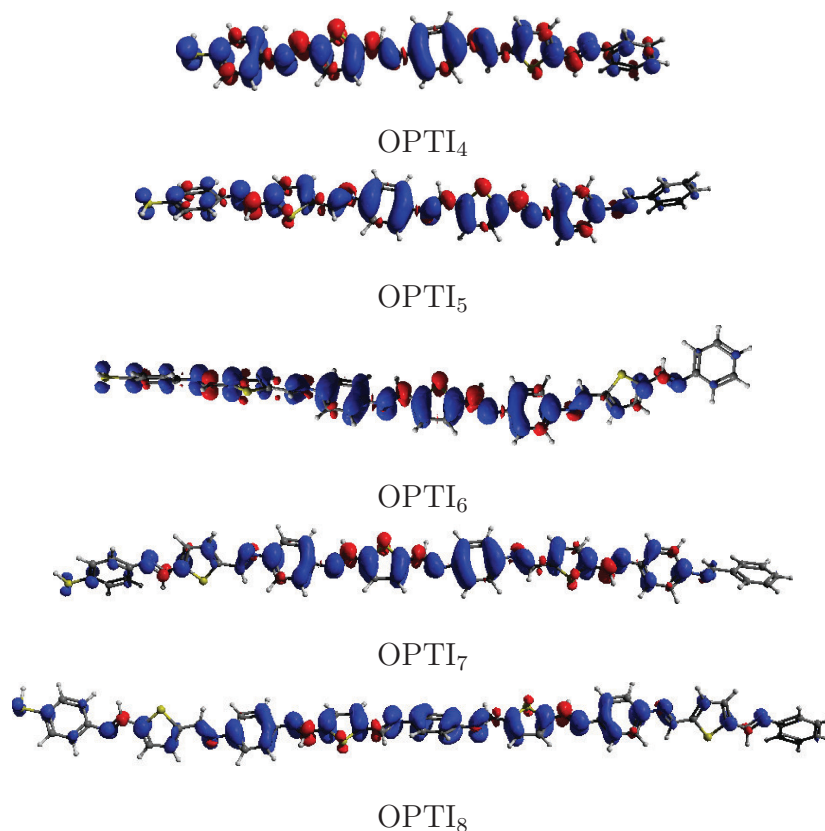


Figure A.12: Spin densities of isolated OPTI_n wires optimized with the BLYP35 functional and Ahlrich's def2-TZVP basis set.

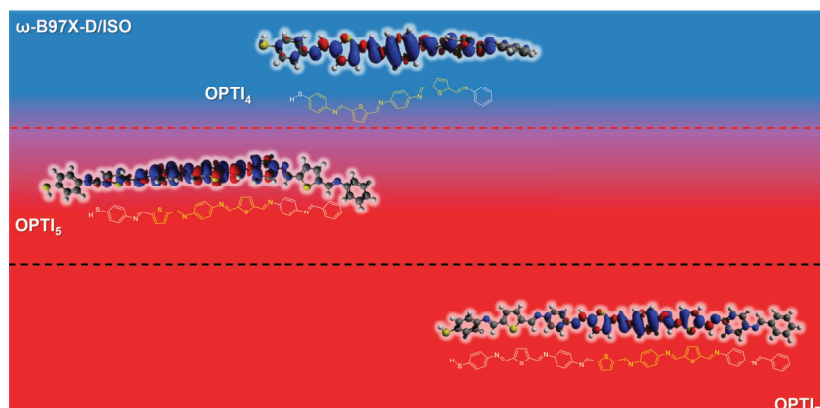


Figure A.13: Spin density isosurfaces of isolated OPTI_n radical cations from molecular structure optimizations with the ω -B97X-D functional and Ahlrich's def2-TZVP basis set. The degree of charge delocalization is coded by the background colour (charge delocalization: blue; increasing localization: red). Black dotted line: Experimental crossover from tunneling to hopping. Red dotted line: Theoretically predicted crossover based on the visual assessment of charge localization.

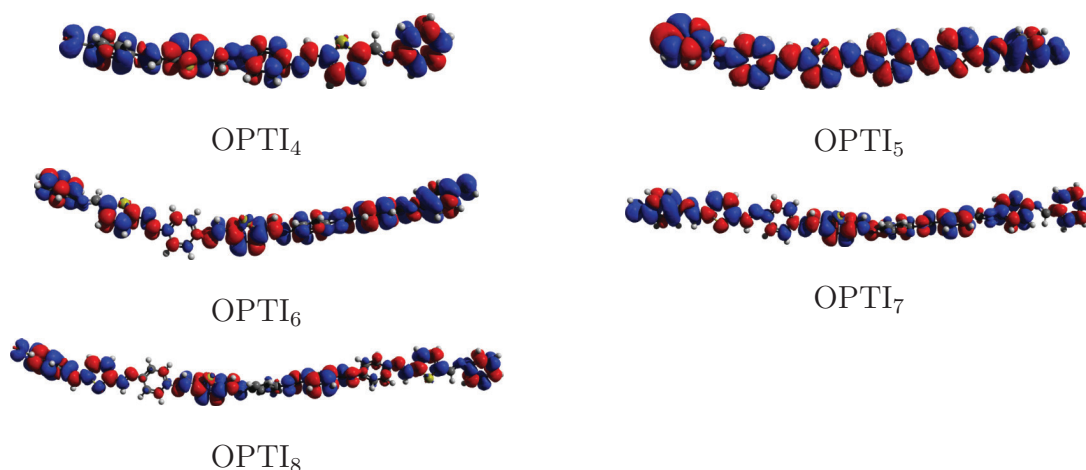


Figure A.14: Spin density isosurfaces of isolated OPTI_n radical cations from molecular structure optimizations with the AM1 method.

B. List of Abbreviations

DFT	density functional theory
KS-DFT	Kohn–Sham density functional theory
(ds)-DNA	(double-stranded) deoxyribonucleic acid
(IEF)PCM	(integral equation formalism) polarizable continuum model
LDA	local density approximation
GGA	generalized gradient approximation
(U)HF	(unrestricted) Hartree–Fock
CI	configuration interaction
RI	resolution-of-identity
LC	long-range corrected
G09	GAUSSIAN 09
TM	TURBOMOLE
NEGF	non-equilibrium Green’s function
SCF	self-consistent field
MO	molecular orbital
PES	potential energy surface
IV-CT	intervalence-charge transfer
NIR	near-infrared
EPR	electron paramagnetic resonance
STM	scanning tunneling microscopy
STM-BJ	STM-based break junction
MCBJ	mechanically controllable break junction
CP-AFM	conductive probe atomic force microscopy

HOMO	highest occupied molecular orbital
LUMO	lowest unoccupied molecular orbital
MV	mixed-valence
D–B–A	Donor–Bridge–Acceptor
DMP	dimethoxy- <i>p</i> -phenylene
OPV	oligo- <i>p</i> -phenylene-vinylene
(Ar ₂ N) ₂ T	oligothiophene-bridged bis(diarylamine)
PTM	perchlorotriphenylmethyl
PPV	<i>p</i> -phenylene-vinylene
TV	thiophene-vinylene
OPTI	oligophenylene-thiophene-imine
OPI	oligophenylene-imine
ONI	oligonaphthalene-fluoroene-imine
OPE	oligophenylene-ethynylene
OAE	oligoarylene-ethynylene
SAM	self-assembled monolayer
AIMD	<i>ab initio</i> molecular dynamics
NPA	natural population analysis
AIM	Atoms in Molecules
DCM	dichloromethane
ACN	acetonitrile
THF	tetrahydrofuran
DMF	dimethylformamide
INDO	Intermediate neglect of differential overlap
ZDO	zero differential overlap
NDDO	neglect of diatomic differential overlap
CNDO	complete neglect of differential overlap
DFTB(A)	(analytical) tight-binding KS-DFT

References

- [1] Scheer, E.; Cuevas, J. C. *Molecular electronics: an introduction to theory and experiment*; volume 1 World Scientific: 2010.
- [2] Heath, J. R.; Ratner, M. A. Molecular electronics *Phys. Today* **2003**, *56*, 43-49.
- [3] Low, P. J.; Marqués-González, S. Molecular wires: an overview of the building blocks of molecular electronics. In *Single-Molecule Electronics*; Springer: 2016.
- [4] Waldrop, M. M. More than Moore *Nature* **2016**, *530*, 144–148.
- [5] McCreery, R. L.; Yan, H.; Bergren, A. J. A critical perspective on molecular electronic junctions: there is plenty of room in the middle *Phys. Chem. Chem. Phys.* **2013**, *15*, 1065–1081.
- [6] Garner, M. H.; Li, H.; Chen, Y.; Su, T.; Shangguan, Z.; Paley, D.; Liu, T.; Ng, F.; Li, H.; Xiao, S.; Nuckolls, C.; Venkataraman, L.; Solomon, G. Comprehensive suppression of single-molecule conductance using destructive σ -interference *Nature* **2018**, *558*, 415–419.
- [7] Jones, L. O.; Mosquera, M. A.; Fu, B.; Schatz, G. C.; Marks, T. J.; Ratner, M. A. Quantum Interference and Substantial Property Tuning in Conjugated Z-ortho-Regio-Resistive Organic (ZORRO) Junctions *Nano Lett.* **2019**, *19*, 8956-8963.
- [8] Garner, M. H.; Koerstz, M.; Jensen, J. H.; Solomon, G. C. The Bicyclo[2.2.2]octane Motif: A Class of Saturated Group 14 Quantum Interference Based Single-Molecule Insulators *J. Phys. Chem. Lett.* **2018**, *9*, 6941-6947.
- [9] Naaman, R.; Waldeck, D. H. Chiral-Induced Spin Selectivity Effect *J. Phys. Chem. Lett.* **2012**, *3*, 2178-2187.

- [10] Mtangi, W.; Kiran, V.; Fontanesi, C.; Naaman, R. Role of the Electron Spin Polarization in Water Splitting *J. Phys. Chem. Lett.* **2015**, *6*, 4916-4922.
- [11] Naaman, R.; Paltiel, Y.; Waldeck, D. H. Chiral molecules and the electron spin *Nature Reviews* **2019**, *3*, 250–260.
- [12] Abendroth, J. M.; Cheung, K. M.; Stemer, D. M.; Hadri, M. S. E.; Zhao, C.; Fullerton, E. E.; Weiss, P. S. Spin-Dependent Ionization of Chiral Molecular Films *J. Am. Chem. Soc.* **2019**, *141*, 3863-3874.
- [13] Aragones, A. C.; Medina, E.; Ferrer-Huerta, M.; Gimeno, N.; Teixido, M.; Palma, J. L.; Tao, N.; Ugalde, J. M.; Giralt, E.; Diez-Perez, I.; Mujica, V. Measuring the Spin-Polarization Power of a Single Chiral Molecule *Small* **2017**, *13*, 1602519.
- [14] Kettner, M.; Maslyuk, V. V.; Nürenberg, D.; Seibel, J.; Gutierrez, R.; Cuniberti, G.; Ernst, K.-H.; Zacharias, H. Chirality-Dependent Electron Spin Filtering by Molecular Monolayers of Helicenes *J. Phys. Chem. Lett.* **2018**, *9*, 2025-2030.
- [15] Maslyuk, V. V.; Gutierrez, R.; Dianat, A.; Mujica, V.; Cuniberti, G. Enhanced Magnetoresistance in Chiral Molecular Junctions *J. Phys. Chem. Lett.* **2018**, *9*, 5453-5459.
- [16] Zöllner, M. S.; Varela, S.; Medina, E.; Mujica, V.; Herrmann, C. Insight into the Origin of Chiral-Induced Spin Selectivity from a Symmetry Analysis of Electronic Transmission *J. Chem. Theory Comput.* **2020**, *16*, 2914-2929.
- [17] Anariba, F.; McCreery, R. L. Electronic Conductance Behavior of Carbon-Based Molecular Junctions with Conjugated Structures *J. Phys. Chem. B* **2002**, *106*, 10355-10362.
- [18] Bergren, A. J.; McCreery, R. L.; Stoyanov, S. R.; Gusarov, S.; Kovalenko, A. Electronic Characteristics and Charge Transport Mechanisms for Large Area Aromatic Molecular Junctions *J. Phys. Chem. C* **2010**, *114*, 15806-15815.

- [19] Yan, H.; Bergren, A. J.; McCreery, R. L. All-Carbon Molecular Tunnel Junctions *J. Am. Chem. Soc.* **2011**, *133*, 19168-19177.
- [20] S. Kawanishi, Y. Hiraku, S. O. Mechanism of guanine-specific DNA damage by oxidative stress and its role in carcinogenesis and aging *Mutat. Res.* **2001**, *488*, 65-76.
- [21] Kawai, K.; Majima, T. Hole transfer kinetics of DNA *Acc. Chem. Res.* **2013**, *46*, 2616-2625.
- [22] O'Neil, M. A.; Barton, J. K. DNA charge transport: conformationally gated hopping through stacked domains *J. Am. Chem. Soc.* **2004**, *126*, 11471-11483.
- [23] Wallace, S. S. Biological consequences of free radical-damaged DNA bases *Free Radical Biol. Med.* **2002**, *33*, 1-14.
- [24] Zhang, Y.; Liu, C.; Balaeff, A.; Skourtis, S. S.; Beratan, D. N. Biological charge transfer via flickering resonance *Proceedings of the National Academy of Sciences* **2014**, *111*, 10049-10054.
- [25] Woiczikowski, P. B.; Kubař, T.; Gutiérrez, R.; Cuniberti, G.; Elstner, M. Structural stability versus conformational sampling in biomolecular systems: Why is the charge transfer efficiency in G4-DNA better than in double-stranded DNA? *J. Chem. Phys.* **2010**, *133*, 035103.
- [26] Shah, A.; Adhikari, B.; Martić, S.; Munir, A.; Shahzad, S.; Ahmad, K.; Kraatz, H.-B. Electron transfer in peptides *Chem. Soc. Rev.* **2015**, *44*, 1015-1027.
- [27] Giese, B.; Eckhardt, S.; Lauz, M. Electron transfer in peptides and proteins *Encyclopedia of radicals in chemistry, biology and materials* **2012**, .
- [28] Hines, T.; Diez-Perez, I.; Hihat, J.; Wang, H. L. Z.-S.; Zhao, J.; Zhou, G.; Müllen, K.; Tao, N. Transition from Tunneling to Hopping in Single Molecular Junctions by Measuring Length and Temperature Dependence *J. Am. Chem. Soc.* **2010**, *132*, 11658-11664.

- [29] Kamenetska, M.; Widawsky, J. R.; Dell'Angela, M.; Frei, M.; Venkataraman, L. Temperature dependent tunneling conductance of single molecule junctions *J. Chem. Phys.* **2017**, *146*, 092311.
- [30] Taherinia, D.; Smith, C. E.; Ghosh, S.; Odoh, S. O.; Balhorn, L.; Gagliardi, L.; Cramer, C. J.; Frisbie, C. D. Charge Transport in 4 nm Molecular Wires with Interrupted Conjugation: Combined Experimental and Computational Evidence for Thermally Assisted Polaron Tunneling *ACS Nano* **2015**, *10*, 4372-4383.
- [31] Smith, C. E.; Odoh, S. O.; Ghosh, S.; Gagliardi, L.; Cramer, C. J.; Christopher, J. K.; Frisbie, D. C. Length-Dependent Nanotransport and Charge Hopping Bottlenecks in Long Thiophene-Containing π -Conjugated Molecular Wires *J. Am. Chem. Soc.* **2015**, *137*, 15732-15741.
- [32] Choi, S. H.; Kim, B.; Frisbie, C. D. Electrical Resistance of Long Conjugated Molecular Wires *Science* **2008**, *320*, 1482-1486.
- [33] Choi, S. H.; Risko, C.; Delgado, M. C. R.; Kim, B.; Bredas, J.-L.; Frisbie, C. D. Transition from Tunneling to Hopping Transport in Long, Conjugated Oligo-imine Wires Connected to Metals *J. Am. Chem. Soc.* **2010**, *132*, 4358-4368.
- [34] Zhao, X.; Huang, C.; Gulcur, M.; Batsanov, A. S.; Baghernejad, M.; Hong, W.; Bryce, M. R.; Wandlowski, T. Oligo(aryleneethynylene)s with Terminal Pyridyl Groups: Synthesis and Length Dependence of the Tunneling-to-Hopping Transition of Single-Molecule Conductances *Chem. Mater.* **2013**, *25*, 4340-4347.
- [35] Lu, Q.; Liu, K.; Zhang, H.; Du, Z.; Wang, X.; Wang, F. From Tunneling to Hopping: A Comprehensive Investigation of Charge Transport Mechanism in Molecular Junctions Based on Oligo(p-phenylene ethynylene)s *ACS Nano* **2009**, *3*, 3861-3868.
- [36] Solomon, G. C.; Herrmann, C.; Ratner, M. A. *Molecular Electronic Junction Transport: Some Pathways and Some Ideas*; Springer: 2011.
- [37] Landauer, R. Spatial variation of currents and fields due to localized scatterers in metallic conduction *IBM J. Res. Dev.* **1957**, *1*, 223-231.

- [38] Landauer, R. Electrical resistance of disordered one-dimensional lattices *Philos. Mag.* **1970**, *21*, 863-867.
- [39] Büttiker, M.; Imry, Y.; Landauer, R.; Pinas, S. Generalized many-channel conductance formula with application to small rings *Phys. Rev. B* **1985**, *31*, 6207-6215.
- [40] Marcus, R. A. Exchange reactions and electron transfer reactions including isotopic exchange. Theory of oxidation-reduction reactions involving electron transfer. Part 4.—A statistical-mechanical basis for treating contributions from solvent, ligands, and inert salt *Discuss. Faraday Soc.* **1960**, *29*, 21-31.
- [41] Marcus, R. A. On the theory of electron-transfer reactions. VI. Unified treatment for homogeneous and electrode reactions *J. Chem. Phys.* **1965**, *43*, 679-701.
- [42] Nitzan, A. *Chemical dynamics in condensed phases: relaxation, transfer and reactions in condensed molecular systems*; Oxford university press: 2006.
- [43] Nitzan, A. The Relationship between Electron Transfer Rate and Molecular Conduction. 2. The Sequential Hopping Case *Isr. J. Chem.* **2002**, *42*, 163-166.
- [44] Migliore, A.; Schiff, P.; Nitzan, A. On the relationship between molecular state and single electron pictures in simple electrochemical junctions *Phys. Chem. Chem. Phys.* **2012**, *14*, 13746-13753.
- [45] Nitzan, A. A Relationship between Electron-Transfer Rates and Molecular Conduction *J. Phys. Chem. A* **2001**, *105*, 2677-2679.
- [46] Giannini, S.; Carof, A.; Blumberger, J. Crossover from Hopping to Band-Like Charge Transport in an Organic Semiconductor Model: Atomistic Nonadiabatic Molecular Dynamics Simulation *J. Phys. Chem. Lett.* **2018**, *9*, 3116-3123.
- [47] Giannini, S.; Carof, A.; Ellis, M.; Yang, H.; Ziogos, O. G.; Ghosh, S.; Blumberger, J. Quantum localization and delocalization of charge carriers in organic semiconducting crystals *Nat. Commun.* **2019**, *10*, 1-12.

- [48] Kubař, T.; Elstner, M.; Popescu, B.; Kleinekathöfer, U. Polaron Effects on Charge Transport through Molecular Wires: A Multiscale Approach *J. Chem. Theory Comput.* **2017**, 286-296.
- [49] Wolter, M.; Elstner, M.; Kleinekathöfer, U.; Kubař, T. Microsecond Simulation of Electron Transfer in DNA: Bottom-Up Parametrization of an Efficient Electron Transfer Model Based on Atomistic Details *J. Phys. Chem. B* **2017**, 121, 529-549.
- [50] Renz, M.; Kaupp, M. Predicting the Localized/Delocalized Character of Mixed-Valence Diquinone Radical Anions. Toward the Right Answer for the Right Reason *J. Phys. Chem. A* **2012**, 116, 10629-10637.
- [51] Renz, M.; Kess, M.; Diedenhofen, M.; Klamt, A.; Kaupp, M. Reliable Quantum Chemical Prediction of the Localized/Delocalized Character of Organic Mixed-Valence Radical Anions. From Continuum Solvent Models to Direct-COSMO-RS *J. Chem. Theory Comput.* **2012**, 8, 4189-4203.
- [52] Kaupp, M.; Renz, M.; Parthey, M.; Stolte, M.; Würthner, F.; Lambert, C. Computational and spectroscopic studies of organic mixed-valence compounds: where is the charge? *Phys. Chem. Chem. Phys.* **2011**, 13, 16973-16986.
- [53] Parthey, M.; Kaupp, M. Quantum-chemical insights into mixed-valence systems: within and beyond the Robin-Day scheme *Chem. Soc. Rev.* **2014**, 43, 5067-5088.
- [54] Kröncke, S.; Herrmann, C. Designing Long-Range Charge Delocalization from First-Principles *J. Chem. Theory Comput.* **2019**, 15, 165-177.
- [55] Cramer, C. J.; Truhlar, D. G. Density functional theory for transition metals and transition metal chemistry *Phys. Chem. Chem. Phys.* **2009**, 11, 10757-10816.
- [56] Mori-Sanchez, P.; Cohen, A. J.; Yang, W. Localization and Delocalization Errors in Density Functional Theory and Implications for Band-Gap Prediction *Phys. Rev. Lett.* **2008**, 100, 146401.
- [57] Herrmann, C.; Yu, L.; Reiher, M. Spin States in Polynuclear Clusters: The [Fe₂O₂] Core of the Methane Monooxygenase Active Site *J. Comput. Chem.* **2006**, 27, 1223-1239.

- [58] Zhao, Q.; Kulik, H. J. Where Does the Density Localize in the Solid State? Divergent Behavior for Hybrids and DFT+U *J. Chem. Theory Comput.* **2018**, *14*, 670-683.
- [59] Maier, T. M.; Arbuznikov, A. V.; Kaupp, M. Local hybrid functionals: Theory, implementation, and performance of an emerging new tool in quantum chemistry and beyond *WIREs Comput. Mol. Sci.* **2019**, *9*, e1378.
- [60] Tao, N. J. Electron transport in molecular junctions *Nat. Nanotechnol.* **2006**, *1*, 173-181.
- [61] Day, P.; Hush, N.; Sand, C.; Robin, J. Mixed valence: origins and developments *Philos. Trans. R. Soc. London, Ser. A* **2008**, *366*, 5-14.
- [62] Hankache, J.; Wenger, O. S. Organic Mixed Valence *Chem. Rev.* **2011**, *111*, 5138-5178.
- [63] Heckmann, A.; Lambert, C. Organic Mixed-Valence Compounds: A Playground for Electrons and Holes *Angew. Chem. Int. Ed.* **2012**, *51*, 326-392.
- [64] Stuyver, T.; Zeng, T.; Tsuji, Y.; Fias, S.; Geerlings, P.; de Proft, F. Captodative Substitution: A Strategy for Enhancing the Conductivity of Molecular Electronic Devices *J. Phys. Chem. C* **2018**, *122*, 3194-3200.
- [65] Stuyver, T.; Fias, S.; Proft, F. D.; Geerlings, P.; Tsuji, Y.; Hoffmann, R. Enhancing the conductivity of molecular electronic devices *J. Chem. Phys.* **2017**, *146*, 092310.
- [66] Xiang, L.; Palma, J. L.; Bruot, C.; Mujica, V.; Ratner, M. A.; Tao, N. Intermediate tunnelling-hopping regime in DNA charge transport *Nat. Chem.* **2015**, *7*, 221-226.
- [67] Xiang, L.; Palma, J. L.; Bruot, C.; Mujica, V.; Ratner, M. A.; Tao, N. Corrigendum: Intermediate tunnelling-hopping regime in DNA charge transport *Nat. Chem.* **2017**, *9*, 295-295.
- [68] Husch, T.; Vaucher, A. C.; Reiher, M. Semiempirical molecular orbital models based on the neglect of diatomic differential overlap approximation *Int. J. Quantum Chem.* **2018**, *118*, e25799.

- [69] Stewart, J. Reviews in computational chemistry. In *Semiempirical molecular orbital methods*; VCH New York: 1990.
- [70] Kubař, T.; Elstner, M. A hybrid approach to simulation of electron transfer in complex molecular systems *Journal of The Royal Society Interface* **2013**, *10*, 20130415.
- [71] Kubař, T.; Elstner, M. Efficient algorithms for the simulation of non-adiabatic electron transfer in complex molecular systems: application to DNA *Phys. Chem. Chem. Phys.* **2013**, *15*, 5794–5813.
- [72] Gaus, M.; Cui, Q.; Elstner, M. Density functional tight binding: Application to organic and biological molecules *WIREs Comput. Mol. Sci.* **2014**, 49-61.
- [73] Chen, F.; Hihath, J.; Huang, Z.; Li, X.; Tao, N. Measurement of single-molecule conductance *Annu. Rev. Phys. Chem.* **2007**, *58*, 535-564.
- [74] Chen, F.; Li, X.; Hihath, J.; Huang, Z.; Tao, N. Effect of Anchoring Groups on Single-Molecule Conductance: Comparative Study of Thiol-, Amine-, and Carboxylic-Acid-Terminated Molecules *J. Am. Chem. Soc.* **2006**, *128*, 15874-15881.
- [75] Reed, M. A.; Zhou, C.; Muller, C.; Burgin, T.; Tour, J. Conductance of a molecular junction *Science* **1997**, *278*, 252–254.
- [76] Li, Z.; Han, B.; Mészáros, G.; Pobelov, I.; Wandlowski, T.; Błaszczuk, A.; Mayor, M. Two-dimensional assembly and local redox-activity of molecular hybrid structures in an electrochemical environment *Faraday Discuss.* **2006**, *131*, 121–143.
- [77] Khoo, K. H.; Chen, Y.; Li, S.; Quek, S. Y. Length dependence of electron transport through molecular wires—a first principles perspective *Phys. Chem. Chem. Phys.* **2015**, *17*, 77–96.
- [78] Li, G.; Movaghar, B.; Nitzan, A.; Ratner, M. A. Polaron formation: Ehrenfest dynamics vs. exact results *J. Chem. Phys.* **2013**, *138*, 044112.
- [79] Li, G.; Govind, N.; Ratner, M. A.; Cramer, C. J.; Gagliardi, L. Influence of Coherent Tunneling and Incoherent Hopping on the Charge

- Transfer Mechanism in Linear Donor-Bridge-Acceptor Systems *J. Phys. Chem.* **2015**, *6*, 4889-4897.
- [80] Kastlunger, G.; Stadler, R. Density functional theory based direct comparison of coherent tunneling and electron hopping in redox-active single-molecule junctions *Phys. Rev. B* **2015**, *91*, 125410.
- [81] Imry, Y. *Physics of nanoscopic systems*; World Scientific: 1986.
- [82] Dong, B.; Ding, G. H.; Lei, X. L. Time-dependent quantum transport through an interacting quantum dot beyond sequential tunneling: second-order quantum rate equations *J. Phys.: Condens. Matter* **2015**, *27*, 205303.
- [83] Datta, S. *Quantum Transport: Atom to Transistor*; Cambridge University Press: Cambridge, England, 2005.
- [84] Mahan, G. D. *Quantum Many Particle Physics*; Plenum Press: New York, 1990.
- [85] Kohn, W.; Sham, L. Self-Consistent Equations Including Exchange and Correlation Effects *Phys. Rev. A* **1965**, *140*, 1133-1138.
- [86] Hohenberg, P.; Kohn, W. Inhomogeneous Electron Gas *Phys. Rev. B* **1964**, *136*, 864-871.
- [87] Herrmann, C.; Solomon, G. C.; Subotnik, J. E.; Mujica, V.; Ratner, M. A. Ghost transmission: How large basis sets can make electron transport calculations worse *J. Chem. Phys.* **2010**, *132*, 024103.
- [88] Carey, R.; Chen, L.; Gu, B.; Franco, I. When can time-dependent currents be reproduced by the Landauer steady-state approximation? *J. Chem. Phys.* **2017**, *146*, 174101.
- [89] Liu, H.; Zhao, Z.; Wang, N.; Yu, C.; Zhao, J. Can the Transition from Tunneling to Hopping in Molecular Junctions Be Predicted by Theoretical Calculation? *J. Comput. Chem.* **2011**, *32*, 1687-1693.
- [90] Nitzan, A. Electron Transmission through molecules and molecular interfaces *Annu. Rev. Phys. Chem.* **2001**, *52*, 681-750.

- [91] Berlin, Y. A.; Hutchison, G. R.; Rempala, P.; Ratner, M. A.; Michl, J. Charge Hopping in Molecular Wires as a Sequence of Electron-Transfer Reactions *J. Phys. Chem. A* **2003**, *107*, 3970-3980.
- [92] Segal, D.; Nitzan, A.; Davis, W. B.; Wasielewski, M. R.; Ratner, M. A. Electron transfer rates in bridged molecular systems 2. A steady-state analysis of coherent tunneling and thermal transitions *J. Phys. Chem. B* **2000**, *104*, 3817-3829.
- [93] Hush, N. S. Adiabatic Rate Processes at Electrodes. I. Energy-Charge Relationships *J. Chem. Phys.* **1958**, *28*, 962-972.
- [94] Chidsey, C. E. D. Free Energy and Temperature Dependence of Electron Transfer at the Metal-Electrolyte Interface *Science* **1991**, *251*, 919-922.
- [95] Strange, M.; Thygesen, K. Image-charge-induced localization of molecular orbitals at metal-molecule interfaces: Self-consistent GW calculations *Phys. Rev. B* **2012**, *86*, 195121.
- [96] Friis, E. P.; Kharkats, Y. I.; Kuznetsov, A. M.; Ulstrup, J. In Situ Scanning Tunneling Microscopy of a Redox Molecule as a Vibrationally Coherent Electronic Three-Level Process *J. Phys. Chem. A* **1998**, *102*, 7851-7859.
- [97] Thygesen, K. S.; Rubio, A. Renormalization of Molecular Quasiparticle Levels at Metal-Molecule Interfaces: Trends across Binding Regimes *Phys. Rev. Lett.* **2009**, *102*, 046802.
- [98] Neaton, J. B.; Hybertsen, M. S.; Louie, S. G. Renormalization of Molecular Electronic Levels at Metal-Molecule Interfaces *Phys. Rev. Lett.* **2006**, *97*, 216405.
- [99] Aradhya, S. V.; Venkataraman, L. Single-molecule junctions beyond electronic transport *Nat. Nanotechnol.* **2013**, *8*, 399-410.
- [100] Giese, B.; Amaudrut, J.; Koehler, A.-K.; Spormann, M.; Wessely, S. Direct observation of hole transfer through DNA by hopping between adenine bases and by tunnelling *Nature* **2001**, *412*, 318-320.
- [101] Xu, B.; Zhang, P.; Li, X.; Tao, N. Direct Conductance Measurement of Single DNA Molecules in Aqueous Solution *Nano Lett.* **2004**, *4*, 1105-1108.

- [102] Livshits, G. I.; Stern, A.; Rotem, D.; Borovok, N.; Eidelstein, G.; Migliore, A.; Penzo, E.; Skourtis, S. J. W. R. D. F. S. S.; Cuevas, J. C.; Gurevich, L.; Kotlyar, A. B.; Porath, D. Long-range charge transport in single G-quadruplex DNA molecules *Nat. Nanotechnol.* **2014**, *9*, 1040-1046.
- [103] Renaud, N.; Berlin, Y. A.; Lewis, F. D.; Ratner, M. A. Between Superexchange and Hopping: An Intermediate Charge-Transfer Mechanism in Poly(A)-Poly(T) DNA Hairpins *J. Am. Chem. Soc.* **2013**, *135*, 3953-3963.
- [104] Smit, R. H. M.; Untiedt, C.; Rubio-Bollinger, G.; Segers, R. C.; van Ruitenbeek, J. M. Observation of a Parity Oscillation in the Conductance of Atomic Wires *Phys. Rev. Lett.* **2003**, *91*, 076805.
- [105] Tada, T.; Nozaki, D.; Kondo, M.; Hamayama, S.; Yoshizawa, K. Oscillation of Conductance in Molecular Junctions of Carbon Ladder Compounds *J. Am. Chem. Soc.* **2004**, *126*, 14182-14189.
- [106] Grib, N. V.; Ryndyk, D. A.; Gutiérrez, R.; Cuniberti, G. Distance-dependent coherent charge transport in DNA: crossover from tunneling to free propagation *Biophys. Chem.* **2010**, *1*, 77-85.
- [107] Büttiker, M. Coherent and sequential tunneling in series barriers *IBM J. Res. Dev.* **1988**, *32*, 63-75.
- [108] Kim, H.; Kilgour, M.; Segal, D. Intermediate Coherent-Incoherent Charge Transport: DNA as a Case Study *J. Phys. Chem. C* **2016**, *120*, 23951-23962.
- [109] Wasielewski, M. R.; Niemczyk, M. P.; Johnson, D. G.; Svec, W. A.; Minsek, D. W. Ultrafast photoinduced electron transfer in rigid donor-spacer-acceptor molecules: modification of spacer energetics as a probe for superexchange *Tetrahedron* **1989**, *45*, 4785-4806.
- [110] Lindeman, S. V.; Rosokha, S. V.; Sun, D.; Kochi, J. K. X-ray Structure Analysis and the Intervalent Electron Transfer in Organic Mixed-Valence Crystals with Bridged Aromatic Cation Radicals *J. Am. Chem. Soc.* **2002**, *124*, 843-855.

- [111] Rosokha, S.; Sun, D.-L.; Kochi, J. Conformation, Distance, and Connectivity Effects on Intramolecular Electron Transfer between Phenylene-Bridged Aromatic Redox Centers *J. Phys. Chem. A* **2002**, *106*, 2283-2292.
- [112] Sun, D.; Lindeman, S. V.; Rathore, R.; Kochi, J. K. Intramolecular (electron) delocalization between aromatic donors and their tethered cation-radicals. Application of electrochemical and structural probes *J. Chem. Soc.* **2001**, *2*, 1585-1594.
- [113] Hush, N. S. Homogeneous and heterogeneous optical and thermal electron transfer *Electrochim. Acta* **1968**, *13*, 1005-1023.
- [114] Hush, N. Distance Dependence of Electron Transfer Rates *Coord. Chem. Rev.* **1985**, *64*, 135-157.
- [115] Creutz, C.; Newton, M. D.; Sutin, N. Metal-ligand and metal-metal coupling elements *J. Photochem. Photobiol., A* **1994**, *82*, 47-59.
- [116] Coropceanu, V.; Malagoli, M.; Andre, J. M.; Bredas, J. L. Electronic Couplings in Organic Mixed-Valence Compounds: The Contribution of Photoelectron Spectroscopy *J. Am. Chem. Soc.* **2002**, *124*, 10519.
- [117] Barbara, P. F.; Meyer, T. J.; Ratner, M. A. Contemporary Issues in Electron Transfer Research *J. Phys. Chem.* **1996**, *100*, 13148-13168.
- [118] Barlow, S.; Risko, C.; Chung, S.-J.; Tucker, N. M.; Coropceanu, V.; Jones, S. C.; Levi, Z.; Bredas, J.-L.; Marder, S. R. Intervalence Transitions in the Mixed-Valence Monocations of Bis(triarylamines) Linked with Vinylene and Phenylene-Vinylene Bridges *J. Am. Chem. Soc.* **2005**, *127*, 16900-16911.
- [119] Odom, S. A.; Lancaster, K.; Beverina, L.; Lefler, K. M.; Thompson, N.; J.; Coropceanu, V.; Bredas, J.-L.; Marder, S.; Barlow, S. Bis[bis-(4-alkoxyphenyl)amino] Derivatives of Dithienylethene, Bithiophene, Dithienothiophene and Dithienopyrrole: Palladium-Catalysed Synthesis and Highly Delocalised Radical Cations *Chem. Eur. J.* **2007**, *13*, 9637-9646.
- [120] Yang, J.; Zhang, W.; Si, Y.; Zhao, Y. Intramolecular Electronic Couplings in Class II/III Organic Mixed-Valence Systems of Bis(1,4-dimethoxybenzene) *J. Phys. Chem. B* **2012**, *116*, 14126-14135.

- [121] Mangaud, E.; de la Lande, A.; Meier, C.; Desouter-Lecomte, M. Electron transfer within a reaction path model calibrated by constrained DFT calculations: Application to mixed-valence organic compounds *Phys. Chem. Chem. Phys.* **2015**, *17*, 30889-30903.
- [122] Lacroix, J. C.; Chane-Ching, K. I.; Maquère, F.; Maurel, F. Intrachain Electron Transfer in Conducting Oligomers and Polymers: The Mixed Valence Approach *J. Am. Chem. Soc.* **2006**, *128*, 7264-7276.
- [123] Reuter, L. G.; Bonnard, A. G.; Stückland, A. C.; Heand, B.; Patiand, P. B.; Zade, S. S.; Wenger, O. Charge Delocalization in a Homologous Series of α,α' -Bis(dianisylamino)-Substituted Thiophene Monocations *J. Phys. Chem. A* **2012**, *116*, 7345-7352.
- [124] Marcus, R. A.; Sutin, N. Electron transfers in chemistry and biology *Biochim. Biophys. Acta* **1985**, *811*, 265-322.
- [125] Brunschwig, B. S.; Sutin, N. Energy surfaces, reorganization energies, and coupling elements in electron transfer *Coord. Chem. Rev.* **1999**, *187*, 233-254.
- [126] Reimers, J. R.; Hush, N. S. The effects of couplings to symmetric and antisymmetric modes and minor asymmetry on the spectral properties of mixed-valence and related charge-transfer systems *J. Chem. Phys.* **1996**, *208*, 177-193.
- [127] Szabo, A.; Ostlund, N. S. *Modern quantum chemistry: introduction to advanced electronic structure theory*; Courier Corporation: 2012.
- [128] Cramer, C. J. *Essentials of Computational Chemistry - Theories and Models*; Wiley: 2 ed.; 2013.
- [129] Jensen, F. *Introduction to computational chemistry*; John wiley & sons: 2007.
- [130] Vosko, S. H.; Wilk, L.; Nusair, M. Accurate spin-dependent electron liquid correlation energies for local spin density calculations: a critical analysis. *Can. J. Phys.* **1980**, *58*, 1200-1211.
- [131] Becke, A. D. Density-functional exchange-energy approximation with correct asymptotic-behavior *Phys. Rev. A* **1988**, *38*, 3098-3100.

- [132] Perdew, J. P. Density-functional approximation for the correlation energy of the inhomogeneous electron gas *Phys. Rev. B* **1986**, *33*, 8822.
- [133] Lee, C.; Yang, W.; Parr, R. Development of the Colle-Salvetti correlation-energy formula into a functional of the electron density *Phys. Rev. B* **1988**, *37*, 785-789.
- [134] Perdew, J. P.; Burke, K.; Ernzerhof, M. Generalized gradient approximation made simple *Phys. Rev. Lett.* **1996**, *77*, 3865.
- [135] Stephens, P. J.; Devlin, F. J.; Chabalowski, C. F.; Frisch, M. J. Ab-Initio Calculation of Vibrational Absorption and Circular-Dichroism Spectra Using Density-Functional Force-Fields *J. Phys. Chem.* **1994**, *98*, 11623-11627.
- [136] Adamo, C.; Barone, V. Toward reliable adiabatic connection models free from adjustable parameters *Chem. Phys. Lett.* **1997**, *274*, 242-250.
- [137] Chai, J.-D.; Head-Gordon, M. Long-range corrected hybrid density functionals with damped atom-atom dispersion corrections *Phys. Chem. Chem. Phys.* **2008**, *10*, 6615-6620.
- [138] Schmidt, T.; Kraisler, E.; Kronik, L.; Kümmel, S. One-electron self-interaction and the asymptotics of the Kohn-Sham potential: an impaired relation *Phys. Chem. Chem. Phys.* **2014**, *16*, 14357-14367.
- [139] Yanai, T.; Handy, D. P. A new hybrid exchange-correlation functional using the Coulomb-attenuating method (CAM-B3LYP) *Chem. Phys. Lett.* **2004**, *393*, 51-57.
- [140] Rivero, P.; de P. R. Moreira, I.; Illasand, F.; Scuseria, G. E. Reliability of range-separated hybrid functionals for describing magnetic coupling in molecular systems *J. Chem. Phys.* **2008**, *129*, 184110.
- [141] Zhao, Y.; Truhlar, D. G. Density Functional for Spectroscopy: No Long-Range Self-Interaction Error, Good Performance for Rydberg and Charge-Transfer States, and Better Performance on Average than B3LYP for Ground States *J. Phys. Chem. A* **2006**, *110*, 13126-13130.
- [142] Klawohn, S.; Kaupp, M.; Karton, A. MVO-10: A Gas-Phase Oxide Benchmark for Localization/Delocalization in Mixed-Valence Systems *J. Chem. Theory Comput.* **2018**, *14*, 3512-3523.

- [143] Clark, A. E.; Davidson, E. R. Local spin *J. Chem. Phys.* **2001**, *115*, 7382-7392.
- [144] Herrmann, C.; Reiher, M.; Hess, B. A. Comparative Analysis of Local Spin Definitions *J. Chem. Phys.* **2005**, *122*, 034102.
- [145] Ramos-Cordoba, E.; Matito, E.; Mayer, I.; Salvador, P. Toward a Unique Definition of the Local Spin *J. Chem. Theory Comput.* **2012**, *8*, 1270-1279.
- [146] Bader, R. F. W. *Atoms in molecules: a quantum theory*; Oxford University Press: New York, 1994.
- [147] Davidson, E. R. Electronic Population Analysis of Molecular Wavefunctions *J. Chem. Phys.* **1967**, *46*, 3320-3324.
- [148] Reed, A. E.; Weinstock, R. B.; Weinhold, F. Natural population analysis *J. Chem. Phys.* **1985**, *83*, 735-746.
- [149] Ahlrichs, R. *et al.* "TURBOMOLE V7.0", software, University of Karlsruhe and Forschungszentrum Karlsruhe GmbH, 1989-2007, TURBOMOLE GmbH, since 2007, 2015.
- [150] Weigend, F.; Ahlrichs, R. Balanced basis sets of split valence, triple zeta valence and quadruple zeta valence quality for H to Rn: Design and assessment of accuracy *Phys. Chem. Chem. Phys.* **2005**, *7*, 3297-305.
- [151] Grimme, S. Semiempirical GGA-type density functional constructed with a long-range dispersion correction *J. Comput. Chem.* **2006**, *27*, 1787-1799.
- [152] Frisch, M. J. *et al.* "Gaussian 09 Revision A.1.", software, Gaussian Inc. Wallingford CT, 2009.
- [153] Miertuš, S.; Scrocco, E.; Tomasi, J. Electrostatic Interaction of a Solute with a Continuum. A Direct Utilization of ab initio Molecular Potentials for the Prevision of Solvent Effects *Chem. Phys.* **1981**, *55*, 117-129.
- [154] Cossi, M.; Barone, V.; Cammi, R.; Tomasi, J. Ab initio study of solvated molecules: A new implementation of the polarizable continuum model *Chem. Phys. Lett.* **1996**, *255*, 327-335.

- [155] Hanwell, M.; Curtis, D.; Lonie, D.; Vandermeersch, T.; Zurek, E.; Hutchison, G. Avogadro: an advanced semantic chemical editor, visualization, and analysis platform *J. Cheminf.* **2012**, *4*, 1-17.
- [156] Schaftenaar, G.; Noordik, J. H. Molden: a pre- and post-processing program for molecular and electronic structures *J. Comput. Aided Mol. Des.* **2000**, *14*, 123-134.
- [157] van Haare, J. A. E. H.; Havinga, E. E.; van Dongen, J. L. J.; Janssen, R. A. J.; Cornil, J.; Brédas, J.-L. Redox States of Long Oligothiophenes : Two Polarons on a Single Chain *Chem. Eur. J.* **1998**, *4*, 1509.
- [158] Neugebauer, J.; Hess, B. A. Fundamental vibrational frequencies of small polyatomic molecules from density-functional calculations and vibrational perturbation theory *J. Chem. Phys.* **2003**, *118*, 7215-7225.
- [159] Winter, R. F. Half-Wave Potential Splittings $\Delta E_{1/2}$ as a Measure of Electronic Coupling in Mixed-Valent Systems: Triumphs and Defeats *Organometallics* **2014**, *33*, 4517-4536.
- [160] Gilbert, M.; Albinsson, B. Photoinduced charge and energy transfer in molecular wires *Chem. Soc. Rev.* **2015**, *44*, 845-862.
- [161] Jahnke, A. C.; Proppe, J.; Spulber, M.; Palivan, C. G.; Herrmann, C.; Wenger, O. S. Charge Delocalization in an Organic Mixed Valent Bithiophene Is Greater Than in a Structurally Analogous Biselenophene *J. Phys. Chem. A* **2014**, *118*, 11293-11303.
- [162] Wang, D.; Talipov, M. R.; Ivanov, M. V.; Rathore, R. Energy gap between the poly-*p*-phenylene bridge and donor groups controls the hole delocalization in donor-bridge-donor wires *J. Am. Chem. Soc.* **2016**, *138*, 16337-16344.
- [163] Solomon, G. C.; Andrews, D. Q.; Goldsmith, R. H.; Hansen, T.; Wasielewski, M. R.; Dwyne, R. P. V.; Ratner, M. A. Quantum Interference in Acyclic Systems: Conductance of Cross-Conjugated Molecules *J. Am. Chem. Soc.* **2008**, *130*, 17301-17308.
- [164] Segal, D.; Nitzan, A.; Ratner, M.; Davis, W. B. Activated Conduction in Microscopic Molecular Junctions *J. Phys. Chem. B* **2000**, *104*, 2790-2793.

- [165] Herrmann, C.; Elmisz, J. Electronic communication through molecular bridges *Chem. Commun.* **2013**, *49*, 10456-10458.
- [166] Proppe, J.; Herrmann, C. Communication through molecular bridges: Different bridge orbital trends result in common property trends *J. Comput. Chem.* **2015**, *36*, 201-209.
- [167] Hansen, T.; Solomon, G. C.; Andrews, D. Q.; Ratner, M. A. Interfering pathways in benzene: An analytical treatment *J. Chem. Phys.* **2009**, *131*, 194704.
- [168] Solomon, G. C.; Herrmann, C.; Hansen, T.; Mujica, V.; Ratner, M. A. Chemical structures and tunnelling pathways: When currents through molecules don't follow bonds *Nat. Chem.* **2010**, *2*, 223-228.
- [169] Ke, S.-H.; Yang, W.; Baranger, H. U. Quantum-Interference-Controlled Molecular Electronics *Nano Lett.* **2008**, *8*, 3257-3261.
- [170] Markussen, T.; Stadler, R.; Thygesen, K. S. The relation between structure and quantum interference in single molecule junctions *Nano Lett.* **2010**, *10*, 4260-4265.
- [171] Patoux, C.; Coudret, C.; Launay, J.-P.; Joachim, C.; Gourdon, A. Topological Effects on Intramolecular Electron Transfer via Quantum Interference *Inorg. Chem.* **1997**, *36*, 5037-5049.
- [172] Sautet, P.; Joachim, C. Electronic Interference Produced by a Benzene Embedded in a Polyacetylene Chain *Chem. Phys. Lett.* **1988**, *153*, 511-516.
- [173] Tsuji, Y.; Hoffmann, R.; Strange, M.; Solomon, G. C. Close relation between quantum interference in molecular conductance and diradical existence *Proceedings of the National Academy of Sciences* **2016**, *113*, E413-E419.
- [174] Tsuji, Y.; Hoffmann, R.; Movassagh, R.; Datta, S. Quantum interference in polyenes *J. Chem. Phys.* **2014**, *141*, 224311.
- [175] Lineberger, W. C.; Borden, W. T. The synergy between qualitative theory, quantitative calculations, and direct experiments in understanding, calculating, and measuring the energy differences between the lowest singlet

- and triplet states of organic diradicals *Phys. Chem. Chem. Phys.* **2011**, *13*, 11792–11813.
- [176] Borden, W. T.; Davidson, E. R. Effects of electron repulsion in conjugated hydrocarbon diradicals *J. Am. Chem. Soc.* **1977**, *99*, 4587–4594.
- [177] Borden, W. T.; Iwamura, H.; Berson, J. A. Violations of Hund’s rule in non-Kekule hydrocarbons: theoretical prediction and experimental verification *Acc. Chem. Res.* **1994**, *27*, 109–116.
- [178] Wartini, A. R.; Valenzuela, J.; Staab, H. A.; Neugebauer, F. A. Intramolecular Electron Transfer between 2, 5-Dimethoxy-1, 4-phenylene Units in [*nn*] Paracyclophane Radical Cations *Eur. J. Org. Chem.* **1998**, *1998*, 139–148.
- [179] Wu, X.; Davis, A. P.; Lambert, P. C.; Kraig Steffen, L.; Toy, O.; Fry, A. J. Substituent effects on the redox properties and structure of substituted triphenylamines. An experimental and computational study *Tetrahedron* **2009**, *65*, 2408 - 2414.
- [180] Lloveras, V.; Vidal-Gancedo, J.; Ruiz-Molina, D.; Figueira-Duarte, T. M.; Nierengarten, J.-F.; Veciana, J.; Rovira, C. Influence of bridge topology and torsion on the intramolecular electron transfer *Faraday Discuss.* **2006**, *131*, 291–305.
- [181] Rovira, C.; Ruiz-Molina, D.; Elsner, O.; Vidal-Gancedo, J.; Bonvoisin, J.; Launay, J.-P.; Veciana, J. Influence of Topology on the Long-Range Electron-Transfer Phenomenon *Chem.–Eur. J.* **2001**, *7*, 240–250.
- [182] Lloveras, V.; Vidal-Gancedo, J.; Figueira-Duarte, T. M.; Nierengarten, J.-F.; Novoa, J. J.; Mota, F.; Ventosa, N.; Rovira, C.; Veciana, J. Tunneling versus Hopping in Mixed-Valence Oligo-p-phenylenevinylene Polychlorinated Bis(triphenylmethyl) Radical Anions *J. Am. Chem. Soc.* **2011**, *133*, 5818-5833.
- [183] Franco, C.; Burrezo, P. M.; Lloveras, V.; Caballero, R.; Alcón, I.; Bromley, S. T.; Mas-Torrent, M.; Langa, F.; López Navarrete, J. T.; Rovira, C.; Casado, J.; Veciana, J. Operative Mechanism of Hole-Assisted Negative Charge Motion in Ground States of Radical-Anion Molecular Wires *J. Am. Chem. Soc.* **2017**, *139*, 686-692.

- [184] Fung, E.-D.; Gelbwaser, D.; Taylor, J.; Low, J.; Xia, J.; Davydenko, I.; Campos, L. M.; Marder, S.; Peskin, U.; Venkataraman, L. Breaking Down Resonance: Nonlinear Transport and the Breakdown of Coherent Tunneling Models in Single Molecule Junctions *Nano Lett.* **2019**, *19*, 2555-2561.
- [185] Nelsen, S. F.; Konradsson, A. E.; Weaver, M. N.; Telo, J. P. Intervalence Near-IR Spectra of Delocalized Dinitroaromatic Radical Anions *J. Am. Chem. Soc.* **2003**, *125*, 12493-12501.
- [186] Nelsen, S. F.; Weaver, M. N.; Konradsson, A. E.; Telo, J. P.; Clark, T. Electron Transfer within 2,7-Dinitronaphthalene Radical Anion *J. Am. Chem. Soc.* **2004**, *126*, 15431-15438.
- [187] Nelsen, S. F.; Weaver, M. N.; Zink, J. I.; Telo, J. P. Optical Spectra of Delocalized Dinitroaromatic Radical Anions Revisited *J. Am. Chem. Soc.* **2005**, *127*, 10611-10622.
- [188] Nelsen, S. F.; Weaver, M. N.; Telo, J. P. Solvent Control of Charge Localization in 11-Bond Bridged Dinitroaromatic Radical Anions *J. Am. Chem. Soc.* **2007**, *129*, 7036-7043.
- [189] Jozefiak, T. H.; Almlöf, J. E.; Feyereisen, M. W.; Miller, L. L. Mixed-valence, conjugated semiquinones *J. Am. Chem. Soc.* **1989**, *111*, 4105-4106.
- [190] Rak, S. F.; Miller, L. L. Mixed-valence, conjugated quinone and imide anion radicals. An ESR investigation *J. Am. Chem. Soc.* **1992**, *114*, 1388-1394.
- [191] Gautier, N.; Dumur, F.; Lloveras, V.; Vidal-Gancedo, J.; Veciana, J.; Rovira, C.; Hudhomme, P. Intramolecular Electron Transfer Mediated by a Tetrathiafulvalene Bridge in a Purely Organic Mixed-Valence System *Angewandte Chemie* **2003**, *115*, 2871-2874.
- [192] Blumberger, J. Recent Advances in the Theory and Molecular Simulation of Biological Electron Transfer Reactions *Chem. Rev.* **2015**, *115*, 11191-11238.

- [193] Kröncke, S.; Herrmann, C. Toward a First-Principles Evaluation of Transport Mechanisms in Molecular Wires *J. Chem. Theory Comput.* **2020**, *16*, 6267–6279.
- [194] Whittleton, S. R.; Vazquez, X. A. S.; Isborn, C. M.; Johnson, E. R. Density-functional errors in ionization potential with increasing system size *J. Chem. Phys.* **2015**, *142*, 184106.
- [195] Sun, H.; Autschbach, J. Influence of the Delocalization Error and Applicability of Optimal Functional Tuning in Density Functional Calculations of Nonlinear Optical Properties of Organic Donor–Acceptor Chromophores *Chem. Phys. Chem.* **2013**, *14*, 2450–61.
- [196] Brédas, J. L.; Street, G. B.; Thémans, B.; André, J. M. Organic polymers based on aromatic rings (polyparaphenylene, polypyrrole, polythiophene): Evolution of the electronic properties as a function of the torsion angle between adjacent rings *J. Chem. Phys.* **1985**, 1323.
- [197] Frei, M.; Aradhya, S. V.; Koentopp, M.; Hybertsen, M. S.; Venkataraman, L. Mechanics and Chemistry: Single Molecule Bond Rupture Forces Correlate with Molecular Backbone Structure *Nano Lett.* **2011**, *11*, 1518–1523.
- [198] Seminario, J. M.; Zacarias, A. G.; Tour, J. M. Theoretical Interpretation of Conductivity Measurements of a Thiitolane Sandwich. A Molecular Scale Electronic Controller *J. Am. Chem. Soc.* **1998**, *120*, 3970–3974.
- [199] Khairul, W. M.; Fox, M. A.; Schauer, P. A.; Yufit, D. S.; Albesa-Jové, D.; Howard, J. A. K.; Low, P. J. The electronic structures of diruthenium complexes containing an oligo(phenylene ethynylene) bridging ligand, and some related molecular structures *Dalton T.* **2010**, *39*, 11605.
- [200] Perrin, M. L.; Verzijl, C. J.; Martin, C. A.; Shaikh, A. J.; Eelkema, R.; Van Esch, J. H.; Van Ruitenbeek, J. M.; Thijssen, J. M.; Van Der Zant, H. S.; Dulić, D. Large tunable image-charge effects in single-molecule junctions *Nat. Nanotechnol.* **2013**, *8*, 282–287.
- [201] Peng, G.; Strange, M.; Thygesen, K. S.; Mavrikakis, M. Conductance of Conjugated Molecular Wires: Length Dependence, Anchoring Groups, and Band Alignment *J. Phys. Chem. C* **2009**, *113*, 20967–20973.

- [202] Heimel, G.; Romaner, L.; Zojer, E.; Bredas, J.-L. The Interface Energetics of Self-Assembled Monolayers on Metals *Acc. Chem. Res.* **2008**, *41*, 721-729.
- [203] Obersteiner, V.; Egger, D. A.; Zojer, E. Impact of Anchoring Groups on Ballistic Transport: Single Molecule vs Monolayer Junctions *J. Phys. Chem. C* **2015**, *119*, 21198-21208.
- [204] Hofmann, O. T.; Egger, D. A.; Zojer, E. Work-Function Modification beyond Pinning: When Do Molecular Dipoles Count? *Nano Lett.* **2010**, *10*, 4369-4374.
- [205] Lazić, P.; Alaei, M.; Atodiresei, N.; Caciuc, V.; Brako, R.; Blügel, S. Density functional theory with nonlocal correlation: A key to the solution of the CO adsorption puzzle *Phys. Rev. B* **2010**, *81*, 045401.
- [206] Janthon, P.; Vines, F.; Sirijaraensre, J.; Limtrakul, J.; Illas, F. Adding Pieces to the CO/Pt(111) Puzzle: The Role of Dispersion *J. Phys. Chem. C* **2017**, *121*, 3970-3977.
- [207] Patra, A.; Peng, H.; Sun, J.; Perdew, J. P. Rethinking CO adsorption on transition-metal surfaces: Effect of density-driven self-interaction errors *Phys. Rev. B* **2019**, *100*, 035442.
- [208] Bahlke, M. P.; Wahl, P.; Diekhöner, L.; Herrmann, C. Co(CO)_n/Cu(001): Towards understanding chemical control of the Kondo effect *J. Appl. Phys.* **2019**, *125*, 142910.
- [209] Liu, Z.-F.; Egger, D. A.; Refaely-Abramson, S.; Kronik, L.; Neaton, J. B. Energy level alignment at molecule-metal interfaces from an optimally tuned range-separated hybrid functional *J. Chem. Phys.* **2017**, *146*, 092326.
- [210] Liu, Z.-F.; da Jornada, F. H.; Louie, S. G.; Neaton, J. B. Accelerating GW-Based Energy Level Alignment Calculations for Molecule–Metal Interfaces Using a Substrate Screening Approach *J. Chem. Theory Comput.* **2019**, *15*, 4218–4227.
- [211] Hush, N.; Cheungand, A. Ionization potentials and donor properties of nucleic acid bases and related compounds *Chem. Phys. Lett.* **1975**, *34*, 11-13.

- [212] Lambert, C.; Nöll, G. The Class II/III Transition in Triarylamine Redox Systems *J. Am. Chem. Soc.* **1999**, *121*, 8434.
- [213] Dewar, M. J. S.; Zoebisch, E. G.; Healy, E. F.; Stewart, J. J. P. Development and use of quantum mechanical molecular models. 76. AM1: a new general purpose quantum mechanical molecular model *J. Am. Chem. Soc.* **1985**, *107*, 3902-3909.
- [214] Stewart, J. J. Optimization of parameters for semiempirical methods V: modification of NDDO approximations and application to 70 elements *J. Mol. Model.* **2007**, *13*, 1173-1213.
- [215] Zheng, G.; Witek, H. A.; Bobadova-Parvanova, P.; Irle, S.; Musaev, D. G.; Prabhakar, R.; Morokuma, K.; Lundberg, M.; Elstner, M.; Köhler, C.; Frauenheim, T. Parameter Calibration of Transition-Metal Elements for the Spin-Polarized Self-Consistent-Charge Density-Functional Tight-Binding (DFTB) Method: Sc, Ti, Fe, Co, and Ni *J. Chem. Theory Comput.* **2007**, *3*, 1349-1367.
- [216] Foster, M. E.; Sohlberg, K. Empirically corrected DFT and semi-empirical methods for non-bonding interactions *Phys. Chem. Chem. Phys.* **2010**, *12*, 307-322.
- [217] Zheng, G.; Witek, H. A.; Bobadova-Parvanova, P.; Irle, S.; Musaev, D. G.; Prabhakar, R.; Morokuma, K.; Lundberg, M.; Elstner, M.; Köhler, C.; Frauenheim, T. Parameter Calibration of Transition-Metal Elements for the Spin-Polarized Self-Consistent-Charge Density-Functional Tight-Binding (DFTB) Method: Sc, Ti, Fe, Co, and Ni *J. Chem. Theory Comput.* **2007**, *3*, 1349-1367.
- [218] Pecher, L.; Tonner, R. Deriving bonding concepts for molecules, surfaces, and solids with energy decomposition analysis for extended systems *WIREs Comput. Mol. Sci.* **2019**, *9*, e1401.
- [219] Hirshfeld, F. L. Bonded-atom fragments for describing molecular charge densities *Theor. Chem. Acc.* **1977**, 129-138.

Declaration on oath

I hereby declare upon oath that I have written the present dissertation independently and have not used further resources and aids than those stated. The written version submitted corresponds to the one on the electronic storage medium. I hereby declare that I have not previously applied for a doctorate (PhD studies) with this thesis.

Eidesstaatliche Versicherung

Hiermit versichere ich an Eides statt, die vorliegende Dissertation selbst verfasst und keine anderen als die angegebenen Hilfsmittel benutzt zu haben. Die eingereichte schriftliche Fassung entspricht der auf dem elektronischen Speichermedium. Ich versichere, dass diese Dissertation nicht in einem früheren Promotionsverfahren eingereicht wurde

Hamburg, 20. Januar 2021

Susanne Kröncke